

**Bergische Universität Wuppertal**

# Simulation of Ion Dynamics in Atmospheric Pressure Ionization Sources

## **Dissertation**

zur Erlangung des akademischen Grades  
Doktor der Naturwissenschaften (Dr. rer. nat.)

vorgelegt von

Walter Wißdorf

Bergische Universität Wuppertal  
Fachbereich C - Mathematik und Naturwissenschaften  
Physikalische und Theoretische Chemie

Wuppertal 2014

Die Dissertation kann wie folgt zitiert werden:

urn:nbn:de:hbz:468-20141009-103409-0

[<http://nbn-resolving.de/urn/resolver.pl?urn=urn%3Anbn%3Ade%3Ahbz%3A468-20141009-103409-0>]

## **Danksagung**

Niemand schreibt eine solche Arbeit aus sich heraus, sondern die Umstände bieten eine Gelegenheit. Ohne diese, von Menschen bestimmten, Umstände gäbe es diese Arbeit nicht.

Ich möchte diesen Menschen danken: Jeder von ihnen kennt seinen Anteil an dieser Arbeit und meinem Leben. Danke für alle diese Anteile, egal wie groß oder klein sie sein mögen. Fehlte auch nur einer, alles wäre anders. Sie definieren, wer und was ich bin.

*Unsere Taten sind nur Würfe in des Zufalls blinde Nacht*  
- Franz Grillparzer

# Erklärung

“Ich versichere an Eides statt, dass ich die von mir vorgelegte Arbeit selbstständig angefertigt und andere als die angegebenen Hilfsmittel nicht benutzt sowie jede wörtlich oder inhaltlich übernommene Stelle kenntlich gemacht habe.”

Neuss, den 13.07.2014

Walter Wißdorf

## Abstract

Over the last three decades, the numerical simulation of ion trajectories within collision free environments was established as basis for the design of mass analyzers, electrostatic lenses and other ion optical devices. With the advent of atmospheric pressure ionization (API), ions are generated at elevated background gas pressures and in chemically reactive environments. Today, numerical simulations of charged particles have to consider physical and chemical interactions with the background gas. At the same time, the continuously increasing performance of modern computer systems allows to apply computationally demanding numerical models on such simulation problems. In this work, the motion of gas phase ions at atmospheric and intermediate pressure is simulated to investigate the performance, validity and applicability of numerical methods for typical simulation problems in API. Furthermore, new numerical models are developed to simulate the chemical dynamics of charged particles in reactive environments.

This work is structured in three sections: First, two established numerical approaches, particle tracing in SIMION with the Statistical Diffusion Simulation (SDS) extension and electrokinetic flow simulation in Comsol Multiphysics, are validated with a benchmark experiment. A bulk gas flow simulation performed in Comsol serves as input for both ion migration models. The SIMION calculation reproduces the experimental result well, while the electrokinetic flow simulation exhibits a significantly lower validity. Second, the ion migration in a complex commercial ion source (MPIS) is simulated with SIMION/SDS. A validated simulation of the complex bulk gas flow, which is required as input, is available from a joint research project. The comprehensive set of SIMION/SDS simulations reproduces the experimental spatially resolved ion signal (DIA) in the ion source very well. This demonstrates that the simulation approach is valid. In contrast, the temporal evolution of the ion signal is not well reproduced by the simulations. Rationales for the discrepancies are discussed and assessed with proof-of-concept calculations.

In the third part, Reaction Simulation (RS), a module for the Monte-Carlo simulation of chemical kinetics of ions, is presented. The dynamics of proton bound water clusters are simulated with RS to describe the observed drift of the Reactant Ion Peak in Ion Mobility Spectrometry. Comparison with experimental data validates the simulation results gathered with RS. Furthermore, RS is expanded with a model for the increasing effective ion temperature at elevated electrical fields. With this extension the simulation of high field ion dynamics and chemical kinetics with significant electrical heating of ions is possible with RS, allowing the simulation of ion dynamics in e.g. RF ion guides or ion funnels. The validity of the modified RS module is assessed by comparing simulations of high field devices (e.g., collision cells, differential ion mobility analyzers) with literature data.

The simulations performed in this work require the transfer of data from gas dynamics calculations to the ion dynamics models. This is achieved with custom programs which are described in detail. The analysis of raw simulation data and the visualiza-

tion of the calculation results is also conducted with custom software. Particularly, a web based data browser (DIA explorer) is presented, which visualizes calculated and experimental DIA in a complex multidimensional parameter space.

This work demonstrates the feasibility of the developed numerical methods for productive ion dynamics simulations, for example in the domains of instrument design and fundamental research and outlines future development opportunities.

# Contents

<b>1</b>	<b>Introduction</b>	<b>1</b>
1.1	Background . . . . .	1
1.2	Scope and aim of this work . . . . .	3
<b>2</b>	<b>Dynamics of gas phase ions at atmospheric pressure</b>	<b>4</b>
2.1	Introduction . . . . .	4
2.2	Ion transport at atmospheric pressure . . . . .	5
2.2.1	Ion transport by electric and magnetic fields . . . . .	5
2.2.2	Ion transport by diffusion and convection in flowing gas . . . . .	7
2.2.3	Convection, diffusion and migration: Nernst-Planck equations - electrokinetic transport . . . . .	8
2.2.4	The bulk gas flow: Navier-Stokes equations . . . . .	9
2.3	Chemical transformations . . . . .	10
<b>3</b>	<b>Approaches of gas phase ion simulation at AP</b>	<b>14</b>
3.1	Continuum model . . . . .	16
3.2	Numerical solution of PDE problems by discretization . . . . .	17
3.2.1	Finite element method . . . . .	17
3.2.2	Finite volume method . . . . .	20
3.2.3	Finite differences method . . . . .	21
3.3	Particle tracing models . . . . .	22
3.3.1	Interaction with background gas particles / Collision models . . . . .	23
3.3.2	Space charge handling . . . . .	26
<b>4</b>	<b>Software Packages</b>	<b>30</b>
4.1	Comsol Multiphysics . . . . .	30
4.2	SIMION charged particle simulator . . . . .	31
<b>5</b>	<b>Simulation of ion migration in a slow gas flow</b>	<b>33</b>
5.1	Introduction / Motivation . . . . .	33
5.2	Experimental verification . . . . .	34
5.3	Numerical Models . . . . .	36
5.3.1	Simulation of the fluid flow (CFD) . . . . .	36
5.3.2	Electrokinetic flow simulation . . . . .	37
5.3.3	Particle tracing simulation . . . . .	39

5.4	Results . . . . .	42
5.4.1	Experimental verification . . . . .	42
5.4.2	Numerical Results . . . . .	44
5.5	Conclusions . . . . .	61
<b>6</b>	<b>Simulation of ion acceptance distributions (DIA)</b>	<b>64</b>
6.1	Introduction . . . . .	64
6.2	Experimental . . . . .	65
6.2.1	Photoionization . . . . .	65
6.2.2	Atmospheric Pressure Laser Ionization . . . . .	67
6.2.3	Measurement Principle . . . . .	68
6.2.4	AP Ion source and MS setup . . . . .	69
6.2.5	Experimental determination of DIAs . . . . .	74
6.3	Numerical Model and Simulation . . . . .	76
6.3.1	CFD model of the MPIS . . . . .	76
6.3.2	CFD result data transformation . . . . .	79
6.3.3	Ion migration simulation . . . . .	81
6.4	DIA Visualization . . . . .	85
6.4.1	Interactive DIA visualization: Web DIA Explorer . . . . .	86
6.5	Results . . . . .	86
6.5.1	CFD Simulations: Bulk gas flow in MPIS . . . . .	87
6.5.2	DIA Simulations: Effects of ion source parameters . . . . .	90
6.5.3	Ion trajectories . . . . .	100
6.5.4	Effects of simulation parameters . . . . .	101
6.5.5	3d DIA . . . . .	108
6.5.6	Ion transfer times . . . . .	110
6.6	Numerical Costs . . . . .	115
6.7	Conclusions . . . . .	117
<b>7</b>	<b>Simulation of reacting ions at AP</b>	<b>120</b>
7.1	Reaction Simulation (RS), a monte carlo model for chemical reactions . . . . .	121
7.1.1	Linearized reaction probability model . . . . .	121
7.1.2	RS implementation . . . . .	123
7.2	Simulation of the proton bound water cluster RIP in AP-IMS . . . . .	125
7.2.1	Ion Mobility Spectrometry . . . . .	126
7.2.2	Proton bound water-cluster Reactant Ion Peak (RIP) . . . . .	128
7.2.3	Experimental determination of the water cluster RIP drift time . . . . .	130
7.2.4	Numerical Models . . . . .	131
7.2.5	Results . . . . .	134
7.2.6	Conclusions . . . . .	146
7.3	An outlook towards ion temperature simulation . . . . .	147
7.3.1	Ion temperature model . . . . .	148
7.3.2	Model examples . . . . .	152

*Contents*

7.3.3 Conclusions . . . . .	164
<b>8 Final conclusions and outlook</b>	<b>166</b>
<b>9 Appendix</b>	<b>169</b>
9.1 Deduction of viscous damping . . . . .	169
9.2 Linearization of reaction probabilities . . . . .	170
<b>Glossary</b>	<b>174</b>
<b>List of Symbols</b>	<b>176</b>
<b>Bibliography</b>	<b>181</b>

# 1 Introduction

## 1.1 Background

Analytical methods to investigate the molecular nature of substance samples are essential for many disciplines in the natural sciences and also for numerous applied fields, for example engineering or modern industrial processes. Therefore, chemical analysis has achieved its status as distinct and significant discipline among the diverse fields of chemistry. Naturally, there is a common theme observable in the development of chemical analytics: The samples becomes increasingly complex while the concentration of individual compounds in the sample (the *analytes*) is even declining.

One of the most important methods to face both challenges is the weighing of individual molecules, which is termed *mass spectrometry* (MS) more formally. The particle mass is a fundamental characteristic of atoms and molecules. It can be used to identify distinct particles in a complex mixture, but this is only one application of MS. In fact, there is a whole family of sophisticated mass spectrometric methods, which are able to identify the composition and structure of molecules of virtually all sizes. It is for example possible to unequivocally determine the elemental composition of an unknown molecule from high resolution mass spectrometry.

In principal, a mass spectrometer is a device, which separates particles (atoms or molecules) according to their masses and subsequently detects them. In reality, there are many types of mass separating devices (mass analyzers), which rely on different basic principles, but all mass analyzer types share one common characteristic: They use *electromagnetic forces* for the mass separation, thus they only separate charged particles (ions). In addition, they do not separate according to the particle mass  $m$ , but to the ratio of charge  $q$  and mass ( $m/q$ ). To analyze electrically neutral molecules with mass spectrometry, the sample molecules have to be converted to molecular ions, which is generally a complex physicochemical process. It follows that the choice and parameterization of the sample ionization is generally an integral part of the development of a mass spectrometric analysis method. The investigation and optimization of ionization techniques is therefore in itself an interesting and rich research field.

There is a second shared characteristic within mass spectrometers: High vacuum conditions are required in the mass analyzer region. All common mass analyzer designs perform the mass separation by forcing the ions on mass to charge ratio ( $m/q$ ) dependent trajectories. Collisions with background gas particles would scatter the ions and the ion trajectories would disperse, which would in turn adversely affect the mass

## 1 Introduction

separation. Therefore, the background gas pressure has to be sufficiently low, so that the mean free ion path in the mass analyzer is longer than the ion trajectories. Typical background gas pressures in common mass analyzers are in the range of  $10^{-3}$  mbar for some types of ion traps down to  $10^{-10}$  mbar for ion cyclotron resonance analyzers [1].

The low pressure requirement is a particular challenge for the design of mass spectrometric equipment, because today ionization is performed predominantly at atmospheric pressure (AP). The combination of atmospheric pressure ionization (API) methods with mass spectrometry (API-MS) has a number of benefits: Particularly, the hyphenation with pre-separation stages as for example liquid chromatography (LC) [2, 3] and the non-destructive ionization of large biomolecules with electrospray ionization (ESI) [1, 2, 4] has led to the importance API methods have today.

Despite its wide application, API remains challenging though: A substance sample has to be vaporized and the analytes have to be ionized, ideally with high specificity, to mask unwanted components in the sample which in turn reduces the complexity of the analysis. Subsequently, the analyte ions have to be separated from the background bulk gas and have to be efficiently transferred into the high vacuum region of the mass analyzer. The required reduction of the background pressure by many orders of magnitude is typically performed in multiple differential pumping stages. The analyte ions, which should reach the mass analyzer region as efficiently as possible, are electrically extracted from the bulk gas. They are actively guided to the downstream pressure reduction stages, while the bulk gas is pumped away.

In general, this transfer process results in severe ion losses. The ion current reaching the detector is often orders of magnitude smaller than the initial ion current generated in the ion source. Therefore, the whole ionization and ion transfer process offers opportunities for significant optimizations, which in turn lead to considerable improvements of analytical methods. Due to the high complexity of the interactions of ions with each other, the background gas and the present electro-magnetic fields, the ion dynamics at atmospheric and medium pressure ( $4$  to  $1 \times 10^{-1}$  mbar) conditions are generally difficult to describe. Thus, the design of mass spectrometers was often performed by “trial and error” in the past.

Fortunately, the continuously growing performance of computing hardware and theoretical models has reached a level, which allow the simulation of basic ion dynamics at elevated pressure has become feasible; even on affordable, advanced consumer class computer systems. This opens a promising way to gain a deeper understanding of the complex and often surprising dynamics in existing ion optical devices. Such knowledge would be a valuable foundation for the concept of new mass spectrometric systems, which would be then designed in a model driven process which is probably more productive than the former “trial and error” approach.

## 1.2 Scope and aim of this work

The scope of this work was the investigation of the dynamics of small gas phase molecular ions and ion-bound clusters in ion sources at atmospheric or near atmospheric pressure conditions. In this work the term “ion dynamics” refers to the transport of charged particles considering the effects of electrical fields, bulk gas flows, as well as their interactions with the bulk gas particles including the “chemical dynamics”. This latter term refers to chemical transformations of ions and charged clusters caused by reactive collisions with bulk gas components in addition to molecular effects induced by the electrical field.

Due to the very low ion concentrations relative to the abundance of bulk gas particles at AP phenomena occurring in highly ionized plasmas [5] or related to magnetohydrodynamics [6] are intentionally excluded from this work. The ion current and the kinetic energies of the charged particles considered here are sufficiently low, so that the magnetic field generated by the particles is not relevant for their motion. In addition, the low ion concentrations renders the effect of the ion motion on the bulk gas flow in AP ion sources (bulk gas flow heating, change of bulk gas flow velocity field, effect of the “ion wind”) insignificant. Therefore, the bulk gas flow is generally considered fully decoupled from the ion motion for the conditions discussed in this work. In short, this work investigated diluted gas phase ions in neutral background gas flows rather than the dynamics of an ionic fluid.

The initial goal of this work was the application of numerical methods to provide a basic set of tools for routine modeling the ion dynamics in AP ion sources. To achieve this goal, the existing methods were adapted to the specific requirements of this problem. The adapted numerical model results were then compared with experimental data and the validity of different modeling approaches were critically assessed.

In addition to validation of the simulation methods, the modeling results were used to gain insight into the complex dynamics in an existing AP ion source, the Multi Purpose Ion Source - MPIS. This led directly to a new ion source design which was later shown to have an improved analytical performance.

Finally, one of the existing numerical methods, the particle tracing with the statistical diffusion simulation (SDS) approach, was substantially extended by a model of chemical reactions of gas phase ions. This extended approach was successfully used to describe the extremely fast reaction kinetics of ion-bound clusters in the drift region of an atmospheric pressure ion mobility spectrometer (IMS).

Therefore it was possible to significantly widen the scope of the adapted and validated numerical models, which potentially opens whole new application fields for the simulation of ion dynamics.

## 2 Dynamics of gas phase ions at atmospheric pressure

### 2.1 Introduction

The dynamics of diluted electrically charged particles at elevated pressure conditions is complex. The particle motion is influenced by multiple, physically different forces, which are partly coupled to each other. In contrast to vacuum conditions, where the collisions of ions with background gas particles play only a minor role, if any, ion dynamics at AP is dominated by the intensive interaction of the diluted ions with the background gas.

This is rationalized by a comparison of the mean free path  $\lambda$  at different background pressures. The mean free path is defined as the mean distance a particle travels between the collisions with other particles. If ideal conditions are assumed (no severe deviations from the kinetic gas model [7, 8]) the mean free path in a gas is given by [7, p. 754] [1, p. 10]:

$$\lambda = \frac{\bar{c}}{z} = \frac{kT}{\sqrt{2}\sigma p} \quad (2.1)$$

with the mean particle velocity  $\bar{c}$ , the collision frequency of one particle  $z$ , the Boltzmann constant  $k$ , the thermodynamic temperature  $T$ , the pressure  $p$ , and the collision cross section  $\sigma$ , which is given by:

$$\sigma = \pi d^2 \quad (2.2)$$

with the collision diameter  $d$ , which is equal to the particle diameter for hard sphere particles. Nitrogen ( $N_2$ ) for example has a collision cross section of  $\sigma = 0.43 \text{ nm}^2$  [7, p. 753].

The collision frequency is calculated from the mean relative particle velocity  $\bar{c}_r$ , which is equal to  $\sqrt{2}\bar{c}$  [7, p.783 f.]:

$$z = \frac{\sigma \bar{c}_r p}{kT} = \sigma \bar{c}_r \mathcal{N} \quad (2.3)$$

In the present contexts, it is convenient to use the particle density, which is the number of particles  $N$  per volume  $V$ :  $\mathcal{N} = \frac{N}{V}$ .

The mean particle velocity of thermal particles, with a Maxwell-Boltzmann velocity

## 2.2 Ion transport at atmospheric pressure

distribution, is given by:

$$\bar{c} = \sqrt{\frac{8RT}{\pi M}} \quad (2.4)$$

with the universal gas constant  $R$  and the particle molar mass  $M$ .

At atmospheric pressure (1000 mbar) the mean free path in Nitrogen gas at 298 K is 67 nm, which corresponds to a collision frequency of  $7 \times 10^9 \text{ s}^{-1}$ . It is obvious that at AP conditions the collisions of ions with background gas particles and their interaction with the bulk gas can not be neglected under any circumstances. In contrast, at a typical residual pressure in a mass analyzer of about  $1 \times 10^{-5}$  mbar the mean free path is  $\lambda = 6.7 \text{ m}$  ( $z = 70 \text{ s}^{-1}$ ). In this pressure regime, most particles do not experience any collision and the background gas can safely be considered as non-existent.

Even though the assumption of strong dilution allows some significant simplifications, the description of gas phase ions at high pressures remains a complex multi-physical problem, due to the effects of the high collision frequency.

In the case of AP ion sources of chemical analytical equipment, the interesting ionic species are generally organic molecular ions or clusters of molecular ions and neutral particles (ion-bound clusters). Even a charged molecule basically stays a molecule, which can transform chemically. Therefore, the physical dynamics of gas phase ions is complemented by a number of possible chemical reactions with background gas components or with each other.

## 2.2 Ion transport at atmospheric pressure

### 2.2.1 Ion transport by electric and magnetic fields

Ions experience electromagnetic forces from external electric and magnetic fields. A point charge  $q_0$ , moving in an electric field  $\vec{E}$  and a magnetic field  $\vec{B}$  with the velocity  $\vec{v}$ , experiences an electrical force  $\vec{F}_e$  and a magnetic force  $\vec{F}_B$ , which adds to the electromagnetic Lorentz force  $\vec{F}$  [9]:

$$\vec{F} = \vec{F}_e + \vec{F}_m = q_0 (\vec{E} + \vec{v} \times \vec{B}) \quad (2.5)$$

Under collision free conditions and if gravity is neglected, this would be the sole force accelerating charged particles. In contrast, at elevated pressure, ions are scattered by frequent collisions with background gas particles. For both, electric and magnetic motion components, this has significant, but different, consequences.

In absence of collisions, a charged particle with a particle mass  $m$  and a charge  $q$  gyrates in a homogeneous magnetic field  $B$  on a circular trajectory, with a distinct *Cyclotron-frequency*  $\omega_c$  of [6]:

$$\omega_c = \frac{|q|}{m} B \quad (2.6)$$

The motion of ions in a partly ionized gas (a *plasma*) is called *magnetized* if an

## 2 Dynamics of gas phase ions at atmospheric pressure

ambient magnetic field is able to significantly change the ion trajectories, which would severely affect the ion dynamics. If the ion *Hall parameter*  $\delta$ , the ratio of Cyclotron-frequency and collision frequency  $z$ ,

$$\delta = \frac{\omega_c}{z} \quad (2.7)$$

is small, collisions dominate over the magnetic gyromotion. In this case, the ions are unmagnetized and the magnetic field component can safely be neglected [6, 10].

For a typical small molecular ion (ion mass  $m = 200$  u) at AP and in the presence of a very strong magnetic field (1 T), the Hall parameter would be approximately  $5 \cdot 10^{-4}$ . Therefore, the effects of external magnetic fields on the ion motion are generally ignored in this work.

From the Lorenz force follows that ions in a homogeneous electric field and in a collision free environment would accelerate in direction of the electric field. In the presence of background gas however, a cloud of ions reaches a steady *drift velocity*  $v_d$ , which is proportional to the field strength if the field is weak [11, 12]:

$$v_d = K\mathbf{E} \quad (2.8)$$

The constant  $K$  is called *ion mobility*. The actual ion mobility depends on the gas density  $\mathcal{N}$  of the background gas. For comparison, ion mobilities are generally given as *reduced ion mobility*  $K_0$ , which is normalized to a standard gas density  $\mathcal{N}_0$ , which is expressed in terms of a standard pressure  $p_0$  and a standard temperature  $T_0$ :

$$K_0 = K \frac{\mathcal{N}}{\mathcal{N}_0} = K \frac{T_0 p}{T p_0} \quad (2.9)$$

Electrostatics defines the negative gradient of the electric potential  $\Phi$  as the field strength (Gauss's law,  $E = -\nabla\Phi$ ) [9]. Therefore, the substance flux density  $\mathbf{J}_e$ , of a substance with the concentration  $c$ , driven by the electric force is [13]:

$$\mathbf{J}_e = -Kc\nabla\Phi \quad (2.10)$$

The simple assumption of a steady and field independent ion mobility is only valid for low field intensities or "weak" fields. The mean kinetic energy of the ions, which is gained on a free path between collisions with bulk gas particles, depends on the ratio of the electric field strength and the number density of the background gas particles  $E/\mathcal{N}$  [12, p. 4] [14]. It is beneficial to use this ratio as the *reduced field strength* for the characterization of the physical conditions in an actual device. The unit of the reduced field is the *Townsend* (Td) which is defined as  $1 \text{ Td} = 1 \times 10^{-17} \text{ V cm}^2$ .

With increasing field intensity the mean kinetic ion energy increases as well. If the kinetic energy from the field becomes significantly higher than the mean thermal kinetic energy of the charged particles, the simple relationship between field strength and drift velocity shown in Eq. 2.8 becomes invalid and the ion mobility develops a

## 2.2 Ion transport at atmospheric pressure

frequently complex dependence on the  $E/N$  ratio [12, 15]. Thus, the *low field mobility* is constant while the *high field mobility* is generally a function of the reduced field strength.

On a molecular scale, the presence of a high electrical field strength has some interesting consequences: With increasing field, the thermal kinetic energy of the ions becomes insignificant and their energy distribution becomes different from the thermal Maxwell-Boltzmann distribution. The velocity distribution of the charged particles, which would be equally distributed with respect to the spatial dimensions under low field conditions, becomes anisotropic. The strong electric field imprints two important components on the ion motion: A primary component parallel to the electric field and a random component which results from the ion scattering due to collisions with the bulk gas particles [15, 16].

There is no sharp boundary separating low- and high field conditions, but if the kinetic energy from the field is well below the thermal energy, low field conditions can safely be assumed. This is the case if

$$\left(\frac{M}{m} + \frac{m}{M}\right) eE\lambda \ll kT \quad (2.11)$$

where  $M$  and  $m$  are the molecular and ionic masses respectively and  $e$  is the ion charge [12, p. 4].

### 2.2.2 Ion transport by diffusion and convection in flowing gas

In addition to the electromagnetic forces, gas phase ions experience the same interactions with the bulk gas as diluted neutral gas particles. Therefore the basic transport phenomena induced by this interaction, *molecular diffusion* and *convection*, have to be considered as well, regardless of the charge state of the diluted particles.

On a molecular level, the thermal motion of gas particles in an ideal gas is random due to the extremely frequent collisions, which scatter the gas particles [8, 17]. The resulting random motion (“random walk”) of individual gas particles leads to the disappearance of concentration gradients because it is more likely that particles move from a region of higher concentration into a region with low concentration than in the inverse direction. The resulting mean transport phenomenon is called *diffusion* [18].

From a macroscopic perspective, the transport flux density  $\mathbf{J}_d$  of a species with the concentration  $c$  by diffusion is described by Fick’s Law [8]:

$$\mathbf{J}_d = -D\nabla c \quad (2.12)$$

The coefficient  $D$  between the concentration gradient and the transport flux density is called the *diffusion coefficient*. Under high field conditions this simple correlation changes as well: As a consequence of the non-maxwellian velocity distribution of the ions, the ion diffusion becomes anisotropic. The resulting diffusion tensor has differing components parallel and orthogonal to the electric field [16].

## 2 Dynamics of gas phase ions at atmospheric pressure

If the diffusion equation is substituted into the equation of continuity,

$$\frac{\partial c}{\partial t} = -\nabla \cdot \mathbf{J} \quad (2.13)$$

which describes the conservation of matter over the time  $t$  with a general transport flux density  $\mathbf{J}$ , the *diffusion equation* results (with the Laplace differential operator  $\nabla^2$ ):

$$\frac{\partial c}{\partial t} = D\nabla^2 c \quad (2.14)$$

Ultimately, the molecular diffusion would equalize all concentration differences in a given gas volume.

In addition to the diffusion transport by the undirected random motion of individual molecules, a diluted species can be transported by a macroscopic bulk gas flow, which is a directed motion of a whole gas particle ensemble. The material transport by a bulk gas flowing with a velocity  $\mathbf{u}$ , called the *convection* transport  $\mathbf{J}_c$ , is given by [7, p. 777]:

$$\mathbf{J}_c = c\mathbf{u} \quad (2.15)$$

The rate of concentration change due to convection is therefore given as:

$$\frac{\partial c}{\partial t} = -\nabla \cdot (c\mathbf{u}) \quad (2.16)$$

The diffusive and convective flux density can be combined to the net flux density  $\mathbf{J} = \mathbf{J}_d + \mathbf{J}_c$ . Substitution into the continuity equation (Eq. 2.13) yields the *generalized diffusion equation*, which describes the material transport by diffusion and convection [7, p. 778] [19, p. 25]:

$$\frac{\partial c}{\partial t} = D\nabla^2 c - \nabla \cdot (c\mathbf{u}) \quad (2.17)$$

### 2.2.3 Convection, diffusion and migration: Nernst-Planck equations - electrokinetic transport

The electric, convective and diffusive transport flux can be combined into the continuity equation yielding the *Nernst-Planck equation*, which describes the flux of an ionic species in a flowing fluid in the presence of a weak electric field [13, 20]:

$$\frac{\partial c}{\partial t} = D\nabla^2 c - \nabla \cdot (c\mathbf{u}) - Kc\nabla^2 \Phi \quad (2.18)$$

The resulting flow of the ionic species is referred to as *electrokinetic flow*.

### 2.2.4 The bulk gas flow: Navier-Stokes equations

It has become apparent in the previous sections, that the transport of charged particles under AP conditions depends strongly on the dynamics of the bulk gas flow. To describe an electrokinetic flow of ions, the velocity, temperature and pressure distribution of the flowing background gas has to be known.

A gas at atmospheric pressure can be described as a continuous *fluid* neglecting the molecular nature of the gas. This description is generally valid on a macroscopic scale, because the properties of a gas on this scale (pressure, velocity, density etc.) result from large, averaged gas particle ensembles.

Similarly to the considerations in the previous sections, the flow of a fluid is governed by a set of physical conservation laws [19]:

- The mass of the fluid is conserved.
- The momentum change rate is the sum of the forces acting on a fluid particle. A fluid particle in this context is the smallest volume element in which the assumption of a macroscopic fluid is valid and whose macroscopic properties are not affected by the molecular nature of the gas.
- The energy change is equal to the heat flow to and the rate of work performed by a fluid particle, which corresponds to the first law of thermodynamics.

If these conservations are thoroughly analyzed for a small fluid particle, a set of governing partial differential equations are derived, which describe the fluid flow quantitatively. This equation system is called *Navier-Stokes equations*. A detailed derivation would be beyond the scope of this work, but is found in most fluid dynamics textbooks (e.g. in [19, 21, 22]).

In the following, the Navier-Stokes equations for a Newtonian fluid are briefly shown in their conservative formulation as they are presented in [19]. A fluid is called *Newtonian* if the viscous stresses are proportional to the deformation rate, this proportionality is called dynamic *viscosity*  $\mu$  [8, 23, 24].

Mass conservation is given by the continuity of the density  $\rho$ :

$$\frac{\partial \rho}{\partial t} + \nabla \cdot (\rho \mathbf{u}) = 0 \quad (2.19)$$

With the velocity components  $(u, v, w)$ , the momentum equations in the three spatial dimensions  $(x, y, z)$  are given by:

$$\frac{\partial(\rho u)}{\partial t} + \nabla \cdot (\rho u \mathbf{u}) = -\frac{\partial p}{\partial x} + \nabla \cdot (\mu \nabla u) + S_{m_x} \quad (2.20)$$

$$\frac{\partial(\rho v)}{\partial t} + \nabla \cdot (\rho v \mathbf{u}) = -\frac{\partial p}{\partial y} + \nabla \cdot (\mu \nabla v) + S_{m_y} \quad (2.21)$$

$$\frac{\partial(\rho w)}{\partial t} + \nabla \cdot (\rho w \mathbf{u}) = -\frac{\partial p}{\partial z} + \nabla \cdot (\mu \nabla w) + S_{m_z} \quad (2.22)$$

## 2 Dynamics of gas phase ions at atmospheric pressure

The balance of the internal energy, with the internal thermal energy  $i$  of the fluid particle, is given by:

$$\frac{\partial(\rho i)}{\partial t} + \nabla \cdot (\rho i \mathbf{u}) = -p \nabla \cdot \mathbf{u} + \nabla \cdot (k \nabla T) + \Phi + S_{m_i} \quad (2.23)$$

The terms  $S_m$  are sources of momentum or energy respectively. The term  $\Phi$  in the energy equation is a dissipation function which reflects the energetic effects of viscous stresses in the fluid particle<sup>1</sup>.

To close the equation system, two equations of state have to be added. With the assumption of local thermodynamic equilibrium, the pressure of an ideal gas is given by the ideal gas law

$$p = \rho RT \quad (2.24)$$

The internal thermal energy of a perfect gas can be determined from the temperature and the heat capacity  $C_v$ :

$$i = C_v T \quad (2.25)$$

The quite complex system of general governing equations can be significantly simplified if the temperature or the density of the flowing fluid is assumed to be constant. If the density change in the fluid flow is small, the flow is called *incompressible*, which is a good approximation for liquids, but often this assumption is also true for relatively slow gas flows. Similarly, in the absence of significant heat sources or other temperature gradients, e.g. induced by compression, the fluid flow can be assumed as isothermal.

### 2.3 Chemical transformations

Even after ionization, molecular ions stay reactive chemical systems. In addition, the attractive electrostatic forces between ions and neutral but polar molecules often lead to a strongly increased reactivity. Chemical reactions can possibly change all characteristics of an ion. Common properties which are changed by chemical transformations are the charge state or the ion mass which generally corresponds to the size and thus to the mobility of an ion. The consideration of the chemical reaction kinetics is therefore essential for a comprehensive picture of the processes in an AP ion source.

Chemical reactions which happen in a single reaction step on a molecular scale are called *elementary reactions*. Such reaction steps can not be further subdivided and no intermediate species can be isolated. Energetically, only a single transition state is passed upon product formation via an elementary reaction [25].

In the most simple elementary reaction, a single reactant A reacts to a product P in a *unimolecular* Reaction:  $A \longrightarrow P$ .

If the concentration of component A is noted as  $[A]$ , its change rate  $\frac{dA}{dt}$ , which is called the reaction rate, is proportional to the concentration of A which is left at time  $t$ .

<sup>1</sup>The precise definition of  $\Phi$  and its connection to the viscosity can be found in [19, p. 24]

### 2.3 Chemical transformations

This relationship is given by a simple differential equation, which is called *differential rate law* in the context of chemical reaction kinetics [26]:

$$\frac{d[A]}{dt} = -k[A] \quad (2.26)$$

The proportionality  $k$ , which is temperature dependent, is called the *rate constant* of the reaction.

The rate law of a *bimolecular* elementary reaction with two reaction partners A and B ( $A + B \longrightarrow P$ ) is similar. In this case, the reaction rate is proportional to the product of the concentrations:

$$\frac{d[A]}{dt} = -k[A][B] \quad (2.27)$$

This basic pattern could be easily generalized for higher numbers of reaction partners, but it turns out that elementary reaction events with three reaction partners (*termolecular* reactions) are rare in the gas phase [27] and there are only a limited number of termolecular gas phase elementary reactions at all [28]. Gas phase elementary reactions with a higher molecularity than three are not known.

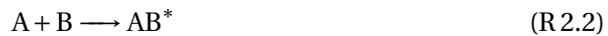
This limitation in molecularity of elementary reactions is caused by the extremely low probability of collisions with more than two simultaneously collision partners in the gas phase. A three body collision is quite rare, while collision events with more partners virtually never happen.

This observation is surprising at first glance, because most in essence bimolecular recombination reactions generally need a third, in itself unreactive, partner M which carries away the excess reaction energy, which is ultimately dissipated as heat to the bulk gas [29]:



In this reaction scheme, the excitation of a species is indicated by the asterisk. In fact, reactions with an inert collision partner, which is most probably  $N_2$  in an API source, do not proceed in a single elementary step. Instead, they are the net result of at least three elementary reactions [29, 30].

At first, the reactants A and B form a product AB, which is energetically excited:



This excited intermediate can either dissociate back to the reactants



or it can be energetically deactivated by a collision with an inert particle:



With the assumption of a short lifetime (i.e. less than a vibrational period of  $\leq 1$  ps) of

## 2 Dynamics of gas phase ions at atmospheric pressure

the excited product complex  $AB^*$ , which leads to a low steady state concentration of this intermediate, the reaction rate is given as [29]:

$$\frac{d[A]}{dt} = -\frac{k_1 k_3 [A][B][M]}{k_2 + k_3[M]} \quad (2.28)$$

where  $k_1$  is the reaction rate constant of reaction R 2.2,  $k_2$  of reaction R 2.3, and  $k_3$  of reaction R 2.4. Two interesting limiting cases are readily following: If the background pressure is very low  $[M]$  becomes small, the assumption  $[M]k_3 \ll k_2$  holds and the reaction rate becomes

$$\frac{d[A]}{dt} = -\frac{k_1 k_3}{k_2} [A][B][M] \quad (2.29)$$

This situation is referred to as the *low pressure limit* of the reaction. In analogy, if  $[M]$  becomes large and therefore  $[M]k_3 \gg k_2$ , the reaction is in the *high pressure limit*. In this case the rate law simplifies to

$$\frac{d[A]}{dt} = -k_1 [A][B] \quad (2.30)$$

More details on the pressure dependence of the presented termolecular mechanism and an analysis of the situation with additional reaction channels is found in chapter 4 of [30].

From a reaction kinetics point of view, the situation in an AP ion source is very different from that at low background pressure. In “vacuum”, and therefore virtually collision free conditions, ions are isolated and generally not in thermodynamic equilibrium with their environment. In fact, they are often relatively highly excited from the ionization process or the transfer into the vacuum, which is generally associated with highly energetic collisions of electrically accelerated ions with residual gas particles. Bimolecular reactions of molecular ions with other reaction partners do not take place in the low pressure region, simply because of the lack of reactive collisions. The consequence is that the primary reactions of ions in the vacuum region of an ion analytical device are unimolecular dissociation or isomerization processes, which are basically internal energy redistributions of the ions [31].

At atmospheric pressure conditions, the situation is at the other extreme. At low field conditions, the kinetic energy from the field is negligible to the thermal energy, thus the ions can be assumed to be in thermal equilibrium with the local environment. As apparent from the presented basic introduction to chemical reaction kinetics, the number of reactive collisions has to be high to have a significant turnover in bimolecular reactions of ions. This is the case if the number concentrations of potential reaction partners are high and the dwell time of the ions in the reactive zone is sufficiently long. Both is the case in AP ion sources. Even if the source is constantly purged with clean nitrogen gas, significant amounts of solvents, water, oxygen or similar impurities and trace substances are inevitable present in an AP ion source at appreciable mixing

### *2.3 Chemical transformations*

ratios (ppmV range). In combination with the long ion residence times due to the relatively low drift velocities at AP, the reaction kinetics are primarily characterized by the, potentially relatively slow, reactions of ions with the neutral background gas components.

### 3 Approaches of gas phase ion simulation at AP

It has become obvious that the dynamics of charged particles under atmospheric pressure is rather complex. Therefore, with exception of some extreme cases, there are no analytical or even simple approximate solutions to AP ion dynamic problems. Instead, they have to be solved with approximate numerical methods and the aid of modern computer systems.

The development and application of robust and efficient numerical algorithms for the solution of complex mathematical problems is a distinct interdisciplinary profession in itself. In the last three decades, the rapid increase of easily available computing power and the increasing efficiency of numerical algorithms have lead to an enormous increase in the relevance of numerical methods, because the problem complexity which can be handled has also drastically increased [32]. As a consequence of the broader application of numerical codes, their implementations have generally become more accessible and user-friendly. Today, there are commercial and also non-commercial open source numerical solver packages available, which allow the solution of rather complex physical problems with a large variety of algorithms and relatively low training requirements for the user.

A model, which is a reductionistic description of a physical phenomenon, is always approximate. The mathematical framework which is used to model complex physical objects, as for example the gas flow in an AP ion source, generally ignores or simplifies some aspects of the investigated phenomenon which are considered insignificant for the actual purpose of the model. An example for this general approach is the assumption of incompressibility for a low velocity, nearly isothermal gas flow. Because it is present in the underlying mathematical framework, both, purely analytical and also numerical models suffer from this basic *model error*.

However, there are some remarkable differences between a purely analytical and a numerical description of an investigated physical object. A number of numerical analysis algorithms are not generally numerically *stable*, it can not be ensured that they will always produce a *convergent* solution. Instead, they can rapidly diverge or become stuck in a stable oscillation. In this case, they produce no usable solution at all. Unfortunately, even if a numerical algorithm converges smoothly, the result can still be far off the physical reality due to instabilities in the mathematical model or the solution algorithm. The computer based execution imposes some additional errors on the numerical operations (discretization errors of the binary representation

of numbers in a digital computer and rounding errors [33]), but often the errors in the model input (e.g. incorrect boundary conditions, an insufficient mathematical model, wrong assumptions in the model deduction, wrong model initialization) are much more relevant than the inevitable errors of the computing machine [34].

A distinct problem of modern and easy to apply numerical methods is that the often relatively impressive result visualizations have the potential to hide fundamental flaws in the setup of the model. Therefore, model results always have to be assessed in comparison to experimental data and the validation of numerical results against experimental benchmarks should be a fundamental part of the modeling process.

### **Continuum vs. Particle Tracing Models**

There are at least two different approaches to describe the migration of gas phase ions at AP: A *continuous* and a *discrete* formulation. In the former, the ions are described as an abstract continuous entity, for example in terms of the scalar field of the ion concentration instead of discrete particles. The electrokinetic flow described by the already presented Nernst-Planck equation (Eq. 2.18) is in this sense a continuous model, even if a numerical formulation of this equation would require spatial and temporal discretization.

In contrast, a *discrete* model describes the charged particles as such, discrete *simulation particles* with distinct characteristics and an individual state which is modified by the interaction with some external forces for example. In this approach, the trajectories of individual charged particles are basically calculated by the numerical integration of the individual equations of motion (particle tracing). The characteristics of a potentially large set of ions in physical reality therefore has to be described by a *representative set* of simulation particles. Due to the limited computing resources, this set generally has to be much smaller than the physical particle number. This potentially leads to modeling problems, e.g. if interactions between particles are important.

In the case of AP ion dynamics, the question which should be answered by an actual model is often an ensemble response of a large group of individual ions. To gain such an answer from a particle tracing model, the set of model particles has to be statistically representative which may result in rather high model particle numbers. The solution of a very complex mathematical problem with a large number of relatively simple to compute *random samples*, is a general idea in numerical analysis which is called *Monte-Carlo Simulation* [35].

At first glance, a continuous approach should be more appropriate than a discrete model for such ensemble modeling, but the simulation of ion dynamics with a particle tracing method is often considerably more stable and numerically more reliable than a continuous model.

### 3.1 Continuum model

The foundations for the continuous ion migration model used in this work were already presented in chapter 2. The Nernst-Planck equation (eq. 2.18) was used to model the migration of ions under atmospheric pressure with the ion concentration ( $c_i$ ) as dependent variable. The bulk gas flow is assumed to be decoupled and is thus determined independently by solving an appropriate version of the Navier-Stokes equations [19]. The resulting velocity, temperature and pressure distributions of such fluid dynamic calculations were used as input parameter for the electrokinetic flow simulation.

The electric potential  $\Phi$  is the second input parameter for the Nernst-Planck model. In the electrostatic case, the electric field is conservative, therefore it is expressed by the well-known *Poisson equation* [36]:

$$\Delta\Phi = -\frac{\rho}{\epsilon_r\epsilon_0} \quad (3.1)$$

In this equation  $\epsilon_0$  is the permittivity of the vacuum,  $\epsilon_r$  is the relative local permittivity (a material constant) and  $\rho$  is a space charge density.

If gas phase ions at elevated pressure are considered, the space charge density may become significant if a relatively large excess concentration of particles of one polarity is present. In this case, the electric field and the ion concentration distribution become tightly coupled and both equations (the Nernst-Planck equation and the Poisson equation) have to be solved simultaneously. If the ion concentration is comparably low, the dependence of the electric potential on the ion distribution can be ignored in good approximation. Thus, the electrostatic field can be solved independently in such situations and the resulting potential can be used as static input parameter for the electrokinetic flow calculation.

Formally a similar coupling between the ion concentration distribution and the bulk gas flow may arise from very high ion concentrations. As stated earlier, in the case of diluted gas phase ions at AP in an ion source of an analytical instrument, it is virtually impossible to generate a relevant effect of the ion motion on the bulk gas flow (“ion wind”).

Overall the continuum model consists of a system of partial differential equations (PDEs), which have to be solved numerically on a defined geometric domain, for a defined set of boundary conditions which represent the model parameters, e.g. material constants or electric potentials of electrode surfaces.

It is be noted, that this continuous model is only one possible approach. A quite different alternative option was shown by the works of Jungroot et al. [37]. Here, an equation system similar to the Navier-Stokes equations was deduced, modeling the *velocity* of ions under the influence of electromagnetic fields and bulk gas collisions, rather than the convective and diffusive flux of an ion concentration.

## 3.2 Numerical solution of PDE problems by discretization

As already mentioned, numerous physical phenomena can be described with systems of partial differential equations (PDE). Formally, such equations have an infinite “resolution”. Per definition they formally hold even on infinitesimal small scales, although this is not true for the physical reality which they describe. The assumption of continuity typically breaks down on molecular scales on which large scale models thus lose their validity.

Since analytical solutions are generally only available for simple and usually non-representative extreme cases, PDE systems are solved with numerical methods. With such, the exact solution of a continuous partial differential is theoretically possible, but only with “infinite” resources, as computing time or infinite long series representations for example. In reality, existing computing machines have finite resources, e.g. limited computing power or memory. Therefore, it is not possible to find the *exact* solution with numerical methods, but it is possible to find a finite *approximation* to the exact solution. The formally continuous PDE problem has thus to be transformed into a discrete, finite problem, it has to be *discretized*.

For physical PDE problems, this discretization is typically performed in the spatial dimensions by the division of the spatial domain into many small, regular or irregular subdomains or *elements*. For time dependent problems, a similar discretization process also has to be performed in the temporal domain for the same reasons. There is a whole family of methods which share this concept of spatial and temporal discretization but differ in their specific realization. In the following, three such methods, which were used in this work are briefly introduced.

### 3.2.1 Finite element method

The finite element method (FEM) is a numerical solution technique for PDE problems. Its origins date back to the beginning of the last century (works by Ritz in 1909 and Galerkin in 1915 [38]). In its beginnings, it was primarily used for problems in structural mechanics and elasticity. Since then, the method was developed towards a much wider scope and today it is an important, generally applicable method in multiple fields of science and engineering, e.g., fluid mechanics, electrodynamics or chemical engineering.

According to [38], an actual PDE problem is the search for an unknown function  $\mathbf{u}$  which satisfies a set of differential equations

$$A(\mathbf{u}) = \begin{Bmatrix} A_1(\mathbf{u}) \\ A_2(\mathbf{u}) \\ \vdots \end{Bmatrix} = 0 \quad (3.2)$$

in a spatial domain  $\Omega$ . In addition, the function  $\mathbf{u}$  has to fulfill a given set of boundary

### 3 Approaches of gas phase ion simulation at AP

conditions

$$B(\mathbf{u}) = \begin{Bmatrix} B_1(\mathbf{u}) \\ B_2(\mathbf{u}) \\ \vdots \end{Bmatrix} = 0 \quad (3.3)$$

on the boundary  $\Gamma$  of the domain. See Figure 3.1 for a two dimensional example of a domain.

As stated earlier, the numerical process can not find the exact solution, therefore, the FEM process searches an approximate function of the form

$$\mathbf{u} \approx \hat{\mathbf{u}} = \sum_{i=1}^n \phi_i a_i = \phi a \quad (3.4)$$

with adequate *shape functions*  $\phi_i$ , which are typically given in terms of the spatial dimensions, and initially unknown parameters  $a_i$ .

Furthermore, it can be shown [38, ch. 3] that the problem can be represented in an integral form

$$\int_{\Omega} G_j(\hat{\mathbf{u}}) d\Omega + \int_{\Gamma} g_j(\hat{\mathbf{u}}) d\Gamma = 0 \quad (3.5)$$

in which  $G_j$  and  $g_j$  are *known* functions or operators.

To perform a spatial discretization, the domain is sectioned into subdomains (elements), a process which is called *meshing*. Typical for FEM is the usage of irregular triangular meshes, as shown in the example presented in Figure 3.1 on the facing page, but regular quadrilateral meshes are also common. In three dimensional space, the equivalents would be meshes consisting of tetrahedral or hexahedral elements. In the FEM method, the shape functions  $\phi_i$  in Eq. 3.4 are local, piecewise defined functions in the subdomains. A particular shape function is therefore only non zero in a single subdomain. The actual value of the modeled quantity in an element is typically described by a linear combination of multiple shape functions. In this context, the free weight parameters  $a_i$ , which describe the modeled value in the whole domain because the shape functions are predefined and thus known, are called *degrees of freedom* (DOF). An example (in one spatial dimension) of this theme with parabolic shape functions [36] is shown in Figure 3.2 on the next page. If the modeled differential equations ( $A_i$ ) are linear, the integral form in 3.5 may be represented as sum over the subdomains [38, p. 40].

This whole process, which is known as *Galerkin-weighted residual approach*, ultimately yields a linear equation system [38]

$$K a + f = 0 \quad (3.6)$$

with the vector of searched parameters  $a$ , a square matrix  $K$  and a vector  $f$  which contains integral expressions which can be numerically calculated (e.g. by numerical quadrature). The dimension of  $K$  and the vectors  $f$  and  $a$  depend on the total number of degrees of freedom of the whole problem. Often the matrix  $K$  is symmetric and

### 3.2 Numerical solution of PDE problems by discretization

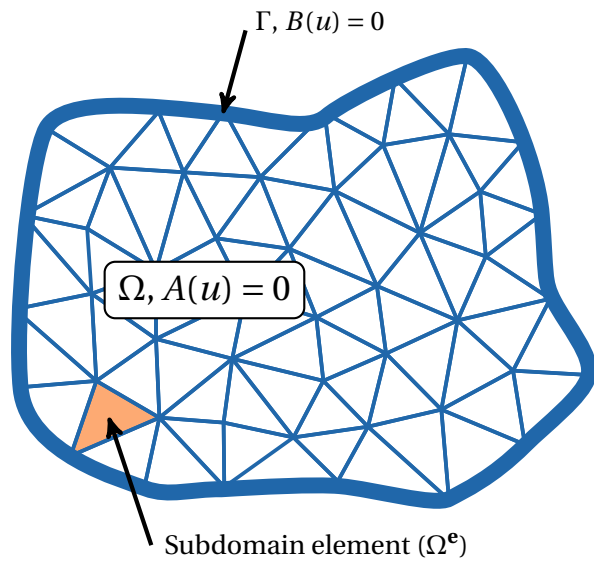


**Figure 3.1:** Example of a two dimensional spatial domain  $\Omega$ , discretized by a mesh consisting of irregular triangle elements. Figure reproduced from [38].

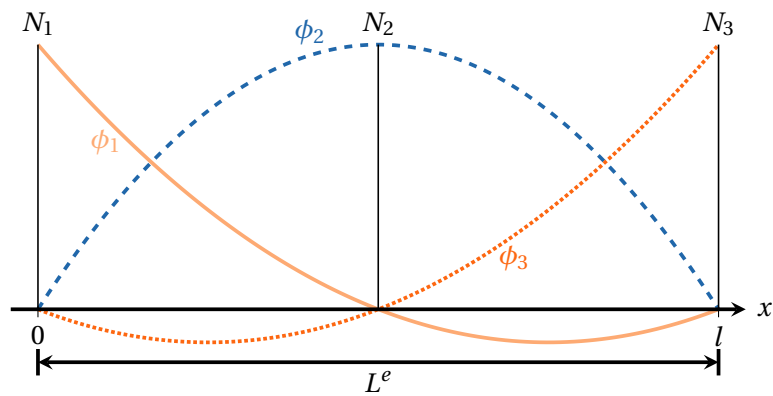


**Figure 3.2:** Examples of parabolic one dimensional shape functions: The modeled value ( $u$ ) in the spatial element  $L^e$  with the length  $l$  is given by a linear combination of the three shown local shape functions  $u = a_1\phi_1 + a_2\phi_2 + a_3\phi_3$ , where  $a_i$  denotes the value of  $\phi_i$  at the  $i$ -th node position ( $N_i$ ). The parameters  $a_i$  are called the *degrees of freedom* (DOF). The exemplary shape functions were taken from [36].

### 3 Approaches of gas phase ion simulation at AP

sparsely populated with non zero values close to the diagonal (band structure). The solution to this linear system, which is potentially huge for real world problems, can be numerically calculated by direct methods (e.g. SPOOLES [39] or PARDISO [40]) or by iterative algorithms (e.g. GMRES [41, 42]) for larger systems.

If the modeled partial differential equation system is not linear, as for example the Navier-Stokes equations, the solution becomes an iterative process. The root of the system can be found in a Newton-procedure [42]. In this case, every Newton iteration requires the solution of a linearized system and thus the execution of the linear solver procedure described above [43,44]. The stability and convergence order of this method depend strongly on the quality of the initial step. Therefore, it is important to preferably provide an accurately guessed initialization.

Details about the finite element method, its mathematical principles, the linear solver algorithms, appropriate meshing algorithms and stabilization techniques are found in the literature, see e.g., [38, 42, 44, 45]

#### 3.2.2 Finite volume method

The finite volume method (FVM) is another discretization method which is often used for the numerical description of partial differential equation systems that model physical conservation laws. Its mathematical principles are related to the finite element method. Like FEM, the finite volume method can be applied to arbitrary geometries and it can use regular as well as unregular calculation meshes [46].

FVM uses an approach of balancing the modeled quantity over the discretization cells, which are often called *control volumes*. The modeled quantity is approximated at the centers of the respective control volumes (in cell-centered FVM approximations). The fluxes over the boundaries of the control volumes are described by integral formulations which are obtained from the divergence theorem [46] [47, p. 69ff].

The resulting equations can be discretized with similar methods as in FEM (Galerkin residual approach), which ultimately also yield a linear equation system (as in eq. 3.6 on page 18) that can be solved numerically with the same methods as in FEM.

An advantageous characteristic of FVM is that the method is locally conservative: The total amount of the modeled quantity is necessarily constant because the net flux over the control volume boundaries is locally balanced out. This behavior is favorable for the simulation of conservation laws. Thus, FVM is an important simulation strategy, especially in the field of computational fluid dynamics (CFD).

As FVM is important to fluid dynamics simulations, its mathematical principles and details on the specific realization of this method on computer hardware are found in most CFD textbooks, e.g. [19] or [48]. Details on the linear solver algorithms are found in most textbooks about numerical analysis, e.g., [47] or [46].

### 3.2.3 Finite differences method

Perhaps the most intuitive discretization approach is the finite differences method (FDM), which is relatively easy to implement in comparison to the FEM or FVM approach.

The spatial domain  $\Omega$  is discretized by a regular rectangle grid, with a fixed grid node distance  $h$ . The differential equation which is modeled,  $f$ , is described by a Taylor expansion at the point  $x$  [49]:

$$f(x+h) = f(x) + h \frac{df}{dx} + \frac{1}{2} h^2 \frac{d^2 f}{dx^2} + \dots \quad (3.7)$$

With sufficiently small values of  $h$ , the higher order terms of the Taylor series can be ignored, and the first derivative of  $f$  is approximated by a simple difference:

$$\frac{df}{dx} \approx \frac{f(x+h) - f(x)}{h} \quad (3.8)$$

Similarly, higher or partial derivatives can also be approximated by such discrete *difference equations*, by reorganizing the Taylor expansion of  $f$ .

This process can be applied to the Laplace equation

$$\nabla^2 \Phi = 0 \quad (3.9)$$

which describes the electrical potential  $\Phi$  in a source free region. It follows that the potential at a point in space is equal to the mean value of the neighboring points. In a two dimensional space, this condition is [49, p. 8]

$$\Phi_{ij} = (\Phi_{i+1,j} + \Phi_{i-1,j} + \Phi_{i,j+1} + \Phi_{i,j-1})/4 \quad (3.10)$$

(five-point centered approximation [47, p. 49]) which is a surprisingly simple property of the solution of the Laplace equation.

Similarly to the FEM / FVM methods, the result of the spatial discretization and approximation of the differentials by discrete difference equations, in combination with appropriate boundary conditions (e.g. the Dirichlet condition that the value of  $f$  is fixed on the boundary), lead to a linear equation system

$$Ax = b \quad (3.11)$$

with a known matrix  $A$  and a known vector  $b$ . For details of this transformation into a linear equation system see for example [47, p. 47ff] or [33, ch. 10]. This potentially large system can be solved for the unknown  $x$  by numerical direct or iterative solvers. As in FEM / FVM the resulting matrix  $A$  has often a symmetric diagonal band structure, which can be exploited in the solution algorithms.

A common iterative solution technique for this kind of problem (particularly for the Laplace equation) is the *relaxation* scheme [50, ch. H] [49, p. 8ff]. For the specific case

### 3 Approaches of gas phase ion simulation at AP

of the Laplace equation the principle of relaxation is rather straight forward. The value of the modeled quantity at a grid node in the next iteration step  $\Phi_{i,j}^{n+1}$  (with the step number  $n$ ) is simply the mean of the neighboring nodes in the last step [49, p. 9]:

$$\Phi_{ij}^{n+1} = (\Phi_{i+1,j}^n + \Phi_{i-1,j}^n + \Phi_{i,j+1}^n + \Phi_{i,j-1}^n)/4 = \Phi_{\text{AVG},ij}^n \quad (3.12)$$

This process is performed for all grid nodes until the change of the value between the last and the actual time-step (the *residual*) falls below a predefined level.

If the new values are all generated from the values of the neighbors in the last step, this principle is called *Jacobi iteration*. If the new calculated value  $\Phi_{i,j}^{n+1}$  is applied immediately to the matrix and the calculations of the next grid nodes are performed with partially updated neighbors, it is called *Gauß-Seidel* method [47, p. 106] [51, ch. 10.4 and 10.5].

These relatively simple methods have the disadvantage that they often converge slowly. Therefore, actual implementations of the relaxation method often use acceleration techniques to improve the convergence order. One approach, called *Over-Relaxation*, increases the change in one iteration artificially by the scaling with a factor  $\omega > 1$ :

$$\Phi_{ij}^{n+1} = \omega \Phi_{\text{AVG},ij}^n + (1 - \omega) \Phi_{ij}^n \quad (3.13)$$

Stable convergence is reached if  $\omega < 2$  [50, p. H-2]. The exact ideal value of  $\omega$  is dependent on the actual problem, thus  $\omega$  is often adapted dynamically.

Another technique to improve the convergence behavior of the relaxation process is to solve the system on different spatial resolutions by *multi-grid methods*. One common approach is to compute an approximate solution on a coarse grid initialization for the relaxation on a finer grid, e.g. with doubled spatial resolution. This scheme helps to quickly propagate large changes through the spatial domain [50, p. H-4 ff] [49, p. 15ff]. However, there are different multigrid schemes which start at the finest grid and travel to coarser grids or repeatedly move forth and back in the grid resolutions several times.

In comparison to the other methods (FEM, FVM), the finite difference approach is relatively simple to implement, but needs a regular grid. This can be a major drawback in simulations with complex geometries or large differences in the local gradients respectively. An irregular mesh could be refined in regions where the local gradients are high or where the simulation needs high local precision. This type of adapted refinements is complicated with regular rectangle meshes used with finite differences. Additionally, the utilization of the FDM method can become complicated in models involving discontinuities (e.g. heterogeneous media) [46].

### 3.3 Particle tracing models

As stated above, the particle tracing approach models the motion of discrete *simulation particles*. To calculate the individual ion trajectories, the *equations of motion*

of the simulation particles has to be integrated numerically. The motion equation of an individual particle describes its motion as a function of the time  $t$ . There are several ways to formulate motion equations (Newtonian classical physics, Lagrange- or Hamilton-formalism). However, the motion of an isolated particle at non relativistic speeds is most intuitively described by *Newtons second law* [9, p. 117],

$$\vec{F} = m\vec{a} \quad (3.14)$$

with  $\vec{F}$  as the net force acting on the particle with mass  $m$  and  $\vec{a}$  is the particle acceleration, which is the change of the particle velocity  $\vec{v}$  with time:  $\vec{a} = \frac{d\vec{v}}{dt}$ . If the particle becomes relativistic, a correction of the acceleration becomes necessary as depicted in [50, p. H-13]. The net force is the sum of all forces acting on the charged particle, e.g., the electromagnetic force as given by the Lorentz-Law (Eq. 2.5 on page 5).

The equation of motion, an ordinary differential equation, can be numerically integrated by standard algorithms. A common approach to solve initial value problems of this kind is the *Runge-Kutta* (RK) method (the widely used charged particle simulation program SIMION for example uses a fourth-order RK algorithm [50, p. H-13]) which is described in detail in numerical analysis textbooks, e.g. in [42, chap. XIV]. The numerical discretization of the initial value problem is performed in this case in the time domain.

The numerical integration of the ion trajectories requires knowledge of the electromagnetic forces acting on the charged particle. Therefore, for a particle tracing simulation, the calculation of the electric and magnetic fields is necessary, which is performed with the discretization methods described in section 3.2 on page 17.

#### 3.3.1 Interaction with background gas particles / Collision models

As presented in the introduction section (Sec. 2.2.2 on page 7), charged particles experience strong interactions with the background gas (collisions) which leads to molecular diffusion and convection. These phenomena cannot be modeled with the basic particle tracing approach presented above, because the net effect of the collisions can not be described by a simple force resulting from a given surrounding field. The random nature of the collision events leads to a partly randomization of the particle paths, which ultimately results in the molecular diffusion. Subtle differences in the collision statistics in different spatial directions, generated by a directed flow of the bulk gas, lead to convective transport of the ions. As a consequence, the detailed statistics of the collisions with the neutral particles governs the exact interaction with the bulk gas. Thus, the viscous drag and the molecular diffusion ultimately depend on ensemble parameters of the background gas (local temperature, pressure and flow velocity) as well as on molecular parameters of ion and bulk gas particles (size mass).

It is indeed possible to model the effect of the viscous drag (Stokes Law [24, ch. 3.2.2]) on the ions and the viscous damping of the ion motion by a field based approach [52]. However, for the complete description of the motion of charged particles,

### 3 Approaches of gas phase ion simulation at AP

an appropriate *collision model* of the bulk gas collisions is required which inevitably includes a random component to model the random nature of the collision events.

#### **Hard Sphere (HS) model**

An intuitive way to model the collisions between ions and bulk gas particles is the direct Monte-Carlo simulation of individual, binary collision events. To a first approximation, the particles are regarded as hard spheres with a thermal velocity distribution of the background gas particles, and the assumption of solely elastic collisions between ions and background gas particles. Such a model determines the probability of a collision event in every simulation time-step. Whether the simulated collision happens, is decided by comparing the local collision probability with a random number. The direction and velocity of the, in most cases thermal, bulk gas particle the collision takes place with is also calculated from random numbers. Detailed formulations of this *hard sphere* approach can be found in [52] and [53].

Hard sphere models were implemented and successfully used in many simulation problems, primarily at medium or low background gas pressure, e.g., for study of collision effects in ion traps [52–54] or in an ion guide device [55]. Despite the fact that hard sphere collision models hold true even under atmospheric pressure conditions [56], the approach is practically not well suited for such high gas pressures. Under conditions of such elevated background gas pressure, the collision frequencies become so high ( $\approx 10^9$  collisions per second which means up to  $10^3$  collisions per typical simulation time-step of  $0.5 \mu\text{s}$ ), that hard sphere models generally become numerically too expensive. At present, typical computing times for single ion trajectories can easily be in the range of hours, even on modern computer hardware.

The drastic acceleration of relatively simple computing algorithms as the hard sphere model, on modern, programmable, highly parallelized, general purpose graphics processing units (GPGPU) has also arrived in the field of ion dynamics simulation [57, 58]. In the future, the direct simulation of hard sphere collisions, or even more complex direct collision models incorporating more precise interaction potentials between ions and bulk gas particles, will probably become feasible for statistically significant large ion ensembles.

Currently this is not the case, therefore an atmospheric pressure collision model has to incorporate a way to reduce the numerical costs to a reasonable level.

#### **Statistical Diffusion Simulation (SDS) model**

To reduce the numerical effort for a high pressure collision model, the number of simulated collision events has to be reduced. Thus, such a model has to describe the net effect (viscous drag and random diffusive motion) of the collisions occurring in every simulation time-step with only one but statistically representative random jump of the simulated ion. The *Statistical Diffusion Simulation* (SDS) algorithm, developed by Appelhans and Dahl [59] as extension to the charged particle simulation program

SIMION [60], implements this basic idea.

SDS treats the random diffusive motion and the directed motion induced by the viscous interaction with the flowing background gas as two distinct phenomena, even though they are both the result of the frequent collisions between ions and bulk gas particles. This separation allows to model both effects with different mathematical models, which leads to a straightforward description of the interactions with the background gas.

**Viscous effects** The viscous effects (viscous damping and convective transport) are modeled in SDS by calculating the average total acceleration  $\bar{a}$  of the ion moving in the continuous fluid in the time interval  $\delta t$  between two simulation time-steps:

$$\bar{a} = f(\delta t) \cdot (a_e - k_0 v(0)) \quad (3.15)$$

In this equation,  $a_e$  is the electromagnetic acceleration of the ion,  $k_0$  is a constant (the *damping constant*) which is inversely proportional to the ion mass and the ion mobility [59]. The term  $v(0)$  is the initial relative velocity at the beginning of the time interval, which is the difference of the ion velocity  $v_i$  and the local bulk gas velocity  $v_g$ :

$$v = v_i - v_g \quad (3.16)$$

The function  $f(\delta t)$  is a time dependent scaling, which is given by

$$f(\delta t) = \frac{1 - e^{-k_0 \delta t}}{\delta t k_0} \quad (3.17)$$

The detailed deduction of the total acceleration (Eq. 3.15 and 3.17) is presented in the appendix 9.1 on page 169.

**Diffusive effects** SDS makes a simplifying assumption to model the diffusive effects: If the collision frequency is high, the diffusive motion of the simulated ions becomes entirely decorrelated between the simulation time-steps by a high number of intermediate collision events. The statistics of the representative random jump (distribution of the jump radius) therefore depends only on local external parameters, e.g., the local mean free path (MFP) of the ion. Thus, it is possible to determine a standard probability function for the radial distance of the diffusive random motion in dependence of the relevant parameters (e.g. the ratio of the molecular masses of the ions and the bulk gas particles, number of collisions in the time-step interval). After the calculation of the ion position in a simulation time-step using the total acceleration defined in Eq. 3.15 in a simulation time-step, the new ion position is modified by a random jump with a radius determined from this probability distribution.

The authors of SDS determined the collision probability function numerically by direct Monte-Carlo simulations of the diffusive random walk of isolated ions (drunkard's walk). The details of this simulation process, the resulting distribution and the scaling

### 3 Approaches of gas phase ion simulation at AP

laws due to the mass ratio between ion and bulk gas particles are presented in great detail in the SDS introduction article [59] and in the user documentation to the SDS implementation.

#### 3.3.2 Space charge handling

As stated in the introduction, diluted ions in an atmospheric pressure region form a type of plasma with a low ionization factor. If the number of charged particles is very small, their electromagnetic interaction with each other and the surrounding environment (space charge effects) can be ignored. Due to the relatively small ion mobility at atmospheric pressure, the space charge effects may become significant, even in the case of the comparably low ion concentrations typical for ion analytical devices.

The space charge has two main effects on the particles: First, charged particles attract or repel each other due to the coulombic interactions of the individual particles. If monopolar ensembles of ions are considered, as relevant to this work, only deflection among the charged particles occurs, which potentially leads to an increased spatial broadening of a given ion package.

The second effect is the damping or *screening* of external electrical fields by mobile charge carriers in the plasma (*Debye shielding*), which results from the reaction of the ions on the field (polarization) [6, 10]. Since the ion density in the cases discussed here is typically low, the field screening is generally insignificant. However, this is not always the case for the situation in ion analytical instruments.

In close vicinity to a corona discharge for example [61], a point to plane discharge with characteristics which is governed by electrical screening [62], the electrical field damping effects of high space charge densities become noticeable. The relevance of this example for AP ion sources stems from the fact that corona discharges are commonly used at AP as ionization source in a method called *Atmospheric Pressure Chemical Ionization* (APCI) [3].

A general space charge model for the conditions discussed in this work has therefore to incorporate the inter-particle coulombic effects as well as the electric field screening. Magnetic effects are generally ignored due to the high collision frequency discussed in chapter 2 (section 2.2.1 on page 5).

The problem of modeling an inter-particle force in a particle tracing simulation is well known in the field of astrophysics. Here, this type of model, called *N-body problem*, is used to simulate the dynamics of objects (satellites, planets, stars etc.) in space [63]. In gravitational simulations no effect similar to the Debye shielding exists because there is no “negative” gravitation. Therefore, such problems are reduced to the calculation of the inter-particle forces. Despite this reduced complexity, the sheer number of simulated particles in large scale simulation projects like the Millenium simulation [64] has led to significant optimizations of the simulation algorithms for inter-particle force calculations [65].

**Calculation of electric inter particle forces (Particle-Particle interaction)** The electrostatic force  $F_{12}$  between two charged particles (point charges)  $q_1, q_2$  is given by the *Coulomb law* [66, Sec. 23.3]:

$$F_{12} = \frac{1}{4\pi\epsilon_0} \frac{q_1 q_2}{r^2} \hat{r} \quad (3.18)$$

where  $\hat{r}$  is the unit vector pointing from  $q_1$  towards  $q_2$ ,  $r$  is the distance between the charges, and  $\epsilon_0$  is the permittivity of vacuum.

The most obvious way to calculate the net force acting on a particle from the surrounding particles is summing up the individual forces from every other particle of the simulation. This net electrostatic force is then considered in the acceleration calculation for the next simulation time-step. Despite the fact that this method is straightforward to implement, it is comparably ineffective. In every time-step of the numerical ion trajectory integration, the distances between every ion pair have to be explicitly determined. The number of calculations for this process scales quadratically with the number of simulated particles  $N$  ( $\mathcal{O}(N^2)$  in O-Notation [67]) [68]. Therefore it is only feasible for a low number of simulated particles [50].

One approach to accelerate the simulation is the *Barnes-Hut* tree or multipole expansion algorithm [69]. The concept of this method is to approximate the effect of multiple distant particles with one representative contribution to the net force; groups of particles are combined to pseudoparticles. To achieve this, the simulation domain is sectioned into a hierarchic cell structure, which is logically represented by a tree data structure, called *octree* in the three dimensional case. After this division process, the smallest spatial cells, which are the leaf nodes of the tree structure, contain no or exactly one simulation particle. The inner (non leaf) nodes, located higher in the hierarchy of the tree, contain, in addition to the links to the child nodes combined information about them. In the case of electrostatics, an inner tree node would know for example the net charge of *all* of its child nodes.

The advantage of this representation of the simulation domain is that it is easy to approximate the combined effects of many simulation particles simply by traversing through the tree. To calculate the net force for a particle, the algorithm traverses the tree starting from its root. For every populated node which is reached, the spatial distance to the particle is determined. If this distance is below a given limit, the algorithm moves to the children of the actual considered node. If the distance is longer than the limit, the considered node represents a distant spatial section and the combined charge value stored in the node is used for the force calculation.

This tree algorithm scales with  $\mathcal{O}(N \log N)$  which is much more favorable for large sets of simulation particles than the direct implementation which has a quadratic runtime dependency. This significant advantage in numerical costs of tree methods as Barnes-Hut is bound to an approximation of the exact force which would be imposed by all simulation particles. In large scale simulations, which include typically a high number of simulation particles, this approximation is generally justified.

**Particle in cell simulation (Particle-Mesh Interaction)** The consideration of the coulomb forces between the simulation particles neglects the effects of the space charge density on a present external electric field, e.g., the Debye shielding.

The *particle in cell* (PIC) method is a common approach to calculate the electrical field including the additional charge density resulting from the presence of mobile charge carriers. In principle, it is an adaption of the calculation techniques described in section 3.2 which considers the distribution of charged particles.

A common basic PIC implementation relates the finite difference discretization described in section 3.2.3: The electric field is described on a regular grid. In every simulation step, the present field distribution is calculated. To achieve this, at first the present spatial distribution of the simulation particles has to be transformed into a charge distribution at the nodes of the grid. There are a number of methods for this transformation. The most simple method is the addition of a charged particle to the nearest grid node. A typical and more accurate method is to divide the charge of a simulation particle and distribute it to the neighboring grid nodes according to their distance to the particle. There are also other higher order interpolation techniques [70, 71].

Then the poisson equation is solved by a numerical solver with consideration of the determined charge distribution on the grid nodes resulting from the charged particles. The obtained electric field distribution is subsequently used to calculate the electric forces acting on the simulation particles. In a particle movement step, a new particle distribution is calculated from the present particle accelerations, and the next simulation time-step begins with the recalculation of the space charge distribution on the grid nodes.

The particle in cell method can also be used on irregular grids [72], which is beneficial for complex geometries. For periodic simulation domains the calculation of the poisson equation is significantly accelerated using efficient fast Fourier transformation (FFT) [73] algorithms.

The article by Dawson [70] gives an introduction to the fundamentals of the PIC method. Birdsall and Langdon authored a widely used standard textbook on computational plasma simulations which rely strongly on particle in cell methods [74].

Hybrid algorithms are often used in complex particle simulations, which combine the simulation of particle-particle (PP) interactions with the calculation of particle-mesh (PM) interactions. Such “P<sup>3</sup>M” algorithms, as for example the *TreePM* algorithm [75] for large scale cosmological gravitational simulations, typically model long range interactions with a particle-mesh approach while close interactions are calculated by direct sums between particles. With such hybrid algorithms, accelerated by FFT methods, it is possible to solve gravitational problems with  $\approx 10^{10}$  individual particles [64], provided access to a large parallel computer system.

There are a lot of specialized and sophisticated codes for the simulation of plasmas, mostly originating from the nuclear fusion and the astrophysical community. However,

### *3.3 Particle tracing models*

SIMION, the software package widely used in the mass spectrometry and ion mobility spectrometry communities for particle tracing, provides only the direct simulation of the particle-particle interactions. Even if there are promising attempts to use more sophisticated algorithms for the simulation of the ion dynamics in devices such as ion traps [57, 58], to date modern particle tracing algorithms including space charge effects optimized for the conditions in ion optical devices are not generally available.

## 4 Software Packages

The numerical simulations presented in this work were performed with two commercial software packages: *Comsol Multiphysics* and *SIMION*, which are introduced and briefly described in this chapter.

### 4.1 Comsol Multiphysics

Comsol Multiphysics [76] is an integrated finite element method simulation environment for modeling applications in physics and engineering. As the name suggests, the system is designed with emphasis on the solution of coupled physical problems or *multiphysics* modeling. A typical example of a multiphysical modeling task is the comprehensive numerical description of a reacting fluid flow within an industry scale chemical reactor. Such a simulation may incorporate the heat flow in the fluid and in the reactor geometry, the flow dynamics of the fluid, and the chemical reaction kinetics in the fluid.

Comsol provides a fully integrated modular environment. The whole modeling process can be accomplished in the system: Comsol integrates a parametric computer aided design (CAD) kernel which allows the generation of simulation geometries, provides methods for the generation of structured and unstructured numerical meshes, allows the solution of the FEM problem with different direct and iterative solver algorithms, and integrates tools for the result analysis and visualization.

The whole system is modularized. The base system can be extended with “application modes” which provide easy to access interfaces to the FEM core of Comsol. They allow the user to operate directly with physically meaningful values and terms instead of relative abstract partial differential calculus. The range of application modes available to date includes a computational fluid dynamics (CFD) module, a chemical engineering module, and a plasma module.

Recently, the computational capabilities of Comsol were extended by a particle tracing module, which allows to perform complex particle based simulations, including the simulation of particle-particle and particle-field interactions with a particle-in-cell type approach.

Despite the high degree of integration, Comsol provides also interfaces (called “Live-Link”) to external CAD systems (e.g., SolidWorks or AutoCAD), the Matlab numerical computing programming environment, and Microsoft Excel.

## 4.2 SIMION charged particle simulator

SIMION [60] is a system for the simulation of the dynamics of charged particles in electro- and magnetostatic fields, focused on applications in mass spectrometry and similar application fields. It has a quite long history, as it was developed in 1973 [77]. Since then, it has become one of the most widely used simulation tools in the mass spectrometry community. Originally solely intended for simulating the trajectories of charged particles under ideal vacuum conditions, SIMION was crucial for the design and optimization of many of today's ion analytical devices.

SIMION uses the finite difference approach (described in section 3.2.3 on page 21) for the calculation of the electric and magnetic fields in the simulation domain. The drawback of this method is that the calculation mesh is always regular, rectangled and equally spaced in all spatial directions, hence the term “potential array” for the solutions of the relaxation process in SIMION.

As a result of the grid structure of the potential arrays, it is not readily possible to handle models with variable mesh resolutions. However, it is possible in SIMION to combine multiple potential arrays, also with different spatial scale factors, in one modeling project, which is called “ion workbench” (IOB). With proficient sectioning of a given geometry, this capability allows increased spatial resolutions in critical regions of a model.

A significant advantage of the FDM approach of SIMION is the so called *fast adjustment* of individual potential arrays [50, Sec. 6-11]. This method allows the calculation of the resulting electromagnetic field under variations of the potentials on the electrodes or magnetic poles in the model without the need for a recalculation of the potential distribution by relaxation. To achieve this, SIMION calculates the potential distribution for every single independent electrode in the simulation separately. The individual potential arrays are then superimposed by a linear combination yielding the net potential distribution. In this scheme, the potentials on the electrodes become scaling factors in the linear combination. Thus, a variation of the electrode potentials requires only a recalculation of the linear combination of individual electrode potential arrays, which is possible without significant numerical costs.

Another notable feature of SIMION is the *user program interface*, which allows to directly interact with the numerical ion trajectory integration. The user can manipulate nearly every parameter of the numerical integration process (e.g. calculation of the ion acceleration, calculation of the ion position, local electric field) with external code segments, defined in hook functions which are called in every time-step of the trajectory calculation. In the recent major SIMION release (SIMION 8), the user program interface was redesigned and is since then based on Lua [78], which was designed as a particularly extensible and lightweight embedded programming language.

The capability of modifying the trajectory calculation “in situ” allows a remarkably high flexibility of SIMION. An experienced user may basically redesign the entire ion dynamics simulation, as demonstrated e.g. by the SDS high pressure collision model [59] which is in its most recent version entirely implemented as a Lua user

#### 4 *Software Packages*

program. As an alternative to the Lua interface, SIMION offers a C/C++ API which is beneficial for performance-critical user programs.

SIMION has only basic integrated CAD features but is able to import CAD files as electrode configurations. As a second option, SIMION integrates a parser for a geometry description language. This allows to build electrode geometries from geometrical primitives (spheres, cylinders etc.) which are combined by boolean operations, e.g. geometric subtraction or union (addition). These geometry defining files (GEM files) may also contain Lua code, which is executed by the geometry description parser. Therefore, even fully parametric complex electrode geometries can be defined in the GEM files.

## 5 Simulation of ion migration in a slow gas flow

In the present and following chapters the migration of ions under dense, essentially atmospheric pressure conditions are investigated. Initially, the transport of ions in an essentially laminar, gas flow is considered. This allows the comparison of different numerical models and an estimation of the accuracy of the simulation results with respect to experimental data. Based on this initial study, an attempt is made to simulate the ion migration in the rather complex flow-field of a commercial AP ion source. This numerical model is used to reproduce a highly convoluted experimental result, the *Distribution of Ion Acceptance* (DIA), which allows the validation of the entire simulation process, including the simulation of the bulk gas flow. In addition to the pure validation, the detailed analysis of the ion migration simulation results is a key to understand the complex physical dynamics which lead to the experimental observations.

The successful simulation of the DIA not only shows that it is indeed possible to simulate such dynamics but also that they were correctly rationalized.

### 5.1 Introduction / Motivation

Particle tracing models [56, 68, 79–82] as well as continuous models [37, 83, 84] have been repeatedly used to simulate the electric drift of gas phase ions at AP. Despite the excellent results obtained in these works, there is no direct comparison between different modeling approaches available. Thus, the necessary effort in terms of model preparation times and numerical costs, and the expected quality of the results at a given level of invested effort, was not known.

Continuous approaches to model ion migration at AP are generally not established in the MS/IMS community. While the number of applications of the SDS collision model grows slowly but steadily, there are essentially only three notable examples of continuous ion migration models in the field of MS/IMS [37, 83, 84]. Whether this imbalance is justified by the actual performance of the approaches, or this has other causes, is not clear from literature.

Therefore, a first step towards the application of ion migration models on complex problem cases was to investigate and compare the capabilities and performance of two numerical approaches, the continuous electrokinetic flow simulation in Comsol

## 5 Simulation of ion migration in a slow gas flow

Multiphysics and the particle tracing simulations in SIMION with the SDS collision model, on a well understood benchmark problem.

The continuous simulation method introduced by Jugroot [37] was not considered because it is not generally available. Even if the actual implementation of the model were available, the necessary effort to adapt this code to the present computer system seemed to be unattractive for a first simulation attempt. The obvious alternative to particle tracing calculations with SIMION/SDS, the particle tracing module of Comsol Multiphysics, was not available at that time. Thus, it is also not considered in this work.

In this first phase of the investigation of ion migration models, an appropriate benchmark problem was necessary. An ideal benchmark problem is numerically feasible, which means that it is possible to produce useful numerical results within reasonable computing times allowing an iterative refinements of the calculations. In addition, the problem has to be experimentally well understood, which allows the assessment of differences between experiment and simulation. Finally, the necessary experimental effort to validate the numerical results has to be feasible, too.

With respect to the simulation of ion migration, a minimal benchmark problem has to include the effects of a static electric field and a static gas flow on the drift motion of ions at AP. Inspired by the elegant miniaturized ion mobility spectrometer presented by Barth and Zimmermann [83], a simple benchmark experiment was designed: Ions are introduced into a chamber by a slow and therefore essentially laminar gas stream. In this chamber, the ions are deflected orthogonally to the direction of the gas flow by an electrostatic field.

This simple idea was experimentally carried out and then modeled with both numerical approaches as presented in the following sections.

### 5.2 Experimental verification

Ion current measurements were conducted with a home-built setup which is depicted schematically in fig. 5.1. Its central part was a sealed cylindrical stainless steel chamber with an inner diameter of 127 mm and a height of 131 mm. Inside this chamber, an assembly of two rectangular aluminum electrodes (48 mm width and 20 mm height), a deflection and a receiver electrode, were mounted electrically isolated on a movable PVC stage. Both electrodes were connected to vacuum BNC ports in the chamber wall.

The chamber was connected to a tubular ion source via a connection tube with an inner diameter of 9 mm and a length of 90 mm on one side and an exhaust tube on the far side of the inlet port. The electrodes were positioned and aligned so that the center axis from the inlet port to the outlet port passed between them. The distance between the electrodes was 18 mm, and the distance from the inlet port to the front edges of the electrodes was 23 mm. Fig. 5.2 shows the inside of the measurement chamber in detail.

The deflection electrode was connected to a laboratory power supply (*Voltcraft*

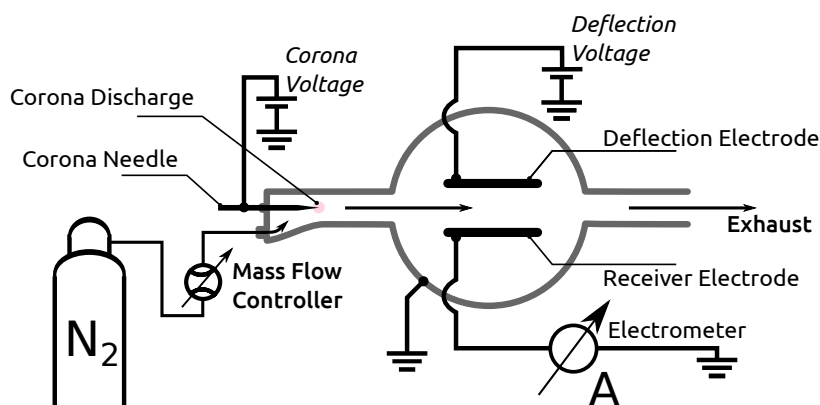


**Figure 5.1:** Schematic overview of the benchmark experiment. Nitrogen gas flows through the ion source and the measurement chamber. Ions are generated upstream by a corona discharge. The ions are transported into the measurement chamber by the bulk gas flow. Here, a potential on the deflection electrode pushes the ions on the receiver electrode. The ion current on the receiver electrode is measured in dependence of the gas flow and the deflection potential.

*PSP 1803; Conrad Electronic SE, Hirschau, Germany*) which allowed a deflection voltage up to 80 VDC. The ion current on the receiver electrode was measured with a digital microammeter (*Model6430 Sub-Femtoamp Remote SourceMeter, Keithley Instruments Inc., Cleveland, OH, USA*).

Ions were generated in a custom built tubular ion source by a DC corona discharge [61]. The ion source consisted of an aluminum tube with an inner diameter of 8 mm and a length of 50 mm. The tip of a corona needle from a commercial APCI ion source (*Bruker Daltonics, Bremen, Germany*) was used as point electrode. The needle was placed in the central axis of the electrically grounded tubular ion source. The corona discharge voltage of 2 kV DC was provided by a HV laboratory power supply (*HNC 3500-10 ump power supply, Heinziger Electronic GmbH, Rosenheim, Germany*).

Synthetic air of 99.999% purity (*Gase.de Vertriebs GmbH, Sulzbach, Germany*) was fed into the ion source region from a gas cylinder and flushed around the needle. The nitrogen flow was controlled by a 2000 sccm  $\text{min}^{-1}$  mass flow controller (*Bronkhorst High-Tech B.V., Ruurlo, NL*).

The effluent of the measurement chamber was vented into the atmosphere. The pressure in the measurement chamber was monitored with a pressure transducer (*Barocel 600A-1000T, Datametrics/Dresser, Wilmington, MA, USA*), but due to the open exhaust the pressure in the chamber never differed noticeably from the ambient atmospheric pressure.

The ion current on the receiver electrode was digitally recorded from the microammeter with a custom built software. The deflection voltages were recorded manually.

## 5 Simulation of ion migration in a slow gas flow

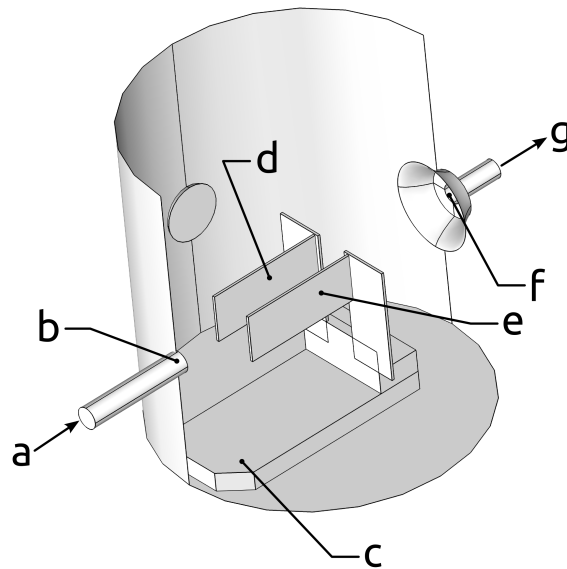


**Figure 5.2:** Geometry of the measurement chamber used in the benchmark experiments.

The chamber had an inner diameter of 127 mm and a height of 131 mm.

**a:** gas flow from ion source, **b:** inlet port, **c:** movable base plate, **d:** deflection electrode, **e:** measurement electrode, **f:** outlet port, **g:** gas flow towards exhaust

The connection between the deflection voltage and the corresponding recorded ion current was established via the sample numbers of the ion current recordings.

The measurement was performed with both corona polarities with respect to ground potential. In both cases, the ion current was recorded with positive and negative deflection potential to investigate the composition of the corona discharge effluent with respect to charge polarity.

## 5.3 Numerical Models

### 5.3.1 Simulation of the fluid flow (CFD)

Comsol Multiphysics (*version 4.0-4.3a, Comsol AB, Stockholm, Sweden*) was used for the simulation of the static, three-dimensional fluid flow in the measurement chamber. The model uses a weakly compressible formulation of the Navier-Stokes equations, which is documented in detail in the Comsol manual [85]. Here, such a weakly compressible formulation is sufficient because compression effects are generally insignificant in slow gas flows below a Mach number  $M < 0.3$  [85]. The gas flows in the presented benchmark model are below  $10 \text{ m s}^{-1}$  which is significantly below this

**Table 5.1:** Parameters of the bulk gas flow simulation

Static temperature	$T = 298.15 \text{ K}$
Background pressure	$p = 1.01 \times 10^5 \text{ Pa}$
Mean outflow velocity	$v_{\text{out}} = 0.15 \text{ to } 1.35 \text{ m s}^{-1}$
Gas density	$\rho = 1.164 \text{ kg m}^{-3}$
Dynamic viscosity	$\mu = 1.744 \times 10^{-5} \text{ Pa s}$

threshold which would be approximately  $100 \text{ m s}^{-1}$  at room temperature.

The simulated fluid was nitrogen; and the temperature dependent functions for the calculation of the gas parameters were taken from the integrated Comsol material library. The simulated fluid was isothermal at room temperature (293.15 K), and the static background pressure was assumed to be the standard atmospheric pressure (1 atm). The actual values of the simulation parameters are listed in table 5.1.

At the boundary of the camber exit port, an outflow with a triangular velocity distribution parallel to the boundary normal was set, which is a simple approximation of a parabolic flow profile. At the inlet port boundary of the simulation domain, a static pressure equal to the background pressure was assumed. On all other boundaries, representing walls, a *no slip* wall condition was set, i.e. the fluid velocity is zero ( $v = 0$ ) at the wall.

The simulation domain was meshed with an irregular (free) general purpose tetrahedral mesh with slightly increased mesh resolution (“Finer” resolution preset setting for a general physics free mesh in Comsol). The resulting mesh had approximately  $1.8 \times 10^5$  elements.

The model was solved with the default solver configuration of Comsol for three dimensional flow problems (GMRES iterative solver with geometric multigrid approach for preconditioning). For the solution, the predefined default configuration of the shape functions and numerical stabilization techniques were also used without alteration.

To simulate the effects of different volume flows through the measurement chamber, the outlet gas velocity was varied, and parametric solutions were generated which consist of a set of solutions according to a set of outflow velocities.

The influence of the turbulence modeling was assessed using two calculated parametric solutions: One without turbulence modeling (called *laminar* solution in the following) and a solution with activated turbulence modeling (*turbulent* solution). The used turbulence model was the  $k - \epsilon$  model in its default configuration [85].

### 5.3.2 Electrokinetic flow simulation

The flow of ions in the presence of the calculated bulk gas flow and an electric field (electrokinetic flow), described by eq. 2.18, was modeled in Comsol Multiphysics using the “Transport of diluted species” application mode. The bulk gas flow input data for the electrokinetic model (flow vector field, pressure scalar field) were taken from

## 5 Simulation of ion migration in a slow gas flow

the Comsol CFD model described above. Due to the low concentration of ions in comparison to the number of bulk gas particles per volume unit, the bulk gas flow was safely assumed to be independent from the electrokinetic flow. Therefore, the bulk gas flow was solved independently as described above, and the analyzed result was used as input for the ion migration simulation.

The electric field, the second input parameter for the electrokinetic flow simulation, was calculated with the “electrostatics” module of Comsol. Similar to the CFD input, the electric field was calculated independently (no space charge effects since there is no significant feedback from the charged particles to the electric field). In the presented model, the electrostatic field was always solved together with the electrostatic flow because the potential on the deflection electrode was varied in a parametric solution.

With exception of the deflection electrode, all boundaries were assumed to be on ground potential in the electrostatic model. The dielectric holder of the measurement and receiver electrode, made from PVC material, was not considered explicitly; it was assumed that there was no significant ion current onto this part and thus no severe charging. The electric potential on the deflection electrode was varied between 0.1 to 80 V. The lowest deflection voltage was not exactly ground potential because the model became numerically unstable without any potential on the deflection electrode.

In the electrokinetic model a static inflow concentration was assumed on the inlet port, convective outflow on the outlet port, and ideal neutralization of the ionic species on the walls in the measurement chamber ( $c_i = 0$  on the wall). In the connection tube from the ion source into the measurement chamber, ideally isolating walls (no mass flux through the boundaries) were assumed to maintain the ion concentration at the inlet port of the simulation domain also at the actual measurement chamber inlet. The static inflow ion concentration was  $6 \times 10^{-12} \text{ mol m}^{-3}$ . It was estimated from the maximum measured experimental ion current to allowing realistic simulations of space charge effects.

In contrast to the SIMION particle tracing model described below, the electrokinetic flow model is not readily handling a distribution of particles with different ion mobilities in one simulation run. Instead, the model uses a single ion mobility per simulated ionic species. In a particle based simulation, the run time is proportional to the number of simulated particles, independent from the ion mobility distribution in the particle ensemble. In the Comsol model, additional ionic species with different parameters, for example ion mobility, are in principle independent problems. Here the run time and memory requirement of the numerical model scales with the number of simulated species. All electrokinetic simulations were therefore performed with monodisperse ion mobilities in one simulation run. Multiple simulation runs were performed to investigate the effect of the ion mobility.

Most of the electrokinetic flow calculations were performed with a monopolar, cationic, ion inflow without consideration of space charge. To investigate the effects of space charge, the electrostatic and the ion migration model were coupled in a subset of the performed simulations by multiplying the ion concentration distribution with

**Table 5.2:** Parameters of the electrokinetic flow simulation

Inflow concentration	$c_{\text{in}} = 6 \times 10^{-12} \text{ mol m}^{-3}$
Deflection voltage	$U_d = 0.1 \text{ to } 80 \text{ V}$
Ion mobility	$K_0 = 1.5 - 3.5 \times 10^{-4} \text{ m}^2 \text{ V}^{-1} \text{ s}^{-1}$
Ion diffusion coefficient	$D = 1 \times 10^{-5} \text{ m}^2 \text{ s}^{-1}$

the Faraday constant. In Comsol the resulting space charge density can directly be considered in the calculation of the electric field by the integrated space charge feature of the electrostatics application mode [36] (monopolar space charge model).

Since some of the experimental results show that the effluent from the ion source transports a partly mixed ion current of anionic and cationic species at specific conditions (see section 5.4.1 for details), the effects of such a situation were investigated in a second series of simulations also considering space charge effects. In these calculations, a second ion species with the same parameters (diffusion coefficient, ion mobility etc.) but opposite charge ( $z = -1$ ) was introduced with a similar static inflow concentration (bipolar space charge model).

The ion mobilities used in the electrokinetic simulations are estimated values for ions with molecular masses between 19 and 300 Da. The fitting function between ion mass and ion mobility which was used to calculate the mobility values is part of the SDS algorithm [59]. SDS was used as bulk gas collision model in the SIMION particle tracing model described below (section 5.3.3). The parameters of the electrokinetic flow simulation are listed in table 5.2.

Similar to the Comsol CFD simulation, the electrokinetic model was solved using the default solver configuration of the selected application mode. It is a segregated approach, which uses individual linear solver configurations for groups of dependent variables of a coupled model. In the case of the ion migration simulation, the electric potential ( $V$ ) was solved using a conjugate gradients solver with an algebraic multigrid preconditioner. The ion concentration distribution  $c_i$  was calculated using the GMRES method with a geometric multigrid preconditioner. The electrokinetic model used the same numerical calculation mesh as the Comsol CFD model described above.

### 5.3.3 Particle tracing simulation

In addition to the continuous electrokinetic flow model, the ion migration in the measurement chamber was simulated with a particle tracing simulation in SIMION using the SDS algorithm describing the interactions between bulk gas and ions.

A simplified version of the simulation geometry in the Comsol models shown in figure 5.2 on page 36 was reproduced manually as SIMION electrode configuration with the geometry description language of SIMION. This simplified geometry did not take into account the connecting tube from the ion source and the outlet tube behind the outlet flange of the measurement chamber. In addition, some of the details of the electrode mounts and the side ports of the measurement chamber were also not

## 5 Simulation of ion migration in a slow gas flow

**Table 5.3:** Parameters of the particle tracing simulation

number of simulated particles	$n = 2000 - 20000$
deflection voltage	$U_d = 0 \text{ to } 80 \text{ V}$
ion mobility	$K_0 = 1.5 - 3.5 \times 10^{-4} \text{ m}^2 \text{ V}^{-1} \text{ s}^{-1}$
collision gas mass	$m = 28 \text{ Da (N}_2\text{)}$
bulk gas temperature	$T = 298.15 \text{ K}$
bulk gas background pressure	$p = 1013 \text{ mbar}$

considered. None of these features seemed to be important for the migration of ions in the measurement chamber with a bulk gas flow field from a valid flow simulation.

The electric field distribution was solved for the resulting electrode configuration using the finite difference approach of SIMION. The field solver was used in its default configuration. Due to the *fast adjustment* feature of SIMION (see section 4.2 on page 31 for details) potential variations on selected electrodes do not require the whole electrostatic model to be recalculated. Similar to the Comsol model, the potential on the deflection electrode was varied between 0 and 80 V while all other electrodes and the measurement chamber wall were at ground potential.

The boundary conditions for the particle tracing simulation were similar to the assumptions made in the electrokinetic model: Ions were started next to the inlet of the measurement chamber, and their trajectories were simulated in the presence of the bulk gas flow and the electrostatic deflection field. Ions hitting any of the walls of the simulated geometry were terminated at the collision position. Following the recommendations of the SDS authors, the trajectory integration parameter (*T.Qual*) was set to zero maintaining a reasonable level of integration performance with activated SDS model.

The ion mobilities used in the particle tracing simulation were estimated from the ion molecular mass by the SDS fitting function [59]. The assumed mass range of the ions was 19 to 300 Da which corresponds to an estimated ion mobility range of  $1.5 - 3.5 \times 10^{-4} \text{ m}^2 \text{ V}^{-1} \text{ s}^{-1}$ .

Typical preliminary simulation runs consisted of 2000 simulated particles. High quality quantitative simulations were performed with a typical number of 20 000 simulated particles to improve the statistical significance of the runs. The parameters of the ion trajectory simulation are listed in table 5.3. Similarly to the Comsol model, a subset of simulations was performed with a bipolar ion current and with activated coulomb repulsion simulation to estimate the significance of space charge effects.

In addition to visualizations of the particle trajectories, the spatial ion termination positions were recorded in the simulation result files. To calculate an estimate of the simulated ion current on the measurement electrode, the result files were analyzed for the number of ions terminating on the measurement electrode in dependence on the deflection voltage. This analysis was initially performed with a custom data analysis script implemented in Matlab [86]. Later it was replaced by an adapted version to be

compatible with Gnu Octave [87].

To simplify the handling of the particle tracing model and to minimize the manual effort required for a comprehensive simulation run, the variation of the deflection voltage was automatized using the command line interface of SIMION. This automatization was implemented in the Python programming language [88].

Similar to the electrokinetic flow model, the particle simulation requires information about the bulk gas flow as input parameters. This was also provided by the flow simulation performed in Comsol as described above. As already mentioned, the bulk gas flow is virtually independent from any ion motion, which allowed the usage of simulated, static flow fields as input parameters for ion migration simulations.

In contrast to the integrated simulation environment provided by Comsol, the fluid dynamic results calculated in Comsol have to be exported and adequately transformed into valid SDS input parameter files.

**CFD result data export and transformation** The SDS algorithm considers fluid dynamic input parameters (flow field, pressure, and temperature distribution) in the ion trajectory simulation. Each parameter has to be provided in an individual input file, which consist of a list of values of the parameter at the spatial positions of the potential array of the SIMION model.

Since the typically irregular numerical mesh of the CFD model, which provides the input data, is different from the regular SIMION calculation grid, a spatial interpolation has to be performed to generate SDS input files from CFD results.

To use the Comsol CFD model of the experimental setup as input for the ion trajectory simulation in SIMION, the values of the required fluid dynamic parameters (components of the flow velocity vector, pressure) at the nodes of the Comsol calculation mesh were exported along with the spatial node positions. For this irregular point cloud, a Delaunay triangulation [89, 90] (tessellation to simplices in  $R^3$ , which are tetrahedra) was calculated. The simplex representation, basically a representation of the initial Comsol mesh, was then used to linearly interpolate the values at the neighboring Comsol mesh nodes to the SIMION grid nodes. The mesh interpolation process was initially performed in a custom Matlab program, which used the `griddata3` function for the triangulation and interpolation. Later, this program was reimplemented in Python using the `interpolate.griddata` function of the open source library SciPy [91] because Matlab became unavailable.

The whole interpolation process is essentially the same as described in section 6.3.2. Most of the developed transformation tools described there were used in both models but were adapted here for the input data from Comsol.

## 5 Simulation of ion migration in a slow gas flow

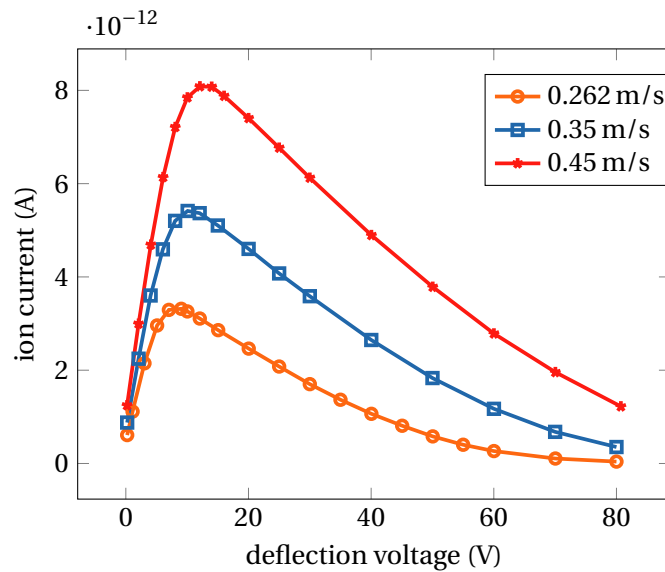


**Figure 5.3:** Experimentally determined ion current on the receiver electrode (labeled  $e$  in fig. 5.2) in dependence on the voltage at the deflection electrode ( $d$  in fig. 5.2) for different mean bulk gas velocities. The ions were generated by a corona discharge in positive mode (4.8 kV corona voltage).

## 5.4 Results

### 5.4.1 Experimental verification

The ion current in dependence of the deflection voltage was measured with the setup described above. The bulk gas volume flow into the ion source was varied between 0.5 and 1.9 l min<sup>-1</sup>. If incompressibility of the bulk gas is assumed, the volume flow range results in a mean inflow velocity into the measurement chamber between 0.13 and 0.50 m s<sup>-1</sup>, since the connection tube between the ion source and the measurement chamber had an inner diameter of 9 mm.

Figure 5.3 presents the results of the ion current measurement under variation of the bulk gas flow. In this measurement series, the corona was operated in positive mode with a discharge voltage of 4.8 kV. The figure shows the typical observed shape of the ion current signal: With increasing deflection voltages, the recorded ion current steeply rises until an absolute maximum between 15 and 25 V deflection potential is reached. From there, the signal drops with a much lower slope until it approaches zero at the highest deflection voltages applied. In the rise phase of the ion current, the recorded ion signal increases almost linearly with respect to the deflection voltage. In the decline phase, the ion current signal shows a slight curvature. To a first approximation, the ion current is approximated by two linear functions and a smooth transition region between the rise and the decline region.

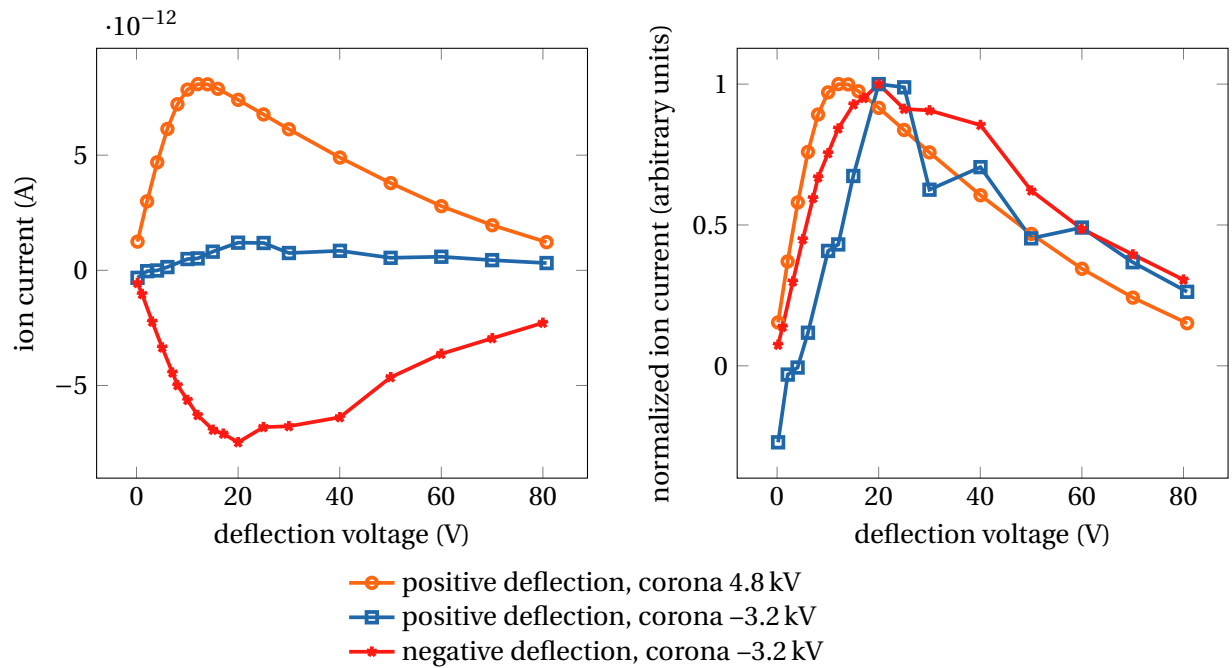


**Figure 5.4:** Experimentally determined ion current on the receiver electrode (labeled with  $e$  in fig. 5.2) in dependence on the deflection voltage on the deflection electrode ( $d$  in fig. 5.2) for different corona and deflection polarities. The bulk gas flow was  $0.45 \text{ m s}^{-1}$ .

The general shape of the ion current signal is not severely affected by the variation of the bulk gas flow but the signal intensity increases significantly with rising gas velocity. This effect is visible in figure 5.3. It is probably caused by a more efficient viscous transport of the gas phase ions which cause less wall losses. Diffusive as well as electrostatically induced wall losses should decline with increasing bulk gas flow. This notion is supported by the observed dependence of the absolute ion current. It should be noted that an influence of the bulk gas flow on the ion generating corona discharge can not be excluded. The observed dependence of the ion current on the bulk gas flow could therefore also be caused by a variation of the primary ion current generated by the corona discharge instead of an increased ion transport efficiency.

As seen in figure 5.3 the ion current signal is shifted towards higher deflection voltages with higher bulk gas velocities. The position of the ion current maximum increases in the deflection voltage dimension and the declining region of the current signal is shifted towards higher deflection voltages. As shown in the following sections, this shift is probably caused by the dynamics of the ions in the measurement chamber under influence of the present electric field and viscous forces induced by the bulk gas flow.

## 5 Simulation of ion migration in a slow gas flow

The experimental results obtained by variation of the corona and deflection polarities are depicted in figure 5.4. The signal response with positive corona and positive deflection voltage is comparable to the signal with negative corona and negative deflection voltage. In contrast to the measurements with positive corona the ion current with negative corona discharge was significantly more unstable and the measured signal showed higher random noise as in the positive case. This is also visible in the negative signal in figure 5.4, which is not as smooth as with positive corona discharge and positive deflection potential. In addition to the lower stability of the ion current signal in comparison to the positive case, the maximum is significantly shifted towards higher deflection voltages, cf. right panel of figure 5.4. This indicates a lower mean ion mobility and therefore a potentially increased mean ion size for the anionic ion ensemble, because that would lead to a notable difference in the position of the ion current maximum with respect to the deflection voltage.

Another notable difference becomes apparent if the deflection polarity is opposite to the discharge polarity. If the corona discharge is operated in positive mode, no ion current is detectable with negative deflection voltage. In contrast, with a negative corona discharge and a positive deflection voltage, a small but well detectable positive ion current is measured. It is speculated that in the positive mode a purely cationic ion current is transported into the measurement chamber. With the corona in negative mode, a partly mixed ion ensemble reaches the measurement chamber, consisting of a primary anionic ion current and a small fraction of cations.

### 5.4.2 Numerical Results

#### 5.4.2.1 Fluid dynamics (CFD)

The flow of the neutral bulk gas was simulated in Comsol as described in section 5.3.1. Figure 5.5 present the results with activated turbulence model ( $k - \epsilon$ , denoted as “turbulent” flow in the following), figure 5.6 shows the calculated bulk fluid flow without any turbulence modeling (called “laminar” flow in the remaining sections of this chapter).

In both models, the dominant visible feature in the flow velocity field is the gas stream which passes straight from the inlet port to the exhaust port through the measurement chamber, between the deflection and the measurement electrodes. Outside this central gas flow, in the bulk volume, the velocity is generally very low. The flow lines in both figures show that the gas motion outside the main flow is probably instationary. In both models, similar vortex patterns are visible. This motion of the gas is probably driven by the friction between the main flow and the gas in the bulk volume of the measurement chamber. In addition, a small fraction of the widened main flow is skimmed by the sharp edges of the outlet flange. This gas from the outer layers of the main stream is reflected back into the measurement chamber and drives the vortex motion of the gas in the chamber bulk volume. The gas reflection is most clearly visible in the laminar flow model (fig. 5.6), but with increased inflow velocity it is also

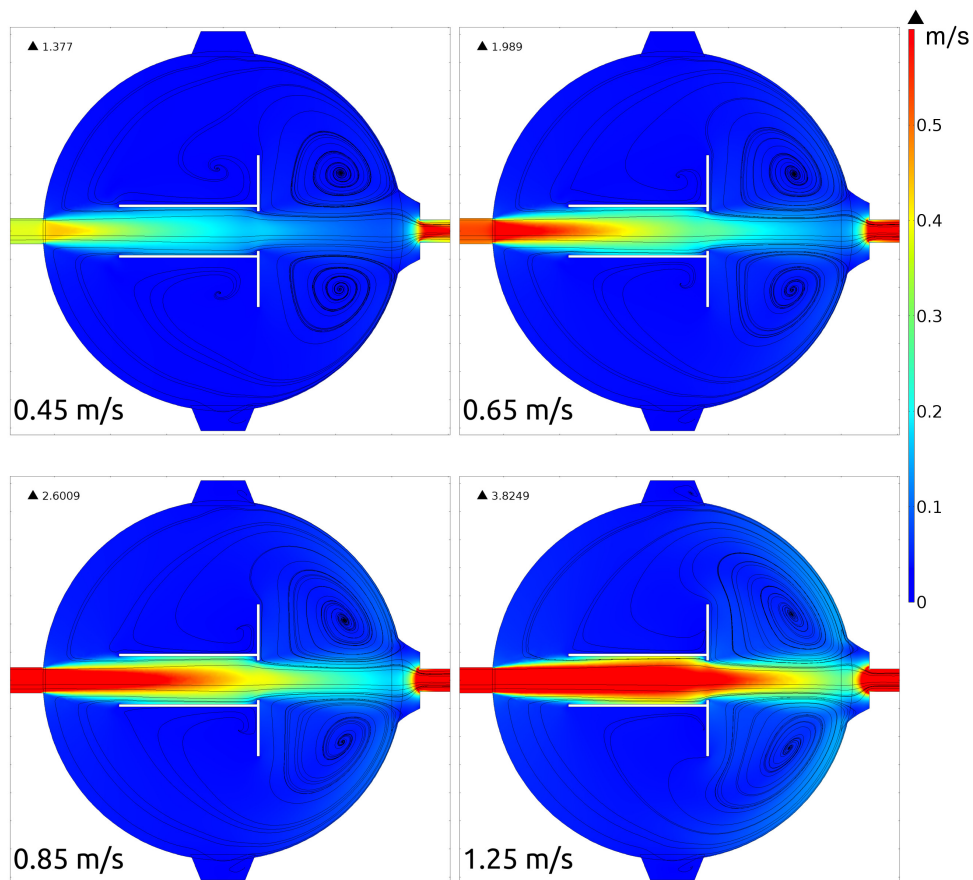


**Figure 5.5:** *Bulk gas flow simulation:* Static turbulent (activated  $k-\epsilon$  turbulence model) flow simulations for different outflow gas velocities. Color encoded: Gas velocity magnitude, black lines: flow lines. The maximum gas velocity is shown in the upper left corner of each panel.

discernible in the turbulent flow simulation ( $1.25 \text{ m s}^{-1}$  in fig. 5.5). The exemplary depiction of the three dimensional flow structure in figure 5.7 supports the notion about the flow in the measurement chamber obtained from the two dimensional cut-planes in figure 5.5 and 5.6. Although if the main gas stream widens noticeable, most of the injected gas traverses right through the geometry and remains as a relatively compact almost cylindrical gas stream which is clearly observable by the flow lines starting on the inlet port (colored flow lines in fig. 5.7). The flow reflected on the outlet port, which dissipates rapidly into the volume, is a driver for the very slow drift motion of the gas in the chamber bulk volume.

Naturally, the level of instationarity of the gas motion outside the main flow can not be gathered by the stationary flow simulations. However, the details of the very slow

## 5 Simulation of ion migration in a slow gas flow

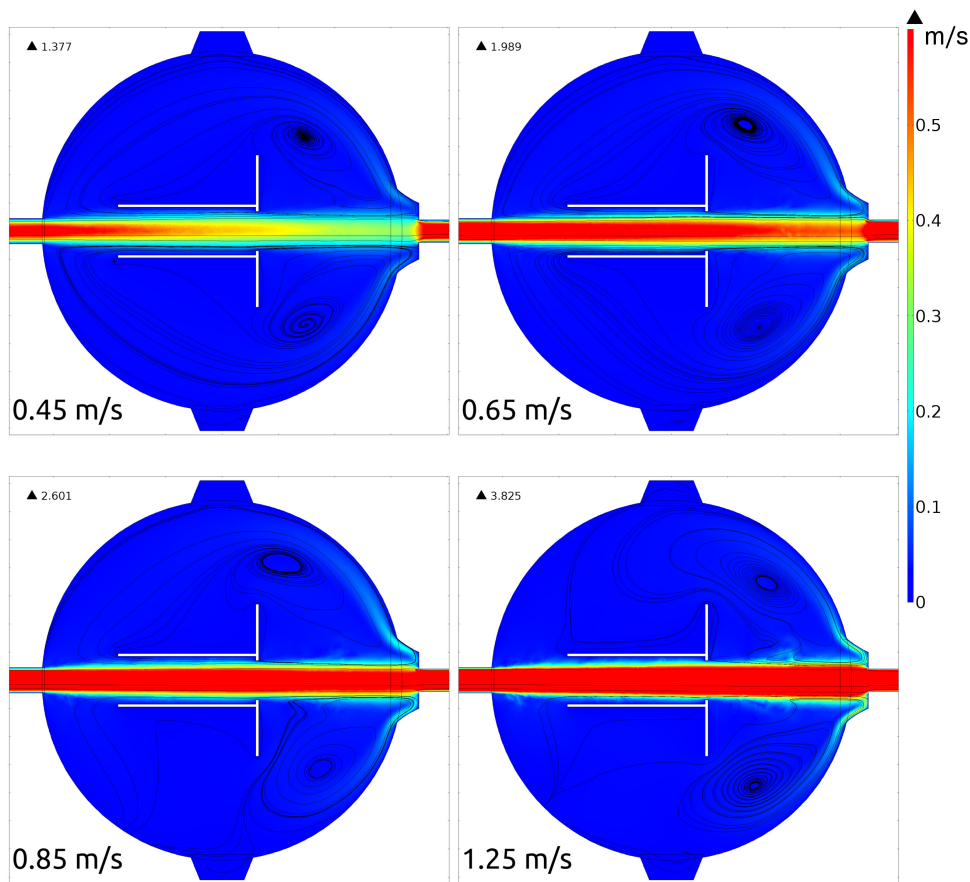


**Figure 5.6:** *Bulk gas flow simulation:* Static laminar (deactivated turbulence model) flow simulations for different outflow gas velocities. Color encoded: Gas velocity magnitude, black lines: flow lines. The maximum gas velocity is given in the upper left corner of each panel.

gas flow outside the main stream have a low relevance for the ion motion because in comparison to the main flow velocity, the gas is almost static here and the convective or diffusive exchange of material between the slow moving bulk gas and the main flow is relatively low.

The width of the center gas flow is primarily governed by the diameter of the inlet tube between ion source and measurement chamber, particularly in the laminar case. The velocity profile on a cutline perpendicular to the main axis of the primary gas stream is almost parabolic in both cases, with and without turbulence model. Figure 5.8 shows the velocity profile of the main gas stream on a cut-line close to the front edges of the deflection and receiver electrodes.

As figures 5.5 and 5.6 show, an increase of the gas inflow primarily leads to an

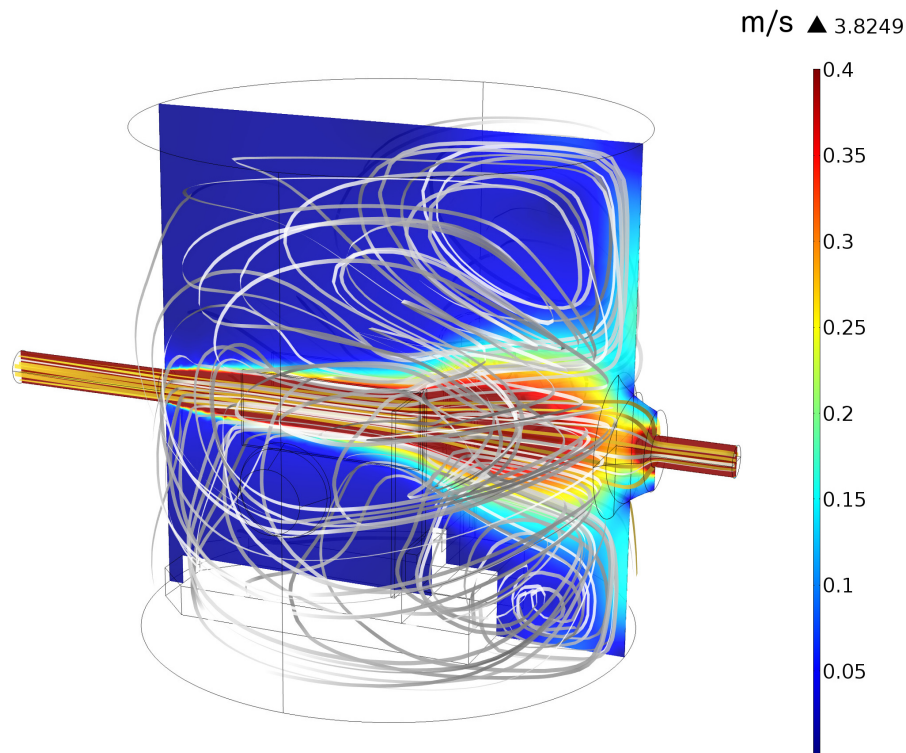


**Figure 5.7:** *Bulk gas flow simulation:* Three dimensional representation of the turbulent bulk gas flow for  $1.25 \text{ m s}^{-1}$  outflow velocity. The white flow bands start in the bulk volume while the orange flow bands start at the inlet port. The gas velocity magnitude in  $\text{m s}^{-1}$  is presented color encoded on the central plane. The main gas flow is confined on the axis between inlet and outlet port while the gas in the bulk volume moves very slowly in a complex large scale eddy structure.

acceleration of the main gas stream through the measurement chamber, but the general shape of the flow structure is not significantly altered by this acceleration. This is depicted by the patterns of flow lines in the measurement chamber which are relatively unaffected by the acceleration of the main flow. The position and the shape of the main vortexes in the bulk volume changes slightly but the general pattern stays almost the same. This finding is supported by data presented in figure 5.8 which shows that the velocity profile is scaled but not altered in its overall shape by the acceleration of the inflow into the measurement chamber.

The comparison of the turbulent and the laminar flow solution yields some notable differences: Firstly, with activated turbulence model the flow field is generally more diffuse and the turbulence model induces a significantly increased dissipation of the flow velocity. Figure 5.5 and figure 5.6 show that in the turbulent model the main flow

## 5 Simulation of ion migration in a slow gas flow

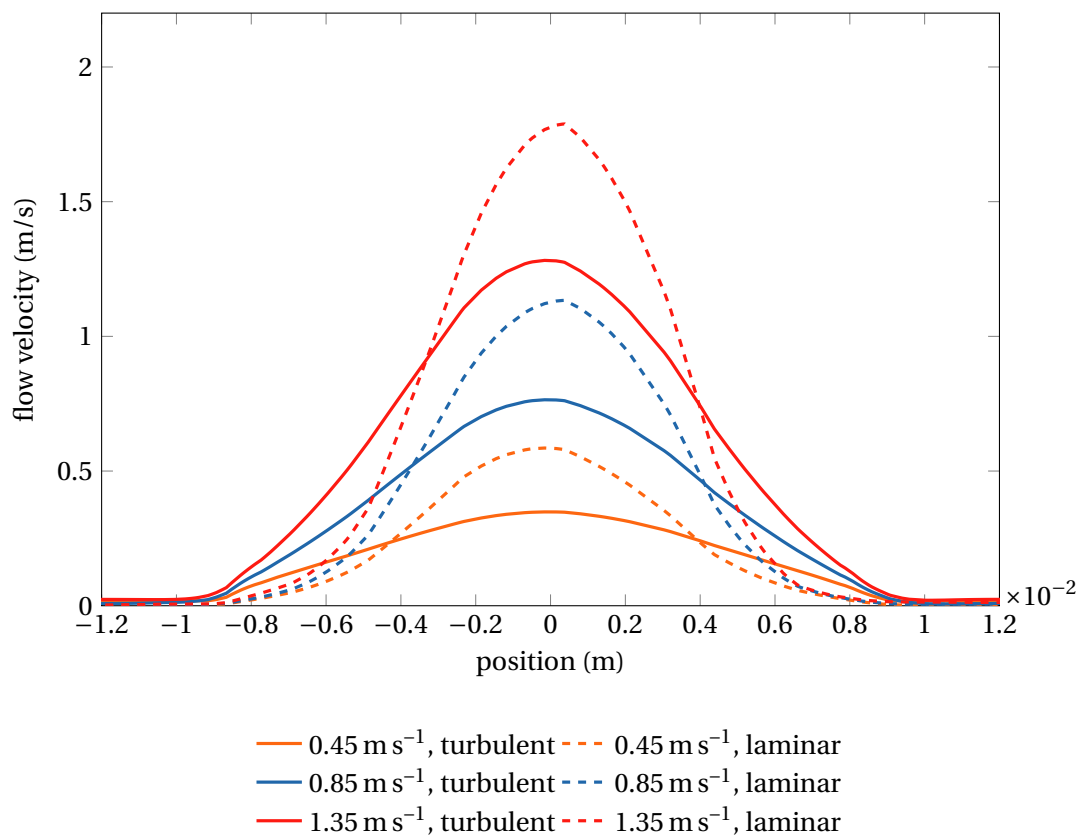


**Figure 5.8:** *Flow simulation results:* Velocity profile of the main gas flow. The axial position of the shown cross section was next to the front edges of the electrodes (labeled *e* and *d* in fig. 5.2)

velocity drops notably stronger axially, and the gas stream widens further than in the laminar flow model. This notion is supported by the velocity profiles in figure 5.8. Even with activated turbulence model, the free gas stream shows a parabolic velocity profile but in this case the velocity distribution is significantly wider and flatter than in the laminar case.

Since the inner diameter of the inlet port is smaller than the distance between the electrodes, in the laminar model the compact gas stream does virtually not interact with the electrodes. In contrast, the widened stream in the turbulent flow model experiences a noticeable interaction with the electrodes. The confined space between the electrodes and the electrode holders have a slight nozzle effect on the gas stream which is visible in figure 5.5 and 5.7 in the region between the electrodes and the outlet port.

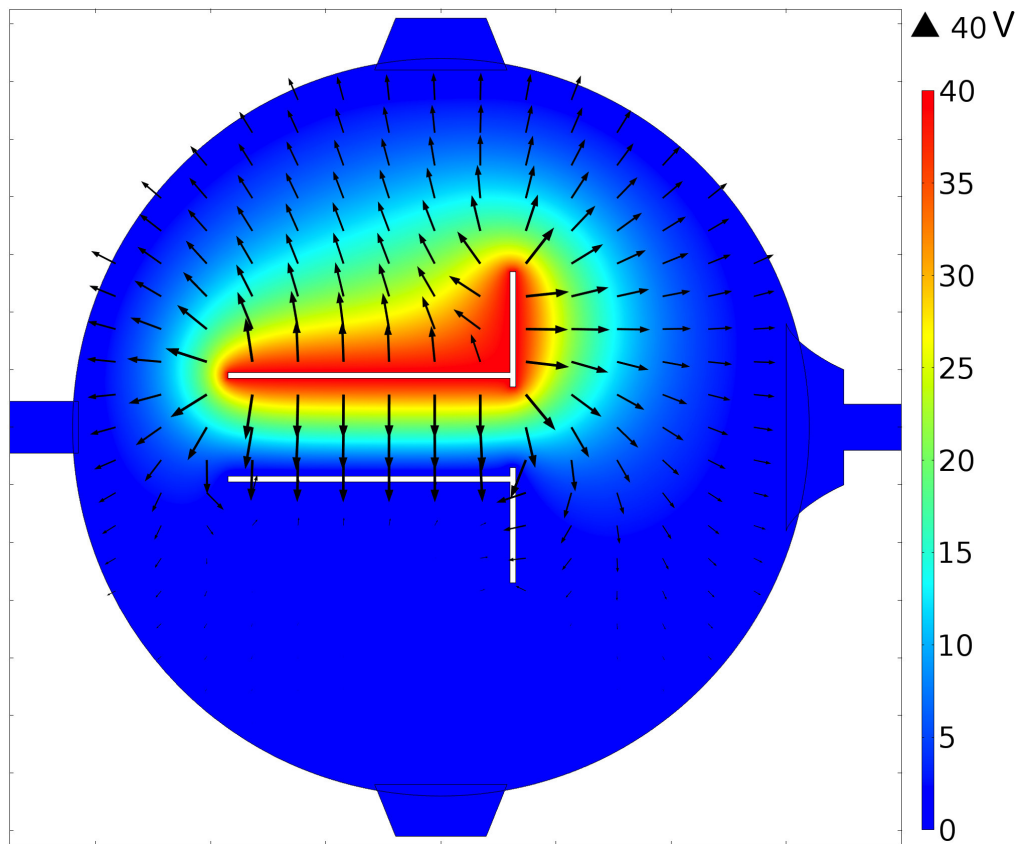


**Figure 5.9:** *Simulation of the static electric field in the measurement chamber:* The electric potential distribution is presented color encoded (given in V) while the electric field is depicted by the vectors (black arrows). The arrow size is proportional to the logarithmically scaled field strength.

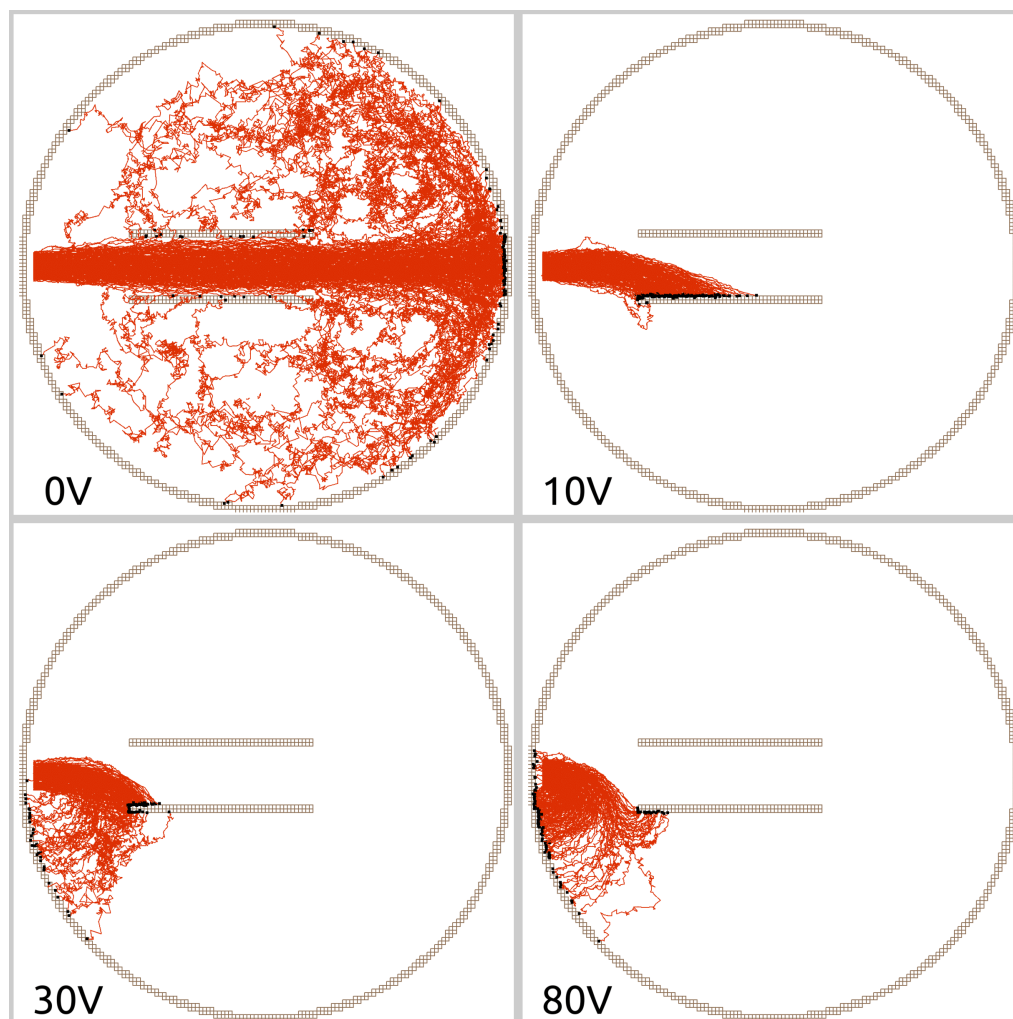
#### 5.4.2.2 Particle tracing simulation

Figure 5.9 depicts the electric field in the measurement chamber which is established by the potential on the deflection electrode. The presented field distribution was calculated with Comsol. Within the numerical deviations induced by the different calculation mesh and the different mathematical approach, the calculated electrostatic fields were identical in the SIMION model. Since the deflection electrode is the sole element having a non-zero electric potential, the electric field shown in figure 5.9 is just scaled with a factor by a variation of the deflection potential.

Figure 5.10 and 5.11 show the results of ion trajectory simulations with SIMION / SDS under consideration of the turbulent flow solution discussed in section 5.4.2.1 and the deflection field for two different bulk flow velocities.

Without a potential on the deflection electrode (0 V in fig. 5.10 and 5.11), the ions are

## 5 Simulation of ion migration in a slow gas flow



**Figure 5.10:** *SIMION simulation results:* Simulated ion trajectories with  $0.45 \text{ m s}^{-1}$  outlet velocity of the turbulent simulated bulk gas flow. The increasing electrical force on the ions is clearly visible. The deflection voltage is given in the panels. The masses of the simulated ions were uniformly distributed between 19 and 350 Da (estimated  $K_0 = 3.56 - 1.04 \times 10^{-4} \text{ m}^2 \text{ V}^{-1} \text{ s}^{-1}$ )

transported by convection and molecular diffusion only. Under the given conditions, the convective flux is significantly larger in comparison to the diffusive flux. Therefore, in absence of a deflection field most of the simulated ions essentially follow the bulk gas stream through the measurement chamber and terminate in the outlet port region. This situation is shown in the upper left panel of figure 5.11.

With lower flow velocity, clearly the stream of charged particles widens due to increased diffusion relative to the convective transport induced by the main gas flow.

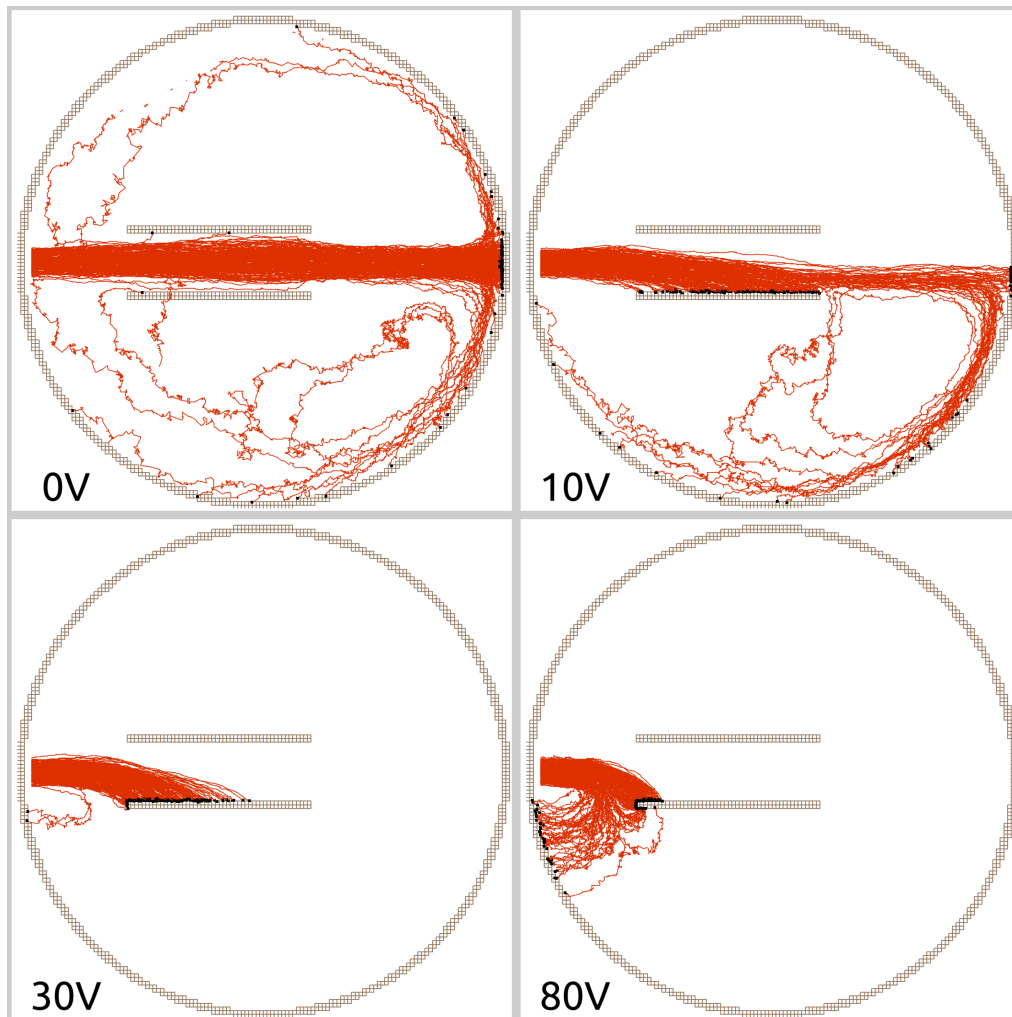


**Figure 5.11:** *SIMION simulation results:* Simulated ion trajectories with  $1.25 \text{ m s}^{-1}$  outlet velocity of the turbulent simulated bulk gas flow. In comparison to fig. 5.10 the increased effect of the bulk gas flow is visible. The deflection voltage is given in the panels. The masses of the simulated ions were uniformly distributed between 19 and 350 Da (estimated  $K_0 = 3.56 - 1.04 \times 10^{-4} \text{ m}^2 \text{ V}^{-1} \text{ s}^{-1}$ )

As a consequence, more particles are mixed into the reflected gas flow which dissipates into the large, almost static, gas volume in the measurement chamber. Here the ions drift until they terminate on a chamber wall or one of the electrodes. The upper left panel of figure 5.10 illustrates this observation.

With a potential on the deflection electrode, the situation obviously changes significantly: Between the measurement and the deflection electrode, which essentially

## 5 Simulation of ion migration in a slow gas flow

form a plate capacitor, an uniform electric field is established which pushes the ions towards the receiver electrode. If the deflection field is sufficiently strong, the ions terminate quantitatively on the receiver electrode, as shown in the simulation run with 10 V deflection potential in figure 5.10. If the deflection potential is too low relatively to the viscous drag force, only a fraction of the ions is pushed onto the receiver electrode (see 10 V in fig. 5.11).

If the deflection potential is further increased, the repulsive electrostatic force acting on the ions before they reach the region between the electrodes starts to overcome the viscous drag of the bulk gas flow. As a result an increasing fraction of ions is deflected onto the measurement chamber wall (see 30 V and 80 V in 5.10).

If the bulk gas flow and thus the viscous drag force acting on the ions is increased, higher electric potentials are required to deflect the ions. This is clearly discernible if the simulations presented in fig. 5.10 and 5.11 are compared.

The overall shape of the quantified simulated ion current on the receiver electrode in dependence on the deflection potential is presented in fig. 5.12 for different flow velocities. As experimentally observed (cf. fig. 5.3 and 5.4), the ion current raises quickly and reaches a maximum when most of the ions are deflected on the measurement electrode. With further increasing deflection potential, the ions are entirely deflected and the ion current starts to drop. As expected from the analysis of the ion trajectory plots, with increasing bulk gas flow, the entire ion current distribution is shifted in the deflection potential dimension towards higher deflection voltages with increasing bulk gas flow, while the overall shape of the distribution is not significantly changed.

Figure 5.12 presents experimentally determined ion current data in comparison to simulated results. The rapidly increasing section (0 to 8 V deflection potential) and the transition section (8 to 15 V) of the ion current signal are only qualitatively reproduced by the simulations. As seen in the left panel of fig. 5.12, the slope of the simulated signal in the rising section of the ion current signal is significantly steeper than the rising slope of the experimental signal. Additionally, the simulation predicts a vanishing ion current with no deflection potential (0 V deflection potential in fig. 5.12) which is also not reproduced experimentally. The experiments show in contrast a remaining ion current of approximately 20% of the maximum value.

In the declining region of the ion current signal, the qualitative agreement between simulation and experiment is much better. As shown in the right panel of fig. 5.12, the slopes and the curvature of the simulated and measured ion current signals are well comparable in the declining region between 20 and 80 V deflection potential.

However, despite the good qualitative reproduction of the shape of the signal in this region, there is a significant deviation between simulation and experiment: Figure 5.12 shows that the simulation nearly reproduces the experimentally found ion current e.g., with an assumed mean bulk gas velocity of  $0.45 \text{ m s}^{-1}$  while the mean flow velocity in the experiment was  $0.65 \text{ m s}^{-1}$ . To reproduce the declining part of the ion current signal, the assumed mean bulk gas velocity in the simulation is a factor of approximately 1.5 higher than in the experiment. Possible explanations for this deviation are an invalid fluid dynamic simulation or a wrongly assumed ion mobility

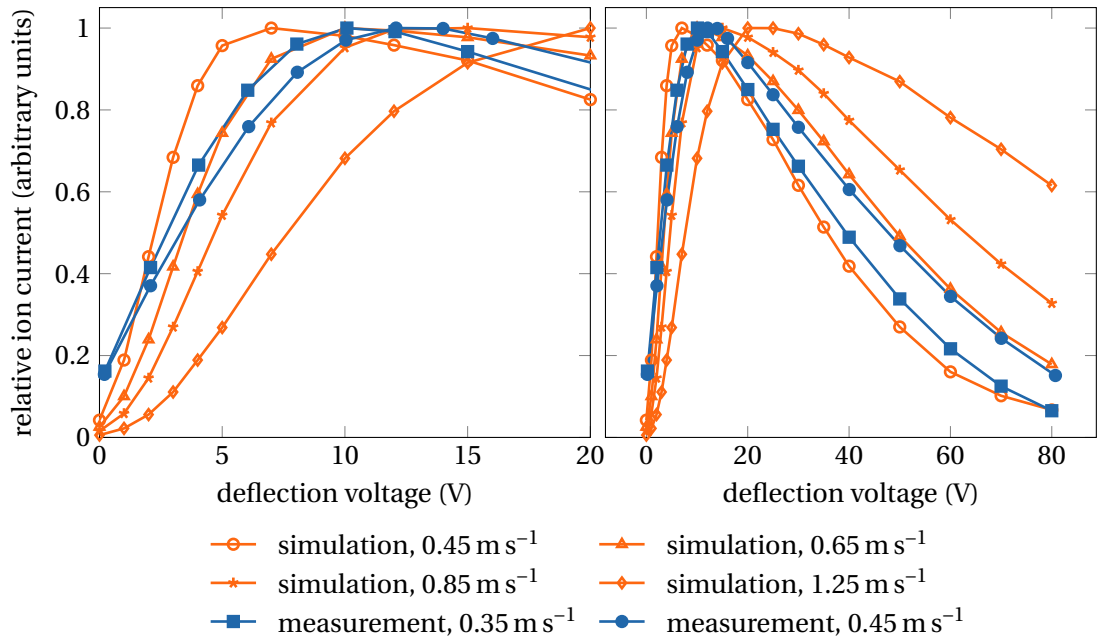


**Figure 5.12:** *SIMION simulation results:* Simulated ion current on the receiver electrode for different bulk gas flow velocities in comparison to the experimentally determined ion current. The masses of the simulated ions were uniformly distributed between 19 and 350 Da (estimated  $K_0 = 3.56 - 1.04 \times 10^{-4} \text{ m}^2 \text{ V}^{-1} \text{ s}^{-1}$ )

distribution, which governs the relative effects of the electric field on the simulated ions. In the simulation runs presented in figure 5.12 the simulated ion masses were uniformly distributed between 19 and 350 Da which corresponds to an estimated ion mobility of  $K_0 = 3.56 - 1.04 \times 10^{-4} \text{ m}^2 \text{ V}^{-1} \text{ s}^{-1}$ .

To investigate the relative effects of the bulk gas velocity and the ion mobility, a set of simulations was performed with monodisperse ion distributions. Figure 5.13 presents the results. Under the given conditions, variations of the bulk flow and variations of the ion mobility have essentially inverse effects, even if a slight deviation between the signals becomes visible in the simulation runs with ions which are relatively low susceptible to the electric field ( $0.45 \text{ m s}^{-1}$ , 271 Da and  $1.35 \text{ m s}^{-1}$ , 20 Da simulations in figure 5.13). The ion mobility can thus be considered in good approximation as a simple scaling between orthogonal forces. Since a deviation of the simulated mean flow speed of a factor of approximately 1.5 relative to the experiment seems to be unlikely, the cause of the divergence between simulation and experiment is probably due to a wrongly assumed ion mobility distribution.

Figure 5.14 presents the effects of the variation of the turbulence modeling in the

## 5 Simulation of ion migration in a slow gas flow

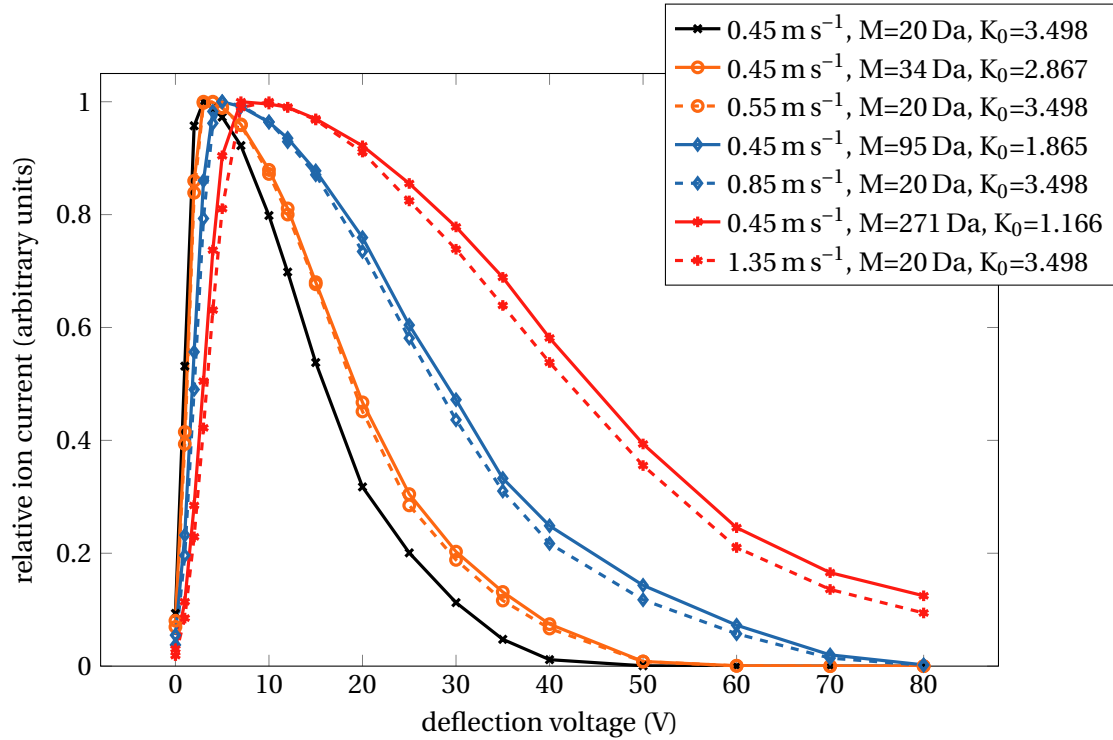


**Figure 5.13:** *SIMION simulation results:* Effects of variations of the ion mobility and the bulk gas flow velocity on the simulated ion current on the receiver electrode. The ion mobility and the bulk gas flow velocity (outlet port boundary condition) have almost inverse effects on the simulated ion current. The reduced ion mobility ( $K_0$ ) is given in  $10^{-4} \text{m}^2 \text{V}^{-1} \text{s}^{-1}$ .

fluid dynamic simulation. Despite the noteworthy differences between the CFD solutions with and without turbulence modeling, the simulated ion current is relatively insensible to this change. Particularly in the region of steep rise of the ion current, almost no difference between the different CFD solutions is visible. In the declining part of the ion current distribution, the turbulent and laminar fluid models noticeably differ with increasing fluid flow velocity. However, with the deflection voltage approaching 80 V, the ion current simulations begin to re-converge, particularly as visible in the simulations with  $0.45 \text{ m s}^{-1}$  and  $0.64 \text{ m s}^{-1}$  in figure 5.14.

It is reasonable to assume that the dynamics which governs the ion current primarily takes place in the region from the inlet port to the first half of the electrode assembly and contributes to the relatively small differences between the laminar and turbulent simulations. In this area, the divergence between the CFD solutions is relatively small as well. Interestingly, the notably higher maximum flow velocity in the laminar case (see fig. 5.8) seems to be, at least partially, compensated by the widened flow profile in

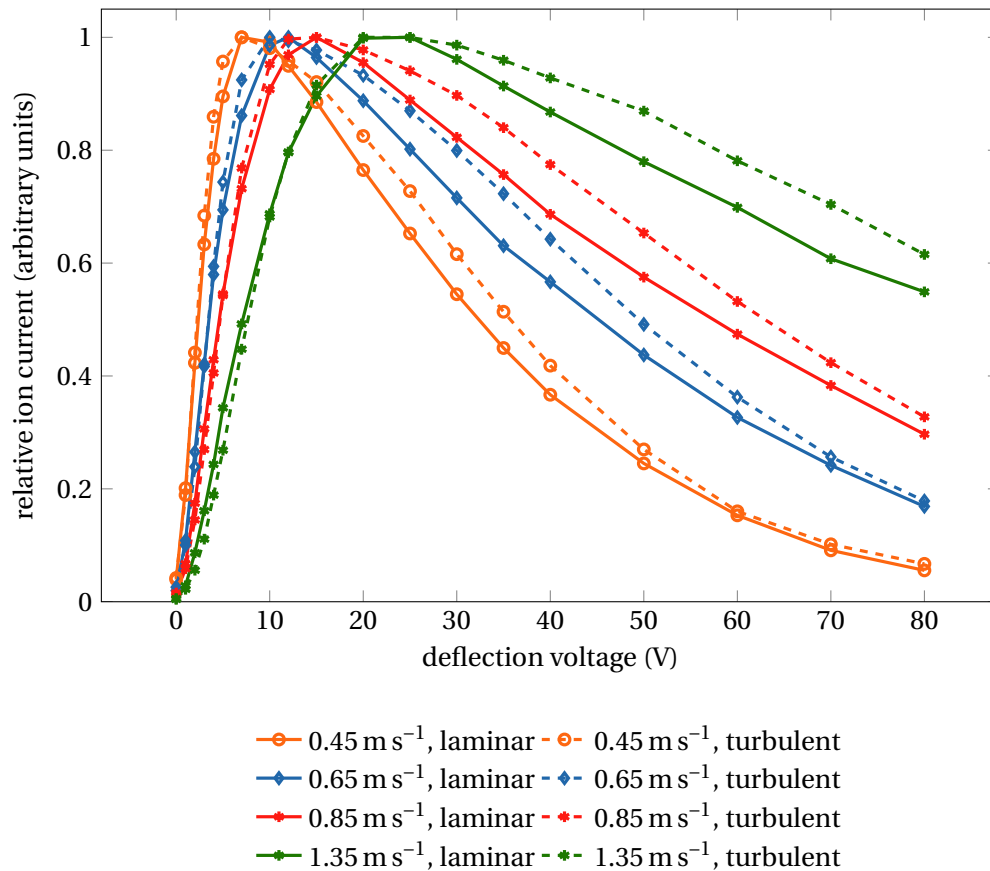


**Figure 5.14:** *SIMION* simulation results: Effects of the turbulence model on the simulated ion current on the receiver electrode. The general shape of the simulated ion current response on the deflection voltage without turbulence modeling (“laminar”) and with  $k-\epsilon$  turbulence model (“turbulent”) is similar but with turbulence modeling the effect of the bulk gas flow is significantly more pronounced.

the turbulent case.

Additional simulations were performed with activated coulomb repulsion modeling using the integrated coulomb repulsion simulation feature of *SIMION*, which is a direct summation approach (see section 3.3.2 on page 26). To investigate the hypothetical effects of a mixed ion inflow the set of simulations was performed with mono- and bipolar configurations of simulated ions.

The quadratic run time behavior of the coulomb repulsion algorithm limited the number of simulated particles significantly. The maximum feasible particle number was approximately 4000. The consideration of pure coulomb repulsion had no significant effect, even if the charge weighting factor of the individual simulated particles was

## 5 Simulation of ion migration in a slow gas flow

raised considerably. In simulation runs with drastically increased charge weighting sometimes numerical artifacts were clearly observable, e.g. the formation of artificial, very stable “ion pairs” in the simulations with mixed ion inflow.

### 5.4.2.3 Electrokinetic flow

In general, the electrokinetic flow simulations performed in Comsol qualitatively reproduce the general findings of the ion migration calculations in SIMION. Figure 5.15 shows an exemplary set of Comsol simulations with different deflection potentials.

As discussed for the particle tracing simulations in SIMION, with negligible deflection potential, the ions are transported primarily by convection induced by the bulk gas flow (0.1 V in fig. 5.15). With increasing deflection potential, the ions are pushed towards the receiver electrode (10 V in fig. 5.15) before the electrophoretic force overcomes the viscous drag and the ions are finally entirely deflected (80 V in fig. 5.15). The flow lines in figure 5.15, indicating the total flux (the combination of diffusive, electrophoretic, and convective flux) show a remarkable similarity to the ion trajectories simulated with SIMION, if the diffusive random motion, which is not part of the electrokinetic flow lines, is ignored.

The static ion concentration distribution calculated in the electrokinetic model also gives an indication of the ion migration: The region of high ion concentration also corresponds with the flow lines of the electrokinetic flow. Interestingly, the concentration distribution is surprisingly diffuse, and the ion concentration tends to drop quickly.

A possible explanation for this behavior, which is not observed in the SIMION results, is the effect of the wall boundary conditions. In the presented model a vanishing static concentration ( $c_i = 0$ ) was assumed on all walls. Hence, the walls of the simulated geometry are ideal sinks for the simulated ionic species, which induces a strong diffusive transport towards them. This additional “drag” is not existing in the SIMION model because in the statistical approach used here diffusive transport effects are not explicitly modeled but rather the consequence of the random component of the ion motion. Therefore, despite the fact that the simulated ions terminate on first contact with the walls in the SIMION model, the walls have no direct effect of the individual ion trajectories, and the SIMION model is less sensitive to this kind of wall effects.

The assumption that the walls of the chamber and the electrodes behave as ideal sinks for ions is possibly not justified by the physical reality. In contrast to the conditions at high vacuum, at atmospheric pressure metal surfaces are coated with an adsorbed layer of water and other components of the present gas phase in addition to oxide layers. Inevitably, the dynamics and involved kinetics of the ion migration through this layer, which is most probably hindered by the interaction between the ions and the layer components, would have to be considered in the Comsol model. Beside the assumption of a vanishing ion concentration on the wall, there are further predefined boundary condition options available in the used Comsol application mode. None of them (e.g. convective flux through an “open boundary”, or a fixed total flux) satisfactory model the assumed situation of an adsorbed boundary layer with low

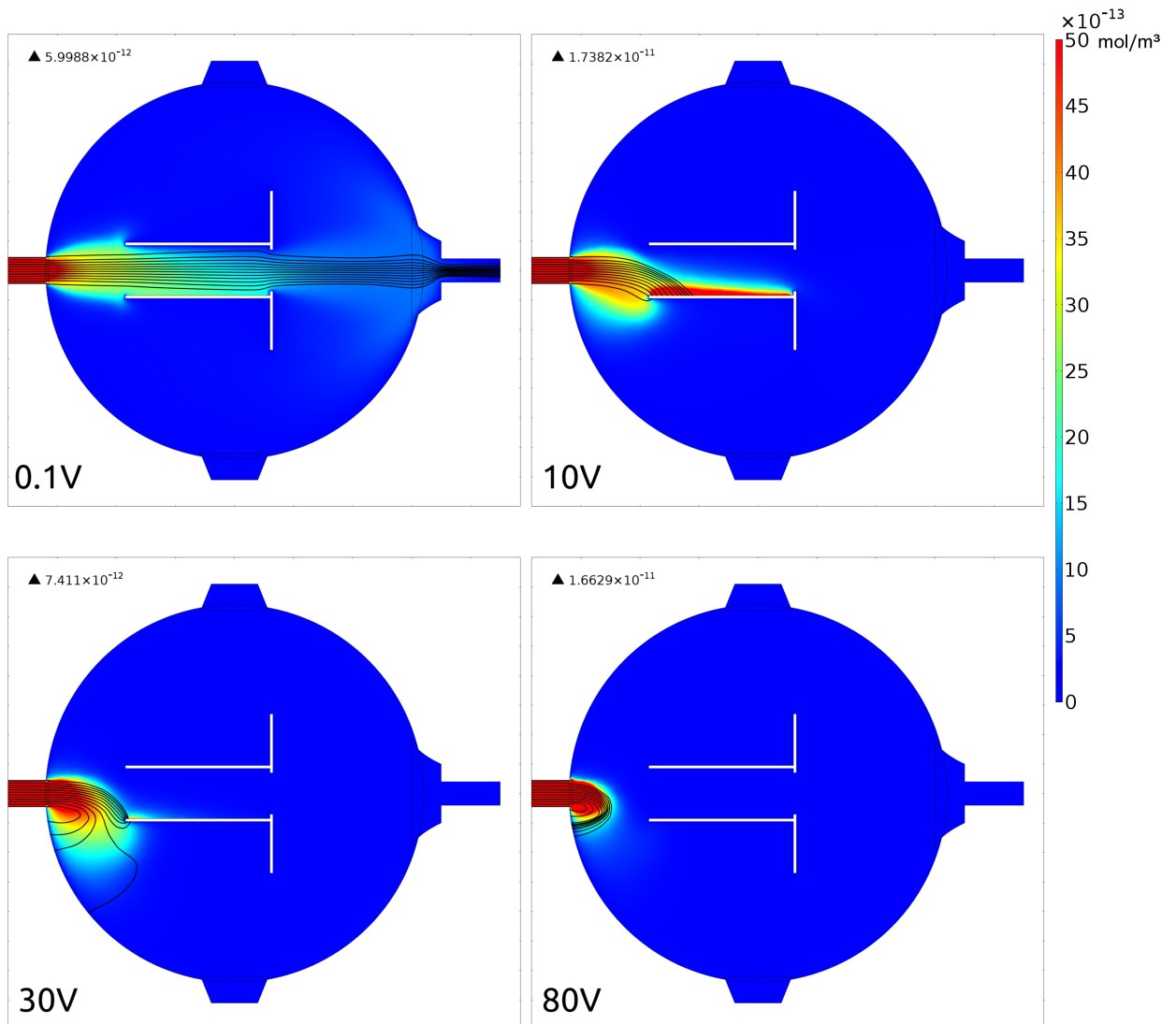


**Figure 5.15:** *Comsol simulation results:* Static steady state ion concentration distribution (color encoded) and flow lines of the total ion flow (black lines) in the electrokinetic model for different deflection voltages. The outlet velocity of the simulated turbulent bulk gas flow was  $0.45 \text{ m s}^{-1}$ . The general shape of the electrokinetic flow is similar to the SIMION results in fig. 5.10. The ion mobility was  $K_0 = 3.49 \times 10^{-4} \text{ m}^2 \text{ V}^{-1} \text{ s}^{-1}$ . The maximum concentration value is given in the upper left corner of each panel.

## 5 Simulation of ion migration in a slow gas flow

ion conductance. It should be indeed possible to derive a valid mathematical model for the assumed boundary layer behavior. Even if such a model was readily available, it would have to be correctly parameterized. The required parameters, e.g. boundary layer diffusion coefficients of the modeled ionic species, are unknown for the given experimental conditions. An experimental determination of such parameters is ambitious and requires a considerable amount of experimental effort, which was not achievable in the available time frame of this work.

A second feature of the ion concentration distribution depicted in figure 5.15 is the build up of a “cushion” zone with high ion concentration on the measurement electrode which is clearly seen in the simulation run with a deflection potential of 10V. This is caused by the combination of the electrophoretic push towards the measurement electrode and the low gas velocity in close vicinity to the electrode surface. This induces a zone in which the ion transport is primarily governed by diffusion and electrophoretic drift, which leads to the formation of the high local ion concentration.

The analysis of the Comsol simulations reveals that the simulated ion current follows a similar pattern as in the particle tracing calculations. Figure 5.16 shows results for an exemplary set of electrokinetic simulations. Similar to the results of the SIMION model, the ion current rises to a maximum and then drops to zero. As well as in the particle tracings, the slope of the ascend is significantly higher than the one of the decent. The starting point of the ion current distribution derived from the Comsol simulations is slightly increased because the Comsol model was unstable and did not converge well in absence of any deflection potential. Therefore, the first simulated point had already a deflection potential of 0.1 V. In the steep ascent of the ion current signal even a small deflection potential leads to a noticeable increase of the simulated ion current.

The curvature of the declining phase is considerably higher in the Comsol calculations as compared to the SIMION results, cf. figure 5.12. The SIMION simulation runs with monodisperse sets of simulated ions presented in figure 5.13 also show an increased curvature. This indicates that the more linear decline in the SIMION simulations with a wide ion distribution is probably a consequence of the assumed wide ion mobility distribution.

The Comsol model was not able to reproduce the experimental ion current distribution at all. This in contrast to the SIMION model, which was able to reproduce the shape of the actual experimentally found ion current distribution well in the declining part of the ion current signal, even if the bulk gas flow parameters differed significantly from the experimental ones. As figure 5.16 clearly shows, none of the performed simulation runs traces the experimental ion current signal. The satisfactory measurement run fitting best in the ascending part ( $1.35 \text{ m s}^{-1}$ ,  $K_0 = 3.5 \times 10^{-4} \text{ m}^2 \text{ V}^{-1} \text{ s}^{-1}$  in fig. 5.16) falls off much quicker in the descending part than the experimentally found ion current. In addition, due to the increased curvature in the declining simulated ion current signal, none of the performed electrokinetic calculations reproduced the almost linearly dropping experimental ion current signal. Considering the most favorable fits

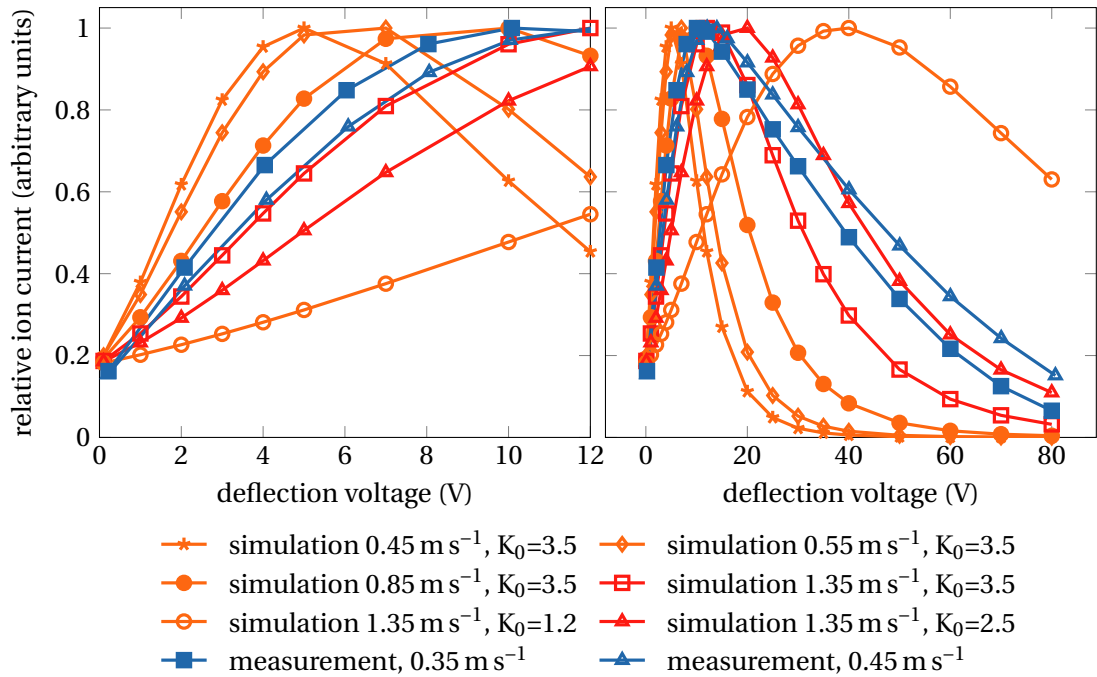


**Figure 5.16:** *Comsol simulation results:* Comparison of simulated ion current on the receiver electrode with experimental data. The general effects of variations of the bulk gas flow or the ion mobility in the Comsol simulations are similar to the results of the SIMION simulations shown in fig. 5.12 and 5.13. The electrokinetic model was not able to reproduce the experimental results over the deflection voltage range.

between experiment and Comsol simulation (e.g.  $1.35 \text{ m s}^{-1}$ ,  $K_0 = 2.5 \times 10^{-4} \text{ m}^2 \text{ V}^{-1} \text{ s}^{-1}$  in fig. 5.16) it becomes evident that the deviations of the simulated parameters (bulk gas flow, ion mobilities etc.) from the experimental ones are much larger in the electrokinetic simulations than in the SIMION model.

Figure 5.17 shows that also in the electrokinetic model, the ion mobility and bulk gas flow velocity have almost inverse effects on the simulated ion current. The decline of the ion current after the global maximum, which much steeper as compared to the experimental findings, was barely affected by a change of the electric mobility of the simulated ionic species. The small systematic difference between the simulation series with increased bulk gas flow and the series with decreased ion mobility is insignificant with respect to the large deviation of the electrokinetic flow model from the actual ion current measurements.

An increased sensitivity of the Comsol ion migration model with respect to the underlying bulk gas flow simulation is also evident in the comparison of ion current

## 5 Simulation of ion migration in a slow gas flow

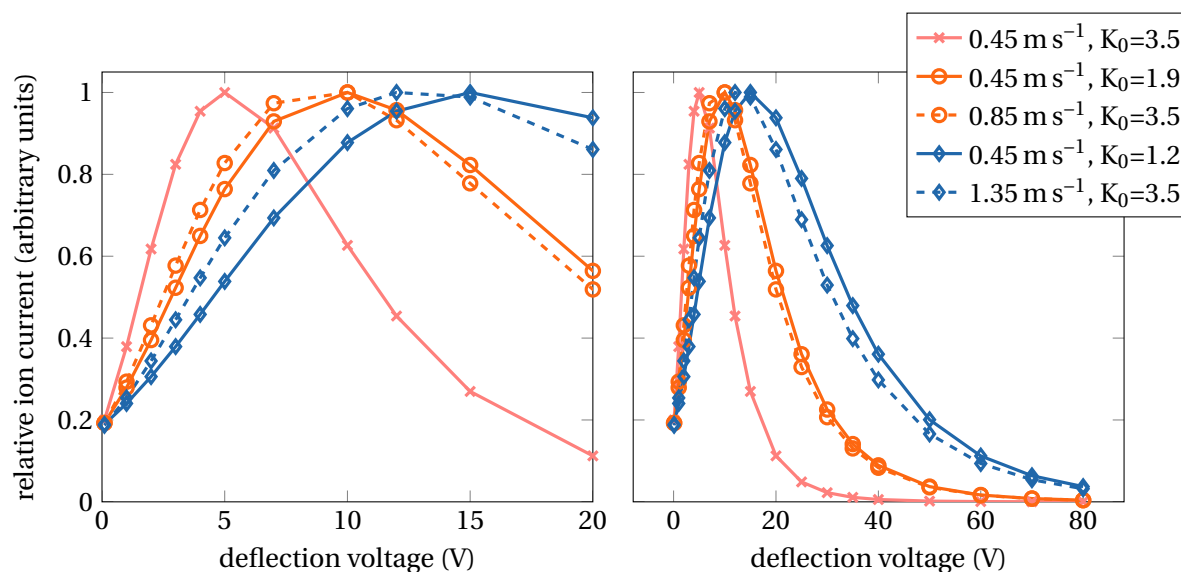


**Figure 5.17:** *Comsol simulation results:* Effects of variations of the ion mobility and the bulk gas flow velocity on the simulated ion current on the receiver electrode. Similar to the SIMION results shown in fig. 5.13, the ion mobility and the bulk gas flow velocity have almost inverse effects on the simulated ion current. The reduced ion mobility ( $K_0$ ) is given in  $10^{-4} \text{ m}^2 \text{ V}^{-1} \text{ s}^{-1}$ .

simulations with turbulent and laminar bulk gas flow, presented in figure 5.18. In contrast to the SIMION model which showed noticeable but relatively subtle effects of the turbulence modeling on the simulated ion current, the Comsol simulations show a considerable shift of the ion current maximum towards higher deflection voltages in the turbulent case. This shift increases with increasing bulk gas flow.

According to the presented particle tracing simulations a subset of electrokinetic calculations was performed with activated space charge modeling as described in section 5.3.2. Figure 5.19 presents an exemplary set of simulated ion current signals for different ion mobilities and simulated bulk gas flow velocities. Due to a wrongly labeled measurement range selector on the used electrometer, which was not yet revealed when the electrokinetic simulation runs were performed, the assumed ion concentration in the numerical model was one order of magnitude higher than the actual one in the experiment. Therefore, the space charge density was significantly overestimated in the electrokinetic model.

The simulations considering space charge in a unipolar model depicted in figure 5.19, represent the largest possible extent of space charge effects at a given ion concentration range because any charge neutralization resulting from a mixed ion current

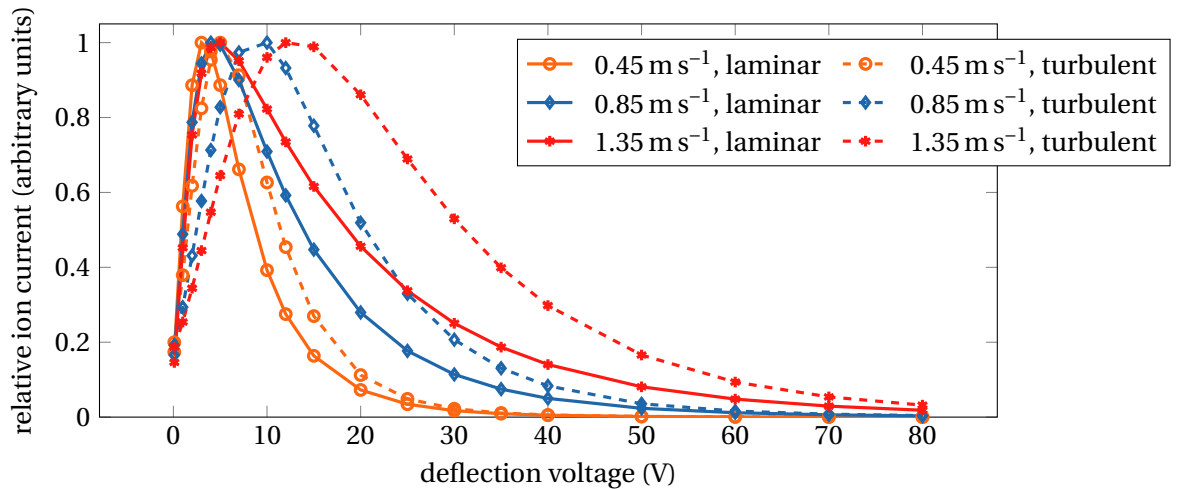


**Figure 5.18:** *Comsol simulation results:* Effects of the turbulence model on the simulated ion current on the receiver electrode. As in fig. 5.14, due to the widened gas stream with activated turbulence model, the gas flow has a significantly more pronounced effect on the electrokinetic flow.

reduces the space charge effects on the present electric field. The figure clearly shows that there was a noticeable influence of the space charge density on the simulated ion current. Considering the large overemphasis of space charge effects in the unipolar model with a tenfold overestimation of the ion density, it is concluded that space charge effects are probably negligible in the experiment.

## 5.5 Conclusions

Upon comparing the numerical results in this section, it becomes apparent that the qualitative motion of ions in the bulk gas flow is generally reproduced by both models. If the simulation results are quantified, significant differences are observed. Despite its more sophisticated mathematical approach, the Comsol model gives only poor results in terms of quantitative agreement with the experimentally found ion current. The SIMION model at least correctly predicts the experimental data in the declining part of the ion current signal with a deviation in terms of the bulk gas flow velocity of about 1.5. In contrast, the agreement of the best fitting Comsol simulations is significantly poorer than the results of the SIMION model, while the deviation from the experiment in terms of assumed ion mobility and bulk gas velocity is much larger. In addition, the Comsol model is much more sensitive towards effects of the bulk gas flow simulation, e.g. the application of a turbulence model.

If the SIMION/SDS model, which is the much better fitting one, is compared with

## 5 Simulation of ion migration in a slow gas flow

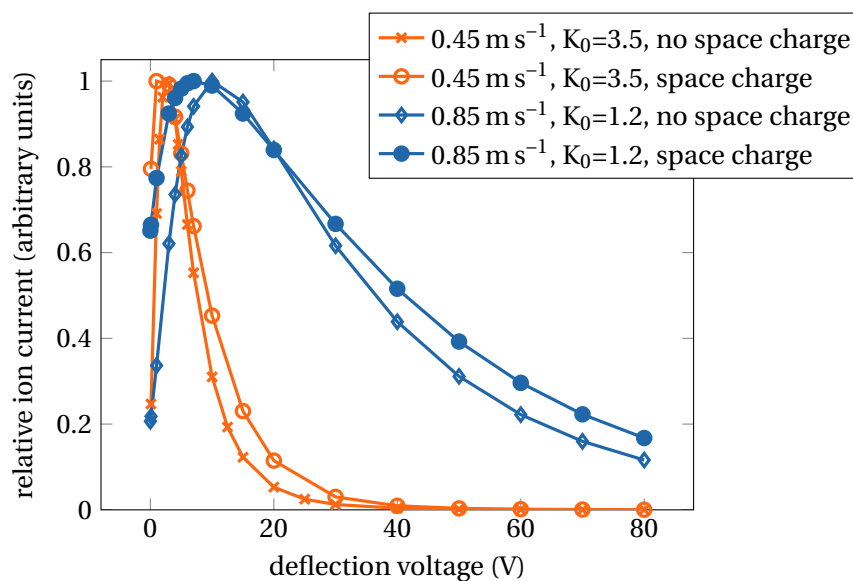


**Figure 5.19:** *Comsol simulation results:* Effects of space charge modeling on the simulated ion current on the receiver electrode. The consideration of space charge effects in the electrokinetic model (with laminar flow) affects the simulated ion current only to a minor extent.

the actual experimental data, possible causes for the already mentioned remaining deviation factor of about 1.5 have to be discussed. As shown in fig. 5.13 on page 54, in the presented SIMION/SDS model the ion mobility and the bulk gas velocity have virtually inverse effects on the simulated ion current. Thus, the deviation between simulation and experiment is explainable by an inaccurate bulk gas flow simulation, by a wrongly assumed ion mobility distribution or a combination of both, respectively.

Taking into account that the simulated bulk gas flow is not particularly complex, the overall flow velocity is relatively low, there are no sharp gradients in any flow parameter (no shocks) present, and the general turbulence level is low, a significant inaccuracy in the resulting flow profile is unlikely. In addition, the SIMION model is comparably insensitive to changes of the overall flow profile of the main gas stream as observable in figure 5.14 on page 55. Thus, probably the inaccuracy of the bulk gas flow simulation is not sufficiently high to solely explain the observed difference between simulation and experiment.

Furthermore, as presented in detail in chapter 7 on page 120, the ion mobility of individual proton bound water clusters  $([H_2O]_nH)^+$  is estimated with comparably high precision (well within 10%) from the individual cluster mass. Thus, it is also unlikely that a wrong estimation of the ion mobility from the ion mass is the sole cause for the observed deviation of the numerical model from the experiment. It is reasonable to assume that both discussed aspects contribute to a certain extend to the observed

deviation of the calculated results from the experiments. An increased ion diffusion resulting from the potentially relevant turbulent mixing of a partly turbulent bulk gas flow is also a possible cause for a difference between the performed simulations and the experiments. The development of a valid model for the effects of parameters of the turbulence model of the bulk gas flow simulation on the simulated ions would be a worthwhile goal for further work.

Naturally, the presented discussion is based on the assumption that the electrical and chemical conditions are consistent between simulation and experiment. If the actual ion distribution present in the experiments differs from the assumed one in the numerical model (uniform mass distribution between 1 and 350 Da), e.g., induced by the presence of unknown contaminants, invalid numerical results could occur. Likewise, electrical effects in the measurement chamber which are not accounted for, e.g. a notable charging of the measurement electrode due to a surface layer with reduced ion transmission, could also lead to the observed differences between simulation and experiment.

The presented SIMION/SDS model is advantageous in comparison to the Comsol model not only in terms of the higher agreement of the calculations and the experimentally observed ion current, but also in terms of numerical performance and numerical stability. While the Comsol model incorporates an iterative solving process which relatively often fails to converge, the SIMION model is not unstable in this sense and always produces a solution. A significant disadvantage of the SIMION / SDS model is the inability of the integrated space charge handling (model of coulomb repulsion between ions) to be used with a sufficiently high number of simulated ions (at least several thousand).

Despite these restrictions, for the presented benchmark problem, the particle tracing approach of SIMION/SDS is clearly better suited than the continuous electrokinetic Comsol model.

## 6 Simulation of ion acceptance distributions (DIA)

### 6.1 Introduction

The conditions in most commercial AP ion sources designed for routine analysis are generally fairly complex [1, 3, 31, 92], even if the complicated dynamics in the first pressure reduction stages [37, 93], which potentially significantly impacts on the final result of the ionization process [94], is not considered.

A typical basic design [95] of a general purpose ion source for the coupling of liquid chromatographic (LC-MS) pre-separation stages to a mass spectrometer is characterized by at least two orthogonally aligned heated gas flows, which interact in a complex way in a relatively large ion source enclosure [96]. The gas flows not only govern the motion and the distribution of the neutral analyte, but also affect, in combination with the present electric fields, the trajectories of the analyte ions. In addition to the physical dynamics in terms of particle motion, the ionization and ion transfer process depend also on the chemical kinetics in the ion source. Ionization techniques which use chemical interactions for the final charge transfer on the analyte particles, e.g. AP chemical ionization (APCI) [3], are particularly dependent on the, potentially complicated, chemical reaction kinetics in the ion source. If heterogeneous desorption processes are involved, as in most “ambient ionization” techniques (for example Direct Analysis in Real Time - DART [97]), or complex spray phenomena are part of the ionization process as in the many varieties of Electro-Spray Ionization (ESI) [3], it becomes increasingly difficult to fully apprehend the dynamics in the ion source.

The high complexity of the involved dynamics essentially led in the past to a “trial-and-error” approach for the design of new ion sources or similar devices. In contrast, the development of advanced simulation methods, e.g. the statistical diffusion simulation (SDS) algorithm (see section 3.3.1 on page 24) and the rapidly increasing numerical performance of readily available computer hardware enables a model driven approach for the design of new AP ion sources. Ideally, a new ion source concept would be designed, tested, and optimized entirely in a numerical model before the first construction of an actual physical prototype device.

To validate the applicability of a simulation method on a given problem domain the direct comparison of simulations with appropriate experimental results is necessary. In the case of a general purpose AP ion source, the numerical reproduction of the

experimentally determined distribution of ion acceptance (DIA) serves as an ideal benchmark problem for the validation of fluid dynamic calculations (CFD simulations) and the simulation of the ion trajectories in the ion source enclosure. This is due to the fact that the experimentally observed DIA is the combined result of the neutral analyte distribution and the ion motion under the effects of the bulk gas flows and the electric fields in the ion source as the following sections will show.

As outlined above, the ion acceptance distributions are the result of the convoluted dynamics (electrical, fluid dynamical, and chemical) occurring in the ion source chamber. In addition to the sole validation of numerical ion trajectory models, the simulation of the DIA give insight in forces, which form the at first glance often very surprising DIA shape. Therefore, the calculations are also a helpful tool for the thorough characterization of the investigated commercial AP ion source, which subsequently allows to optimize its basic design.

In this chapter, the numerical simulation of the DIAs is presented. The simulation outcomes are analyzed in detail and compared with experimental results. The measurement of DIAs, which is presented in great detail in a preceding dissertation [98] and a journal contribution [99] by Matthias Lorenz, is here briefly summarized.

**Definition of the Distribution of Ion Acceptance (DIA)** In this work, the term “Distribution of Ion Acceptance” (DIA) refers to the ion signal intensity recorded by an ion detector in dependence on the spatial position of the ionization location in the ion source. To record such a spatially resolved distribution, the region in which primary ion generation occurs has to be confined and readily controllable by an automation mechanism. Therefore, direct photoionization with laser radiation, which can be easily focused and controlled by lenses and mirrors, is an ideal tool for the measurement of ion acceptance distributions.

## 6.2 Experimental

The principle of the measurement of ion acceptance distributions is the spatially resolved resonance enhanced multi photon ionization (REMPI) of suitable analytes with laser radiation at atmospheric pressure (atmospheric pressure laser ionization - APLI [100]).

In the following sections, the principles of multiphoton ionization and the experimental setup are briefly described.

### 6.2.1 Photoionization

Atmospheric pressure laser ionization (APLI) is a direct photoionization method for particular analyte substance classes utilizing ultraviolet (UV) laser radiation. Essentially, the principle of direct photoionization of an analyte M is the excitation of an electron above the ionization energy (IE) so that the electron can leave the system

## 6 Simulation of ion acceptance distributions (DIA)

yielding a radical cation ( $M^+$ ) [101]:

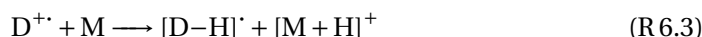


Most of the common non polar organic analyte molecules have ionization energies below 10 eV [102–105], corresponding to a photon wavelength of  $\lambda = 124$  nm, which is in the vacuum ultraviolet (VUV) regime. Most LC solvents, Helium as a GC carrier gas, and bulk components in air ( $N_2$ ,  $H_2O$ ,  $O_2$ ) have ionization energies well above this value [103, 106]. Therefore it is in principle possible to ionize organic analytes in one step by the irradiation with VUV light. In single photon ionization at atmospheric pressure (Atmospheric Pressure Photo Ionization - APPI) typically discharge lamps (e.g.,  $H_2$  discharge [103] or Kr discharge [107] lamps) are used to generate the VUV radiation. Direct single photon ionization is depicted as **a** in figure 6.1. Despite the fact that the matrix components are not ionized by the VUV radiation, with exception of  $N_2$  and He all of them, e.g. the common LC solvent Acetonitrile ( $CH_3CN$ ), strongly absorb light with photon energies around 10 eV. As a consequence, the irradiated VUV light is strongly attenuated which results in poor sensitivities of APPI under typical analytical conditions [105]. In addition, chemical reactions induced by the highly photo-excited and photo-dissociated neutral matrix components potentially lead to chemical transformations of analyte ions [108] which also have a negative impact on the sensitivity of a direct APPI source.

Caused by the relatively low performance of direct APPI, a variation of the ionization principle described above was introduced. In this case, a *dopant* D (e.g., Toluene) which is introduced in relative large concentrations into the ion source [3, 103, 105] is primarily photoionized. If the dopant is chosen appropriately, the dopant charge is transferred to the analyte molecules by chemical reactions, e.g. by direct electron transfer



or protonation of the analyte molecules



respectively. Typical liquid dopant flow rates under LC conditions are in the range of 10% of the liquid LC solvent flow [109]. This method is called *Dopant Assisted* APPI (DA-APPI). In contrast to direct APPI, dopant assisted methods are very similar to chemical ionization (APCI) because the final charge transfer to the analyte is a chemical reaction. Thus DA-APPI has relative low ionization yields with nonpolar analytes, which are relatively insensitive to chemical ionization [105] and which would be therefore the main analytes for direct photoionization [3, 107].

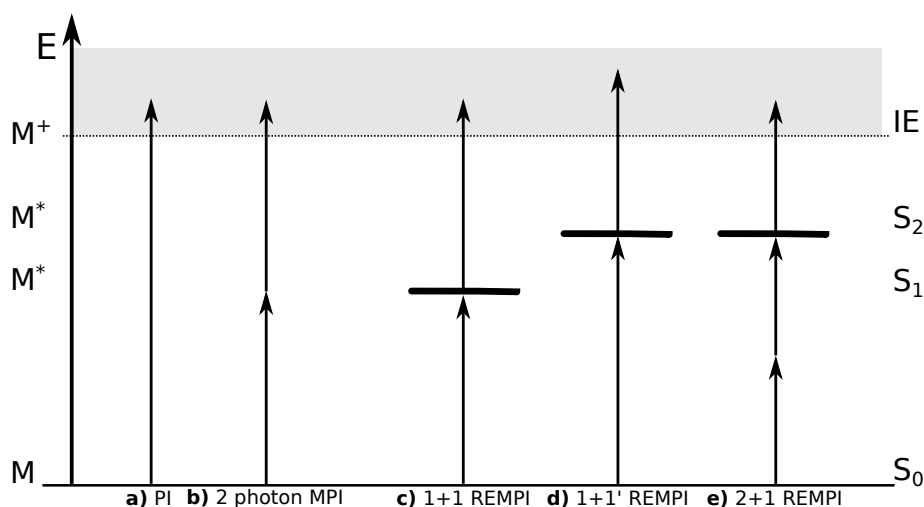


**Figure 6.1:** Schematics of different photoionization modes: **a:** non resonant one photon photoionization (PI), **b:** non resonant two photon photoionization, **c:** one color resonant multiphoton ionization (REMPI), **d:** two color resonant multiphoton ionization (REMPI), **e:** one color resonant ionization with a non resonant first multiphoton excitation (2+1 REMPI), graphic reproduced after [110]

### 6.2.2 Atmospheric Pressure Laser Ionization

When the photon densities of the irradiated light becomes very high, nonlinear photo-excitation processes occur, which allow to overcome the ionization energy of an analyte molecule with the absorption of multiple photons before the molecule relaxes [110]. In the simplest case, two photons with the same wavelength are absorbed without an intermediate resonant level present. In this case, the lifetime of the excited state, a so called *virtual* state, is determined only by the uncertainty-relation and is in the range of  $10^{-15}$  s [98, 110]. This ionization method, called *Multi Photon Ionization - MPI*, is depicted schematically in figure 6.1 **b**.

The stepwise photoionization process can also be achieved via an electronic, so called *resonant*, state of the molecule, which may also be repulsive. Even if this state is repulsive, it has a significantly longer lifetime than virtual states in the range of  $10^{-14}$  to  $10^{-12}$  s [98]. If the state is non-repulsive, its lifetime may exceed to the nanosecond ( $10^{-9}$  s) region [111]. As a consequence, the required photon densities for resonant multiphoton ionization become much smaller than for MPI. Those former are of the order  $10^6$  W/cm<sup>2</sup> and readily achieved with relatively small laser systems with ns pulsewidth [105]. Ionization via resonant states is called *Resonant Enhanced Multiphoton Ionization* (REMPI). Atmospheric pressure laser ionization (APLI) uses two-photon one-color (1+1) REMPI with photon energies around 5 eV ( $\lambda = 248$  nm) for the direct photoionization of selected organic molecules, in particular polycyclic

## 6 Simulation of ion acceptance distributions (DIA)

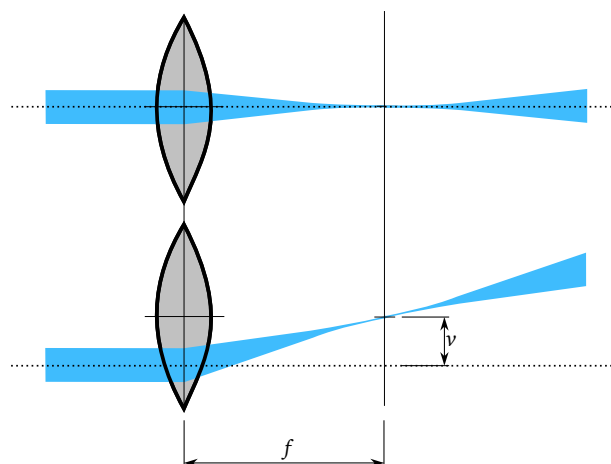


**Figure 6.2:** Basic principle to move the ionization location in the DIA measurements. The ionizing laser beam is sent through a movable lens with a focal length of  $f$ . If the lens is moved while the inbound beam stays fixed, the focal point is displaced in a plane perpendicular to the laser beam axis.

aromatic hydrocarbons (PAHs), at AP [104, 105]. The multiphoton ionization mode used by APLI is depicted in figure 6.1 c. There are other modes for multiphoton ionization. For example, the ionization could be accomplished by two photons with different wavelengths (1+1' REMPI, d in figure 6.1) or by more than one photon via a resonant and a virtual state (2+1 REMPI, e in figure 6.1). Details about multiphoton ionization as ionization technique for mass spectrometry is found e.g. in Weikhard et al. [110]. The dissertation of Matthias Lorenz [98] and the tutorial article from Thorsten Benter [105] give further information about MPI in general and APLI in particular.

In contrast to direct APPI, the laser radiation used in APLI is not absorbed significantly by the matrix components. Thus, the ionizing light penetrates the entire ion source, and the photo-induced neutral radical chemistry is generally suppressed [105]. As a consequence, APLI offers increased sensitivity and fewer chemical interferences than direct APPI [104, 105, 112]. In addition, as suggested above, the laser based ionization technique APLI offers the ability to determine ion acceptance distributions by scanning the ion source with the ionizing laser beam as described in the following sections.

### 6.2.3 Measurement Principle

To determine a DIA in an APLI source, the laser beam has to be controlled and spatially translated which can be achieved in many ways. In the experiments which provide the basis for this thesis, an experimentally relatively simple way was chosen. As figure 6.2 shows, the laser beam was focused with a convergent quartz lens. When this lens is moved in a plane perpendicular to the incident light, the beam focus moves

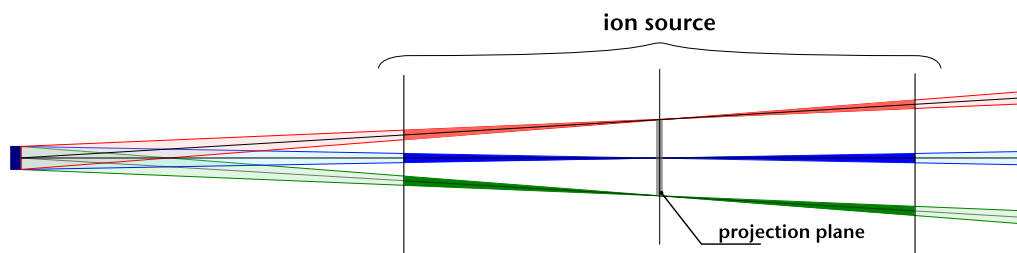


**Figure 6.3:** Projection of volume elements: The entire ion signal in the inclined double cone shaped ionization volume is projected onto the central plane. The drawing is true to scale and shows the maximum inclination of the ionizing laser beam in the vertical ( $y$  in fig. 6.6) axis.

accordingly in a plane in the distance of the focal length  $f$  of the lens. As shown in figure 6.3 this setup creates distorted double cone shaped irradiation regions which are connected at their tip by the beam focus if the laser beam is assumed to follow strictly geometric optics. In the data processing, the ion signal from the irradiated area (ionization volume) is assigned to one spatial point, the beam focus position on the focal plane of the setup. Thus, the data represent a *projection* of the signal from the ionization volumes onto the central plane. If the ionization volumes overlap in areas with significant contribution to the ion signal, this projection becomes difficult to interpret because this ion signal is assigned to multiple points on the projection plane. Figure 6.4 shows a scaled depiction of the area along the beam path where no overlapping of the ionization volumes occurs [98]. Even with 0.5 mm spatial resolution this undisturbed area is larger than the entire region from where ion signal originate as will be shown by experimental and numerical results. Therefore it is possible to accurately measure DIA with this principle of beam control on a commercial API-MS, as described in the following sections.

#### 6.2.4 AP Ion source and MS setup

All presented DIA measurements were performed on a commercial orthogonal API-time of flight (TOF) mass spectrometer [1, 31] (micrOTOF, Bruker Daltonics, Bremen, Germany). The system is a benchtop instrument, originally designed for LC-MS hyphenation using primarily ESI and APCI. Thus, it has a modular ion source concept: Different ion sources which provide several ionization methods (e.g. ESI, APCI, APPI, or APLI) can be readily attached to a standardized MS interface which is common to the whole Bruker API-MS instrument series.

The transfer of ions from the AP source to the high vacuum of the mass analyzer is performed by a transfer system which consists of differential pumping stages and electrical ion focusing elements, which is depicted schematically in figure 6.5. The first pressure reduction occurs over an *inlet capillary*, a glass capillary of 0.5 mm inner diameter and 180 mm length. The chamber connected to the downstream part of this

## 6 Simulation of ion acceptance distributions (DIA)

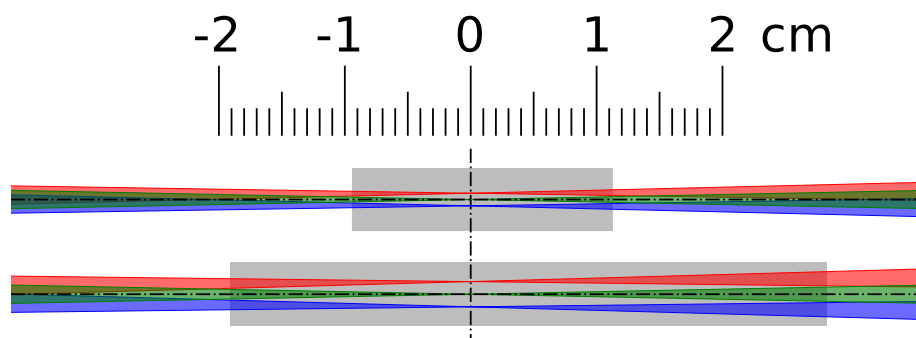


**Figure 6.4:** Laser beam shape, approximated with geometrical optics, in vicinity of the central projection plane in the ion source, for 1 mm (above) and 0.5 mm (below) distance between the spatial points of the DIA measurement. The beam has an initial width of 5 mm, the movable lens has a focal length of  $f = 120$  mm. The shaded areas indicate the area in which the ionization volume elements do not overlap, which is larger than the typical features in the experimentally recorded DIAs. The figure was reproduced and modified from [98].

capillary is pumped by the rough pump of the MS vacuum system while the gas flow through the inlet capillary is fluid dynamically limited (choked flow) [108]. Therefore, the capillary essentially acts as a flow restrictor, resulting in a fixed reduced pressure, which is in this case approximately 4 mbar.

After this first stage, the pressure is further reduced by two subsequent differential pumping stages, which are separated by skimmer orifices. Here, the ion-beam is collimated by two RF only multipoles, in which the radial velocity components of the ions are removed by collisional cooling. Then the beam is focused by electrostatic lenses into the pusher of the orthogonal TOF mass analyzer which is maintained at a background pressure of approximately  $10^{-7}$  mbar. The mass analyzer uses a “V” configuration with a single electrostatic ion mirror (reflectron) [4, 113]. The analyzer has a mass resolution of  $R = 20\,000$  with an usable mass range of approximately 60 to 20 000 Da. It is noted that the lower end of the mass range is not limited by the mass analyzer but primarily by the RF generators of the multipoles in the transfer stage. The ion detection is performed with a microchannel plate (MCP) assembly, as common in TOF instruments. The MS instrument generates single TOF spectra with a frequency (push-rate) of 20 kHz. The individual spectra are summarized by the digital transient recorder (“digitizer”) yielding a mass spectrum which is transferred to the data acquisition computer of the MS. Typical transfer rates are in the range of 0.5 to 4 Hz.

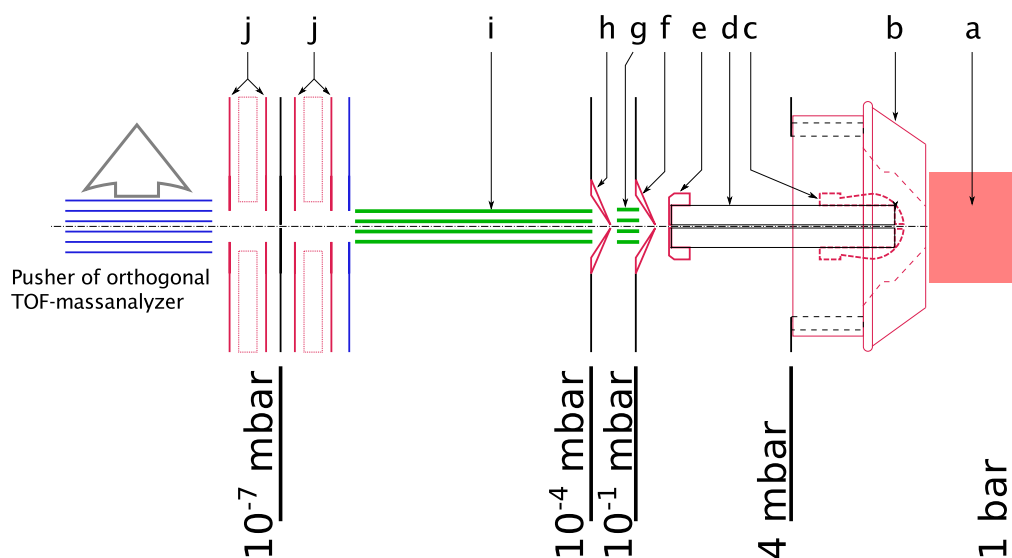


**Figure 6.5:** Schematic overview of the transfer and pressure reduction stage of the MS used for the DIA measurements (Bruker microTOF). Graphic reproduced after [98], not to scale.

**a:** ionization volume, **b:** spray shield, **c:** inlet capillary cap, **d:** inlet capillary, **e:** capillary cap (low pressure side), **f:** first skimmer, **g:** focusing hexapole, **h:** second skimmer, **i:** focusing octapole, **j:** electrostatic lenses

**AP Ion Source** For the DIA measurements presented here, the system was equipped with a multi purpose ion source (MPIS) [98, 114] equipped with the required UV transparent windows for the ionizing laser radiation. The design of the MPIS is based on common commercial AP ion sources for mass spectrometry in combination with liquid chromatography preseparation stages [3, 95]. As suggested by its name, the ion source can be reconfigured for different ionization techniques and hyphenations with preseparation stages. For example it is also possible to attach a gas chromatographic (GC) separation stage to the MPIS via a heated transfer line [114]. Alternative ionization methods which can be readily performed in the MPIS in addition to APLI are APCI and ESI.

The MPIS is basically an aluminium chamber which is attached to the front end of the MS interface. Since the ion source and the MS interface essentially form a unit, the whole assembly is discussed as “ion source” in the following. Figure 6.6 shows schematically the ion source in its LC configuration along with the laser beam optics.

In all presented DIA experiments, the MPIS was used in the LC configuration. In this case, the analyte is introduced with a liquid solution into the source. This solution is pneumatically nebulized and vaporized in a heated nebulizer (**f** in fig. 6.6). To achieve the nebulization, the liquid analyte solution (**2** in figure 6.6) is pumped by a HPLC pump (*Hitachi Ltd, Tokio, Japan*) through a small needle with approximately 0.3 mm

## 6 Simulation of ion acceptance distributions (DIA)

inner diameter (**f** in fig. 6.6) which is aligned in a nozzle (**h** in fig. 6.6) through which a flow of *nebulizer gas* runs (nitrogen gas, **1** in figure 6.6). The nebulizer block is heated to a typical temperature of about 350 °C to desolvate the analyte by vaporizing the solvent droplets resulting from the nebulization. The nebulizer gas pressure can be adjusted by the MS control software, typically it has values about 3 bar. The resulting nebulizer gas volume flow into the ion source depends on the detailed positioning of the nebulizer needle in the nebulizer nozzle. Typical values are in the range of 3 l min<sup>-1</sup> at 3 bar nebulizer gas pressure.

A second gas flow into the ion source is the so called *dry-gas* (**3** in fig. 6.6) which is a heated nitrogen gas flow introduced between MS inlet capillary (**c** in fig. 6.6) and spray-shield (**e** in fig. 6.6). This gas flow is controlled by the MS with an internal flow controller. The dry-gas volume flow and the dry-gas heater temperature can be adjusted, typical values are 3.0 l min<sup>-1</sup> and 200 °C which result in a measured gas temperature of about 70 °C at the spray-shield entrance.

Analyte ions which are generated in the ion source have to reach the inlet capillary to be sampled by the MS. Since the dry-gas flow is oriented towards the intended motion direction of the ions, the ions have to be moved through the dry-gas flow by electrical forces. Therefore, the inlet capillary cap (**d** in fig. 6.6) and the spray-shield can be set to adjustable attractive electrical potentials while the remaining ion source geometry is fixed on ground potential. To be electrically attractive for cations (positive ion mode), the capillary cap is set to higher potentials than the spray-shield. In combination, both elements form an electrostatic lens, which focuses the ions on the inlet capillary tip, from where they are transported into the MS transfer stage by the gas inflow into the capillary. Typical capillary and spray-shield potentials are in lower kV range (1 to 4 kV), but the actual potentials depend strongly on the used ionization method and the analytical conditions.

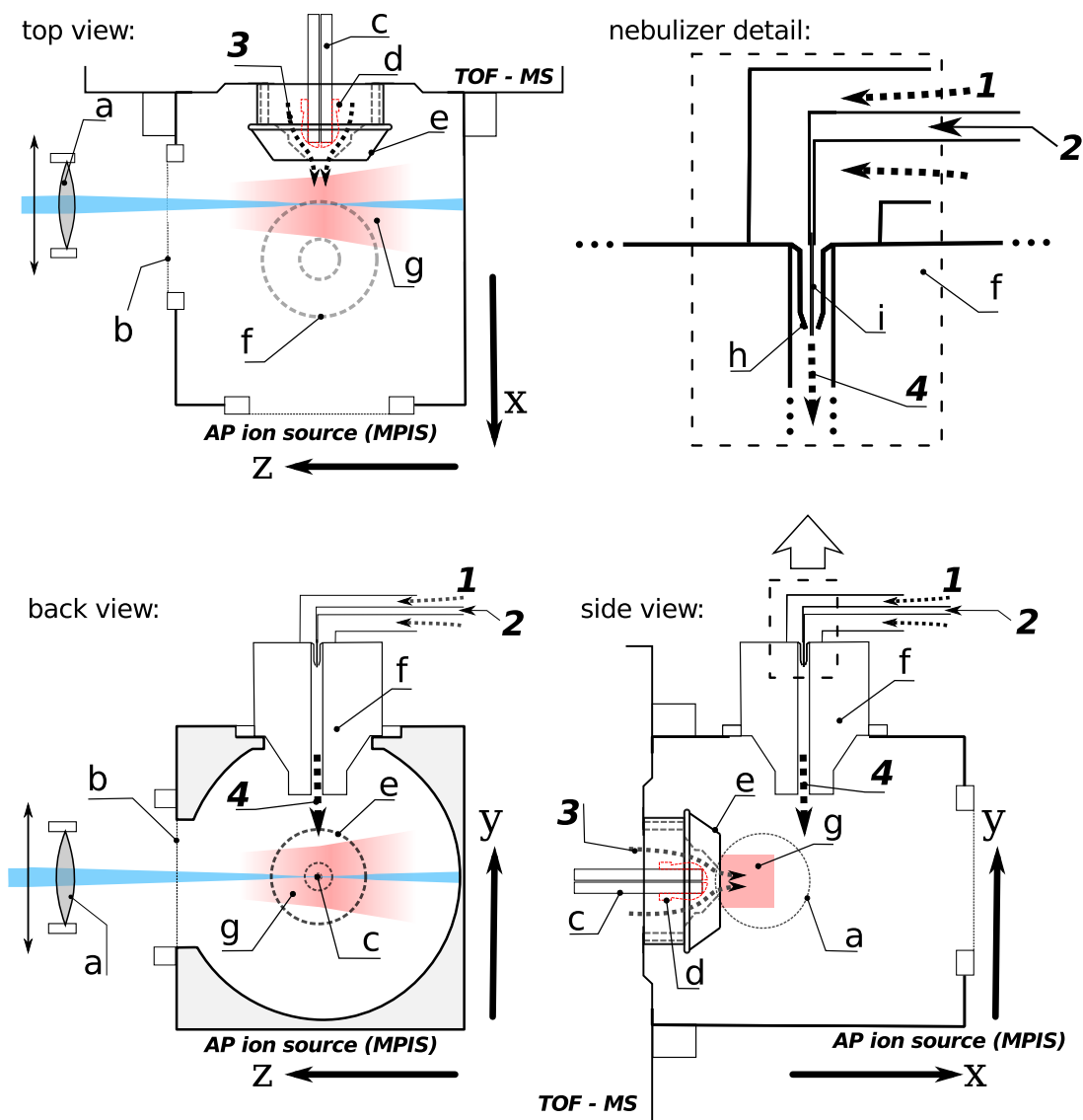


**Figure 6.6:** Schematic overview of the experimental setup for DIA measurements.  
**a:** movable lens, **b:** UV transparent window, **c:** MS inlet capillary, **d:** capillary cap, **e:** spray shield, **f:** nebulizer block (heated), **g:** ionization zone, **h:** nebulizer nozzle, **i:** liquid analyte capillary  
**1:** nebulizer gas, **2:** liquid analyte solution, **3:** dry gas, **4:** nebulizer gas (with analyte vapor)

## 6.2.5 Experimental determination of DIAs

To measure DIA, the MS was equipped with a custom experimental setup which is described in this section.

### 6.2.5.1 Optics / Laser System

For all presented DIA measurements, a KrF\* excimer laser (*Atlex 300 SI, ATL Lasertechnik GmbH, Wermelskirchen, Deutschland*) with a wavelength of  $\lambda = 248$  nm was used. Typically, the laser was operated with a pulse frequency of 100 Hz and 0.9 mJ pulse energy. The unfocused laser beam had a beam profile of  $4 \times 6$  mm and a specified pulse length of 6 ns.

The laser beam was directed by a mirror and was sent through a convergent quartz lens with a focal length of  $f = 120$  mm, which was mounted on a position table movable in the plane perpendicular to the laser beam axis. The position of the lens assembly on the beam axis was set so that the focal point of the focused laser beam was located in  $z$  direction on the center  $xy$ -plane of the ion source, in close vicinity to the inlet capillary. See figure 6.6 for the position of the beam focus and the definition of the spatial coordinate system.

The custom built [98, 99] lens stage was operated with step motors (*Fuji Co., Tokio, Japan*) which could be controlled by a personal computer. The custom lens control software allowed to execute a scan on a predefined spatial grid. The positions of the individual grid points and the integration times were defined as a simple list in a so called *scan file*. By changing the scan files, different spatial resolutions, integration times, and scan areas were achieved. If not noted otherwise, the presented DIA measurements were recorded with a rectangular scan grid of  $27 \times 33$  spatial points, with a distance of 0.5 mm and an integration time of 2 s per point.

The alignment of the optical setup was controlled with a test target holder which could be placed in the center  $xy$ -plane of the ion source instead of the nebulizer assembly. A piece of paper was used as test target for the focused laser beam which burned visible marks into it at the spatial grid positions. By inspecting the pattern of burn marks on the paper target, the correct optical alignment was verified.

### 6.2.5.2 MS parameter automatization

To perform fully automated series of DIA measurements, variations of the ion source parameters were automatized as well. A segmentation function in the MS control software (*micrOTOFcontrol, Bruker Daltonics, Bremen, Germany*) was used, which was originally intended to allow variations of the MS and ion source configurations in a LC run. The user is able to define arbitrary chronological segments for which individual parameter configurations are defined. In the case of the DIA measurements, one segment represented a single spatial scan with its own ion source configuration. To avoid the inconvenient setup of the segments in the graphical user interface (GUI) of *micrOTOFcontrol*, a program was developed which allowed the generation of segment

**Table 6.1:** Operational parameters of the AP ion source (MPIS) in the DIA measurements

Voltage on capillary cap	<b>d</b> in fig. 6.6	0–5000 V
Voltage on spray shield	<b>e</b> in fig. 6.6	0–80 V
Dry-gas flow	<b>3</b> in fig. 6.6	0.5–5.0 l min <sup>-1</sup>
Dry-gas temperature	<b>3</b> in fig. 6.6	20–200 °C
Nebulizer-gas pressure	<b>1</b> in fig. 6.6	0.0–5.0 bar
Nebulizer temperature	<b>f</b> in fig. 6.6	20–400 °C

definition files, called “methods” in the microTOFcontrol nomenclature. Method files are relatively simple human readable files written in Extensible Markup Language (XML) which was easily reverse engineered and reproduced by a custom program.

Synchronization of the start of the spatial scans with the begin of the segments, by monitoring the control communication between MS instrument and MS control computer which was established via a serial (RS232) connection. An unused data channel for the voltage on the obsolete corona needle, was utilized to send start and reset signals from microTOFcontrol to the lens control system.

The spray-shield voltage was controlled in a similar way. It was provided by an external, programmable laboratory power supply (*Voltcraft PSP 1803, Conrad Electronic SE, Hirschau, Deutschland*). A program on the MS control computer also monitored the serial control channel between MS and control computer, interpreted the original control commands sent to the MS, and transformed them into according control commands for the external power supply.

Table 6.1 presents the variation ranges of the individual ion source parameters.

### 6.2.5.3 Data acquisition and data processing

Data acquisition was performed with microTOFcontrol. Mass spectra were recorded with a sample frequency of 2 Hz. From the recorded mass spectra the total ion current (TIC) and the mass trace of the analyte was extracted and saved along with the meta data of the measurement (MS method file).

The ion signal intensity at a spatial position is the averaged recorded ion signal while the ionizing laser beam was at this location. A stack of custom software constructed the two dimensional spatially resolved DIA from the extracted mass traces and the corresponding scan files. The scan files implicitly contain the information required to relate the spatial position of the ionizing laser beam and the time passed since the start of the spatial scan which is synchronized with the segment begin. The resulting data were additionally spatially averaged (convolution with a two dimensional gauss kernel which had a diameter of 3 spatial data points) to smooth the result. The final result of the process was exported as color encoded two dimensional graphic (contour plot).

## 6.3 Numerical Model and Simulation

It has been discussed in the preceding chapter that knowledge about the bulk gas flow in an AP device as the MPIS is essential for an accurate ion trajectory model. Thus, the numerical simulation of DIA, which is essentially a specialized ion migration calculation, also requires fluid-dynamic data of the bulk gas flow in the region of interest. To actually simulate an ion acceptance distribution in a monte carlo simulation [35], the migration of a large number of ions in the MPIS is simulated with SIMION/SDS. A detailed analysis of the termination positions of the simulated ions allows to calculate the ion distribution as presented in this section.

### 6.3.1 CFD model of the MPIS

As mentioned, the bulk gas flow in the MPIS is determined by two gas inflows, the dry-gas and the nebulizer gas stream, and two gas sinks, the inlet capillary to the MS and a drain outlet at the MS interface plate. The resulting flow structure in the ion source is relatively complex, since the heated and orthogonally oriented dry-gas and nebulizer flows interact directly in the ionization region of the ion source.

For an accurate CFD model, a quite complex numerical calculation is required: It has to be threedimensional, since there is no symmetry which could be exploited to reduce the spatial dimensionality of the numerical calculations. Furthermore, it has to incorporate a heat transport model due to the non-isothermic conditions induced by the two heated gas flows into the ion source. Finally, a convection/diffusion model for the determination of the spatial distribution of the neutral analyte has to be part of the calculations, since the analyte distribution strongly affects the resulting DIA. The model emerging from those demands, in combination with the requirement to validate such numerical calculations experimentally, overexerted the available capabilities of the physical chemistry group in terms of experimental hardware, computing power, software, and expertise. Thus, the bulk gas flow and the neutral analyte concentration distribution in the MPIS were modeled in cooperation with the Institute of Jet Propulsion and Turbomachinery (Institut für Strahltriebwerke und Turboarbeitsmaschinen - IST) at RWTH Aachen University. This work was described in detail in [96] and is briefly presented here.

#### 6.3.1.1 CFX Model

The numerical simulation of the time averaged static bulk gas flow in the MPIS was performed with the commercial CFD package CFX (*CFX v.12.1, Ansys, Canonsburg, PA, USA*), which is a finite volume solver (see section 3.2.2 on page 20). It solved the Navier-Stokes equation system (see section 2.2.4 on page 9) in a conservative form [48] in which momentum-, mass-, and heat-transfer is considered [96].

The simulation mesh was generated with a commercial meshing system (*ICEM CFD 11.0, Ansys, Canonsburg, Pennsylvania, USA*). The resulting mesh had about  $1 \times 10^7$

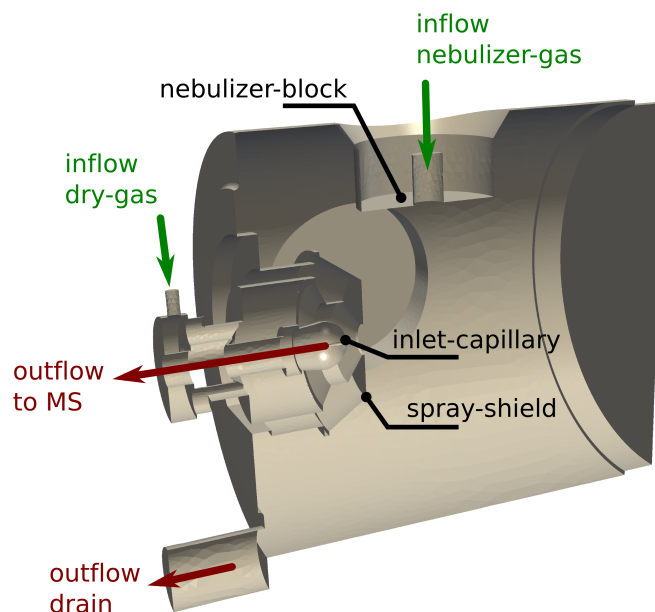


**Figure 6.7:** Cutaway view of the simulation domain and gas flows in the CFD model of the MPIS

tetrahedral and  $6 \times 10^6$  prism elements, resulting in a detailed spatial resolution of the bulk gas flow. The boundary layers in close vicinity to critical walls were resolved with multiple layers of prism elements, which ensure a good resolution of the steep flow gradients in proximity to the walls and allows a correct turbulence modeling there [48, 96]. Due to the high numerical effort necessary for prism elements, only boundary layers on walls which have a significant influence on the flow field were modeled in this way. Figure 6.7 shows the simulation domain with the gas in- and outflows.

Air as simulated fluid was assumed to behave ideally, thus the ideal gas law and the properties of air determined the fluid state. To simulate turbulences in the bulk gas flow with reasonable numerical effort, the Shear-Stress-Transport (SST) model [115] was used as a dedicated turbulence model. To model the relative concentration distribution of the neutral analyte in the ion source, an additional transport equation (see equation 2.17 on page 8) was introduced, which was solved along with the Navier-Stokes equation system. The molecular diffusion coefficient of the neutral analyte was assumed to be  $D = 7 \times 10^{-6} \text{ m}^2 \text{ s}^{-1}$ . The solution of the Navier-Stokes equations provided the bulk gas density and velocity field as parameters for this neutral analyte transport simulation.

For a numerical solution of the Navier-Stokes equation system, boundary conditions have to be defined on the borders of the simulation domain. In the CFX simulation, all walls of the ion source geometry were assumed to be isothermal with a static

## 6 Simulation of ion acceptance distributions (DIA)

temperature of 348.15 K. The nebulizer inflow was assumed to be nearly laminar with a low fractional turbulence level (1%), due to its comparably low mean flow velocity. The nebulizer mass flow was  $0.0237 \text{ g s}^{-1}$  which corresponds to a volume flow of  $1.7 \text{ l min}^{-1}$  at the elevated nebulizer temperature of  $183 \text{ }^\circ\text{C}$ . The dry gas inflow, which is located in relatively large distance to the spray shield outlet (see figure 6.7 on the previous page), was assumed with an increased turbulence level (5%). The temperature of the nebulizer gas inflow was also  $183 \text{ }^\circ\text{C}$ , the dry gas temperature was  $131 \text{ }^\circ\text{C}$ . As part of the cooperation with the IST, two fluid-dynamic configurations (*operation points*) of the ion source were simulated. The selection of those operation points, which differed only in the dry gas mass flow, was based on experimental observations, which are presented in the results section. At the low dry gas operation point, the dry gas mass inflow was  $3.337 \text{ mg s}^{-1}$  which corresponds to a volume inflow of  $2.0 \text{ l min}^{-1}$ . In the high dry gas case, the mass inflow was  $5.269 \text{ mg s}^{-1}$  which is a volume inflow of  $3.8 \text{ l min}^{-1}$  at the increased dry-gas temperature.

As outflow boundary conditions, static pressures were assumed at the corresponding boundaries. At the drain outlet, the simulated back pressure was 1 bar, since this outlet is essentially open to the atmosphere in the experiments. The conditions in the MS inlet capillary are more complex, since the gas flow becomes turbulent and highly compressible due to the acceleration and expansion along this first pressure reduction stage into the MS. At 1 bar gas pressure in front of the inlet capillary and approximately 4 mbar background pressure in first pumping stage, the flow velocity approaches the speed of sound at the capillary exit [98, 116]. In this *choked flow* condition, which is reached when the pressure difference along the capillary is higher than a critical ratio of approximately  $p_{\text{out}} = 0.5 p_{\text{in}}$  [117], the gas flow through the capillary becomes independent from the background pressure.

The compressible flow through the capillary can be numerically solved for a given static wall temperature [118]. This treatment yields a set of parameterized functions which describe the velocity- and pressure profiles along the capillary in dependence of the background pressures at the inlet and outlet port. Due to the known pressure profile, it is not required to simulate the entire capillary flow including the expansion into the first reduced pressure stage. Instead, only a section of the capillary was part of the simulation domain and a reduced pressure given by the known profile was assumed at the end of this section. In the simulations used as input parameters for the DIA simulation this pressure was 830 mbar.

Since the neutral analyte was introduced into the ion source through the nebulizer, in the numerical model the relative neutral analyte concentration in the nebulizer gas was assumed to be one, while the dry gas was free of neutral analyte.

### 6.3.1.2 Model verification with particle image velocimetry

A numerical simulation of the bulk gas flow is only an approximation of the real physical processes in the ion source. Under unfavorable conditions, the results may entirely differ from the experimental ones. Thus, an experimental verification of the numerical

solution is necessary to proof its validity, in particular if the simulated data serve as input for further numerical calculations. In the case of the CFX simulation of the bulk gas flow in the MPIS, this verification was conducted with a method called particle image velocimetry (PIV) [96, 119, 120]. The principle of PIV is to introduce (*seed*) small particles, in this case small oil droplets, into the gas flow under investigation. The particles are virtually weightless and follow the gas flow without any significant effect from particle inertia. Therefore, their movement corresponds directly to the velocity field of the gas flow. Particles are traced within the volume of interest by irradiation with a sheet of laser light. The particles scatter the light, which is detected with a suitable camera oriented perpendicular to the laser sheet. If the laser is pulsed two times with a known time delay between the pulses, two scatter images can be recorded, which show the positions of the particles before and after the time delay. With appropriate auto- and crosscorrelation algorithms it is possible to extract the flow velocity field from the particle motion. Details about PIV are found in dedicated textbooks about this topic, e.g. [121] or [122].

Due to experimental restrictions, the verification of the CFX model of the MPIS was not performed for the operation points described above. Instead, the nebulizer- and dry-gas mass flows were increased, and the gas flow was not heated and therefore at room temperature (20 °C) in the verification experiments. Details about the verification operation points are found in [96]. The results of flow simulations considering the verification operation point conditions were compared to the experimental PIV results. This comparison showed that the flow simulation accurately describes the gas flow at the verification operation points and reproduces all significant features of the bulk gas flow within the experimental uncertainty [96].

The operation points of the MPIS at which the DIA measurements were performed do not differ significantly from the verification operation points. Therefore, it was concluded that the CFX simulation is valid for the conditions of the DIA measurements. The results of the CFX calculation were thus directly used as input parameters for the ion trajectory and DIA simulations.

#### 6.3.2 CFD result data transformation

As described in section 3.2.3 SIMION as finite difference solver generally finds its solutions on a regular rectangular calculation grid, while the CFX solution has an irregular discretization mesh. The SDS extension for SIMION is able to consider externally calculated flow solutions as input parameters as list of flow velocities at the nodes of the SIMION calculation grid. In contrast, the CFD data are given as values of the fluid-dynamic parameters (e.g. velocity, temperature, pressure) at the spatial positions of the calculation mesh nodes which is essentially an irregular point cloud. Thus, the result from the CFD simulation has to be transformed to be applicable as input data set for the ion trajectory simulation.

This transformation, the interpolation of field data defined by an irregular point cloud to a regular grid, is similar to the generation of a digital terrain model from spotty

## 6 Simulation of ion acceptance distributions (DIA)

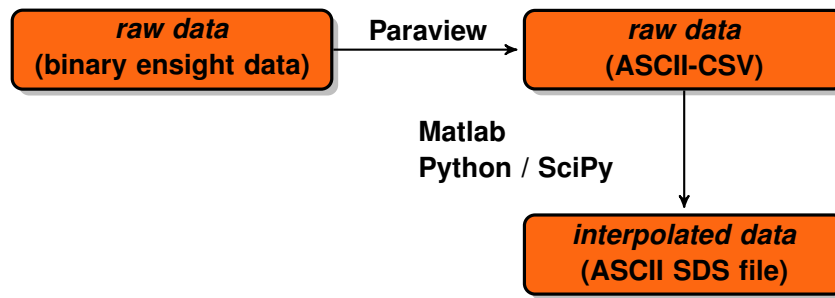


**Figure 6.8:** Toolchain for the interpolation of CFX-CFD data

height measurements. In this case, the height is the value which is interpolated, instead of the fluid dynamic parameters. This interpolation can be numerically performed by a Delaunay triangulation, a method which finds a triangular mesh with maximal inner triangle angles, connecting the given irregular point cloud [90, chapter 9]. The resulting mesh is used for a linear interpolation of the field value at the regular grid node positions.

Several methods are available to find the Delaunay triangulation of a point set. One efficient algorithm, which reduces the problem to the finding of convex hulls, is the Quickhull algorithm [123], which is freely available in an open source implementation<sup>1</sup>.

The commercial numerical computing language Matlab [86] provided with the `griddata` and `griddata3` functions a convenient, but in the meantime deprecated, implementation of the required interpolation functionality based on the Quickhull algorithm. This was initially used in a custom script for the transformation of the irregular point data, given as delimited text files (ASCII CSV files), to parameter input files for the SDS algorithm. Since the Matlab package became unavailable during the preparation of this thesis, the interpolation script was reimplemented in Python [88] utilizing the `scipy.interpolate.griddata` method of the SciPy [91] scientific computing library, which provides essentially the same functionality as the mentioned Matlab functions.

The CFX raw data were exported as binary Ensight case files [124], from which the relevant data fields had to be exported into ASCII files before the interpolation to avoid the implementation of a binary reader for the raw files. This task was performed with the open source Paraview [125] scientific visualization tool, which is based on the open source visualization library Visualization Toolkit (VTK) [126, 127].

Figure 6.8 illustrates the toolchain for the transformation of the CFD data.

---

<sup>1</sup><http://www.qhull.org/>

### 6.3.3 Ion migration simulation

Simulated DIA are obtained by replicating, the processes occurring in an experimental DIA measurement. In particle based simulations, as for example SIMION/SDS, ensemble phenomena as a DIA are typically simulated by an analysis of a statistically significant sample of simulated particles, because it is numerically not feasible to simulate the real number of physical particles in an actual experiment. In the following, the principle and some implementation details of the DIA simulation are discussed.

#### 6.3.3.1 Simulation principle

In a DIA measurement, analyte ions are generated in a controlled zone, which is spatially and temporally well defined by the ionizing laser pulse. The generated *ion package* migrates through the ion source, driven by the viscous drag from the bulk gas flow, the present electric fields, and by diffusion. A fraction of the ion package ultimately reaches a zone in close vicinity to the MS capillary inlet, where the fluid dynamic force of the inflow in the capillary overcomes the present electric fields. This zone is clearly discernible as zone of high gas velocity at the inlet capillary tip in the plots of the bulk gas flow (cf. figure 6.12). The ions which have reached this region are transported through the inlet capillary in the first pressure reduction stage of the MS along with the bulk gas flow. Only this fraction of the ion package, reduced by the additional ion losses in the focusing elements of the MS, are sampled by the mass analyzer and contribute to the DIA.

To mimic this situation in a simulation, the experimental processes are essentially reproduced: Initially, a rectangular spatial grid is defined in the simulation domain, similarly to the grid of laser positions in the DIA measurement. Then packages of ions are started from a defined zone according to the grid node positions. Then, the trajectories of those ions are simulated utilizing the SDS algorithm as model for the ion-bulk gas interactions. In the simulation, the termination (“ion splat”) positions of the ions are recorded into individual simulation result files. After this process is performed for every node position of the DIA simulation grid, the DIA is calculated by counting the ions terminating in a predefined *target zone* in close vicinity to the MS capillary inlet. The resulting numerical DIA is the number of those “successfully” terminated ions in dependence of the spatial position of the ion start zone.

As described in the experimental section above, the DIA measurements are merely able to determine two dimensional DIA projections due to the missing spatial resolution along the laser beam path. Naturally, such a restriction does not exist in a simulation. Fully resolved three dimensional DIA were calculated, using a grid spanning in all three spatial directions. The ion start zone was a space filled sphere with a radius of 0.4 mm around the grid node. The two dimensional projection of the DIA, which is required to directly compare the numerical data with experimental results, was calculated by summing up the signal along the laser beam path ( $z$  axis in fig. 6.6 on page 73).

## 6 Simulation of ion acceptance distributions (DIA)

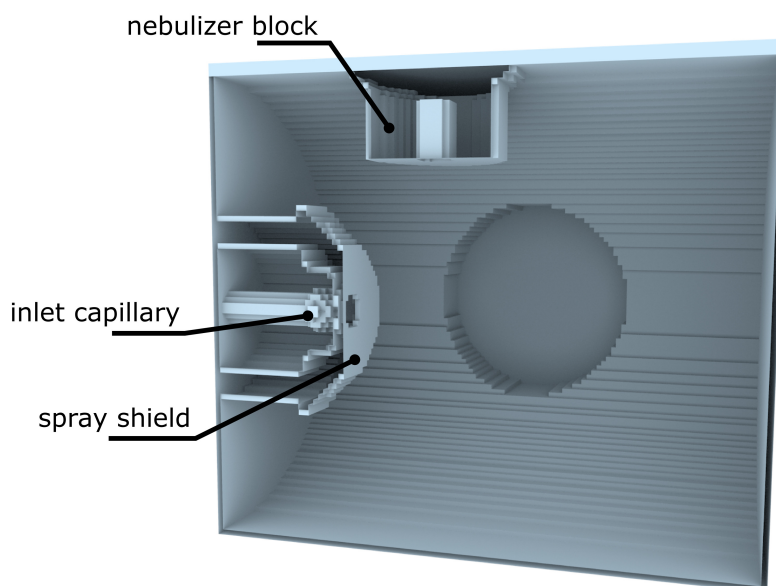


**Figure 6.9:** Cutaway view of the potential array of the SIMION model of the MPIS. The rendering, generated from the exported SIMION geometry, shows the electrode surfaces of the potential array. The nebulizer block and the spray-shield are filled electrodes in the actual simion model. The spatial resolution of the SIMION potential array, which consists of a regular rectangular grid, is clearly visible in the rendering.

In the experiment, the number of ions generated in a given space element depends on the local neutral analyte concentration. To reflect this in the DIA calculation, the number of simulated ions in the ion packages was scaled with the local neutral concentration given by the CFX simulation. The linearly interpolated neutral analyte concentration at the ion package starting positions (DIA position grid), which are not necessarily congruent to the SIMION calculation mesh node positions, were calculated with the methods which are used by SDS to calculate the local values for the fluid dynamic fields at the ion positions. Typically, the maximum number of ions in an ion package was 5000.

### 6.3.3.2 DIA simulation: Technical aspects

Based on the technical drawings of the MPIS, a simplified model of the ion source was manually created as SIMION geometry (GEM) file. From this geometry file, SIMION potential arrays representing the MPIS were generated. Figure 6.9 shows a representation of the electrode surfaces in the resulting potential array, which contained two fast adjustable electrodes, the capillary cap and the spray-shield. The remaining ion source chamber was on ground potential.

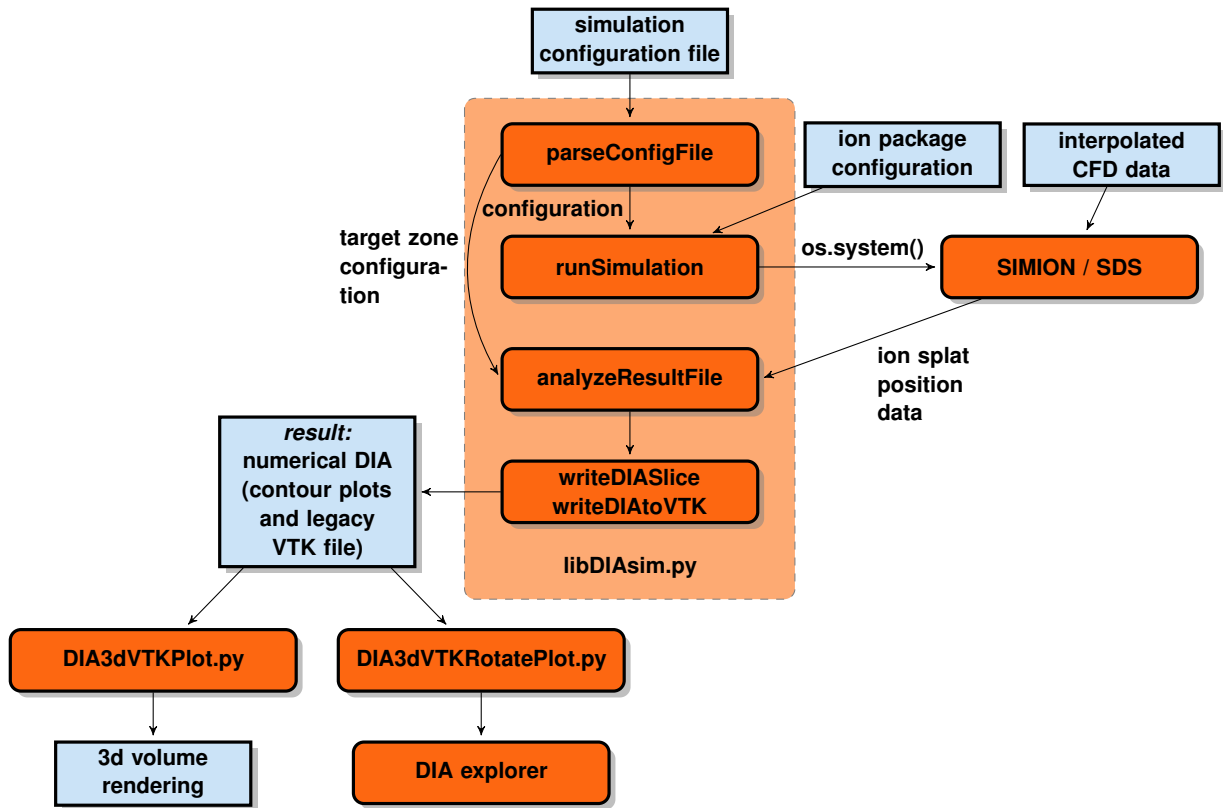


Figure 6.10: Scheme of the DIA simulation process

The simulation of the individual ion packages and the result visualization were fully automatized by Python [88] scripts. All subroutines (methods) implemented for this purpose, were packaged in a small library file (`libDIAsim.py`). Figure 6.10 shows an overview of the DIA simulation process and the interaction of the used programs.

The parameters of the simulation process (e.g., spatial resolution of the DIA simulation grid, target zone configuration, voltages on capillary and spray-shield) were defined in a configuration file. This file was interpreted by a parser (`parseConfigFile` method) which utilizes the Python 2 `ConfigParser` module. The format of the configuration files is relatively simple and complies to the common configuration file format in the Linux / Unix domain: The plain text files are structured in several sections which begin with a section name of the form `[name]`, e.g. `[simulation]` or `[analyzelimits]`. In the individual sections, parameters are defined by key value pairs in the form `key= value`, for example `depletionProbability= 1e-5`.

The parsed configuration information is passed to the DIA simulation subroutine `runSimulation`. This module takes the ion package configuration, creates, in com-

## 6 Simulation of ion acceptance distributions (DIA)

bination with the actual spatial position in the DIA simulation grid, a valid ion start configuration and invokes the SIMION executable, which performs the trajectory simulation of the current ion package. The ion package configuration, which is essentially a SIMION ion configuration (“fly2”) file, contains the spatial shape of the ion package. Placeholders are substituted with the actual parameters (number of ions, spatial coordinates) of the current ion package.

SIMION records the termination positions of the simulated particles of the ion package in a simulation result file which is read by the `analyzeResultFile` subroutine. In combination with the target zone configuration, this module calculates the number of “successful” ions terminating in the target zone, which is the simulated signal intensity from the start position of the ion package.

The spatially resolved signal intensities are recorded into a three dimensional array. The planes in  $x - y$  direction of these data are graphically exported as two dimensional contour plots by the `writeDIASlice` subroutine, which allows to examine the three dimensional simulated DIA along the laser beam path. Finally the data are summed along the  $z$  axis, and the resulting projection of the DIA is exported also as contour plot by `writeDIASlice`. Alternatively, the three dimensional simulated DIA data may be exported to a legacy VTK file [128], an ASCII file format which allows to pass the fully resolved three dimensional data to subsequent visualization modules, which are discussed in detail in the next section.

In the SIMION ion trajectory simulation, a modified version of the SDS implementation bundled with SIMION 8.1 [129] was used. The SDS code was modified to allow the external control of the capillary and spray-shield potentials via variables (adjustables in SIMION nomenclature) in the SIMION user program interface.

**Ion depletion simulation** At atmospheric pressure, ion depletion processes are likely when the analyte ions have a noticeable chemical reactivity. To model the net effect of those processes, a simple ion depletion model was integrated into the SDS user program: In every time step of the particle integration, a predefined depletion probability  $p_d$  is compared to a uniformly distributed random number  $r_d$  in the interval  $[0, 1]$ . If the random value is smaller than  $p_d$  ( $r_d \leq p_d$ ), the ion is considered as “depleted” and is thus removed from the simulation. Essentially, this is a Monte Carlo approach [35] for the simulation of an averaged first order depletion reaction of the ions. It assumes isotropically distributed concentrations of the reaction partners of the ions. In this model, the reaction probability reflects the net effect of all possible depletion reactions, it is thus dependent on various parameters, e.g., temperature and reactant concentrations. Therefore, the depletion probability is only roughly estimated without detailed knowledge about the depletion reactions acting on the ion ensemble. Nevertheless, the simple simulation of a first order ion depletion reaction allows to investigate the principal effect of ion depletion processes by observing the effect of the reaction probability on the simulated DIA.

## 6.4 DIA Visualization

As already mentioned, a numerically calculated DIA is a sampled three dimensional scalar field. It consists of a set of samples  $(x, y, z, v)$  with the spatial coordinates  $x, y, z$  and a dependent scalar value  $v$ , which is the simulated ion intensity in the case of the DIA. The spatially spreaded samples are often called “voxels” in this regard, which is a shortform for “volume element”, analogous to the “pixels” in the two dimensional case which stems from “picture element”. In the DIA simulation results presented here, the voxels are arranged in a regular grid which is relatively common, but of course not necessary, for volumetric scalar data.

The visualization of such data sets is not trivial. Generally, the three dimensional data has to be represented on a two dimensional picture plane, since technical equipment capable of true three dimensional depiction is commonly not available to date. One of the most obvious methods to visualize volumetric data is to cut trough it with a two dimensional plane. The scalar values on this “slice” are visualized with the common methods for the illustration of two dimensional scalar data, e.g. contour plots or color encoded density plots. If the slice is not parallel to one of the axes of the voxel grid, the scalar values on the plane can be determined by interpolation from the volumetric data, which allows arbitrarily oriented slices. By moving the cut plane trough the data set or by defining multiple cut planes, it is possible to inspect the three dimensional structure of the volumetric data.

Another common method to visualize three dimensional scalar fields are surfaces which connect points with equal scalar values, so called *isosurfaces*, which are the equivalent to contour lines (equipotential lines) in two dimensional plots. Since isosurfaces often form convex structures which cannot be inspected well from viewpoints outside the scalar field, often sections are cut out to reveal the inside of the dataset. Usually, the isosurface is colored according to its scalar value but it can be beneficial to use the surfaces for more complex visualizations of other field data. For example, it would be possible to draw the contourlines of another scalar field on the isosurfaces.

A common additional method to depict complex volumetric data sets, which are typical results of medical imaging techniques as for example computer tomography (CT) or magnetic resonance tomography (MRT), is *volume rendering* [130, 131]. Basically, this technique renders a two dimensional projection of the volumetric data set in which it appears to be formed out of partly transparent colored materials. The opacity and color of the individual voxels are determined from the scalar values of the voxels of the rendered data by custom defined transfer functions. A common method for volume rendering is *ray casting* [132], which is a technique to numerically solve the *volume rendering integral* which yields the optical density along a line of sight through the voxel set [131]. To achieve this, rays of sight are shot into the volume for the individual pixels of the final image. The voxels hit by the sight rays are sampled and their contributions to the optical density are summed up to determine the final color information of the pixels in the result image. By the appropriate selection of color and opacity density transfer functions, volume rendering allows an intuitive

## 6 Simulation of ion acceptance distributions (DIA)

representation of three dimensional DIA data. Similarly to the extended possibilities utilizing isosurfaces discussed above, volume rendering also allows more complex visualizations. For example, it is possible to use different scalar fields to determine the opacity and the color information, which allows to point out the correlation between the scalar fields.

All two dimensional representations of DIA in this work, mostly colored contour plots, were rendered with the Matplotlib [133, 134] Python/NumPy [135] visualization library. The volume rendering images presented in this thesis were rendered with VTK [126–128] via its Python programming interface.

### 6.4.1 Interactive DIA visualization: Web DIA Explorer

For an observer of a complex data set, it is generally favorable to be able to interact with the data visualization. The option to change variables of the data set or its presentation allows a thoroughly investigation of dynamic aspects of data, for example ion acceptance distributions in dependence of particular external parameters. Ideally, such an interactive visualization is easily accessible by readily available technical means. Fortunately, with today's common web-technologies, e.g. HTML5 in combination with Java-Script, complex interactive web applications which provide interactive data exploration tools are easily created.

Access to this kind of interactive presentation for DIA data, a simple web based presentation application was build: the "*Web DIA Explorer*". This application interactively shows pre-rendered image sequences along with their meta-data. This allows to present experimental aspects, e.g., the impact of electrical potentials on the DIA, but also presentation parameters as the camera position in a volume rendering.

The image sequences presented by DIA Explorer are given as set of image files and according meta-data information, which is stored in a JSON (Java Script Object Notation) [136] file. This file contains vectors of values of relevant parameters (temperatures, electric potentials, mean signal intensity etc.) for the individual images with links to the image files. In addition, configuration information for DIA Explorer (e.g. names of the presented parameters, which parameters are user controllable variables etc.) are stored in this file. The application reads this file, creates user interface elements for the user controllable variables, and presents the pre-rendered images according to the user input. The application was implemented in Java-Script utilizing the open source jQuery [137] and jQuery mobile [138] Java-Script libraries and HTML-5. Figure 6.11 on the facing page shows a screenshot of the Web DIA Explorer.

## 6.5 Results

In this section, the results of the fluid dynamic simulations and the ion trajectory calculations are presented and discussed in detail. An overview of the experimental DIA results determined in the MPIS can be found in conference contributions [139, 140]. Matthias Lorenz has presented a thorough analysis of a very large set of measured DIA,

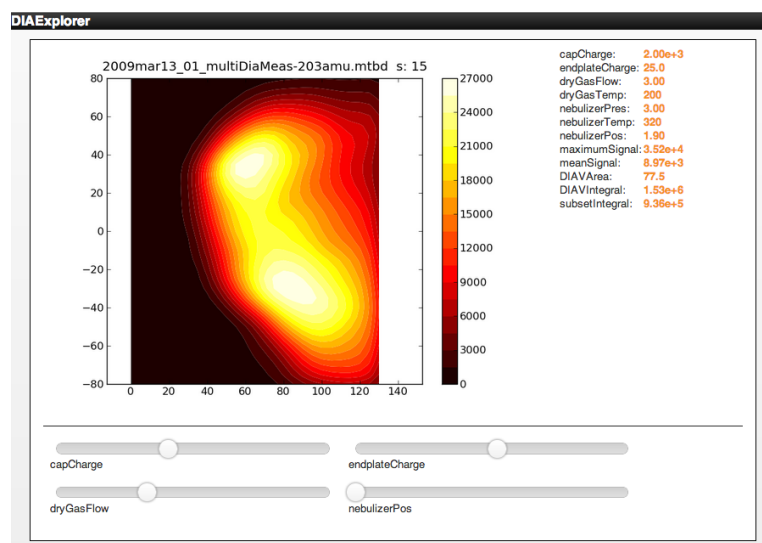


**Figure 6.11:** Screenshot of the Web DIA Explorer.

including the experimentally spatially resolved determination of ion transfer times from ion generation to their detection. This detailed analysis of the dynamic behavior of the DIA in the MPIS can not be fully reproduced here. The result analysis presented in this work is rather geared towards the evaluation and assessment of the numerical results, utilizing only a selected subset of the large experimental DIA result database.

### 6.5.1 CFD Simulations: Bulk gas flow in MPIS

The analysis of the validated CFD simulations [96, 141] reveal several remarkable general aspects of the bulk gas flow in the MPIS. As shown in the representations of the mean velocity in figure 6.12 on the next page, the gas flow in the ion source volume is dominated by the nebulizer-gas and dry-gas streams. The inflow into the inlet capillary is clearly observable as small area of high gas velocity at the inlet capillary tip. Ions have to reach this region to be sampled by the MS, thus the size of this region defines a reasonable target zone for the simulated ions in the DIA simulation. The capillary inflow has no observable direct influence on the flow in the bulk volume, since the dry-gas volume flow ( $\approx 2$  to  $4 \text{ l min}^{-1}$ ) is generally significantly larger than the gas amount which is pumped into the MS by the choked capillary flow ( $\approx 0.8 \text{ l min}^{-1}$  [98, 116]). Therefore, only analyte free dry-gas is transported into the MS and the region under the spray-shield remains generally analyte free. The amount of excess dry-gas which flows into the ion source volume depends on the inlet capillary inflow. Thus, the capillary flow, which is comparably stable under the given conditions, has an indirect influence on the conditions in the ion source volume.

In the MPIS the two orthogonally oriented dominant gas flows impinge each other in front of the spray-shield geometry and get into an intensive interaction. As observed

## 6 Simulation of ion acceptance distributions (DIA)

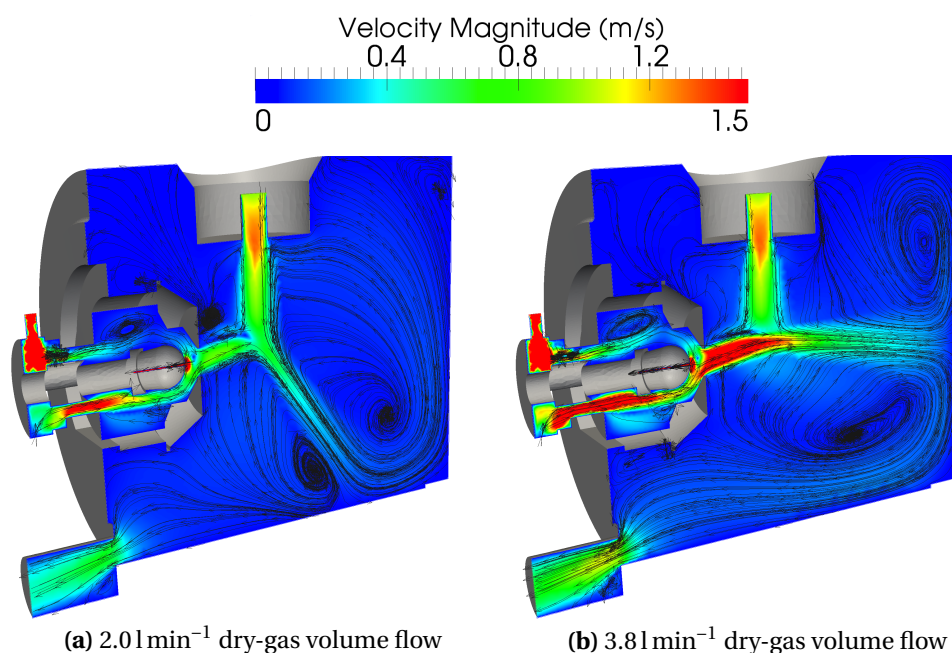


**Figure 6.12:** Simulated gas flow in the MPIS: Bulk gas velocity and surface flow lines on the center  $xy$  plane of the ion source.

in figure 6.12, the amount of deflection of the nebulizer gas flow depends on the mean velocity of the dry-gas flow or its volume flow, respectively, which emerges from the spray-shield. With low dry-gas flow ( $2.01 \text{ min}^{-1}$  in fig. 6.12), the nebulizer gas “jet” is noticeable but not significantly deflected. In contrast, with high dry-gas flow ( $3.81 \text{ min}^{-1}$  in fig. 6.12), the situation changes entirely: Now the nebulizer jet is basically terminated by the dry-gas, and the merged gas jet is directed towards the back of the ion source. The merged gas jet hits either the bottom of the ion source or its back plane, where exactly depends on the ratio of the dry-gas and nebulizer gas flow. The inevitable impingement of the dominant gas flow on the walls of the ion source results in the generation of large scale vortex structures with comparably low mean gas velocities, which are visible as large blue areas with velocities well below  $0.4 \text{ m s}^{-1}$  in fig. 6.12.

Governed by this basic structure of the bulk gas flow in the MPIS, the nebulizer gas, and therefore the neutral analyte, is distributed in the ion source volume. This is revealed by figure 6.13 which shows the relative analyte distribution in the MPIS for the two simulated operation points. The neutral distribution is characterized essentially by three observations: The gas flow from the nebulizer is enriched with neutral analyte, since the analyte is introduced by this gas flow into the MPIS. In contrast, the dry-gas flow, which is analyte free, “washes” the area in front of the opening in the spray-shield free of analyte. This situation leads to a strong concentration gradient in the interaction zone which marks the boundary between the gas streams. This is expected

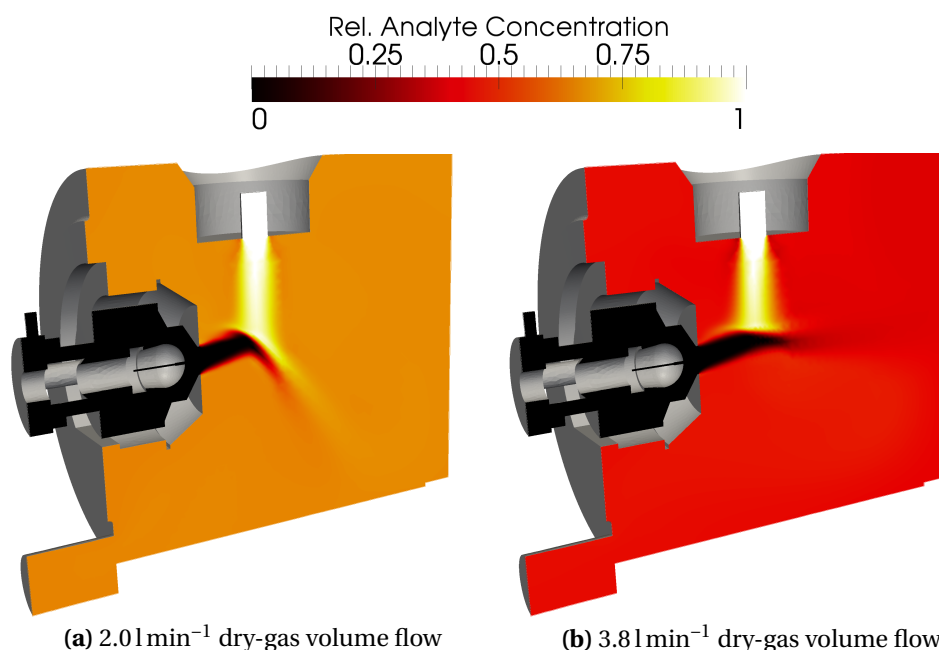


**Figure 6.13:** Simulated gas flow in the MPIS: The cut plane shows the neutral analyte concentration.

from the basic situation of the orthogonally aligned dominant gas flows. Interestingly, the relative neutral analyte concentration distribution in the volume outside the dominant gas streams is virtually isotropical on a relatively high level. This finding underlines the notion that the nebulizer gas with the analyte is rapidly mixed into the bulk volume by the interaction between the gas streams and the impingement of the resulting gas flow on the ion source chamber wall. The background level of the neutral analyte depends on the ratio between nebulizer- and dry-gas inflow. As observable in figure 6.13, the relative background concentration increases from below 0.5 (right panel in fig. 6.13) with high dry-gas inflow to a level significantly above 0.5 with low dry-gas inflow (left panel in fig. 6.13). Beside a possible effect of the changed flow pattern in the bulk volume on the background analyte concentration, the obvious mechanism for the changing background concentration is the dilution of the nebulizer gas and the analyte by the increasing dry-gas flow.

The CFD simulation further suggests the notion of generally long residence times of the bulk gas in the ion source. This is supported by the analysis of the integration times of stream-lines generated with the VTK stream tracer [128] which are shown in figure 6.14 for the high dry-gas solution. The shown stream-lines correspond to the paths small fluid packages or a massless particle would follow in the given flow field. The integration time in the numerical integration process of the stream-line calculation is equivalent to the time a fluid particle would spend following the stream-line.

## 6 Simulation of ion acceptance distributions (DIA)

The stream-lines starting at the nebulizer inlet also emphasize the already discussed large three dimensional vortex structures in the ion source. The spectrum of residence times at the ion source exhaust, where all the gas which is not pumped into the MS exits, underlines the impression of generally long residence times of the neutral gas in the MPIS: Even on the shortest way, a fluid particle from the nebulizer would spend at least 1 s in the ion source chamber while many longer flow-lines show integration times well above 5 s. In addition, there are tendencies visible for the recirculation of fluid from the large slow vortex back into the driving inflows. Both observations are particularly problematic in terms of the hyphenation of the MPIS with chromatographic pre-separation stages. The intensive mixing of the neutral analyte into the slow moving bulk gas vortices, which result in the discussed long residence times, would naturally also diffuse a transient neutral analyte concentration pulse, e.g. an sharp LC peak. The analyte would be washed out only slowly, and individual analyte molecules have multiple times the chance to be ionized. This leads to a poor chromatographic performance of the entire LC-MS combination. This is particularly the case with modern high performance LC systems, e.g. Ultra Performance Liquid Chromatography (UPLC) which produce peakwidths at least in the low second range [142, 143]. It was already experimentally observed that the temporal diffusion of chromatographic peaks was significantly lowered when the neutral gas was actively pumped away through a comparably large exhaust tube which was integrated into the MPIS directly under the nebulizer inlet [144]. However, the optimization of the bulk gas flow and the neutral analyte distribution in an AP-ion source particularly designed for the hyphenation with LC is an active research topic at the time of writing.

The details of the fluid flow in the zone of first interaction of the nebulizer- and the dry-gas stream are depicted in figure 6.15. It becomes apparent, that the flow field is complex particularly in the area where the spatially resolved ion signal occurs experimentally and where therefore the DIA measurements were performed (highlighted in fig. 6.15). The flow in the interaction zone shows three dimensional features, with pronounced flow components in the laser beam ( $z$ ) axis, not seen in the surface stream lines in figure 6.12. The dry gas flow in which the nebulizer flow directly impinges, generates an approximately horseshoe shaped vortex structure in the  $y - z$  plane [96]. Overall, the ion signal is originating in a highly dynamic region in terms of the bulk fluid flow, which probably has unsteady characteristics. The time averaged static CFD simulations presented here are principally not able to resolve this, which has to be considered in the interpretation of the ion trajectory simulations based on them.

### 6.5.2 DIA Simulations: Effects of ion source parameters

The effects of the parameters of the ion source on the experimentally recorded DIA are presented and discussed in previous publications [98, 140, 145]. Therefore, only the subset of DIA measurements which was also reproduced numerically is discussed here.

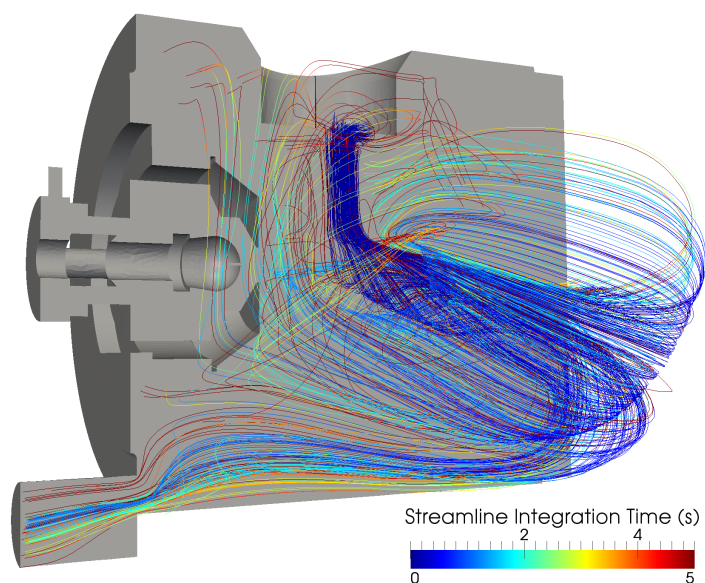


**Figure 6.14:** Flowlines for the simulated bulk gas flow in the MPIS with  $3.8 \text{ l min}^{-1}$  dry-gas volume flow. The flowlines were started at the nebulizer inlet. They are colored with the flow line integration time which corresponds to the residence time of a fluid package following the flow line in the MPIS. Note the spectrum of integration times at the exhaust outlet: The residence time in the ion source is at least around 1 s while many streamlines show residence times well above 3 s. The longest residence time in the shown set of stream lines was above 30 s.

### 6.5.2.1 Electric potentials

There are two relevant electric parameters in the MPIS, the electric potential on the inlet capillary cap and the voltage on the spray-shield. Figure 6.16 shows the effect of the variation of the inlet capillary potential on the experimental and simulated DIA. As clearly seen in the DIA measurements, the increase of the capillary voltage shifts the spatially resolved ion signal away from the MS inlet without a significant change of the general shape of the signal. Per 1000 V increase, the experimental DIA moves roughly 1 mm away from the MS inlet. With further increasing capillary voltage, a noticeable change in the DIA shape occurs, as apparent in the 3000 V and 4000 V panels of figure 6.16: The DIA becomes curved and the MS facing front edges, become more inclined. This leads to a “compression” of the ion signal in the vertical ( $y$ ) axis.

Despite the obvious differences in the shape of the ion signal distributions between simulation and experiment visible in figure 6.16, the general effects of the capillary voltage variation are reproduced by the DIA simulation: The initial DIA at 1000 V is shifted away from the MS inlet with increasing inlet capillary potential. As in the experiments, the shift is roughly 1 mm per 1000 V in the numerical DIA. Another reproduced

## 6 Simulation of ion acceptance distributions (DIA)

feature is the compression in the vertical axis and the increasing inclination of the front region of the ion signal at higher capillary voltage, which is similarly observable in the numerical result. A notable but not necessarily obvious difference between the experimental and numerical DIA is the absolute signal intensity: In the experiments, the maximum intensity of the DIA levels off considerably, while in the DIA simulation the intensity even tends to increase. This becomes apparent by comparing the absolute signal intensities given in the panels in figure 6.16.

In contrast to the capillary voltage, the shape of the DIA is very sensitive to variations of the spray-shield potential. This is shown in figures 6.17 and 6.18: Even with a change of the spray-shield voltage about 50 V, which is moderate compared to the capillary voltage changes shown in figure 6.16, the DIA shape changes significantly. In general, the ion signal becomes elongated in the horizontal axis and compressed in the vertical axis, the same change which was observed with higher inlet capillary voltages. Additionally, a significant shift of the DIA away from the MS inlet is noticeable with increasing spray-shield voltage.

According to the observations with variation of the inlet capillary voltage, the DIA simulation is generally able to reproduce many of the relative effects of the spray-shield variation: Particularly, the variation of the inclination angles of the front region of the DIA is well reproduced in figures 6.17 and 6.18. Other features, which are relatively well reproduced by the simulation are the “compression” of the ion signal in the vertical axis with increasing voltage on the spray-shield and the rough positions of the signal maxima.

As mentioned above, the simulations also show obvious divergences from the experimental DIA: The general shape is similar and certainly correlates between numerical and experimental results, but it is definitely not equal. The simulation tends to predict too wide ion signals and often even additional signal maxima which are not observable experimentally. The latter is clearly shown in the simulations with high dry-gas flow (figure 6.18) while the former is a general observation which can be made in virtually all presented DIA results.

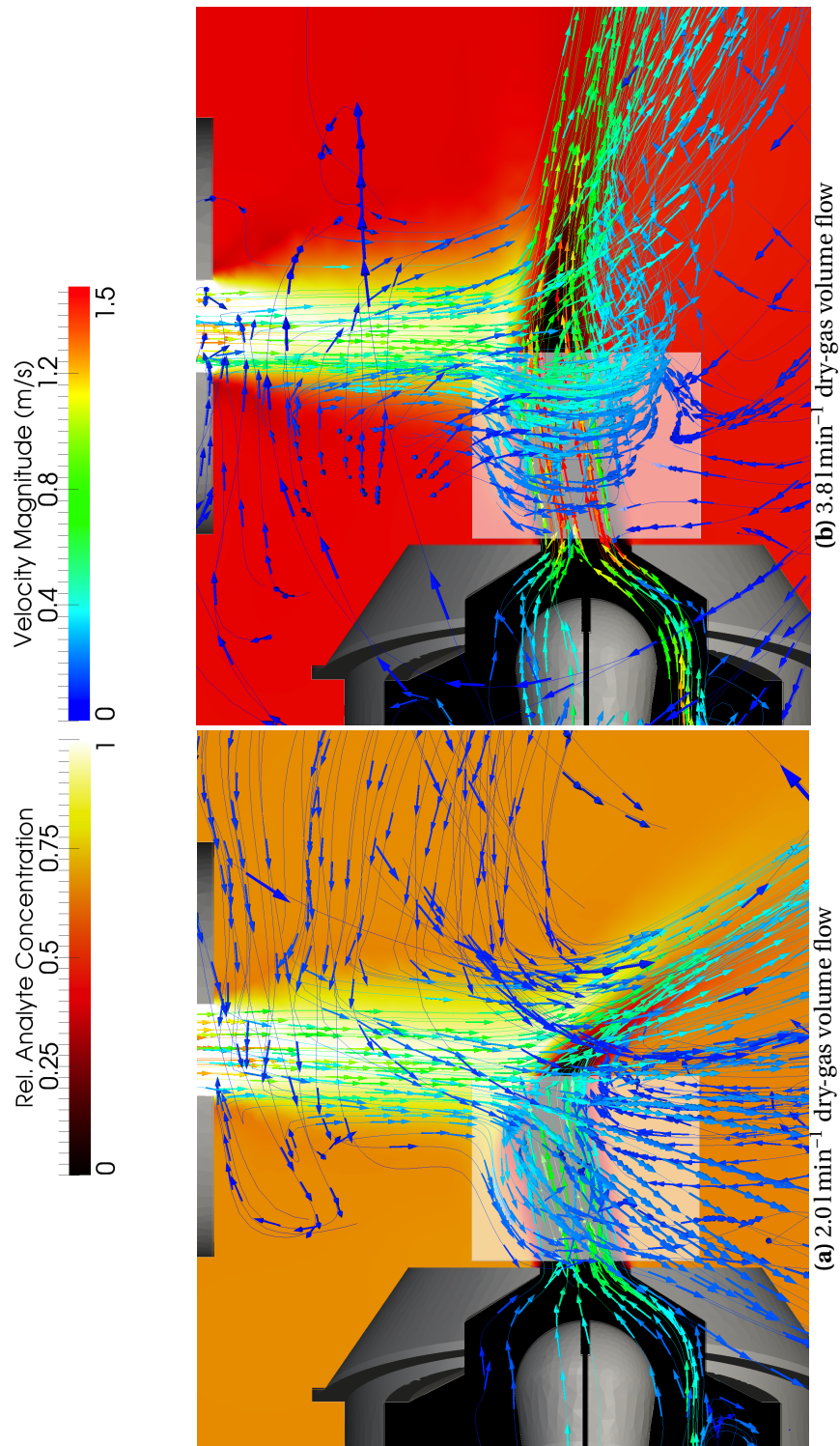


**Figure 6.15:** Simulated gas flow in the MPIIS

## 6 Simulation of ion acceptance distributions (DIA)

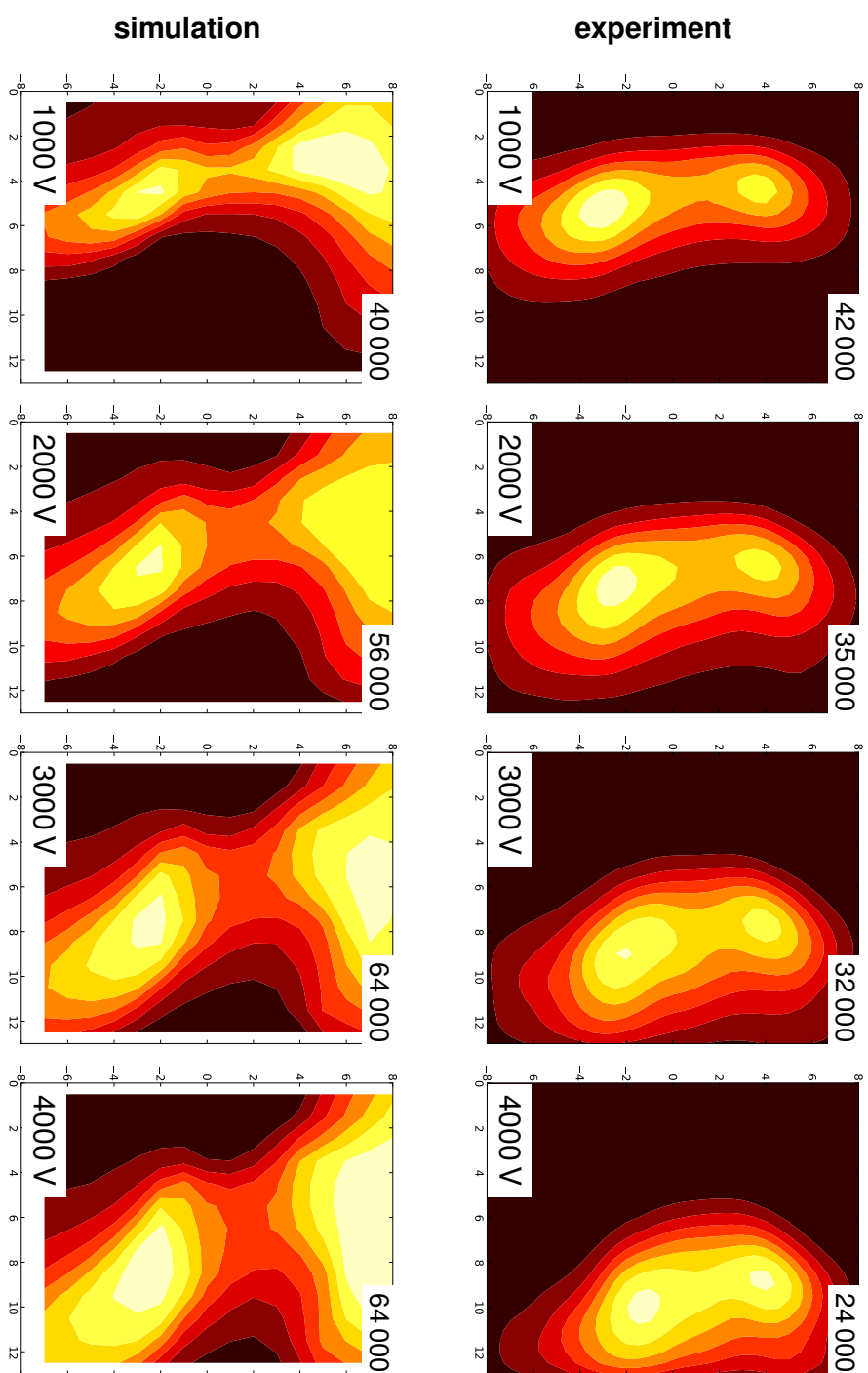


**Figure 6.16:** Experimental and simulated DIA, dependence on Capillary Voltage variation: Spray Shield voltage was 0 V, the dry gas flow was  $2.0 \text{ L min}^{-1}$ , the ion depletion probability was  $10 \times 10^{-5}$ , the capillary voltage is given in the insets, the level of maximum signal (brightest contour level) is given above each plot. The spatial axes are in mm.

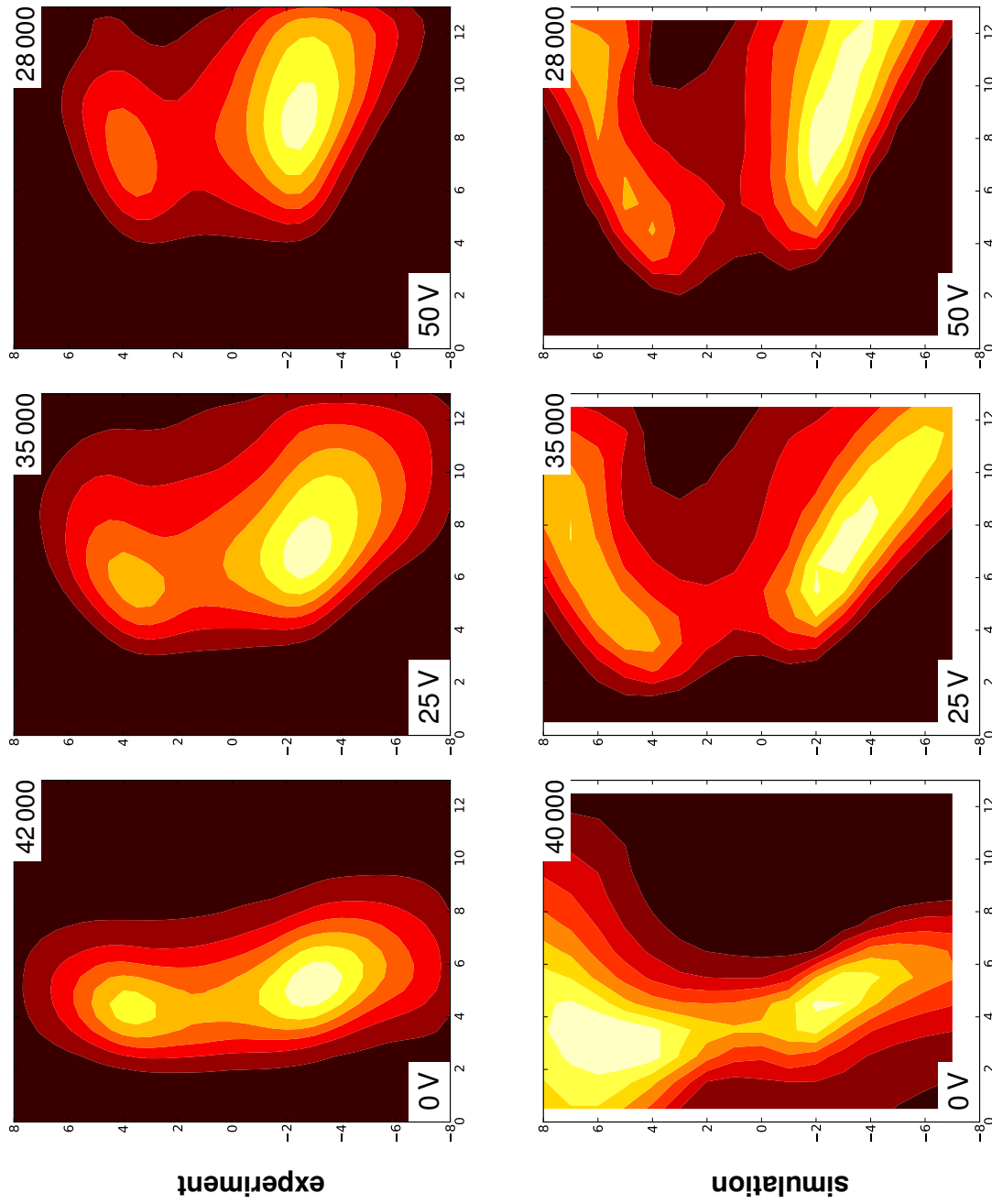


**Figure 6.17:** Experimental and simulated DIA, dependence on spray shield variation: Capillary voltage was 1000 V, the dry gas flow was  $2.0 \text{ L min}^{-1}$ , the ion depletion probability was  $10 \times 10^{-5}$ , the spray-shield voltage is given in the insets, the level of maximum signal (brightest contour level) is given above each plot. The spatial axes are in mm.

## 6 Simulation of ion acceptance distributions (DIA)

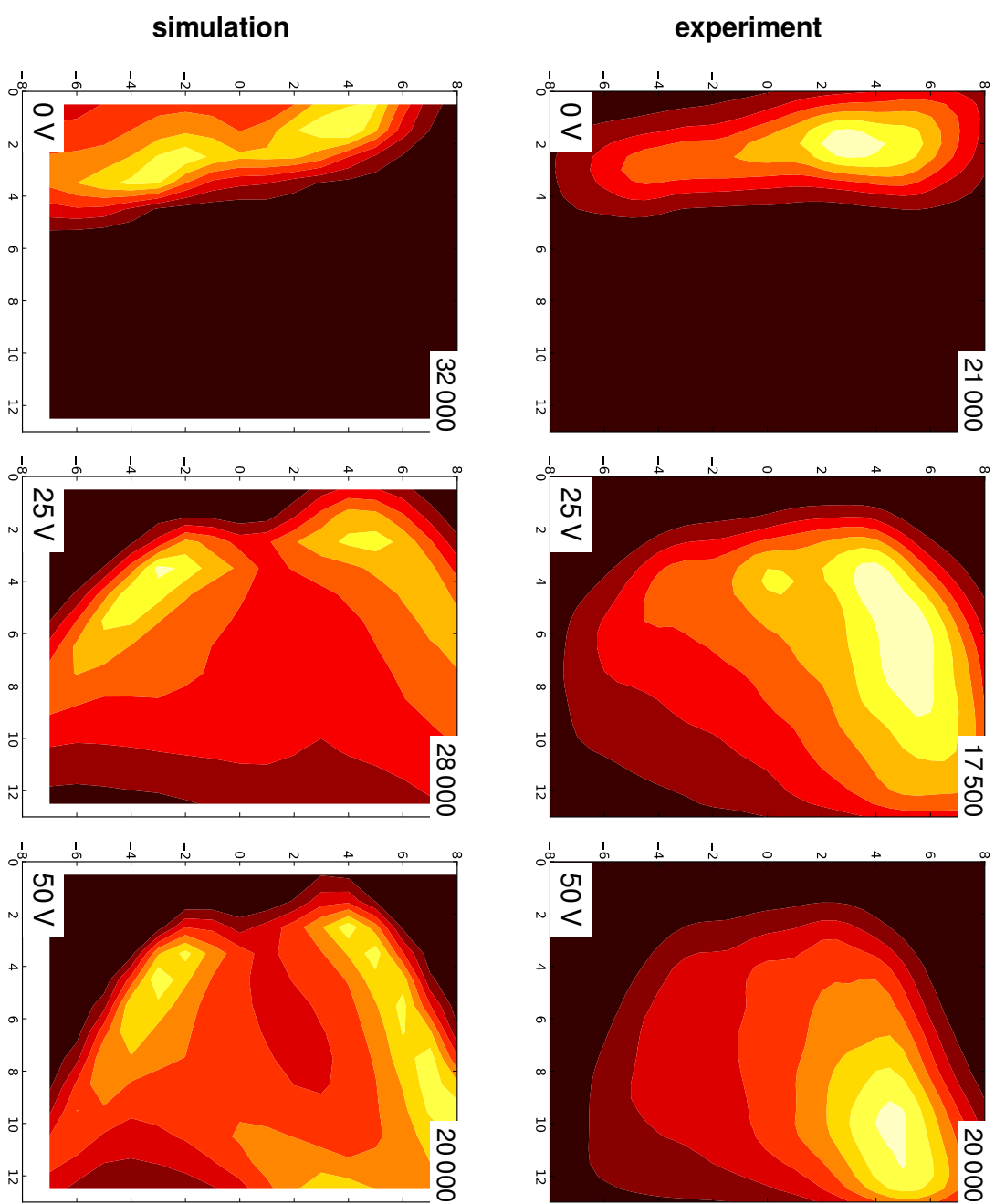


**Figure 6.18:** Experimental and simulated DIA, dependence on spray-shield voltage: Capillary voltage was 1000 V, the simulated dry gas flow was  $3.8 \text{ L min}^{-1}$ , the experimental was  $4.0 \text{ L min}^{-1}$ , the ion depletion probability was  $10 \times 10^{-5}$ , the spray-shield voltage is given in the insets, the level of maximum signal (brightest contour level) is given above each plot. The spatial axes are in mm.

### 6.5.2.2 Dry-gas flow

In comparison to the DIA simulations with selected electric potentials, the set of fluid dynamic operation points of the ion source available as CFD input data for the DIA simulation is rather limited. There are only two final solutions of the bulk gas flow field: A low dry-gas solution with  $2.0 \text{ L min}^{-1}$  dry-gas volume flow and a high dry-gas solution with  $3.8 \text{ L min}^{-1}$ . These operation points were deliberately chosen. The analysis of the experimental DIA data [98, 140] revealed that the DIA shows a surprising abrupt shift or “switch” in dependence of the dry-gas volume flow when the gas flow temperatures and the nebulizer flow is held constant. Figure 6.19 illustrates this behavior of the DIA as an example: Between a dry-gas flow of  $3.0$  to  $3.2 \text{ L min}^{-1}$ , the DIA switches from a state with a global maximum in the lower half of the ionization region to a state with the maximum above the center axis of the ion source. This switch occurs relatively abruptly considering the stability of the DIA between  $2.0$  to  $3.0 \text{ L min}^{-1}$  and  $3.2$  to  $3.8 \text{ L min}^{-1}$ .

Further investigation of this phenomenon in previous work [98, 140, 146] showed that the exact position of the turning point with respect to the dry-gas flow depends also on the temperatures of the gas flows and the nebulizer gas flow. The hypothesis at that time was that this switch was induced by an abrupt change in the bulk gas flow. To investigate this, two operation points on either sides of the switch point were chosen, with a proper distance to it, to be sure that the CFD results show the fully transitioned flow states.

Indeed, the bulk gas simulations (figure 6.12 and 6.15) show a rather different structure of the overall bulk gas flow at the two operation points. Figure 6.20 shows exemplary DIA simulation and measurement results for the two simulated dry-gas flows. Clearly, the transition of the DIA is observable in the upper panels of the figure. In contrast to the experimental result, the numerical outcome is less pronounced though: While the experimental DIA is essentially a monomodal signal which shifts towards the upper half of the scanned area, the simulated DIA shows a bimodal structure in both operation points. Additionally, the relocation of the signal intensity towards the upper half is by far not as complete as in the experimentally found results.

In summary, the ion trajectory simulation with the presented CFD simulation as input data did not reproduce the effect of the dry-gas flow variation well. A possible explanation for the poor performance of the DIA simulations in this regard is the required level of detail for the correct reproduction of the discussed DIA transition by the numerical model. Figure 6.15 gives an impression of the scale of the ionization region within the bulk gas flow field. Despite the fact that the overall flow pattern is reasonably predicted by the CFD model, the DIA simulation depends primarily on the detailed flow in the ionization region. As seen in figure 6.15, in particular in the neutral analyte distribution, the flow changes noticeable but not significantly in this spatial region. It appears as if the available CFD model is able to describe only a rough overall flow pattern, but is not able to correctly reproduce a detailed change of the flow field in the ionization region which is induced by the dry-gas variation. This notion

## 6 Simulation of ion acceptance distributions (DIA)

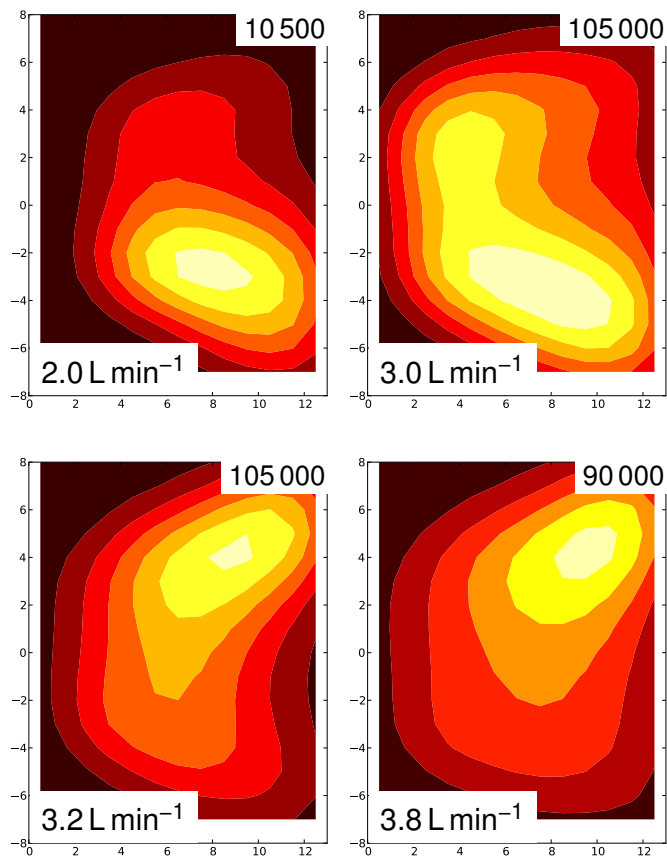


**Figure 6.19:** A abrupt switch of the experimentally found DIA in dependence on the dry-gas flow. The dry-gas volume flow is given in the insets, the level of maximum signal (brightest contour level) is given above each plot.

is supported by the finding that the validating PIV measurements show a noticeable different inclination of the dry-gas stream into the ion source as compared to the prediction of the numerical model [96].

The presented CFD and ion trajectory model is certainly able to give general insight in the dynamics of the ion motion in the MPIS and gives hints for the understanding of the observed DIA shift. However, it is not able to conclusively provide the exact cause for the DIA transition, this task remains for a subsequent, refined numerical models in the future.

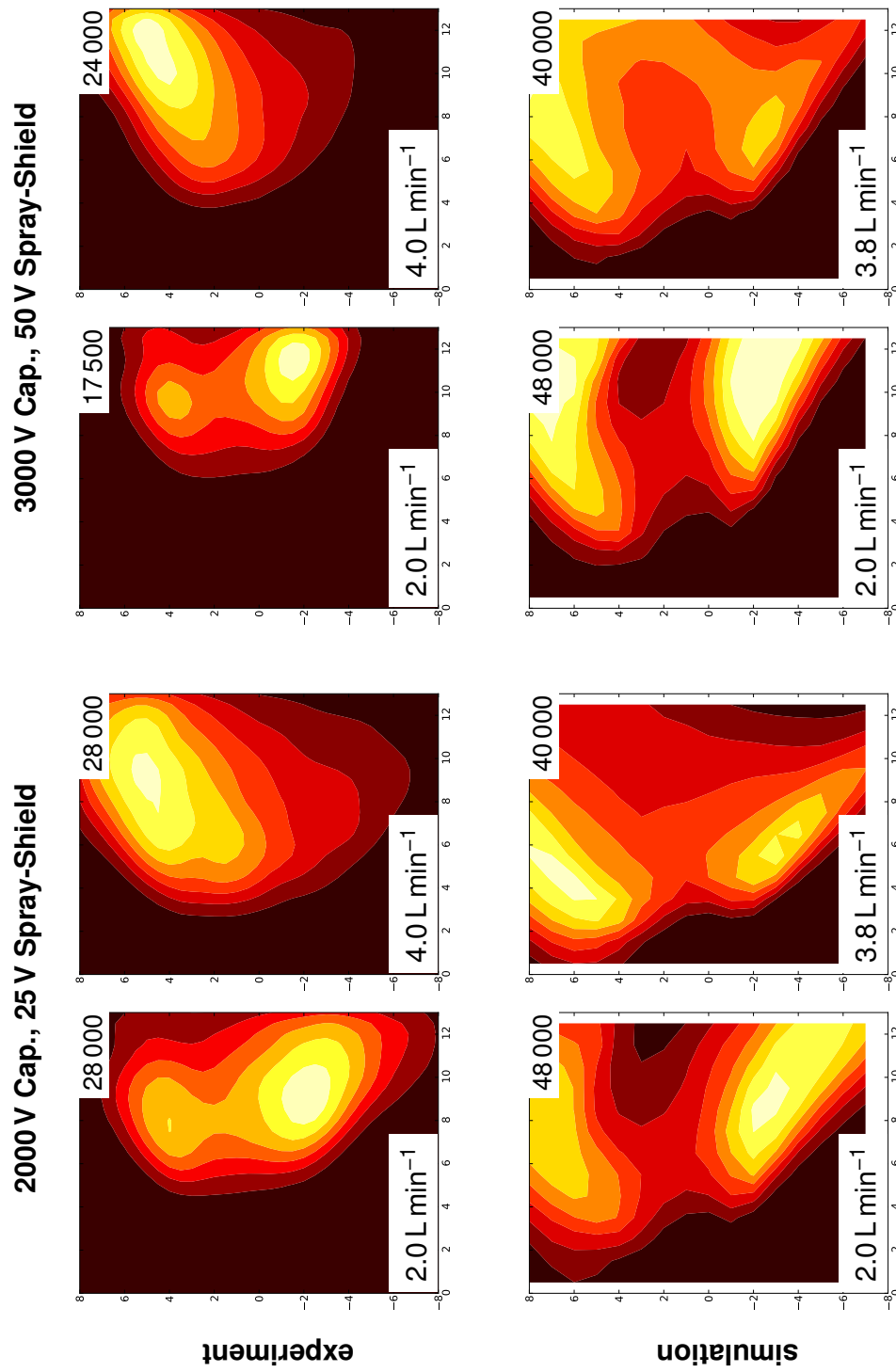


**Figure 6.20:** Experimental and simulated DIA: Variation of the dry-gas flow. The ion depletion probability in the simulations was  $10 \times 10^{-5}$ , the dry-gas volume flow is given in the insets, the level of maximum signal (brightest contour level) is given above each plot. The spatial axes are given in mm.

### 6.5.3 Ion trajectories

Nearly all DIA measured in the MPIS in its LC configuration share common features, which may be surprising at first glance. In particular the pronounced local signal minima in direct proximity to the MS inlet and in the center axis of the DIA are interesting, because ions should have a direct path from these areas into the MS inlet. To understand the mechanisms leading to the particular shapes of the observed DIA, it is useful to analyze exemplary ion trajectories in detail. Figure 6.21 shows simulated ion trajectories along with the neutral analyte distribution of the CFD solution with  $3.8 \text{ L min}^{-1}$  dry-gas volume flow. The figure depicts the trajectories of ion sets which were started on lines parallel to the  $y$  axis with increasing distance to the spray-shield.

Most observed DIA show a pronounced local signal minimum in direct proximity to the spray-shield. The trajectory simulation with 1 mm distance in figure 6.21 shows that there are actually two effects which lead to the described signal minimum: Ions generated near to the center ion source axis in close proximity to the spray-shield opening are attracted and focused on the inlet capillary tip despite the dry-gas flow directed in the opposite direction. However, the dry-gas flow has another effect: It removes neutral analyte from the region in front of the spray-shield opening. Therefore, even if ions would reach the MS inlet from here, there are no ions generated in this zone in the first place. In contrast, ions are generated in the region around the dry-gas stream close to the spray shield, due to the relatively high neutral local analyte concentration here. Remarkably, these ions mostly hit the spray-shield electrode since the strong electric field close to it. Thus, only a small fraction of ions originating at the border between the described regions are able to reach the MS inlet.

With larger distance to the spray-shield the electric field strength decreases rapidly. In particular the 5 and 7 mm solutions in figure 6.21 show clearly the equilibrium between electric and viscous forces as deflective point in the trajectory plots approximately 4 mm in front of the spray-shield near to the central axis of the MPIS. Ions passing this point closer to the spray-shield are electrically attracted towards the MS inlet. Ions passing this point on the far side are blown away from the MS inlet by the dry-gas stream. The curved electric field induced by the capillary cap and the spray-shield, which form essentially a form of electrostatic lens as depicted in figure 6.22, leads to the attraction and focusing of ions originating from regions outside the dry-gas stream onto the inlet capillary. This effect can be observed in the 5 and 7 mm solutions in figure 6.21. The presence of neutral analyte available for ionization leads to the observed bimodal signal structure with local maxima above and below the central axis of the MPIS.

If the distance to the MS inlet becomes too large and therefore the attractive electric force on the ions too low, the viscous force from the dry-gas essentially dominates the ion motion and they are almost completely blown away. Remarkably, those ions are not necessarily lost for sampling by the MS: As seen in the 14 mm solution in figure 6.21, there is a chance for the ions which have already traveled through the ion source volume to be electrically captured by the MS interface. This basic finding of

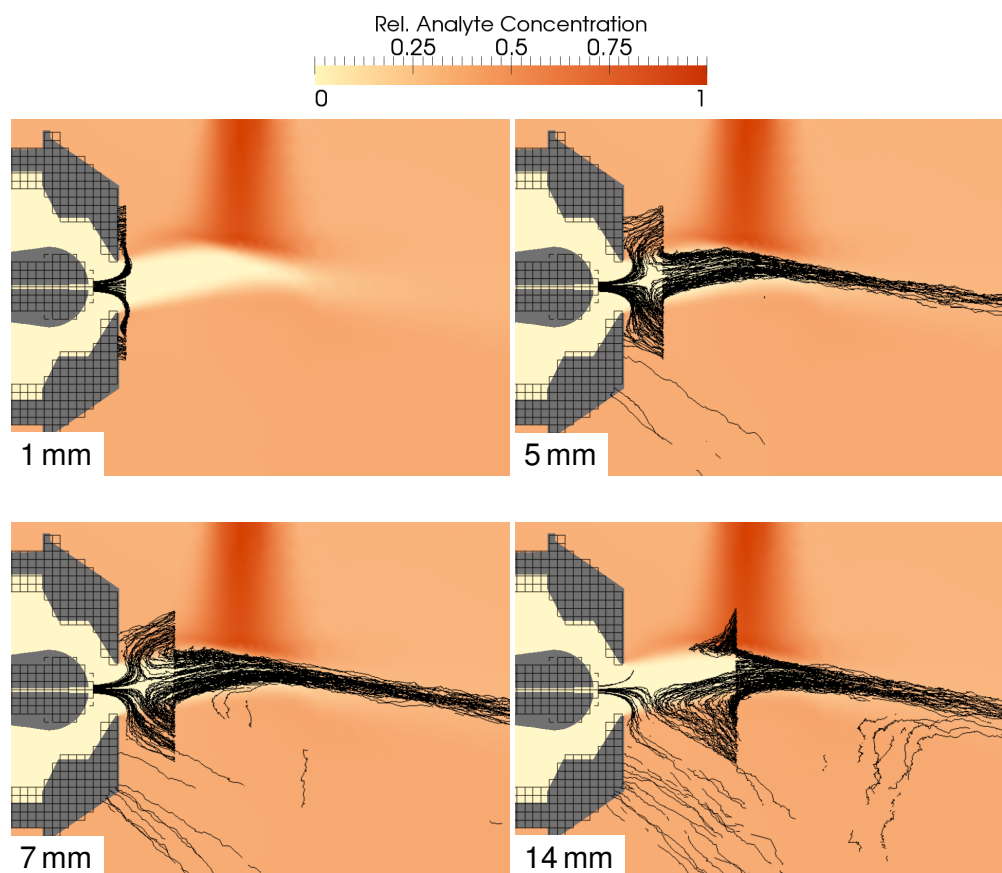


**Figure 6.21:** Exemplary simulated ion trajectories and neutral analyte distribution in the MPIS. Ions were started in a line parallel to the  $y$  axis, the insets show the distance of the ion start zone to the spray-shield. The dry-gas flow was  $3.8 \text{ L min}^{-1}$ , the capillary voltage was 1000 V, the spray-shield voltage was 50 V. For better clarity of the figure, the ion trajectories are plotted only in a narrow slice in  $z$  direction. Some of the trajectories appear therefore as broken.

ions which are sampled after a, possibly very long, journey with the bulk gas through the ion source is supported by the experimentally observed broad spectrum of ion residence times in the ion source [98, 145, 147].

#### 6.5.4 Effects of simulation parameters

In this section, the effects of the parameters of the simulation on the simulated DIA are discussed in detail. The knowledge about the sensitivity of numerical DIA on parameters of the simulation process allows to assess the confidence in the simulation

## 6 Simulation of ion acceptance distributions (DIA)

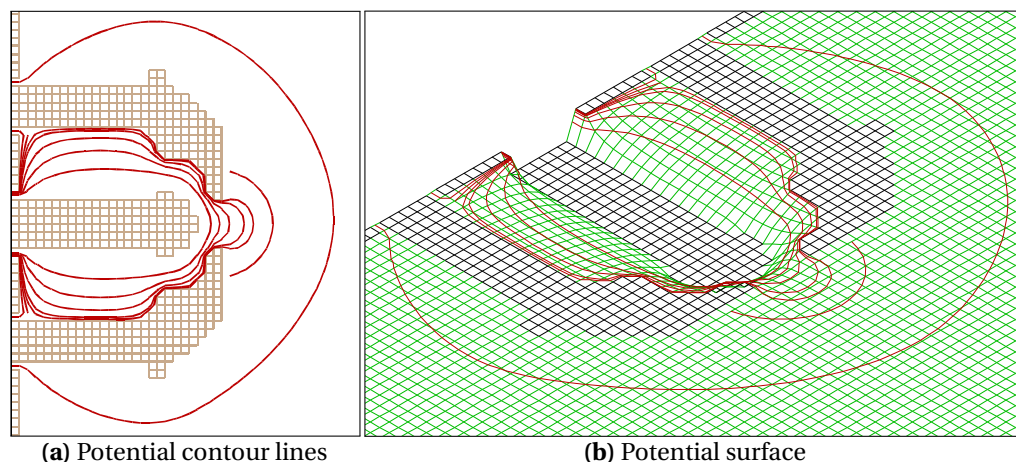


**Figure 6.22:** Potential distribution at the MS interface in the MPIS. The capillary voltage is 2000 V, the spray-shield voltage is 50 V. The depicted contour lines are drawn at 25 V, 50 V, 75 V, 100 V, 200 V, 400 V and 800 V

results and the identification of critical input parameters which has potentially to be known with increased precision.

### 6.5.4.1 Effect of simulation geometry

As seen in figure 6.21, there is a considerable spatial discretization error in the SIMION ion trajectory simulations. In particular, with 1 mm spatial resolution the position of the inlet capillary tip is only relatively poorly resolved by the SIMION calculation grid. This becomes apparent by the notable difference between the capillary tip in the SIMION calculation mesh and its position in the CFX geometry. This discretization inaccuracy potentially leads to a significant error in the simulated DIA if the ion trajectory simulation is highly sensitive to the inlet capillary position.

DIA simulations with varied simulation geometries were performed, to investigate the effect of the described spatial discretization errors on the DIA result. The inlet capillary tip was moved 1 mm, which is one grid unit in the SIMION potential array, in both directions on the  $x$  axis from its base position presented in figure 6.21. With the modified geometries, a representative set of simulations was repeated. In addition, for one of the geometries (capillary 1 mm forward) simulations were performed with activated *surface enhancement*. This is an experimental feature, which became available in SIMION in a late stage of this work. It allows to consider electrode surfaces which do not align to the units of the calculation grid by recording the distance of the electrode surface to the next grid unit and uses this information in the field refinement process. This process may improve the quality of the ion trajectory simulation in particular situations about one order of magnitude [148].

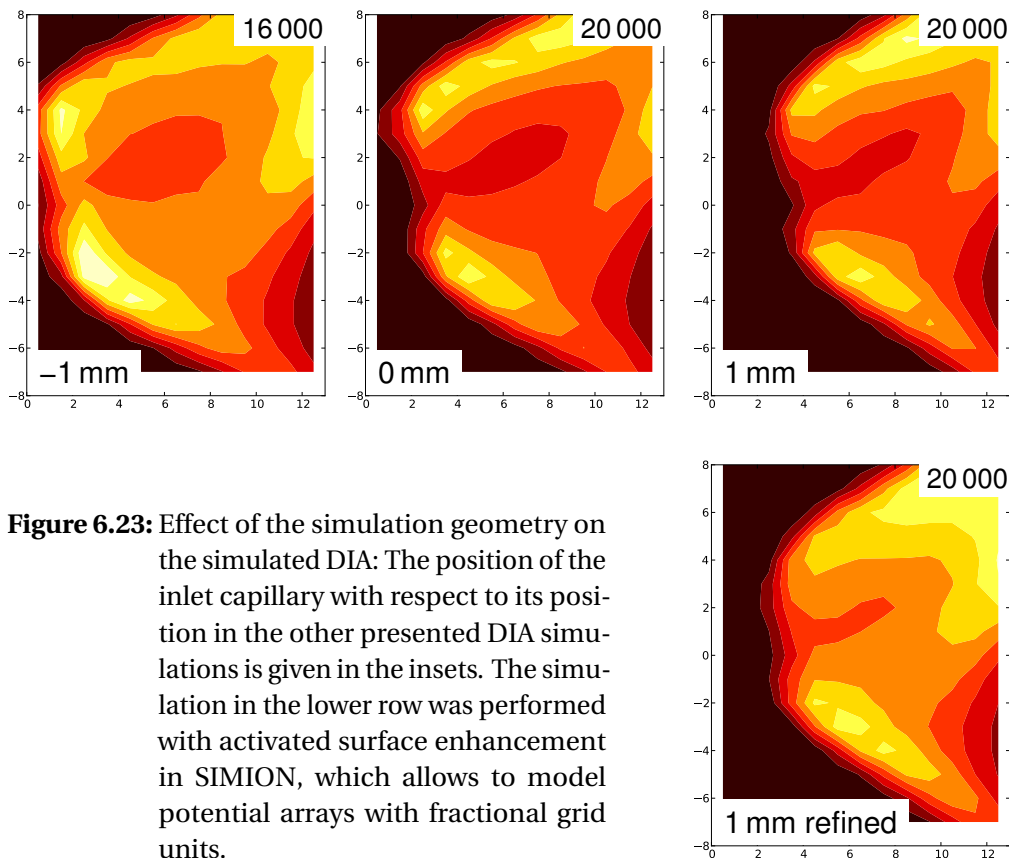


**Figure 6.23:** Effect of the simulation geometry on the simulated DIA: The position of the inlet capillary with respect to its position in the other presented DIA simulations is given in the insets. The simulation in the lower row was performed with activated surface enhancement in SIMION, which allows to model potential arrays with fractional grid units.

Figure 6.23 shows the results of DIA simulations with different geometries. The movement of the inlet capillary tip (upper row in figure 6.23) clearly shows an effect of the capillary position on the simulated DIA. The positions of the signal maxima and the front of the signal distribution in the resulting DIA moves with the capillary position. In addition, the shape of the DIA also changes notably. In particular in the simulation with the capillary one mm retracted from its base position (“-1 mm” in figure 6.23), the signal distribution stretches out significantly in the  $x$  direction, the signal maxima near the front edge of the distribution become more pronounced and the signal shape, in particular the inclination angles, changes notably. Taking into account all capillary positions, the development of the above effects are also visible in the simulations with the capillary in its base configuration (“0 mm” in figure 6.23) in direct comparison to the result with the retracted capillary (“-1 mm” in figure 6.23). Despite the changes in the simulated DIA, the rough shape of the spatially resolved simulated ion signal remains relatively unaffected from the variation of the capillary position. This suggests that the inlet capillary position act essentially linearly on the simulated DIA. Considering the spatial error of the SIMION calculation grid (cf.

## 6 Simulation of ion acceptance distributions (DIA)

figure 6.21), the error in the DIA simulation results is probably not significant. The notion of a relatively insensitive DIA with respect to the detailed geometry of the MS inlet is also supported by the finding that the activation of the surface enhancement feature has only subtle effects on the DIA.

### 6.5.4.2 Effect of ion mobilities

At atmospheric pressure, in the presence of moderate electric fields, the motion of ions is characterized by the reduced ion mobility  $K_0$  as presented in section 2.2.1 on page 5. As defined by equation 2.9 on page 6, the ion mobility gives the proportionality between ion drift velocity and the electric field which is essentially a measure of the ratio of the viscous and electric forces acting on the ions. Therefore, changes in the ion mobility inevitably modify the ion trajectories in the flowing bulk gas of the MPIS.

Figure 6.25 depicts DIA simulations under variation of the ion mobility. As described already in section 5.3.2 on page 37, the Statistical Diffusion Simulation algorithm is able to estimate the ion mobilities from the ion mass. The figure shows clearly that there is an effect of the ion mobility on the simulated DIA. With increasing ion mass and therefore decreasing ion mobility, the ion signal becomes narrower and its maximum focuses towards the front edge of the distribution. In addition, the overall signal intensity tends to decrease with decreasing ion mobility. This becomes visible in the decreasing maximum signal intensity and the decreasing area of the signal distribution in figure 6.25. These observations supports the notion that the spatial region which is electrically “visible” for the MS becomes smaller with decreasing ion mobility as the viscous force on the ions becomes stronger.

Despite the changes in the simulation results, the shape of the DIA is not particularly sensitive to the ion mobility variation. Even with strongly reduced mobility ( $0.70 \times 10^{-4} \text{ m}^2 \text{ V}^{-1} \text{ s}^{-1}$  in figure 6.25 which corresponds to an estimated ion mass of 800 u), the overall shape of the DIA is roughly preserved. Similarly to the simulation results with modifications of the electrode geometry, the dependence of the DIA on the ion mobility appears to be generally linear, without significant discontinuities.

Due to uncertainties of the estimation of the ion mobility from the ion mass or chemical effects as for example clustering of the analyte ions, the ion mobility is often only relatively roughly known. Due to the linear response of the DIA to the ion mobility, even a rough estimation of the ion mobility appears to be sufficient for at least qualitatively valid DIA simulations. Since pyrene was used as analyte, which is chemically comparably inert with respect to clustering reactions due the strongly delocalized positive charge in the extended molecular ring system, the ion mobility is probably relatively well estimated in the presented simulations. In combination with the relative low sensitivity of the simulated DIA to the ion mobility, it appears to be unlikely that a wrong mobility estimation is the primary cause for the deviations between the presented experimental and simulation results.

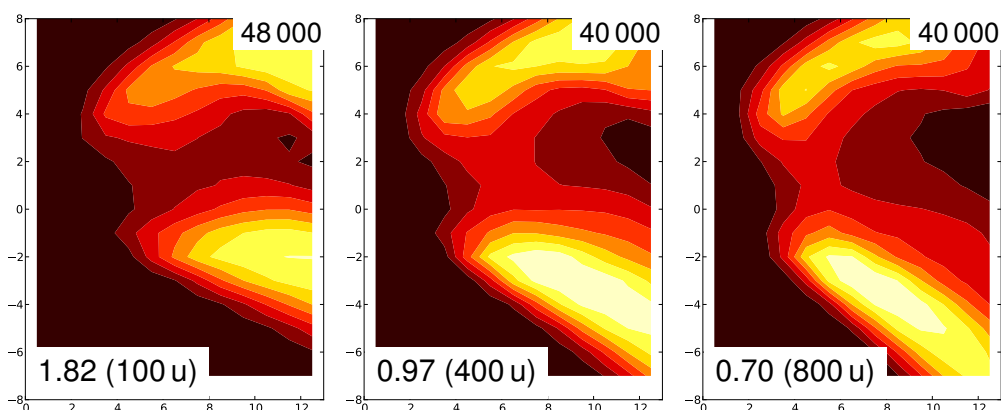


**Figure 6.25:** Simulations of the DIA with different ion mobilities. The calculated reduced ion mobility  $K_0$  (in units of  $10^{-4}\text{m}^2\text{V}^{-1}\text{s}^{-1}$ ) and the ion mass is given in the insets. The dry-gas flow was  $2.0\text{L min}^{-1}$ , the capillary voltage was  $2000\text{V}$ , the spray-shield voltage was  $50\text{V}$ . The level of maximum signal (brightest contour level) is given above each plot. The spatial axes are given in mm.

### 6.5.4.3 Effect of ion depletion probability

Similar to the ion mobility, the ion depletion reaction as defined in section 6.3.3.2 modifies the ion trajectories. As described in section 6.5.3 and shown in figure 6.21 (particularly in the lower right panel with  $14\text{mm}$  distance between spray-shield and ion start zone), ions which follow a long and “indirect” trajectory contribute significantly to the DIA signal. With increasing depletion rate, the effect of the assumed unimolecular ion depletion reaction imposes an effective limitation of the simulated ion trajectory length, since the destruction probability of the individual simulated particles increases accordingly. Therefore, the consideration of an ion depletion reaction leads to the suppression of ions with indirect trajectories, given a sufficiently fast depletion rate.

Figure 6.26 shows the effects of a variation of the depletion rate constant on exemplary DIA simulations. The results show the effects of the trajectory length limitation by the depletion reaction: With increasing depletion rate constant, the intensity of the DIA drops drastically, since the ions are increasingly destroyed on their way to the MS inlet. Despite the signal loss, the DIA shape changes as well: The signal narrows towards the front into two confined, distinct signal maxima, which mark the region from where direct trajectories to the MS inlet are dominant.

The effect of the depletion probability on the DIA intensity and shape is non linear as depicted in figure 6.26: While the increase of the probability about two orders of magnitude from  $1 \times 10^{-7}$  to  $1 \times 10^{-5}$  (which is the default value of the probability used in the remaining DIA simulations) has only a relatively subtle effect in the simulation

## 6 Simulation of ion acceptance distributions (DIA)

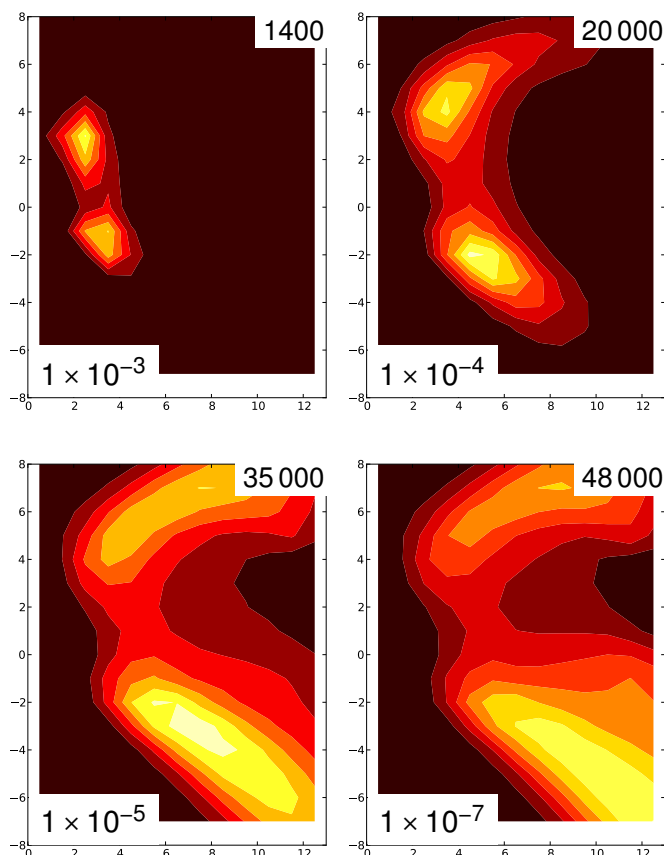


**Figure 6.26:** Simulations of the DIA at different ion destruction rate probabilities which is given in the insets. The dry-gas flow was  $2.0 \text{ L min}^{-1}$ , the capillary voltage was  $1000 \text{ V}$ , the spray-shield voltage was  $25 \text{ V}$ . The level of maximum signal (brightest contour level) is given above each plot. The spatial axes are given in mm.

domain, the increase of the probability to  $1 \times 10^{-4}$  changes the shape of the DIA drastically. With a depletion probability of  $1 \times 10^{-3}$ , another order of magnitude, the DIA signal has almost vanished completely, since in this case only the ions with direct pathway, and eventually only a fraction of them, reach the target zone of the DIA simulation. In contrast, with small ion depletion probabilities, even the most indirect ions reach the MS inlet. Therefore, in this situation the DIA becomes insensitive to the further decrease of the depletion probability, which is also seen in figure 6.26.

A comparison between the experimental DIA measurements and the DIA simulation results shows that the experimental DIA tend to be spatially more confined than the signal distributions predicted by the simulations. A wrongly underestimated ion depletion probability could be one contribution to this systematic deviation. In

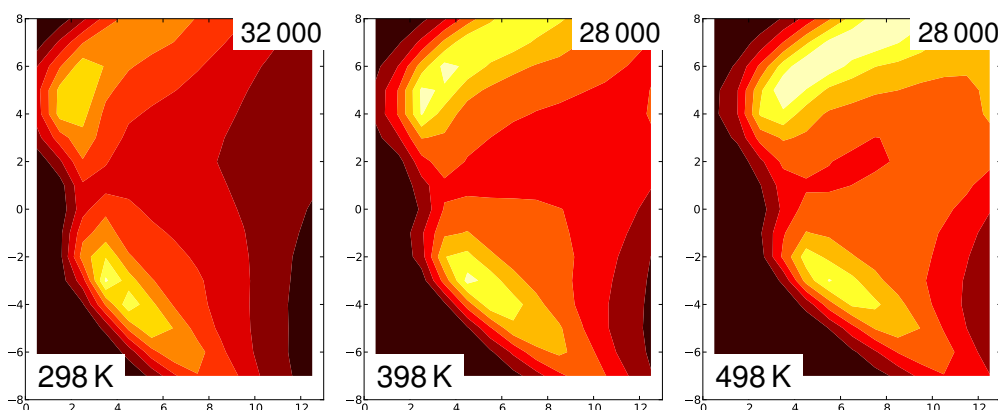


**Figure 6.27:** Simulations of the DIA at different bulk gas temperature which is given in the insets. The dry-gas flow was  $3.8 \text{ L min}^{-1}$ , the capillary voltage was 1000 V, the spray-shield voltage was 25 V. The level of maximum signal (brightest contour level) is given above each plot. The spatial axes are given in mm.

principle it is possible to estimate the rate of ion depletion by systematic comparisons between DIA simulations and measurements. However, since there are probably other effects which potentially lead to a systematic difference between the predicted and the observed DIA shapes (e.g. effects of small scale turbulence in the bulk gas), a systematic assessment of the experimental depletion probability was not performed in this work. As shown by the probability variation, the chosen default value of  $1 \times 10^{-5}$  for the depletion probability has only a relatively gentle effect on the simulated DIA shapes, which most likely do not hinder the observation of other effects affecting the simulated DIA.

#### 6.5.4.4 Effect of bulk gas temperature

Another parameter of the DIA simulation is the bulk gas temperature. It affects the viscosity of the bulk gas, which increases with increasing temperature [8] and therefore also the electric mobility of gas phase ions. Thus, the ion trajectories, and therefore the DIA, are temperature dependent. The bulk gas temperature distribution of the gas flow in the MPIS predicted by the CFD simulation, which is part of the results described in section 6.5.1, but is not presented explicitly in this work, was not considered in the ion trajectory simulation. Instead, isothermal conditions were assumed.

To justify this simplification, a set of exemplary DIA simulations under variation of the bulk gas temperature was performed. The result of this simulation series is presented in figure 6.27. As seen, the increase of the isothermal background temperature about 200 K has a visible but comparably subtle effect on the DIA. The shape of the ion signal response remains surprisingly stable: The positions of the local signal maxima

## 6 Simulation of ion acceptance distributions (DIA)

shift about 2 mm away from the spray-shield with the strong temperature rise. The overall signal intensity is also not particularly sensitive to the bulk gas temperature. In summary, the effect of the bulk gas temperature variation is qualitatively comparable to a gentle increase of the voltage on the spray-shield or the inverse effect of an ion mobility change as depicted in figure 6.25.

As the maximum temperature difference in the bulk gas temperature field of the DIA simulation domain predicted by the CFD simulation is below 100 K, the assumption of isothermal conditions in the DIA simulations is generally justified by the relative insensitivity of the calculation results to the temperature.

### 6.5.5 3d DIA

The analysis of the fully resolved DIA simulation data reveals a relatively complex three dimensional structure of the ion acceptance distribution, which is not discernible in the two dimensional signal intensity projections. Figure 6.28 shows volume renderings of a selected set of three dimensional DIAs. The corresponding two dimensional signal projections are presented in part in figure 6.17 and 6.18.

All volume renderings clearly show the effect of the dry-gas flowing into the ion source by a pronounced, nearly circular, signal minimum around the center axis of the ion source. Here, the clean dry-gas washes out the neutral analyte, as described in section 6.5.1 and shown in figure 6.13, which leads to a complete signal loss from this area. The shape of the signal minimum is not affected by the electrical configuration of the ion source, since this effect depends solely on the neutral analyte distribution: Regardless of the electric potentials, the minimum in the ion acceptance distribution is comparably static. Around the central signal minimum, the DIA extends into the ion source volume, which has a circular or horseshoe like structure in close vicinity to the dry gas flow. The basic DIA structure visible in figure 6.28, with a pronounced asymmetry on the  $y$  (vertical) axis, is also a consequence of the asymmetric bulk gas flow structure in the ion source, namely the nebulizer gas flow. In many of the three dimensional results (e.g., the upper left panel of figure 6.28 with  $2.01 \text{ min}^{-1}$  dry-gas flow, 0 V spray-shield voltage, and 1000 V capillary voltage), the nebulizer gas interaction is clearly observable by a sharp signal drop at the upper ( $xy$ ) border of the DIA simulation domain. The asymmetric DIA structure in close vicinity to the spray shield corresponds to asymmetric vortex patterns generated by the interaction between dry- and nebulizer-gas, which are discussed in detail in a peer reviewed paper by Thorsten Pöhler et al. [96]. The size of the fully resolved simulated ion signal is comparable in all three spatial dimensions, which is an expected result, considering the relatively symmetric structure of the electric field in the MPIS.

The variations of the spray-shield voltage in figure 6.28 reveal that the DIA is not translated away from the MS inlet with increasing potential on the spray-shield. Instead, the distribution transforms entirely and narrows into a cone like shape. In particular with high dry-gas flow ( $3.81 \text{ min}^{-1}$ ), the DIA “flips” in an umbrella motion. Interestingly, the frontal edge of the ion signal around the central minimum, i.e. the

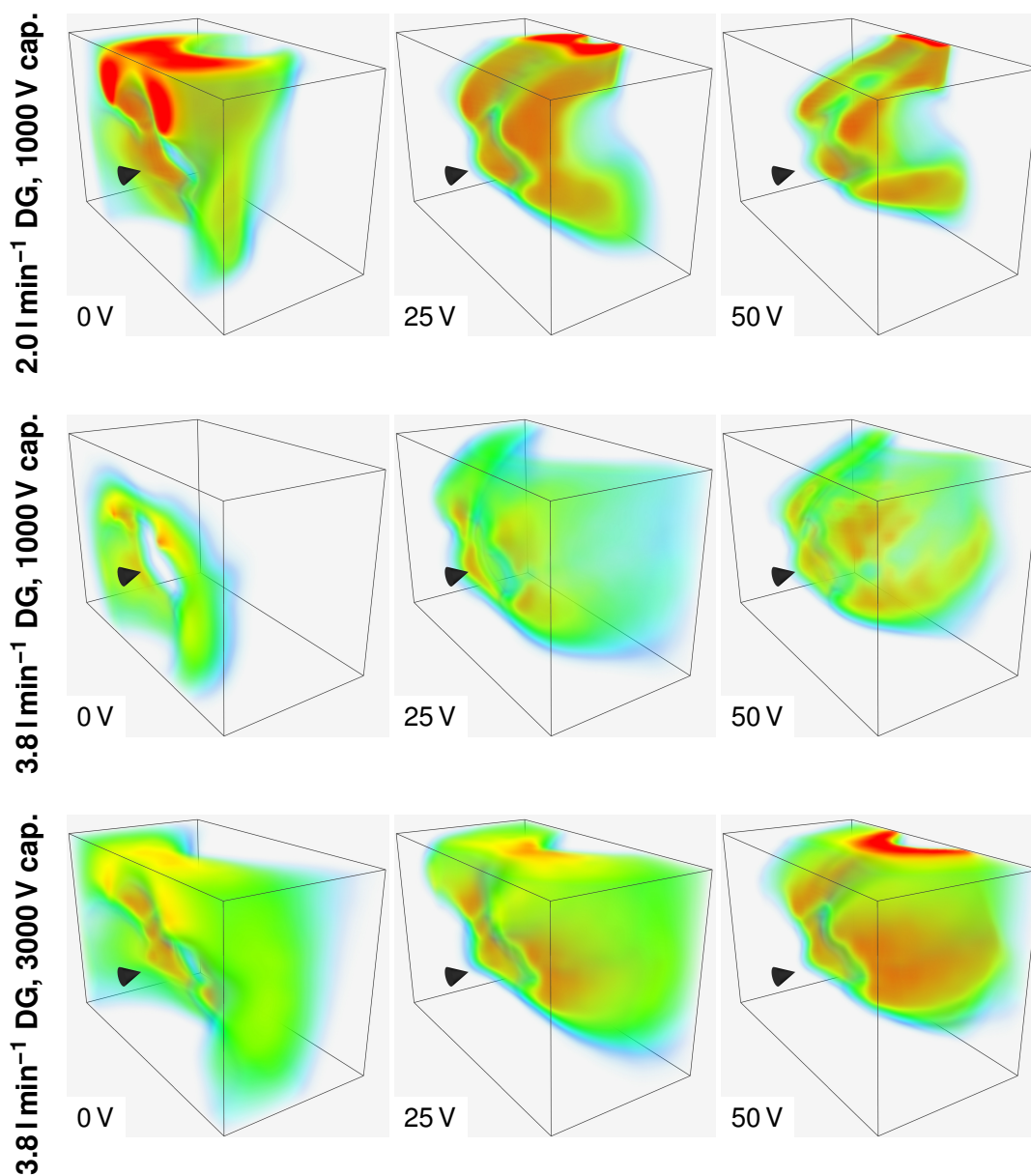


**Figure 6.28:** Volume renderings of a set of DIA simulations resolved in all spatial directions (3d DIA). The dry-gas (DG) flow and the capillary (cap.) voltage is given on the left of each row, the spray-shield voltage is given in the insets. The position of the MS inlet (origin of the coordinate system defined for the two dimensional DIA projections in this work) is marked with the cone. The outline of the DIA simulation domain is marked by the frame.

## 6 Simulation of ion acceptance distributions (DIA)

region from where the most direct signal is expected, is insensitive to the spray-shield potential. The significant shift of the DIA projection with the spray-shield voltage, as seen in figure 6.17 and 6.18 is therefore primarily due to the changes in the outer regions of the simulation domain. The center and lower rows of figure 6.28 show that the basic structure of the DIA is not significantly altered by the variation of the inlet capillary voltage given a potential on the spray-shield. Instead, the signal intensity from the remote areas of the DIA increases. This also contributes, along with the also occurring capillary voltage dependent shift away from the MS inlet, which also is observable in the 3d DIA, to the response of the DIA projection on the capillary voltage.

The variation of the dry-gas flow presented in figure 6.28 has a profound and complex effect on the fully resolved DIA. Generally, the simulated ion signal becomes much more diffuse and less compact with increased dry-gas flow. The top and center row of figure 6.28 show this effect. Notably, the position of the front of the ion signal is not significantly affected by the dry-gas flow variation, which supports the notion of a relatively stable zone from where ions are directly transported to the MS inlet. In summary, the presented three dimensional DIA simulations show that the ion signal is even more complex than suggested by the experimentally determined DIA projections. Thus, it would be worthwhile in future works to independently verify the fully resolved simulations with adequate experiments. Since the presented DIA projection simulations, which are calculated from the fully resolved three dimensional DIA, have achieved a reproducible level of qualitative agreement in comparison to the experimental results, it is likely that the three dimensional results share a similar confidence level. However, an exemplary experimental verification in subsequent works appears to be necessary for a critical assessment of this statement.

### 6.5.6 Ion transfer times

In addition to the spatially resolved ion signal intensity, the temporally distribution of the ions reaching the MS inlet, the *transfer time* distribution, provides an additional measure to compare simulation and the experimentally observed ion behavior. Similarly to the spatially resolved measurements, the ionization with pulsed laser light at atmospheric pressure (APLI) allows the direct observation of ion transfer times, because it provides spatially and temporally well defined “ion packages”. Even if the principle of transfer time measurements with APLI, direct observation of the times between ion generation and detection, is relatively simple, the technical realization with the used commercial instrument is rather elaborate.

Matthias Lorenz has developed an experimental setup for the determination of ion transfer time distributions. The detection principle, technical details and an exemplary set of transfer time measurements are found in his comprehensive PhD thesis [98] in addition to conference contributions [145, 147]. The measurement principle incorporated the manipulation of the timing of the pusher pulses of the microTOF instrument with a variable delay between laser pulse and start of the pusher

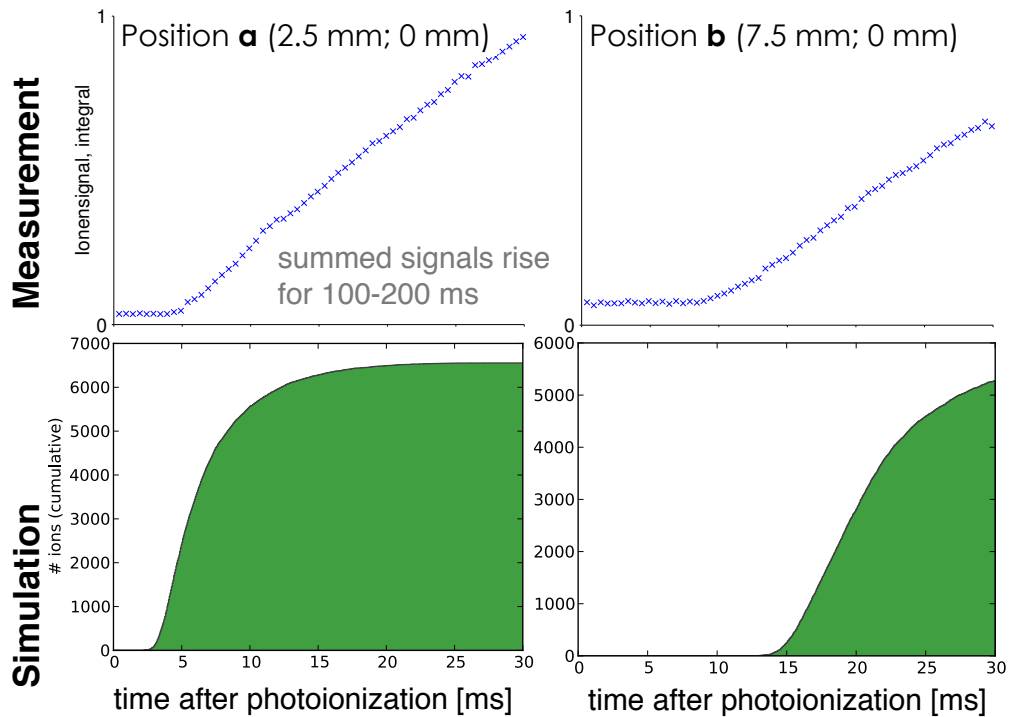
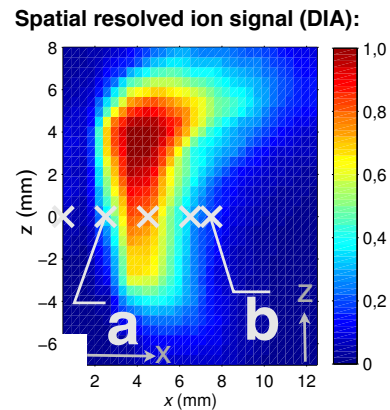


**Figure 6.29:** Comparison of experimental and simulated temporally resolved cumulative (integral) ion signal for two spatial positions ( $a, b$ ) in the DIA. The experimental data were taken from the thesis by Lorenz [98]. Note that the experimental cumulative signal rises for at least 100 ms, which is clearly not reproduced by the simulations, which show maximal ion transfer times in the range of 30 ms.



pulse sequence. The temporal ion signal distribution was measured in a summed (integral) way. Instead of the intensity of the ion signal in dependence of the time, the experiments record the sum of the detected ions since the laser pulse in dependence of the time.

Figure 6.29 shows the results of such measurements for two spatially positions on the center axis of the ion source. Both signals follow the same pattern: After an initial phase without ions reaching the detector, an essentially linear rise of the summed ion signal is observable in the recorded time frame of 30 ms. As noted in the figure, this signal rise is experimentally observed for at least 100 ms, in many cases even

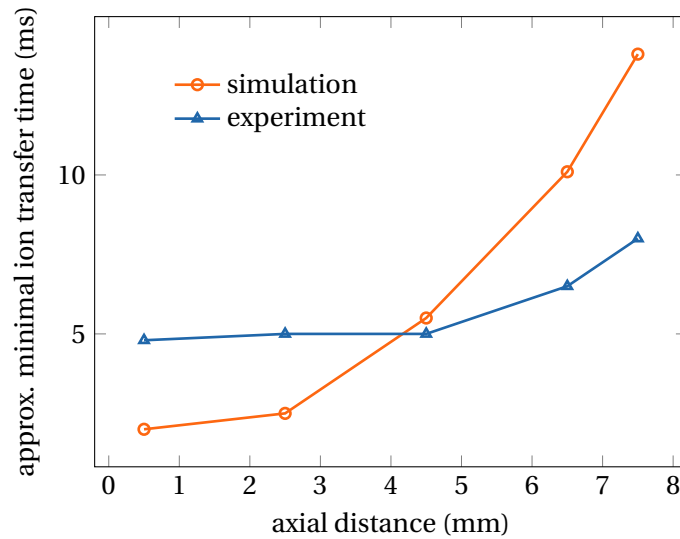
## 6 Simulation of ion acceptance distributions (DIA)

significantly longer. It follows that the “pulse” of ions reaching the detector after laser irradiation is surprisingly broad and has a temporal width in the range of at least 0.1 s. In fact, in the standard operation mode of APLI with laser pulse frequencies in the range of 100 Hz, the temporally resolved ion current becomes almost stationary since the individual wide ion pulses merge [98, p. 84-88]. Since there are no elements in the transfer stage of the mass spectrometer between ion source and detector which lead to such long ion dwell times, the cause for the wide ion signal is likely located in the ion source.

The experimentally observed temporal behavior of the ion signal is not reproduced by the ion trajectory simulations. The simulated integral ion signal has rise times in the range of 10 to 50 ms as shown in figure 6.29. Thus, the simulated ion pulse is significantly, upto one order of magnitude, shorter than the experimentally observed. This is surprising, since the ion signal intensity distribution is qualitatively well reproduced by the numerical calculations.

A second notable feature of the measured temporally resolved ion signal is the delay between photoionization and the initial rise of the integral ion signal, which directly corresponds to the dwell time of the fastest ions in the ion source. For two exemplary positions in the ion source figure 6.29 shows that this delay depends strongly on the ionization position and generally tends to rise with the distance to the MS inlet. This is demonstrated in figure 6.30 for all five spatial positions marked in the DIA of figure 6.29. The simulated cumulative ion signals exhibit qualitatively the same behavior: Even the fastest simulated particles have a notable dwell time in the ion source which leads to a similar position-dependent delay between the time of ion generation and begin of the ion signal rise. Even if this observation is reproduced by the simulation, the length of this delay is not predicted correctly. Figure 6.30 indicates that the ion dwell time is roughly in the same range as in the experimental measurement, but the distance dependence is not well predicted by the calculation. The trajectory simulation predicts a generally higher sensitivity of the dwell time on the distance to the MS inlet than observed in the experiments.

A comprehensive analysis of all spatial positions reveals that the simulation predicts comparably short mean ion transfer times in the entire simulation domain. Figure 6.32 depicts the spatially resolved mean ion transfer times along with the DIA for a subset of the simulation runs presented in figure 6.28 and partly in figure 6.18. The mean transfer times are mostly well below 50 ms which is a clear contradiction to the experimental results. Therefore, the presented simulations generally miss an effect which induces significant broadening of the transfer time distribution in the MPIS. One possible explanation may be the assumptions made in the CFD calculations which the trajectory simulations are based on. As carried out in section 6.3.1, the fluid dynamic simulations assumed a *static* flow field, which is probably an over-simplification of the actual conditions in the ion source. The individual frames of the PIV experiments, which were used to verify the static CFD simulations, suggest that the gas flow in the MPIS in fact oscillates, in particular in the relatively turbulent mixing zone of the nebulizer and dry-gas flow. The individual simulated ion trajectories presented in



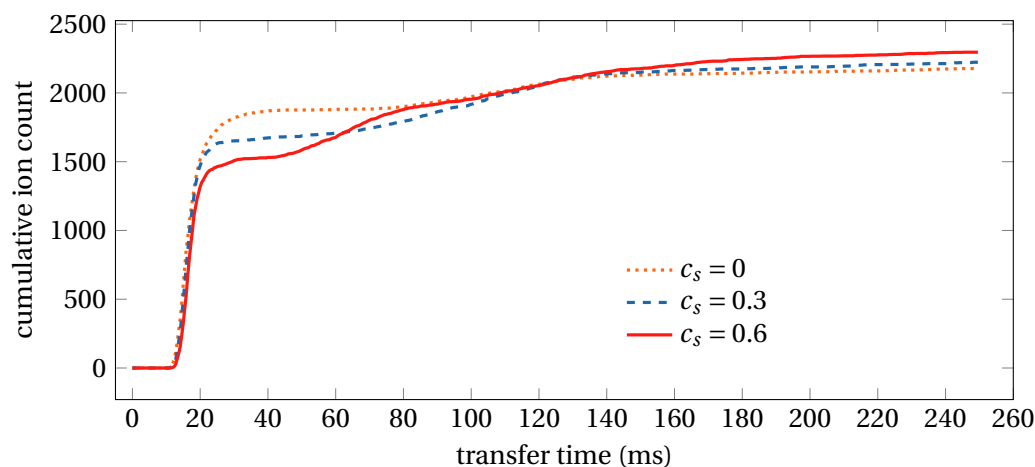
**Figure 6.30:** Comparison of experimental and simulated minimal ion transfer times: The range of the numerically and experimentally observed minimal transfer times are in the same range, but the slope of the ion transfer time in dependence on the axial distance is not correctly predicted by the DIA simulations.

figure 6.21 show distinct regions where the fluid dynamic forces overcome the electric forces and vice versa. Like a drainage divide, this leads to a sharp border between ions which terminate immediately at the MS inlet and ions which are transported into the ion source volume. Since one of the forces in the underlying force balance is the viscous interaction with the bulk gas flow, this “ion divide” also oscillates with the flow fluctuations. In this situation, ions which would never had reached the MS inlet in the simulation because they never get on the right side of the static divide, could be indeed sampled by the MS because the divide oscillates in fact with time. This notion was already carried out with additional graphics in a conference contribution [149]. To support it, an experimental set of simulations was conducted, in which the bulk gas velocity vector  $\vec{V}$  was oscillated with a simple sine function

$$\vec{V} = \vec{V}_0 + \vec{V}_0 c_s \sin(tc_f) \quad (6.1)$$

with the unmodified velocity vector  $\vec{V}_0$ , a scaling constant  $c_s$ , a frequency constant  $c_f$  and the time  $t$ . Figure 6.31 shows the result of the bulk flow modification. Even with a relatively strong artificial flow oscillation defined by a scaling factor of  $c_s = 0.6$ , the experimentally observed temporal ion signal is not fully reproduced. Nevertheless, the temporal ion distribution changes in the intended direction: The fraction of ions with long transfer times increases notably, and the distribution becomes slightly smoother beginning with 80 ms transfer time. However, reliable conclusions require further ion

## 6 Simulation of ion acceptance distributions (DIA)



**Figure 6.31:** Effect of an artificial oscillation of the bulk gas flow: The ions were started at position  $b$  in figure 6.29. Even with a high scaling factor of  $c_s = 0.6$ , the experimentally observed temporally resolved ion signal is not reproduced, but the fraction of ions which exhibits long residence times increases notably.

trajectory calculations based on validated instationary flow simulations or measured instationary flow fields, which was not available for this work.

A detailed temporal analysis of the spatially resolved simulation data sets show that the mean ion transfer time is always well below 100 ms. This is depicted for two DIA simulations in figure 6.32. This analysis also reveals that the mean ion transport times exhibit no clear correlation to the signal intensity or the ionization position. Nevertheless, even in relative remote zones near to the border of the simulation domain the transfer time changes notably, e.g. with the electric potentials in the ion source. Despite the difference between simulation and experiment, this observation underlines the high complexity of the DIA genesis. Figure 6.33 shows a similar spatially resolved analysis of the simulated minimum ion transfer times. In contrast to the mean ion transfer times, the minimum transfer times expose a systematic correlation with the spatial position: The greater the distance between ionization position and MS inlet, the longer the minimum transfer time, even when the slight asymmetry of the distribution in the vertical ( $z$ ) axis is considered. This suggests that from every start region of the simulated two dimensional DIA projection, some ions immediately reach the MS inlet. Furthermore, there is no direct correlation between the shapes of the signal intensity and the minimal transfer times distribution. Additionally, the distribution of minimum transfer times is often relatively insensitive even to notable changes of the DIA shape, which is shown for example in the lower row of figure 6.33. This result in particular was also observed experimentally [98, p. 140]. Therefore,

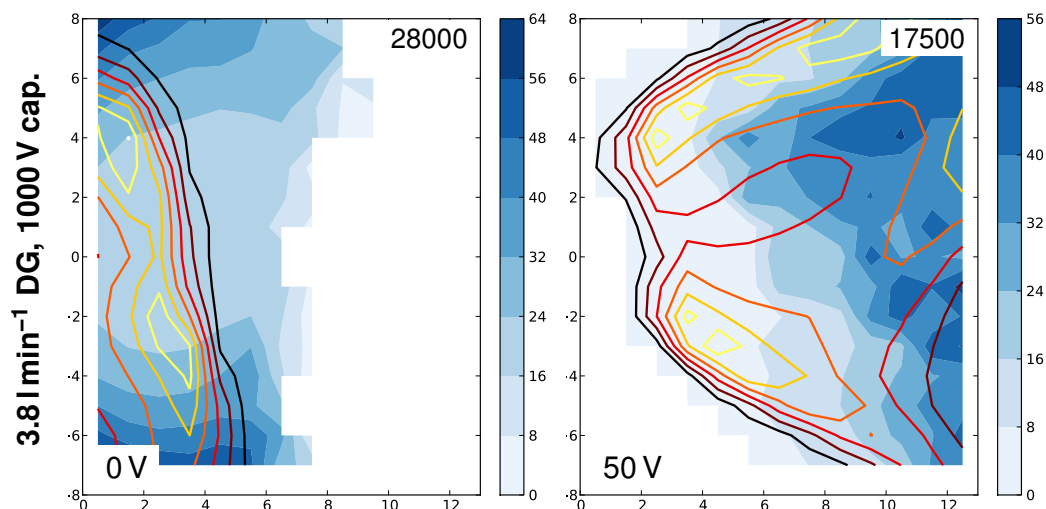


**Figure 6.32:** Two dimensional projections of spatially resolved mean ion transfer time in ms (filled contours in blue shades) and the corresponding DIA (black to yellow shaded line contours) for 0 V and 50 V spray-shield voltage. The maximum DIA value is given in the upper right insets. Missing (white) areas in the mean transfer time image indicate regions with no ion intensity.

in contrast to the mean ion transfer times, the agreement between simulation and experiment is notably better regarding the minimum ion transfer times. In summary, the DIA simulations strongly support the notion that in the MPIS the ion transfer time distribution is not reflected by the position of a local maximum in a spatially resolved mass signal, which was proposed earlier for a different AP ion source [150].

## 6.6 Numerical Costs

The computational power required for the fast generation of DIA calculations is available on advanced consumer class computer hardware. A typical DIA simulation with a spatial resolution of  $13 \times 12 \times 16$ , which results in roughly 2500 data points, takes a couple of hours runtime on a single core of a common server grade processor (*Intel Xeon E5530*). The typical upper limit of the simulated particle number per DIA data point was 5000. Due to the scaling of the simulation particle number with the concentration distribution of the neutral analyte, a typical total simulation particle number in the range of  $1.5 \times 10^6$  to  $2.0 \times 10^6$  results. This combination of simulation particle number and DIA data point number reflects a tradeoff between simulation runtime, spatial resolution, and statistical validity. However, with increasing computational performance, it is feasible to significantly increase the total number of simulated particles. If space charge is not considered as in the presented calculations, the DIA simulations

## 6 Simulation of ion acceptance distributions (DIA)

can readily be parallelized on multiple processors and processor cores. This is straight forward because the trajectory calculations of the individual simulated ions are independent from each other. Thus, the presented DIA simulations would scale well on

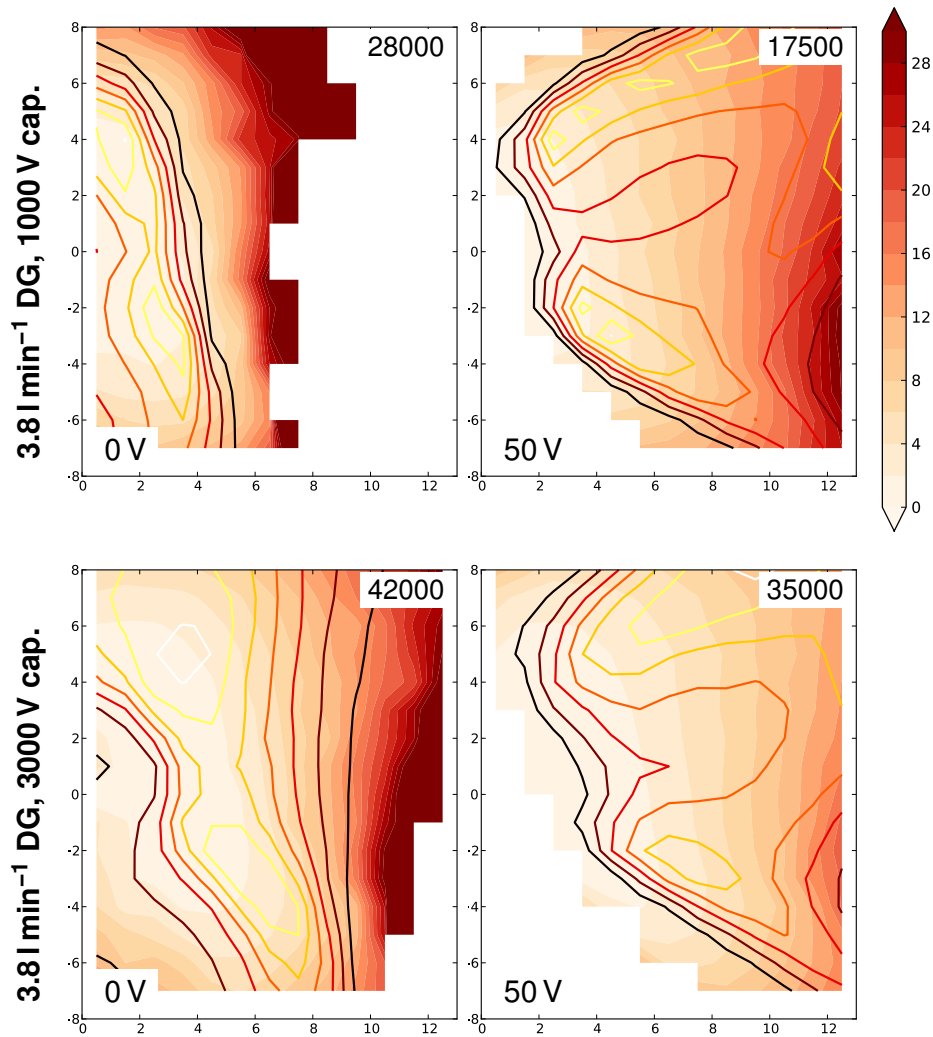


**Figure 6.33:** Two dimensional projections of spatially resolved *minimal* ion transfer time in ms (filled contours in orange shades) and the corresponding DIA (black to yellow shaded line contours) for 0 V and 50 V spray-shield voltage. The maximum DIA value is given in the upper right insets. Missing (white) areas in the mean transfer time image indicate regions with no ion intensity. Note, that the upper contour of the transfer time contains all values above 28 ms.

a multiprocessor computer architecture, even if this type of parallelization was not implemented for this work due to time constraints. The announced revision of the particle tracing code in SIMION, which will include also a parallel implementation of the particle tracing algorithm and the replacement of the internal Lua interpreter with a just in time compiler for Lua (luajit) will probably increase the performance of the DIA simulations significantly. If space charge is considered in the ion trajectory simulations, the numerical effort increases considerably. With the existing implementation of coulomb repulsion simulation in SIMION, which is based on an explicit summation of the electric forces acting on the simulated particles as described in section 3.3.2, a DIA simulation with activated coulomb repulsion calculation is not feasible. A test simulation with reduced spatial resolution took about a month to finish which shows that the runtime behavior of  $\mathcal{O}(N^2)$  of the available implementation clearly renders the coulomb repulse simulation impractical. However, as already stated in detail in section 3.3.2, with more efficient approximation algorithms, as the Barnes-Hut method, a strong improvement of the simulation performance is estimated. In combination with an optimized implementation of the algorithm, in particular for highly parallelized computing hardware, the consideration of coulomb repulsion becomes technically possible on affordable advanced consumer class hardware, even for the relatively high number of simulated particles in DIA calculations. The consideration of the inter-particle electrostatic forces requires the exchange of information between the individual particle trajectory calculations. Therefore, the individual calculation processes are not independent in this case, and efficient ways to minimize the inevitable overhead for this information exchange has to be used. The simulation of all space charge effects, including the effect of the space charge density on the present electric field, require more advanced methods, e.g., particle in cell methods as also briefly described in section 3.3.2. Given an appropriate implementation of such an algorithm, even calculations including all space charge effects become feasible on affordable hardware.

## 6.7 Conclusions

The presented calculation results show that, if appropriate and valid flow dynamic input data is available, ion trajectory simulations under complex fluid dynamic conditions, and therefore DIA simulations, are possible. With the achieved level of agreement between numerics and experiment in terms of the spatially resolved ion signal intensity, the calculations are able to qualitatively reproduce most distinct features of the experimentally observed DIA. Examples are the shape of the DIA, the location and size of noticeable local signal minima, and the effect of ion source parameters on the DIA. In particular, the qualitative effects of variations of the electrical ion source parameters, i.e. the inlet capillary voltage, and spray-shield voltage, are well reproduced by the simulations. Compared to DIA measurements, numerical simulations of the ion acceptance distribution provide detailed information about the dynamics in the

## 6 Simulation of ion acceptance distributions (DIA)

AP ion source, which would be difficult if not impossible to be obtained solely from experiments. The analysis of the pronounced local minimum in direct proximity to the spray shield and the minimum along the center axis of the two dimensional DIA demonstrates this: The combination of CFD model and ion trajectory simulation allow to investigate the ion dynamics for the identification of the causes of both minima. The presented three dimensional DIA demonstrate also the value of the numerical DIA calculations. The experimental determination of fully resolved three dimensional DIA requires two color REMPI ionization. Therefore, it is experimentally and technically demanding and was thus not yet realized. In contrast, the presented calculated DIA data give at least a good qualitative insight in the three dimensional structure of the ion acceptance. Since the two dimensional DIA projections directly result from the three dimensional data, the level of agreement between the three dimensional simulation results and the three dimensional ion acceptance distribution is comparable to the agreement in the two dimensional case.

The analysis of the temporally resolved ion signal reveals that the simulation also qualitatively reproduces the experimentally observed minimal ion transfer times. While the, experimentally demanding, temporally resolved measurements were carried out for a small number of sampled positions, the simulations give insight in the systematic structure of the distributions of the minimal transfer times. In contrast, the mean transfer times and the width of the temporal ion distribution is significantly underestimated by the simulations. Even the presented simulations with intensive artificial oscillation of the bulk gas flow field do not agree well with the experimental data. Obviously, the simulations miss an effect which leads to significant temporal dispersion of the ions.

There are some candidate mechanisms possibly leading to such effects, which should be evaluated in subsequent work: Firstly, the conducted simulations with activated artificial bulk flow oscillation (section 6.5.6, figure 6.31) suggest only a relative subtle scale of the proposed influence of large scale bulk gas flow oscillations with a comparably low frequency [149]. Nevertheless, this simplified approach could wrongly underestimate the actual effects. They could be amplified for example by an unexpected amplitude of the flow oscillation or by the specific geometric structure of the flow oscillation in the experiment which is not reproduced by the artificial isotropic modification of the gas velocity vectors presented here. Further investigations of the actual effect of large scale flow oscillation, require valid instationary fluid dynamic data, either a non-static CFD simulation or measured data as input for the ion trajectory simulation. The SDS algorithm implementation, which originally expects a static flow field, needs to be modified for this type of input data. This is readily possible and was already demonstrated with a simple test case.

In addition to large scale oscillations and fluctuations of the bulk gas flow, small scale turbulence induces an increased *turbulent* diffusion of gas phase particles. This additional diffusion, which is typically much larger than the molecular diffusion, could also contribute to an increased temporal distribution of the ions. The turbulent diffusion is linked to the turbulence of the bulk gas flow, which is probably non-static

and spatially not isotropically distributed. In principle, when CFD input data are used, information about the flow turbulence can be determined from the parameters of the employed turbulence model. Considering the available numerical performance today, such a turbulence model has to be used, since the broad spectrum of turbulence features can currently not be resolved numerically in general [21, 151]. Typical parameters of turbulence models are *turbulent kinetic energy*, which indicates the magnitude of turbulent energy and a scale parameter, which is a measure of the size of the turbulence features in the flow. In principle it should be possible to determine the turbulent diffusion of the simulated ions from similar turbulence model parameters, but this connection for the investigated gas phase ions not known yet, probably complex and specific to the used turbulence model. Nevertheless, subsequent work should investigate this topic to derive at least a simplified model of the turbulent diffusion of ions at atmospheric pressure.

A third potential contributor to the experimentally observed temporal dispersion of the ions is space charge. As already stated in section 6.6, the consideration of the coulomb interaction between the ions and even the consideration of the field interaction of the space charge distribution is technically possible on available computer hardware. However, due to the relatively low charge density in spatially resolved APLI experiments, space charge effects most likely play only a minor role for the observed increased temporal ion dispersion.

Further subsequent improvements of the DIA simulations could include the consideration of chemical reactions of the ions. The next sections will show that the simulation of the chemical reaction dynamics of gas phase ions is possible if the kinetic parameters of the reaction systems are known. In the presented DIA experiments, a chemically inert system was deliberately chosen to suppress chemical reactions of the ions. Nevertheless, there are DIA measurements in a different AP ion source, which show a significant difference between the spatially resolved signals of species which are generated by different chemical pathways [98, 150]. Appropriate ion trajectory and DIA simulations could serve as useful tool to investigate the mechanisms leading to this experimental finding.

Finally, probably one of the next steps for the further development of the DIA simulations is the application of the developed simulation technique on new ion source geometries. A modified version of the MPIS, which was developed to minimize the residence time of the neutral analyte by an optimized bulk gas flow, was already examined with DIA measurements [144]. The determination of a valid flow field for this geometry and a series of DIA simulations based on it would most likely allow to significantly improve the understanding of the dynamics in the new ion source and would provide more experience with the presented simulation method. Similarly the investigation of chemical ionization sources including gas phase discharges as primary charge generating source and the various modern spray sources, as electrospray (ESI) or heated electrospray (HESI) for example, with DIA measurements would provide many new opportunities for useful applications of the presented simulation technique.

## 7 Simulation of reacting ions at AP

At elevated gas pressures, the interaction of ions with components of the background gas gains relevance due to the increasing collision frequency as presented in the introduction in chapter 2. Depending on the reactivity of the colliding particles, the collisions can lead to chemical transformations of reactive gas phase ions. The dynamics of such reactions is described by basic chemical kinetics which is introduced in section 2.3. Chemical transformations become particularly important at atmospheric pressure. This is due to the very high number of collisions which lead to a high number of potentially reactive collisions, even with species which are present only in comparably low concentrations. In addition, ion-neutral reactions are often very fast or even collision controlled [152, 153]. In combination with the often long residence times of ions in potentially chemical reactive environments, e.g., an AP ion source chamber, which contains relatively high amounts of water and similar species as for example LC solvents, in many systems chemical reactions dominate over the transport and dynamics of analyte ions. APCI is an illustrative example. Here, the neutral analyte is ionized by a complex cascade of chemical reactions, starting with fast electrons in a discharge region. While this example marks certainly an extreme in terms of complexity for a model, which considers all occurring physical and chemical phenomena, even apparently much simpler systems can be dominated by chemical kinetics. Therefore, a comprehensive numerical model has to incorporate an appropriate description of chemical reactions and kinetics to be applicable for such chemically active systems which are probably the vast majority of the analytically and technically interesting problems.

In this chapter, a basic numerical model for the description of chemical reactions and its integration in the existing ion trajectory simulations with SIMION/SDS is presented. This model implementation, referred to as *Reaction Simulation* (RS), is then applied to a benchmark problem, the simulation of a Reactive Ion Peak (RIP) in atmospheric pressure ion mobility spectrometry (AP-IMS) which consists of proton bound water clusters. The detailed analysis of the simulation results and the comparison with experimental data allows to assess the validity and limits of the simulation approach, which in turn allows the appropriate usage of RS in further simulation tasks.

## 7.1 Reaction Simulation (RS), a monte carlo model for chemical reactions

As described in the introductory chapter in section 2.3, the temporal description of chemical reactions by chemical kinetics result in ordinary differential equations. For a system of chemical reactions under the consideration of spatially non isotropic conditions, the generalized convection and diffusion equation (eq. 2.17) has to be coupled with the system of reaction equations. This yields a system of partially differential equations, which are numerically solved by the same methods as described in section 3.2, e.g., FEM or FVM approaches. Similarly to the simulation of ion migration under the influence of electrical and viscous interactions, chemical reactions can be alternatively also numerically modeled by a Monte Carlo approach. In this case typically the individual reaction events of a statistically significant number of test particles are explicitly modeled. Despite the higher mathematical elegance of the continuous approach, a Monte Carlo model has particular advantages: Due to the comparably simple mathematical approach, it can be readily implemented, and even relatively complex interactions between individual simulated particles can be modeled without the requirement of a mathematical model in terms of differential equations. In contrast to the solution approaches for PDE problems, the described Monte Carlo approach is in general numerically stable. Often, Monte Carlo simulations exhibit a comparably poor numerical performance which frequently renders the simulation process impractical for actual simulation problems. They generally do not diverge in the sense as finite element or finite volume methods potentially do, which then results in no solution at all. Finally, a particle based simulation method is readily combined with a particle based ion trajectory simulation method as SIMION/SDS. The combination of a differential equation based description of the chemical kinetics with particle based simulations is generally feasible, but a similar and consistent simulation approach for chemical kinetics and ion trajectories is much simpler to implement and maintain. In addition, the results from a particle based simulation method are more conceivable for physical chemists and mass spectrometrists.

In this section, a new Monte Carlo model, referred to as Reaction Simulation, is presented, which was developed to allow the comprehensive simulation of reactive ions at elevated background gas pressure.

### 7.1.1 Linearized reaction probability model

As mentioned above, a straight-forward approach to simulate the chemical reactions of gas phase ions is to calculate the individual reaction events of a statistically significant set of simulated particles. In this sense, such a simulation follows the “chemical trajectories” of the individual simulated particles, similar to a particle tracing simulation, which calculates for example the spatial trajectories of ions in the gas phase.

Given a set of chemical reactions  $\mathbf{R}$  and the set  $\mathbf{C}$  of all chemical species occurring in the reactions, there is a subset of reactions  $\mathbf{R}_i$  for every individual chemical species,

## 7 Simulation of reacting ions at AP

$c_i \in \mathbf{C}$ , where  $c_i$  is part of the reactant side of the reactions in  $\mathbf{R}_i$ . Further given an arbitrary set  $\mathbf{P}$  of simulated particles  $p_j \in \mathbf{P}$ , which undergo reactions from  $\mathbf{R}$  and a chemical identity  $c_j \in \mathbf{C}$ . To simulate the chemical transformation of an individual particle  $p_j$  with a chemical identity  $c_j$  at a simulation timestep  $t_k$ , first the local reaction probabilities  $\Phi_{k,j}$  for all reactions in the reaction subset  $\mathbf{R}_j$  of  $c_j$  are calculated for the local conditions. Then a random process decides if and which reaction actually takes place based on the calculated probabilities. This procedure is repeated for every simulated particle in every timestep of the calculation. If the number of particles is sufficiently high and the time steps are appropriately small, a physical ensemble of particles can be statistically described by this method.

If  $\mathbf{R}$  consists only of reactions with only one reaction partner which is modeled explicitly as particle, which essentially means that all reactions can be considered first order, obviously no potentially reactive collisions between the simulated particles have to be considered. Then, the calculation of  $\Phi_{k,j}$  becomes independent from the state of the remaining simulated particles. The calculation of the individual reaction probability  $\phi_r$  in  $\Phi_{k,j}$  of the, in this case first order, reaction  $r$  from the set  $\mathbf{R}_j$  becomes comparably simple. For sufficiently small time steps the reaction probability is approximated by

$$\phi_r = \prod_i (\gamma_{i,r}) k_r \delta t \quad (7.1)$$

with the concentrations of static background reaction partners occurring on the reactant side of  $r$ ,  $\gamma_{i,r}$ , the reaction rate constant  $k_r$  of the reaction, and the time step length  $\delta t$ .

Section 9.2 of the appendix shows that this simple linearized function, which would inevitably reach unreasonable probability values  $> 1$  for longer time steps, approximates the actual reaction probability distribution of unimolecular reactions for short times. For bimolecular reactions, with two simulated reactant particles, a similar linear approximate function for the reaction probability is derived as also presented in section 9.2 of the appendix. However, as already implied, the calculation of bimolecular reactions require the explicit simulation of the collisions between simulated particles, which generally involve the explicit calculation of inter particle distances in the model. Therefore, the calculation of bimolecular reactions requires in principle a solution for the same problem as the calculation of the coulomb interaction between the particles, including a similar effect on the numerical performance of the simulation process. In addition, the numbers of the simulated particles of the individual chemical species have to reflect the actual concentrations in the physical experiment, which may become challenging, e.g., if one species is present in a vast excess. In such cases, the required number of simulated particles to gather meaningful results from such a calculation can readily render the simulation impractical. Finally, the simulated collision cross section of the particles has to be determined appropriately to reflect the actual physical conditions in an experiment. In the unimolecular case all molecular collision cross sections are part of the reaction rate constant  $k_r$ ; in the bimolecular case the collision rate has to be explicitly calculated by the Monte Carlo simulation. Since the

### 7.1 Reaction Simulation (RS), a monte carlo model for chemical reactions

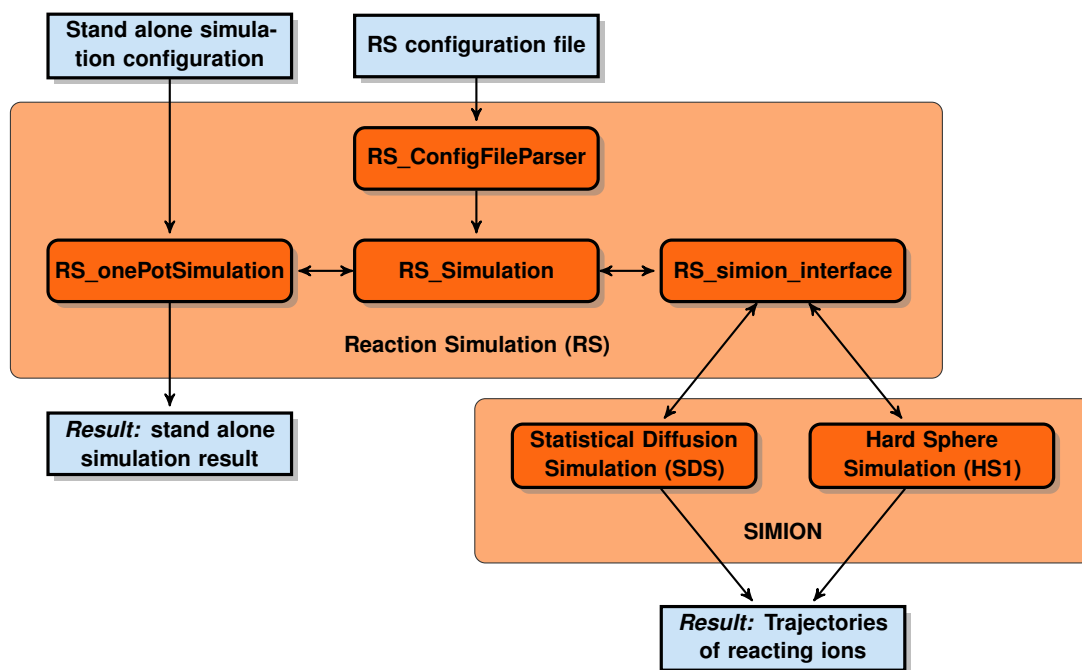


**Figure 7.1:** Schematic overview of the RS algorithm

definition of the bimolecular collision cross section in the simulation is dependent on various parameters, e.g., the ratio of the numbers of simulated and physical particles of a specific chemical species, the calculation of bimolecular reactions requires a significantly higher effort as reaction systems strictly consisting of unimolecular reactions.

#### 7.1.2 RS implementation

The presented simulation approach was implemented in the Lua programming language. This implementation is referred to as RS in the following. Figure 7.1 gives a schematic overview of the modules of RS and the interactions between RS and SIMION.

RS has two operation modes: It can be used stand-alone (“one-pot” mode), without a connection to SIMION. In this case, the spatial trajectories of the simulated particles are not considered, therefore the stand-alone simulation assumes implicitly an ideally stirred reactor, without any concentration gradients present. In the second operation mode, RS is coupled to SIMION via an interface between the chemical simulation and the Statistical Diffusion Simulation (SDS) and Hard Sphere (HS1) collision models of SIMION. This direct interface to SIMION, which makes RS essentially a SIMION user program, motivated the implementation of RS in Lua, since this is the natural

## 7 Simulation of reacting ions at AP

scripting language for SIMION user programs. Both operation modes are controlled by a configuration text file which contains a list of chemical species, represented either by simulated particles with a molecular mass or by a static background concentration of that species, and a list of chemical reactions of the defined species. The reactions are noted in a formal but intuitive way along with their reaction rate constants. Due to the complications of the consideration of bimolecular reactions described in section 7.1.1 and the fact that for the initially intended application of the algorithm, presented in the next section, bimolecular reactions are not relevant, RS is currently limited to first order reactions. Furthermore, due to limitations of the current version of the SIMION user program interface, the presented version of RS assumes a static amount of simulated particles. Thus, processes as ion-ion recombinations or the fragmentation of multiply charged droplets can currently not be modeled with RS.

The simulation configuration is interpreted by the configuration parsing module of RS and is transformed into an abstract representation of the chemical reaction system. Then the linearized Monte Carlo simulation as defined in section 7.1.1 is performed with one significant deviation of the actual implementation from the formal definition given above. To save mathematical operations, RS calculates the reaction probabilities  $\phi_r$  and probes for actual reaction events sequentially. If a reaction event occurs, the chemical identity of the current particle is changed according to the reaction definition, and the probing sequence for this particle in the current time step is aborted. A static order of the reactions in the probing sequence is a potential error source, since individual preceding reactions in the sequence could be unjustifiably preferred. This effect could be leveled by randomizing the reaction probing sequence, which the presented version of RS does *not* do. However, with sufficiently small time steps and therefore low reaction values ( $\phi_r \ll 1$ ), this selection effect becomes less relevant. As presented in the next section, RS correctly reproduces experimental results without probing sequence randomization. Nevertheless, such a randomization measure is a future extension of RS.

In stand alone mode, the number of particles and the maximum time step length are configured by the user with commandline arguments. In this case the result of RS is a table, in plain text format, with the time and the amounts of particles of the individual chemical species as columns. If RS is coupled to SIMION, the number of particles per species is controlled from there by the configuration of the simulated ions. Due to the lack of a freely assignable ion parameter in SIMION, the ion color index, an integer value, is used to represent the chemical identity in SIMION. This has the favorable side effect that reaction events are readily visible in SIMION as color changes. If RS is used in the coupled mode, the chemical reaction simulation is performed for every time step of the SIMION trajectory integration. Thus, the time stepping of RS is also controlled by the configuration of the trajectory simulation in SIMION. The requirements of the chemical simulation and the trajectory calculation in terms of the required maximum time step lengths can differ drastically as presented in the following sections. In the coupled mode, the result of the RS simulation is also written into the simulation record file of the SIMION simulation. RS writes information

## 7.2 Simulation of the proton bound water cluster RIP in AP-IMS

about the parsed chemical reactions and the configuration of the chemical species into the head section of the simulation record file. To allow the monitoring of the temporal development of the chemical system, RS is able to record the amounts of the chemical species into the simulation record in a similar way as in the stand alone mode. The frequency of the samples and duration of this sampling is controlled by user configurable variables.

RS requires a bidirectional connection to the collision model user programs SDS and HS1, since particles generated in SIMION have also to be reflected as particles in the chemical representation of the system, and particular methods of RS have to be called in every time step of the trajectory integration. Therefore, the collision model user programs have to be slightly modified to provide this required backward connection. The first version of RS, providing a connection to the high pressure SDS collision model only, is packaged with SIMION since version 8.1.1.16. This includes the modified but still proprietary SDS code. The non proprietary parts of RS, excluding the modified SDS and HS1 codes, are freely published<sup>1</sup> under an open source license (GNU General Public License version 3<sup>2</sup>). The open source version of RS performs stand alone simulations and due to the quite stable proprietary modules it is generally possible to update the packaged version of RS with more recent versions of the open source version of RS. Therefore, the development of RS is not notably hindered by the fact that it is not possible to freely publish the SDS and HS1 model.

## 7.2 Simulation of the proton bound water cluster reactant ion peak in AP ion mobility spectroscopy

The described chemical reaction model was tested and validated with an appropriate benchmark experiment. As stated in the introduction to chapter 5, an ideal benchmark problem is ideally not too complex and essentially well known, so that the simulation result can be readily assessed in terms of qualitative validity. On the other hand, such benchmark models should require a reasonable level of numerical effort and a minimum calculation complexity allowing the estimation of the numerical performance and the actual technical requirements of the newly developed method. From an experimental standpoint, an ideal benchmark experiment provides clearly quantifiable result parameters, which can also be readily extracted from the raw simulation results to provide direct comparability. Finally, in an ideal case, the benchmark model is also valuable in terms of fundamental science, and the model results can be used in some applied work.

The simulation of chemically active cluster species in IMS represents such a nearly ideal benchmark problem. The chemical system is well known, as shown in the

---

<sup>1</sup>For the public source code repository and a detailed documentation of RS see <http://rs.ipams.uni-wuppertal.de>

<sup>2</sup><http://www.gnu.org/licenses/>

subsequent sections, and the experimental outcome, the spectrum of ion drift times, are easily generated from simulated ion trajectory data.

### 7.2.1 Ion Mobility Spectrometry

IMS is an analytical method which utilizes the specific electric mobility of chemical species,  $K$ , for the separation of analytes [11]. The electric mobility as defined in equation 2.8 is the proportionality between the static drift velocity of ions at a given background gas pressure and the electrical field strength. If the mobility is normalized to the particle density and temperature the *reduced mobility*  $K_0$  results as defined in equation 2.9 [11, 12]. Ion mobility spectrometers are comparably simple instruments: They basically consist of a drift tube with a static uniform electric field gradient. Typically the field gradient is created by a series of ring electrodes, which are connected to a resistor chain connected to the drift voltage on one end and is grounded at the other end of the drift distance. The drift tube is often slowly flushed with clean gas, typically nitrogen or helium, which is referred to as *drift gas* in the IMS context. The pressure in the drift tube can vary significantly between different instruments. Modern systems for routine analytical measurements are generally atmospheric pressure instruments, with drift tubes which are essentially open to pressure equalization with the atmosphere outside the instrument. In this case, the instrument needs a pressure sensor to calculate then pressure dependent reduced mobility, from the measured mobilities.

The ions which are analyzed by the IMS are generated in an ion source region in front of the drift tube. In the case of AP instruments, those ion sources are similar to the systems used in API mass spectrometry. In principle, all API methods [3], e.g., electrospray ionization (ESI), photoionization (PI), laser-multiphoton ionization (APLI), and different types of chemical ionization (APCI), can be used in combination with IMS. In particular APCI, a method in which the analyte molecules are ionized by chemical reactions with primary ions, is widely used in IMS [11]. In contrast to APCI in MS, where the primary ion source is generally a gas phase discharge [3], in IMS often radioactive primary ionization sources are used. Typical electron sources which initiate the reaction cascade leading to the ionization of the analytes are either Nickel ( $^{63}\text{Ni}$ ) [11] or Tritium ( $^3\text{T}$ ). Such radioactive primary sources provide good stability and do not need electrical power to operate, which are the main reasons for their usage in IMS, particularly in portable field measurement systems.

The generated ions are injected into the drift tube as narrow pulses, commonly by an electrical gate of Bradbury-Nielsen type [11, 154]. The ions separate in the drift tube due to their different mobilities and are detected afterwards. The typical detector setup in AP-IMS is a faraday cup or a faraday plate connected to a sensitive current measurement device [11]. The detector plate is generally shielded from inducing effects caused by the approaching ions and interferences from the inlet gate by an additional closely arranged mesh which is held on the local drift potential at that point. Due to the comparably slow temporal gradients of the ion mobility signals, even in high resolution AP-IMS the required rise time of the charge amplifier is in the

## 7.2 Simulation of the proton bound water cluster RIP in AP-IMS

range of 5  $\mu\text{s}$  [155], the signal acquisition is not particularly demanding for modern digital technology. The experimental result of an IMS measurement is the temporal spectrum of the ion current signal often called the “drift spectrum”. Commonly, the data from multiple individual ion injections are computationally combined to a final mobility spectrum. Since IMS is often used in combination with chromatographic pre-separation stages, the data acquisition software of IMS instruments allows to analyze the ion mobility signals in dependence of the runtime of the chromatographic stage of the system. Another application of IMS is the combination with mass spectrometry (IMS-MS). In this case, the IMS drift tube is directly coupled to the inlet stage of a mass spectrometer and adds an additional separation dimension to a mass spectrometric system [156]. This combination, which is commercially available e.g. [157] with a variation of low pressure IMS (traveling wave IMS) [158], is in particular useful for the analysis of biomolecules.

As presented in the introduction chapter in section 2.2.1, the ion mobility becomes a function of the field strength at high-field conditions. Classical AP-IMS generally operates under low-field conditions, since the required field strength to observe high-field effects at atmospheric pressure would be very high, i.e. in the order of  $20 \text{ kV cm}^{-1}$ . This would probably induce complicating electrical effects as for example discharges between the electrodes in the drift-region. A method which in fact uses the difference between the low- and high-field mobility of ions for the separation of ions is *Differential Ion Mobility Spectrometry* (DMS) [159] which is also referred to as *Field Asymmetric Waveform Ion Mobility Spectrometry* (FAIMS) [160]. Here, ions are exposed to a high voltage asymmetric RF field between two electrodes, which results in a transversal drift of the ions if the low- and high-field mobilities differ. This difference between the mobilities of the particle is called *differential mobility* in this context. A DC voltage compensates the transversal motion, so that ions with a given transversal velocity pass through the device. By varying this *compensation voltage* and recording the ion current behind the DMS assembly, a differential mobility spectrum is obtained. The longitudinal transport of the ions is realized by an, often comparably fast, bulk gas flow through the separation region. Since DMS/FAIMS is also a mobility separation method, it has a close connection to IMS. Most of the chemical aspects of IMS discussed in the following can be observed similarly in DMS.

The observed electric mobility of ions is the result of the interactions between the charged particles and the background gas under the influence of the present electric field. Obviously, this interaction depends on the molecular structure of the analyzed ions [12]. If the ions are chemically active and the molecular structure is therefore governed by chemical reactions, the observed electric mobility is also dependent on chemical change. In AP-IMS with chemical ionization, signals of the primary ions of the initial reaction cascade, which are in general chemically very active, are prominent common observations. These *reactant ion peaks* provide therefore a favorable benchmark problem for the assessment of chemical reaction simulation methods as for example RS.

### 7.2.2 Proton bound water-cluster Reactant Ion Peak (RIP)

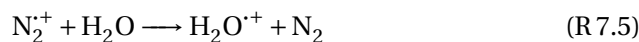
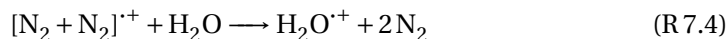
The term *chemical ionization* refers to a method where the charge transfer to the analyte molecule is induced by chemical reactions with primary ions, e.g. electron abstractions or protonation reactions. At atmospheric pressure, the primary ions are formed by a relatively complex chain of reactions, which is initiated by electrons from a physical process, commonly a gas discharge or a  $\beta$ -radiation source [161–164]. The electrons initially have high kinetic energies in the keV region. They thermalize by different mechanisms including stepwise cooling by collisions with bulk gas molecules M:



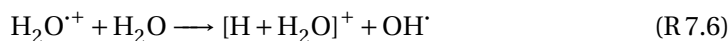
If the kinetic energy has become nearly thermal but is still above the ionization energy of nitrogen, ionization leads to highly reactive nitrogen radical cations ( $N_2^{\cdot+}$ )



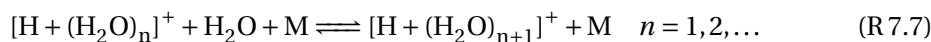
which subsequently react to  $H_2O^{\cdot+}$  radical cations if water vapour is present



Ultimately,  $[H + H_2O]^+$  ions and  $OH^{\cdot}$  radicals are formed by the further reaction with water:



The  $[H + H_2O]^+$  readily form proton bound cluster-ions with additional water, which exist in a dynamic equilibrium [161–163, 165] between cluster formation and destruction reaction:



At room temperature and water mixing ratios of several ppmV, typical values of the cluster size are  $n = 3 - 4$ . In the presented simplified reaction scheme, M denotes a neutral collision partner which is in an ion source of an AP-IMS most likely a nitrogen

## 7.2 Simulation of the proton bound water cluster RIP in AP-IMS

or oxygen molecule. The signal of those proton bound water-clusters, which are also the reagent ions for the ionization of appropriate analyte molecules, is one of the most prominent RIPs in AP-IMS [166]. The governing equilibrium consists of fast reactions: The forward cluster formation reaction of equilibrium R 7.7 is assumed to be in the high pressure limit at elevated pressure, therefore second order and collisionally controlled [152]. Due to the high collision frequency at atmospheric pressure, the reverse cluster destruction reaction also reaches a high reaction rate. Since it is virtually impossible to remove residual water from the drift tube of an AP-IMS instrument with reasonable effort, the minimum attainable water mixing ratio is in the range of a few ppmV. Therefore, the water-cluster system is chemically active also in the drift tube of the IMS. The equilibration time of the water-cluster system is in the  $\mu\text{s}$  range [152, 165], while the typical drift time is in the ms range. As a consequence, it is not possible to resolve the individual cluster species in an AP-IMS: While drifting in the IMS, a protonated water-cluster reacts very often and experiences many cluster growth and destruction events. In fact, considering calculated reaction rates, which are presented in the following, the average time of existence without chemical change of a proton bound water-cluster particle of a given size below  $n < 5$  is only in the 100 ps range. Therefore the whole cluster-system merges to one ion signal with an average mobility, which depends on the mean cluster size  $\bar{n}$ , which is referred to as *water-cluster RIP* in the following.

**Calculation of the rates of the water-cluster formation and destruction reactions** The system of water cluster formation and destruction reactions has been thoroughly studied in the past decades. This resulted in experimentally determined thermodynamic parameters of the the cluster equilibrium R 7.7 for cluster sizes up to  $n \leq 7$  [167, 168], including the reaction Gibbs energies of the clustering steps  $\Delta_R G_{n-1,n}^0$ . To simulate the temporal development of the charged water-clusters in an IMS with SIMION/RS, the individual reaction rate constants of the forward reaction  $k_{n-1,n}$  and the backward reaction  $k_{n,n-1}$  of equilibrium R 7.7 have to be known. In chemical equilibrium, the forward and backward reaction rates are equal, thus the reaction rate constants can be expressed in terms of the equilibrium constant  $K_{n,n+1}$  of the reaction R 7.7 [7, 8]:

$$K_{n-1,n} = \frac{k_{n-1,n}}{k_{n,n-1}} \quad (7.2)$$

The equilibrium constants are calculated from the known free Gibbs energies [7, 8, 165]:

$$\Delta_R G^0 = -RT \ln K \quad (7.3)$$

The forward cluster formation reaction is assumed to be in the high pressure limit and collision controlled for all water-cluster sizes, resulting in a limiting *bimolecular* rate constant of  $2 \times 10^{-9} \text{ cm}^3 \text{ molecule}^{-1} \text{ s}^{-1}$  [152]. With this assumption, the reverse rate constants can be calculated from the experimentally determined thermodynamic data via equation 7.2 and 7.3. The thermodynamic data, estimated equilibrium constants

## 7 Simulation of reacting ions at AP

and reaction rate constants of the water cluster system are presented in table 7.1. Using a chemical kinetics model such as RS with these parameters, the simulation of the described reaction system, and therefore the proton bound water RIP in IMS, becomes feasible.

### 7.2.3 Experimental determination of the water cluster RIP drift time

In cooperation with the *Leibnitz-Institut für Analytische Wissenschaften (ISAS)*, in Dortmund, Germany, the drift time of the water cluster RIP in a common AP-ion mobility spectrometer in dependence of experimental parameters, in particular the mixing ratio of water in the drift gas, was investigated. All experimental data presented in this section were gathered by Luzia Seifert and Wolfgang Vautz at ISAS in Dortmund. The results of the IMS measurements were compared with results from a numerical model of the migration of the reacting water cluster particles. In the following, the experimental setup and the procedures of the IMS measurements are discussed in more detail.

**Ion Mobility Spectrometer** All measurements were performed with a custom built AP-IMS consisting of an APCI ion source including a radioactive primary electron source connected to a Teflon drift tube. The basic setup is also described in publications by ISAS, e.g., in [169] and [170]. In contrast to the common operation of the IMS, the system was used without a chromatographic pre-separation stage. The  $\beta$  radiation source was a Tritium compound with an activity of 500 MBq provided by G.A.S. (Dortmund, Germany). The drift tube machined out of a monolithic block of Teflon, had a length of 121.5 mm and an inner diameter of 15 mm. The 19 stacked ring electrodes, which were mounted at a distance of 5 mm into grooves in the drift tube

**Table 7.1:** Thermodynamic parameters and rate constants for the formation and dissociation reactions for  $[\text{H} + (\text{H}_2\text{O})_n]^+$  clusters. The *termolecular* forward rate constant is considered to be  $k_{n-1,n} = 6.98 \times 10^{-29} \text{ cm}^6 \text{ molecule}^{-2} \text{ s}^{-1}$  for all cluster sizes. The presented data were also published in [165].

Cluster size $n$	$\Delta_R G$ [kJ mol <sup>-1</sup> ] (original data taken from [168])	Equilibrium constant $K$	Cluster dissociation rate constant $k_{n,n-1}$ [cm <sup>3</sup> molecule <sup>-1</sup> s <sup>-1</sup> ]
2	101.70	$5.00 \times 10^{17}$	$4.00 \times 10^{-27}$
3	54.39	$2.95 \times 10^9$	$6.78 \times 10^{-19}$
4	39.75	$8.00 \times 10^6$	$2.50 \times 10^{-16}$
5	23.43	$1.20 \times 10^4$	$1.67 \times 10^{-13}$
6	17.15	$9.70 \times 10^2$	$2.06 \times 10^{-12}$
7	12.55	$1.53 \times 10^2$	$1.30 \times 10^{-11}$

## 7.2 Simulation of the proton bound water cluster RIP in AP-IMS

walls, had an inner diameter of 25 mm and a thickness of approximately 1 mm. A Faraday plate connected to a custom built charge amplifier, which was digitally connected to a data acquisition computer served as detection system. The total voltage drop over the drift distance was 3830 V which resulted in a drift voltage gradient of  $317 \text{ V cm}^{-1}$ . The analyzed ions were gated into the drift tube by a Bradbury-Nielsen entrance gate, which was held open for  $300 \mu\text{s}$  with a repetition time of 100 ms. The drift tube was fed with a constant drift gas counter flow, which was injected at the detector plate and was vented to an exhaust close to the inlet gate. Humidified nitrogen with a variable water mixing ratio was used as drift gas. The preparation of this drift gas and the monitoring of the water mixing ratio is described in the following.

**Water Variation in the Drift Gas** The water mixing ratio in the drift gas was varied with an exponential dilution technique which is presented in [165]. Briefly, a known volume, in this case a glass flask with a volume of 630 ml, is flushed with humid nitrogen with a known water mixing ratio to saturate the container with a defined water concentration. The container is then flushed with dry nitrogen. Due to the dilution of the water content in the container, the mixing ratio of the gas decreases exponentially, which can be calculated. For the presented measurement, a calibration gas generator (*HovaCAL 3834SP-VOC, IAS, Frankfurt, Germany*) provided humidified nitrogen with a water mixing ratio of 2000 ppmV, which served as starting point for the exponential dilution. This mixture was flushed through the glass bottle for two hours to provide a sufficient equilibration of the water content in the flask. The continuous dilution process was then performed with dry nitrogen gas containing residual water of 18 ppmV which was flown through the glass bottle at  $100 \text{ ml min}^{-1}$ . While the exponential dilution, the IMS drift tube was flushed periodically with the resulting gas as drift gas. The time intervals between the flushes were between 10 min for higher water contents in the drift gas and 5 min for lower water mixing ratios. This procedure was chosen to allow proper equilibration of the humidity in the drift tube at higher water mixing ratios. The humidity of the initial gas mixture for the dilution process was validated with a moisture monitor (*Panametrics, Series 35; Hoheim a.T., Germany*). This monitor was also used to measure the moisture of the gas exiting the IMS drift tube.

### 7.2.4 Numerical Models

As described in the introduction, the dynamics of the reactive proton bound water cluster ions was numerically modeled with SIMION in combination with the RS algorithm. In addition to the experimental validation, the results of the RS model were verified with *Chemked* [171], a differential equation solver for chemical kinetics problems. Due to the distinct numerical approach of Chemked in contrast to the Monte-Carlo approach of RS, the comparison of the results from the models allow to independently validate the RS simulations.

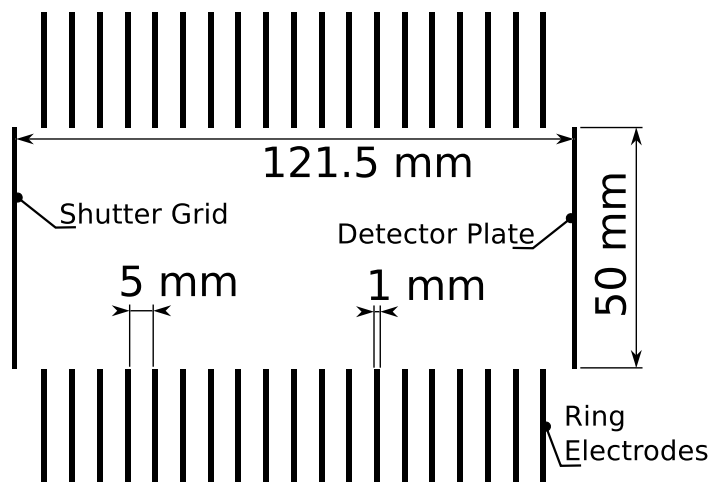


**Figure 7.2:** Schematic of the electrode geometry in the SIMION-RS simulations. The model comprises the migration of the charged water clusters in the drift region of the AP-IMS. The simulated drift tube consists of a series of stacked ring electrodes with a linear potential gradient. The entrance grid and the detector plate are approximated as simple plate electrodes.

#### 7.2.4.1 Simulation of the reacting water cluster ions with SIMION-RS

The migration of the reacting water cluster ions in the drift tube of the AP-IMS was numerically modeled with SIMION (version 8.0.4 [172]) in combination with SDS and RS. The high background gas pressure required the selection of the SDS method as collision model. The bundled version of SDS included with the SIMION package was used with minor modifications for automatization purposes. A simplified electrode geometry, which is depicted schematically in figure 7.2 was used as model of the drift tube. Only the drift region of the IMS was modeled, since the experimental result, the drift time of the water cluster RIP, is governed by the migration of the reacting ions in the drift tube. The dielectrical Teflon body of the drift tube was not explicitly considered and the open space between the electrodes was assumed to be ideal vacuum with respect to the electric field. In absence of significant charging of the Teflon surface, this is justified by the low relative electric permittivity of Teflon ( $\epsilon_r = 2.1$  [173]) and the presence of static electric fields only. The linearly decreasing potential on the individual ring electrodes of the drift tube was calculated from the total drift voltage and controlled by a custom user program which was included in the SIMION simulations.

In comparison to the ion concentration in the experiment, which is limited by the activity of the  $\beta$ -radiation source, the amounts of nitrogen and water in the drift gas are in large excess ( $[[\text{H} + (\text{H}_2\text{O})_n]^+] \ll [\text{N}_2], [\text{H}_2\text{O}]$ ). Therefore, the forward and reverse reactions of the equilibrium in reaction R 7.7 are safely assumed to be first order with

## 7.2 Simulation of the proton bound water cluster RIP in AP-IMS

respect to the ionic clusters. This fact allows to simulate the chemical kinetics of the system of water clusters with the presented version of RS with its model limitations. For the kinetic calculations, the set of rate constants as calculated in section 7.2.2 and listed in table 7.1 was used as input configuration for RS. As described in section 5.3.2 for the SIMION simulations presented in chapter 5, the initially used reduced electric mobility  $K_0$  of the individual water cluster species was estimated from the individual molecular masses by the fitting function included in SDS [59]. A second set of corrected mobility values which led to an improved agreement between simulation and experiment was estimated based on the calculated data.

For the simulation of the motion of the water cluster RIP, a package of ions was started at the entrance of the modeled drift tube and the drift time of the individual reacting ions was recorded into a simulation result file by the logging mechanisms of SIMION. In addition, RS logged the amounts of the individual cluster species for the first 600 time steps of the simulation into the result file.

The length of the time steps of the simulation are governed by the trajectory integration mechanism of SIMION. By default an adaptive algorithm is used for the estimation of an appropriate time step length to ensure valid ion trajectories [50]. However, this algorithm was developed for vacuum conditions. Therefore user programs, in particular gas collision models often require significantly different time steps than calculated by SIMION, which has to be considered in the configuration of the simulation run. The time stepping of SIMION is controlled by a quality parameter *T. Qual*. The exact definition of this parameter and the configuration options of the particle trajectory integration are found in the SIMION user manual [50]. In general, RS also requires the modification of the integration quality: The maximum time step length required by the kinetics simulation is governed by the absolute reaction rates of the simulated chemical reactions. Thus, without steep concentration gradients of reactants in the background which would lead to steep local gradients of the absolute reaction rates, RS requires generally a relatively uniform time step length. Therefore, the adaptive time stepping mechanism of SIMION has generally to be deactivated in combination with RS. This is achieved with negative values of *T. Qual*; a larger absolute value of this parameter means shorter nearly uniform time steps. In the case of the fast proton bound water cluster system, the chemical simulation dominated the time step requirements of the simulation. A typical value of *T. Qual* in the presented simulations was  $-80$  which resulted in a mean time step length of 6 ns. The effects of the time step length, which renders the simulation invalid if it was chosen inappropriately long, are discussed in detail in the results in section 7.2.5.3.

The raw data resulting from the SIMION-RS simulation were interpreted, analyzed and visualized by a set of custom Python scripts similar to the tool chain used for the analysis of the presented DIA simulations, which also used the NumPy [135] extension to Python, the SciPy scientific computing library [91], and the matplotlib [133, 134] visualization library. The developed analysis tools calculate the RIP drift time, plot the temporal development of the individual cluster concentrations and generate a calculated ion mobility spectrum from the raw data of the simulation.

### 7.2.4.2 Chemked simulations

The chemical kinetics of the water cluster system was also simulated with the chemical kinetics solver *Chemked* (CK) [171, 174, 175], which was used repeatedly for kinetics modeling in the domain of atmospheric pressure ionization [94, 108, 116]. Chemked solves the system of differential rate equations, which are ordinary partial differential equations under the assumption of an ideally stirred reactor. Since all cluster formation and destruction reactions are considered first order under the given experimental conditions, this simplification is valid in the case of the water cluster RIP. The Chemked model calculates the temporal development of the individual relative water cluster concentrations in dependence of the given initial conditions. This result is given in a simple text file (CSV format) which can be analyzed and visualized also by the custom developed tools used for the analysis of the SIMION simulations described in section 7.2.4.1. All Chemked simulations were performed with the default configuration of the solver with isothermal conditions with the set of rate constants presented in table 7.1. In particular, the time steps of the numerical integration of the rate equations are chosen adaptively by Chemked. The assessment of the model results presented in section 7.2.5.1 shows that the default solver configuration was appropriate for the simulation of the proton bound water cluster system.

## 7.2.5 Results

### 7.2.5.1 Kinetics of the proton bound water cluster system

The chemical kinetics of the system of proton bound water clusters was simulated with CK and the RS algorithm as described in section 7.2.4.1 and 7.2.4.2. Figure 7.3 shows the temporal evolution of the individual relative cluster concentrations in an exemplary set of calculations. Despite the numerical noise in the RS results, which is inevitable in a particle based Monte Carlo approach, the result of both models is virtually identical in the entire simulated time frame. The equilibrium concentrations and the process of the equilibration of the system from the initial conditions is similarly predicted by both numerical approaches. Thus, the basic assumptions of RS and the implementation of the algorithm are valid under the present conditions, since Chemked is based on a distinct mathematical approach and was validated independently. Therefore, RS correctly simulates the kinetics of reaction systems similar to the proton bound water cluster system if a sufficiently high number of simulation particles and appropriately short time steps are provided which is discussed in detail in section 7.2.5.3.

The temporal evolution of the cluster concentrations at atmospheric pressure presented in figure 7.3 underlines that the water cluster equilibrium with background concentrations of water which are typical for API conditions is very fast. The time for complete equilibration of the cluster system is well below  $3\ \mu\text{s}$  for a water mixing ratio of 50 ppmV (see the upper left panel of figure 7.3), regardless of the initial conditions. If the system is initialized with a cluster size of  $n = 7$ , the equilibration time becomes even shorter. This is a consequence of the rapid dissociation rate of the higher clus-

## 7.2 Simulation of the proton bound water cluster RIP in AP-IMS

ter species. The overall equilibration time is dependent on the water mixing ratio and becomes shorter with an increasing water amount in the background due to the increasing absolute rates of the cluster formation reactions. With decreasing water concentration the system is decelerated, but the system stays comparably fast: Even at very low water mixing ratios of 10 ppmV, the equilibration time is in the range of 20  $\mu\text{s}$ . Since typical drift times in an AP-IMS are in the range of a couple of ms, the water cluster system is considered as fully equilibrated for the entire residence in the drift tube. Even if the conditions relevant for the cluster reactions, e.g., the background

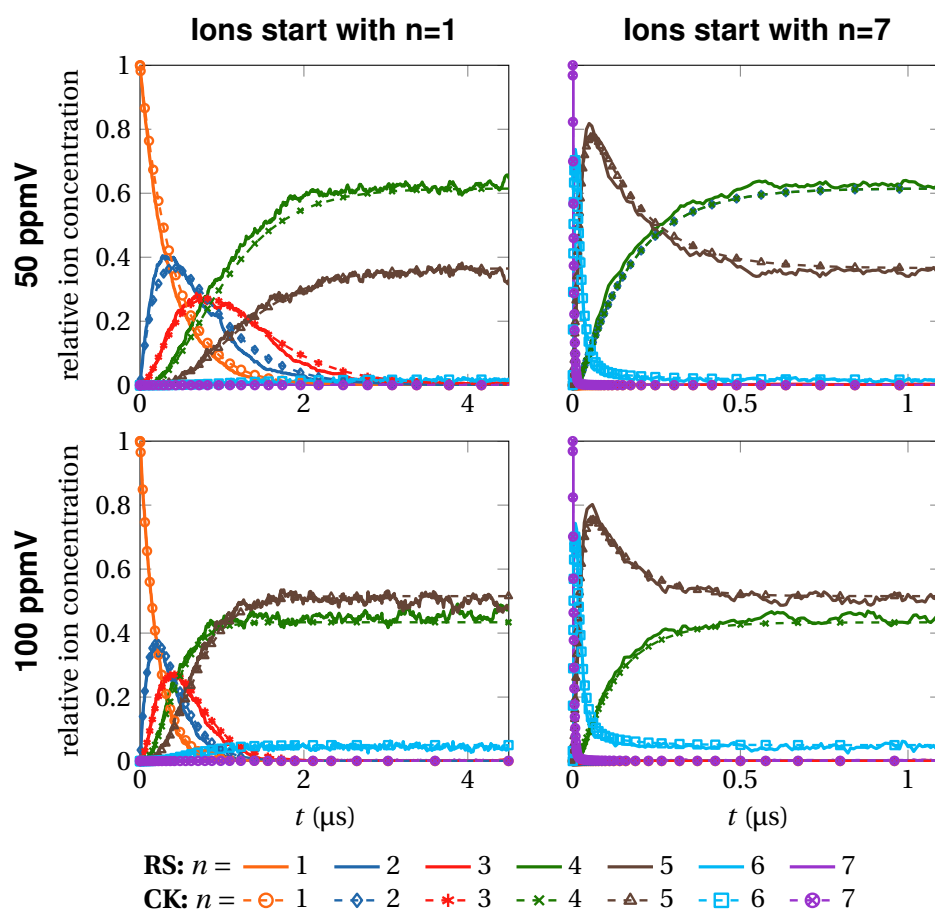


**Figure 7.3:** Comparison of Reaction Simulation algorithm (RS) and Chemked (CK): Simulations of the temporal evolution of the relative water cluster concentrations after initializing the cluster system with clusters of size  $n = 1$  or  $n = 7$  for 50 ppmV and 100 ppmV mixing ratio of water in the background gas. The RS simulations were performed with 1000 simulated particles and a mean time step of 7 ns (T.Qual.=−80). Apart from the inevitable numerical noise in the particle based RS calculation, the simulation results are virtually the same.

## 7 Simulation of reacting ions at AP

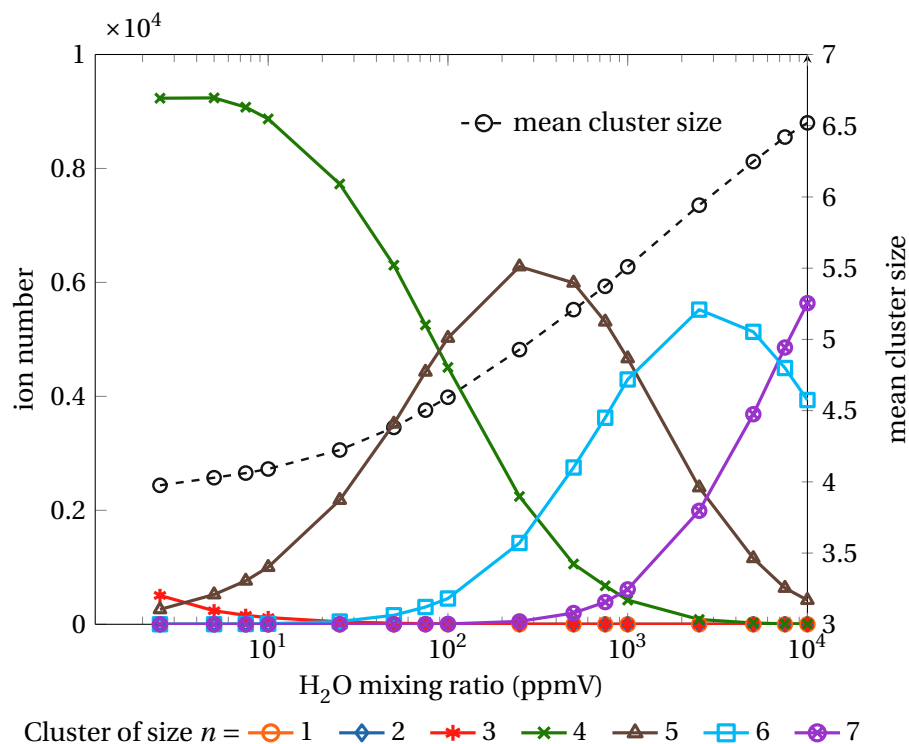


**Figure 7.4:** Relative proton bound water cluster equilibrium concentrations simulated with the RS simulation algorithm in dependence of the water mixing ratio in the background gas. The total number of simulated particles was  $1 \times 10^4$ .

water concentration, would change abruptly at the inlet gate to the drift tube, the time for re-equilibration of the cluster system is negligible in comparison to the drift time. It follows, that the numerically demanding simulation of the RIP drift time with RS is in principle not required. Instead, it is possible to calculate the equilibrium concentrations of the clusters directly from the thermodynamic data in table 7.1, and then calculate the effective ion mobility for the RIP from the weighted sum of the mobilities of the individual clusters. This much simpler and elegant approach was also demonstrated in [176]. Only very low mixing ratios below 1 ppmV, breaks the assumption of fully equilibrated conditions in the drift tube. However, conditions with such extremely low water concentrations are not realistic for common AP instruments. The ion motion in the drift tube was nevertheless explicitly simulated with SIMION and RS to validate and assess the RS model.

The temporally resolved simulation results in figure 7.3 show that both calculations predict the same stable equilibrium state in terms of the individual cluster concentrations, regardless of the simulation initialization. The equilibrium concentrations are also dependent on the water amount in the background gas: With increasing water mixing ratio, the absolute rates of the cluster formation reactions increase, more larger

## 7.2 Simulation of the proton bound water cluster RIP in AP-IMS

clusters are formed, and the final cluster distribution is shifted towards a higher mean size. Figure 7.4 shows this effect systematically: Beginning from a water mixing ratio of 1 ppmV, where the mean cluster size is below  $n = 4$ , the mean cluster size increases up to  $n = 6.5$  at a water mixing ratio of  $1 \times 10^4$  ppmV. The fact that  $n = 4$  and  $n = 3$  are still the dominant species at 1 ppmV underlines the notion that it is virtually impossible to “dry” the water clusters away by reducing the background water concentration.

### 7.2.5.2 Simulation of the water cluster RIP

Since the electric mobility of ions depends on the interaction between the ion and the bulk gas, which is also dependent on the collision cross section of the ion, the observed drift times of the water cluster RIP depend on the mean cluster size. Thus, the dependence of the cluster size on the water amount in the background gas presented in figure 7.4 leads to a considerable water dependence of the observed RIP mobility. Figure 7.5 shows the results of the ion trajectory simulations in comparison to the experimental data gathered at ISAS: In the experiments, the RIP shifts from 18 ms at 20 ppmV to approximately 19.8 ms at 1500 ppmV water mixing ratio in the drift gas. This shift occurs non-linearly in terms of the water concentration (note the logarithmic scale in figures 7.4, 7.5, and 7.6): The effect is more pronounced at low water mixing ratios, and the growth of the clusters tend to level off at high water concentrations.

As described in section 7.2.4.1, the motion of the water cluster ions in the IMS drift tube was simulated with SIMION in combination with SDS and RS. This simulation reproduces the RIP drift times correctly if the kinetics of the chemical reaction system is described accurately and the assumed individual ion mobilities of the cluster species are valid. Therefore, a good agreement of the experimental and simulated results verifies the entire described simulation process at the present conditions. Figure 7.5 shows that the ion trajectory calculation with an unmodified set of cluster mobilities calculated by SDS (*uncorrected* in fig. 7.5) essentially reproduces the general behavior of the water cluster RIP. However, there is a systematic deviation between this simulation and the experimental findings: At high water mixing ratios the results converge, but with decreasing water mixing ratio the simulation systematically predicts too short RIP drift times. This difference is much larger than the scattering of the experimental data presented in figure 7.5. Thus it is considered as a significant error of this SIMION-RS calculation. However, it was shown above that the basic simulation approach of RS was validated by comparison with Chemked, both models produced the exact same outcome. Therefore, it seems unlikely that the RS algorithm models the assumed chemical reaction system incorrectly in the simulation runs presented in figure 7.5. Instead, an invalid set of simulation parameters, which are often only estimated roughly, is probably the cause for the observed deviation. To match the simulated with the experimental results, the ion mobility of the RIP has to be decreased for lower water mixing ratios. This is achieved by lowering the individual mobilities of the dominant cluster species in this region or by shifting the water cluster distribution towards higher mean cluster sizes for low water concentrations. For the former, the

## 7 Simulation of reacting ions at AP

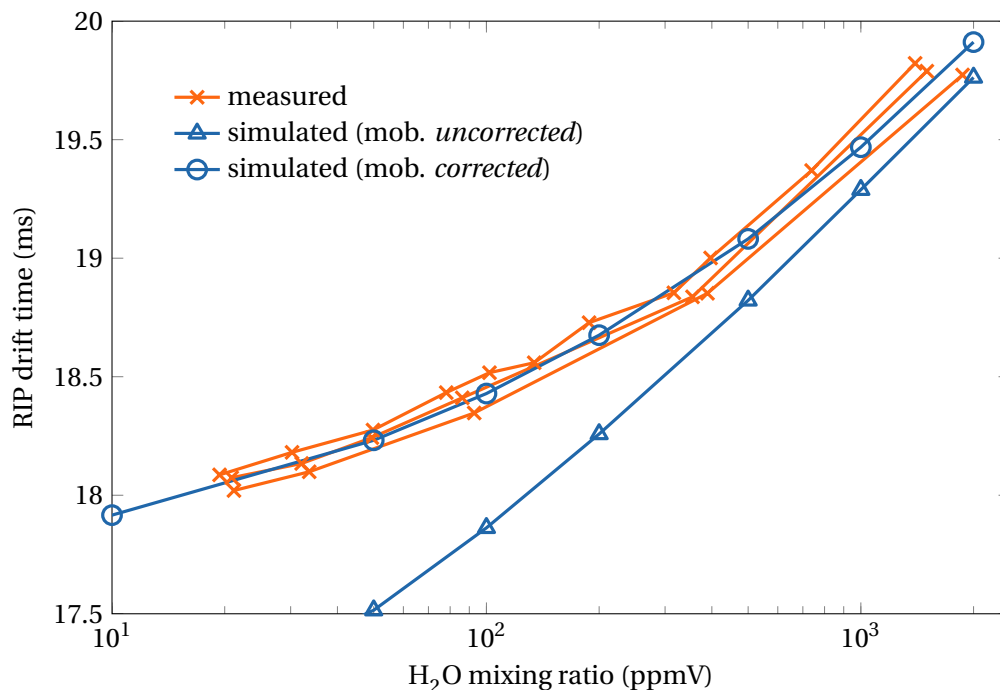


**Figure 7.5:** Simulated drift time of the proton bound water cluster RIP in dependence on the water mixing ratio in the background gas in comparison to experimental results. The *uncorrected* simulation used the ion mobilities calculated by SDS from the ion mass [59]. The *corrected* simulation, which fits the experimental results well, used a modified set of ion mobilities which were estimated manually from the initial uncorrected simulation results. The sets of ion mobility values are presented in table 7.2.

calculated ion mobilities of the critical cluster species is manually adjusted. Figure 7.4 suggests that the primary cluster species in the interesting water concentration region is probably  $n = 4$ . To increase the amount of larger water clusters, the corresponding equilibrium constants of the water cluster system have to be modified manually. In the present case, the amount of the cluster  $n = 5$  can be increased by lowering  $k_{5,4}$  and consequently decelerating the dissociation reaction from  $n = 5$  to  $n = 4$ .

The manual adjustment of the individual ion mobilities immediately leads to very good agreement between simulation and experiment as the *corrected* simulation run in figure 7.5 show: Lowering the ion mobilities of cluster  $n = 4$  and 5 about 5.5% and 1% is sufficient to match the SIMION-SDS-RS simulation with the experimental data. With this modified set of reduced ion mobilities, which is presented in detail in table 7.2 in contrast to the unmodified values, the simulation result lays well within the uncertainty of the experimental data and is thus essentially indistinguishable from that.

**Table 7.2:** Reduced electrical ion mobilities for the individual proton bound water clusters given in units of  $10^{-4} \text{ m}^2 \text{ V}^{-1} \text{ s}^{-1}$ . The initial, *uncorrected* values were calculated from the cluster molecular mass by the SDS algorithm.

Cluster size $n$	$K_0$ (uncorrected)	$K_0$ (corrected)
1	3.57	3.57
2	2.76	2.76
3	2.35	2.35
4	2.09	1.97 (-5.5 %)
5	1.90	1.88 (-1.0 %)
6	1.76	1.76
7	1.64	1.64

In contrast, it is not readily possible to match the ion trajectory simulations with the RIP measurements by adjusting the rate constants to increase the mean cluster size for low water mixing ratios. Figure 7.6 depicts the results of this attempt: The lowering of  $k_{5,4}$  leads to an overall increase of the RIP drift times, in particular below 500 ppmV water. However, to achieve a reasonable agreement between the trajectory calculation and the measurements, a significant deceleration of the cluster destruction reaction from  $n = 5$  to  $n = 4$  to only 20 % of its original calculated rate is required. Even if the modified calculation fits the experimental data much better than the initial unmodified simulation ( $k_{5,4} \cdot 1$  in fig. 7.6), the overall agreement is poor in comparison to the result of the simulation with modified reduced ion mobility. Particularly, the curvature of the experimentally determined RIP drift times is not reproduced by the ion trajectory calculation upon variation of  $k_{5,4}$  as shown in figure 7.6. In combination with the much larger correction required for the rate constant to achieve a reasonable agreement, the initial deviation of the ion trajectory calculation is well explained by a relatively small discrepancies of the reduced individual cluster ion mobilities estimated by SDS. The required correction of the cluster ion mobility is near or even within the uncertainty of the data sources, which were used to determine the fitting function used by SDS for the estimation of the ion mobility from the ion mass [59]. Thus a similar level of uncertainty for the resulting fitting function is to be expected, which justifies the otherwise comparably arbitrary manual correction of particular cluster mobilities. Subsequent works should investigate the individual cluster mobilities and the validity of the mobility correction presented here.

In addition to the analysis of the RIP drift time, the simulated ion trajectories is analyzed in detail. Figure 7.7 shows a section of an exemplary ion mobility spectrum in comparison to time resolved simulation data with 32 ppmV water present. The water cluster RIP is by far the most abundant signal in the experimental mobility spectrum. The small additional signal at 17.1 ms, probably caused by some unknown contaminant in the IMS, is one of a few similar additional signals (not shown in the time

## 7 Simulation of reacting ions at AP

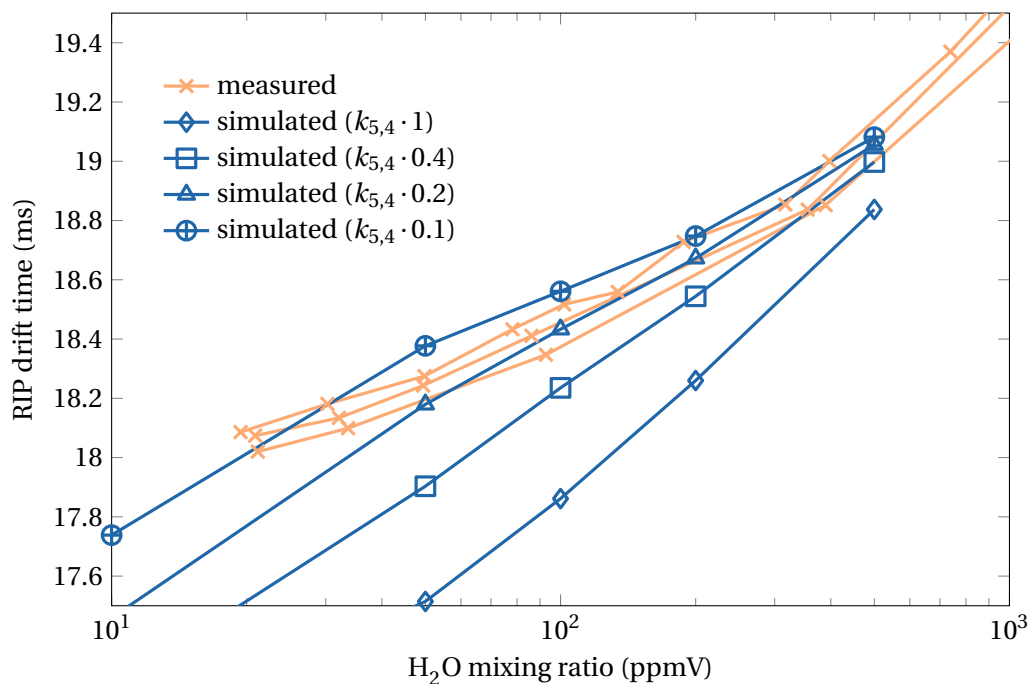


**Figure 7.6:** Simulated drift time of the proton bound water cluster RIP in dependence of the background water mixing ratio under variation of the cluster dissociation rate constant from the cluster with size  $n = 5$  to  $n = 4$  instead of the ion mobility.

frame in figure 7.7) with an identifiable peak shape of which the shown one is the most abundant. The tailing signal on the right side of the RIP continuously loses intensity with increasing drift time and disappears completely until 40 ms. The comparison of the experimental and simulated RIP peak shapes shows that the numerical calculation basically describe the experimental peak shape correctly but tend to underestimate the peak width. Even with activated molecular diffusion simulation in SDS and the same inlet gate opening interval of 300  $\mu\text{s}$ , which is referred to as “start window” ( $sw$ ) in figure 7.7, the simulated peak width is only in the range of 0.6 ms (dark red curve in fig. 7.7). Interestingly, the release of all simulated ions as ideal pulse ( $sw = 0\mu\text{s}$ ) in the calculations with activated diffusion has only a relatively small effect on the simulated peak width. In contrast, the additional deactivation of the diffusion simulation has a strong effect, and the simulated RIP becomes very narrow with a remaining peak width in the range of 0.1 ms. The underestimation of the peak width by the numerical model suggests that the calculations miss an effect which leads to additional axial diffusion of the cluster ions. One possible explanation would be the underestimation of the molecular diffusion of the cluster ions by the SDS model. Since the effect of the

## 7.2 Simulation of the proton bound water cluster RIP in AP-IMS

diffusion simulation is not particularly pronounced, the error in the diffusion model has to be fairly large. A better explanation is a non-ideal behavior of the cluster ions in the instrument: Minor non-ideal field geometries of the drift field, some diffusing effects occurring at the inlet gate [84] and possibly charge repulsion of the analyzed ions are sufficient to explain the observed additional width of the water cluster RIP. Subsequent simulations of the ion motion in different mobility spectrometer systems, for example in a high resolution instrument with optimized field geometries [155], and the experimental investigation of the ion diffusion are well suited to assess this rationale.

In summary, the presented results strongly support the notion that the simulation approach of SIMION in combination with SDS and RS is correctly simulating the chemical kinetics and the motion of highly reactive ionic species as the proton bound

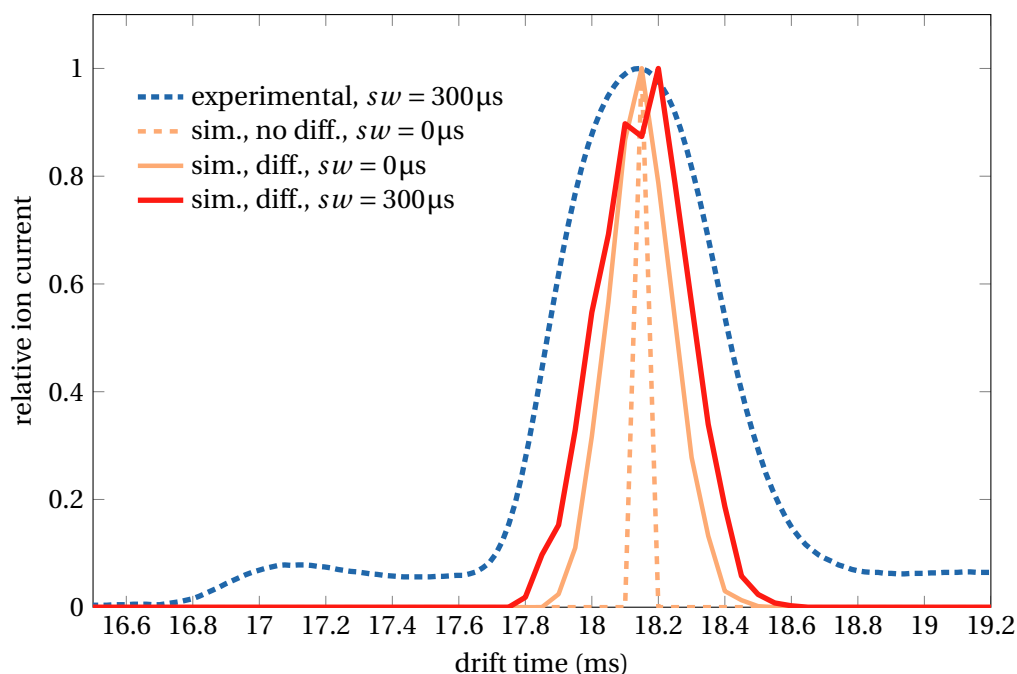


**Figure 7.7:** Comparison of the simulated and the experimental temporally resolved ion signal of the water cluster RIP for 32 ppmV water mixing ratio. The simulated ion mobility signal with activated diffusion simulation (“diff.”) and a start window ( $sw$ ) length of  $300\mu s$  has a similar peak shape but is still significantly narrower than the experimental signal. The irregularities in the maximum region of this simulated signal are an artifact resulting from the limited number of simulated particles in the RS calculation (2500 particles in this simulation) which leads to a noticeable level of numerical noise on the temporally resolved signal.

water clusters at atmospheric pressure conditions.

### 7.2.5.3 Numerical quality and numerical stability

There are two primary parameters which govern the simulation quality of the RS approach: The *number of simulated particles* and the *time step length* ( $\delta t$ ). If the number of simulation particles becomes too low, the simulated particle ensemble becomes statistically insignificant. The exact required particle number depends on the simulated chemical system and the intended simulation quality level. Generally, the number of simulated particles has to increase with rising complexity of the simulated chemical system in terms of the number of simulated reactions. However, small reaction systems can also require a high simulation particle number if there are large differences in the reaction rates or minuscule steady state concentrations of particular components are to be simulated with high precision. Figure 7.8 depicts the effects of the number of simulation particles on the RS simulation of the proton bound water cluster system. The observable numerical noise clearly depends on the number of simulated ions  $k$ : The simulation with 100 ions shows pronounced noise in the signals of the relative cluster concentrations while the noise level in the calculation with 100 000 ions is barely visible. Two aspects are noteworthy in this context: First, the reduction of the simulation particle number does not change the relative mean simulation output itself. Both, the equilibrium concentrations as well as the temporal evolution of the cluster signals are not affected by the simulated particle number if the random noise on the signals is ignored. Second, even very low absolute numbers of simulated ions often produce simulation results with a sufficiently high quality level. Figure 7.8 shows that even 1000 simulated ions are able to describe the water cluster system nearly quantitatively. As presented in the preceding section, this relatively low number of simulated ions was adequate to simulate the water cluster RIP correctly. Since the level of numerical noise is reduced only proportionally to  $\sqrt{k}$ , the advantage of increasing simulation particle numbers levels off quickly. This is also seen in figure 7.8: While the difference between the simulation with 1000 and 10 000 ions is clearly shown, the further noise reduction in the calculation with 100 000 ions is barely noticeable. Generally, for reaction systems comparably to the system of the proton bound water clusters in terms of complexity, simulation particle numbers between 1000 and 10 000 should lead to meaningful results.

The second critical parameter of the RS approach is the time step length  $\delta t$ . In contrast to the number of simulation particles, the time step length has a pronounced lower limit where the assumptions of the linearized approach to calculate the individual reaction probabilities breaks down. Thus, if it falls below this limit, the simulation result becomes entirely invalid. In the case of the water cluster system, the simulation typically starts to oscillate severely with a period of two time steps, which is clearly seen in the left panel of figure 7.9 beginning at  $t \approx 0.4 \mu\text{s}$  and intensifying at  $t \approx 3 \mu\text{s}$ . This effect is caused by neighboring dissociation and association reactions with, obviously faulty, linearized local reaction probabilities  $p > 1$ . In this case, *all* ions of one species

## 7.2 Simulation of the proton bound water cluster RIP in AP-IMS

are interchanged with *all* ions of another species, which leads to the observed oscillations. In the example depicted in figure 7.9 cluster of sizes  $n = 5$  and  $n = 6$  oscillate in this way. In stark contrast to the effect of reducing the simulated particle number, falling below the critical time step length also distorts the calculated mean equilibrium concentrations significantly. In the example, the mean abundance of of cluster  $n = 5$  is significantly lower and cluster  $n = 6$  is notably higher than in the simulation with appropriate  $\delta t$  shown in the right panel of figure 7.9. The point when the simulation becomes distorted is clearly observable as abrupt decrease in the concentration of cluster  $n = 5$  between 0.35 to 0.45  $\mu\text{s}$  in the left panel of figure 7.9. Prior to this time, both simulations produce essentially the same result, after it the faulty calculation clearly diverges, and the described oscillation effects occurs. In summary it becomes clear that wrongly chosen time steps have to be generally avoided in RS simulations. The exact minimum required time step length depends obviously on the modeled chemical reaction system. Therefore, this parameter has to be determined individually for every simulation project. However it is at least possible to provide some assistance for the user of RS to find an appropriate time step length by detecting and reporting the number of “ill” reaction events with local reaction probabilities  $> 1$ . This information can also be used for an adaptive mode of RS in which the time step length is shortened appropriately if ill reaction events were detected. Such an operation mode is a future projects for the further development of the RS algorithm.

7 Simulation of reacting ions at AP

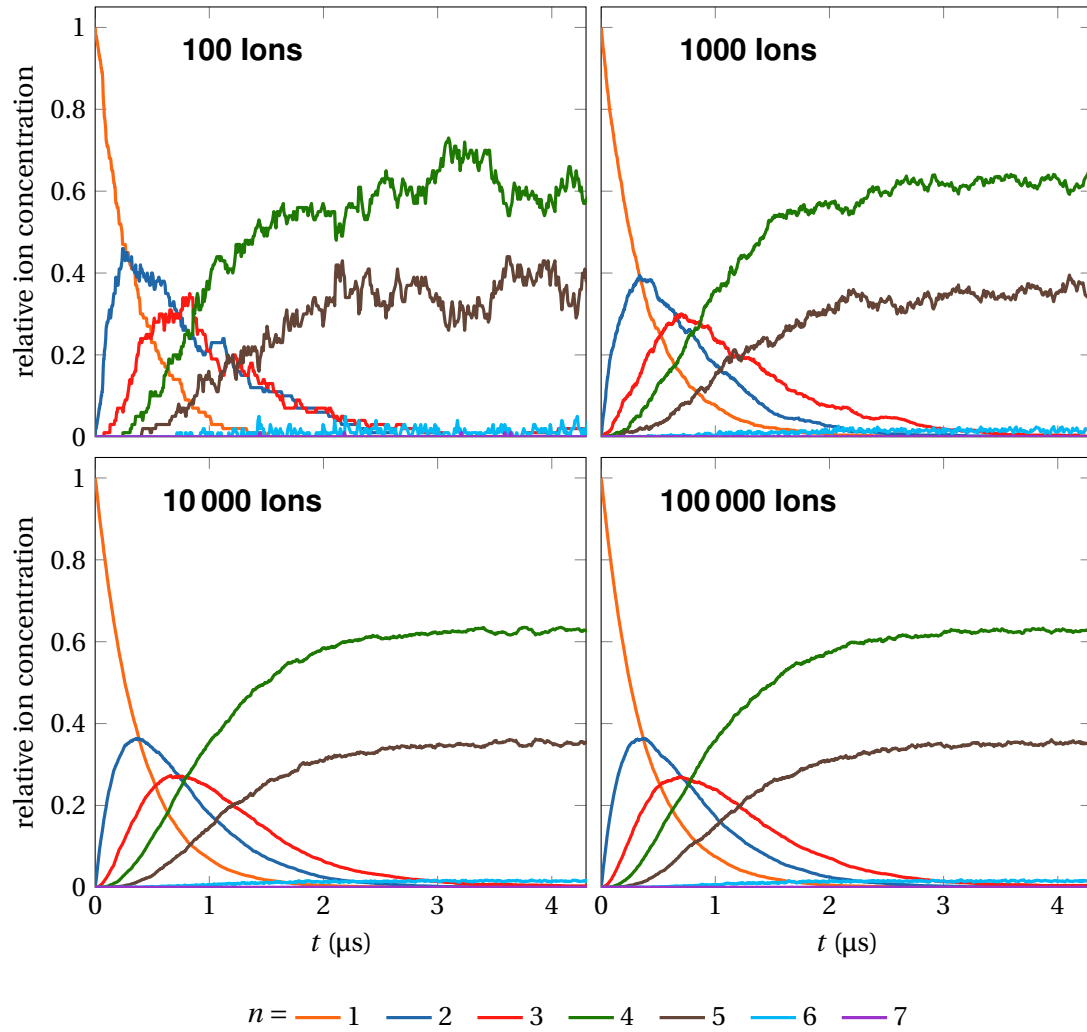


**Figure 7.8:** Effect of the particle number on the result of the RS simulation: The level of numerical noise is reduced with increasing particle number.

## 7.2 Simulation of the proton bound water cluster RIP in AP-IMS

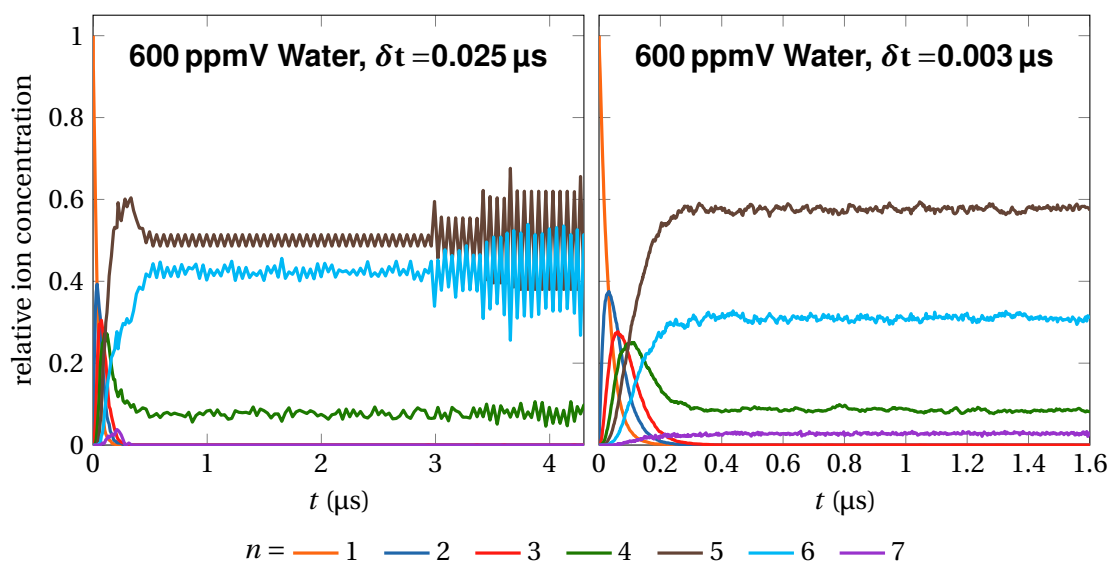


**Figure 7.9:** Effects of inappropriate time step length ( $\delta t$ ) on the RS simulation result: If the time step length becomes too long, the linearized approach of RS to calculate the reaction probabilities becomes wrong which results in reaction probabilities  $\geq 1$ .

### 7.2.6 Conclusions

The presented results show that the RS algorithm in combination with SIMION and SDS is able to correctly model the dynamics of the highly reactive water cluster system in an AP-IMS drift tube. It was possible to handle the numerical effort required for the presented confidence level of the simulations on advanced consumer class computer hardware. Due to the very fast reactions of the individual water clusters and the generally high level of water in the background gas, the water cluster RIP probably marks an upper limit of the overall absolute reaction rate in such a chemical system. Therefore, the water cluster system marks also an upper limit of the required numerical effort per individual modeled reaction, since faster reactions require shorter mean time steps. Thus, almost any reaction system of a comparable complexity in terms of the number of chemical reactions should be solvable on consumer class computer hardware. Furthermore, there are some foreseeable improvements of SIMION and its user program interface in terms of numerical performance. In particular it is planned to utilize a just in time compiler for the Lua user programs and to parallelize the particle tracing algorithm of SIMION for multi-core processors or modern general purpose graphic processors (GPGPU). Such improvements could increase the feasible problem size in terms of simulation particle number or time step length at least about one order of magnitude. This would also widen the range of applications of the RS approach toward more complex reaction systems.

Valid numerical calculations with SIMION and RS require correct input parameters, particularly with respect to the reaction system in terms of individual chemical reactions and the according set of reaction rate constants. Generally, the determination of necessary information, especially the reaction rate constants, demand much more effort than the setup and solution of the numerical model itself. In the presented example of the water cluster system, the rate constants were derived from experimental thermochemical data and the assumption of collision controlled forward cluster association reactions. The thermodynamic data for this approach may also be gathered with *ab initio* quantum chemical calculations. This is demonstrated by the modeling of the ion mobility signal of another cluster system consisting of proton bound acetone water clusters with different approaches including SIMION and RS [176–178] which is discussed also in the subsequent section. In general, if simplifying assumptions can not be made and the chemistry of an interesting reaction system is not known, a simulation project has to start with the determination of the required reaction rate constants which is a classical task in physical chemistry but could potentially be an entire research project of its own.

### 7.3 An outlook towards ion temperature simulation

The simulation of the water cluster RIP in an AP-IMS presented in the preceding section assumed low field and therefore essentially thermal conditions. All effects of the electric acceleration on the ions, in particular the increase of the kinetic energy, are ignored in the presented isothermal RS simulations. While this assumption is certainly correct for the ion motion in an AP-IMS at low reduced field strength, in a lot of relevant cases it is not. The primary cause for a rapidly increasing reduced field strength in ion optical devices is the reduction of the background pressure. In common commercial MS instruments, the low field assumption breaks down immediately after the first pressure reduction stage, which consists either of an inlet capillary or an orifice system [3, 92]. Typical background gas pressures in the region behind this first pressure reduction are in the range of 2 to 10 mbar. At this pressure, high reduced field strengths are readily reachable, even with a relatively low electric field intensity. For example, a reduced field strength of 100 Td, which is generally considered as a good benchmark for conditions where high field effects become apparent, is reached with a field gradient of  $48 \text{ V cm}^{-1}$  at 2 mbar background pressure. This potentially high reduced field intensity increases even more with further reduced pressure as analyte ions pass through the subsequent stages of the inlet system of the MS instrument.

The significant gain in kinetic energy of the ions has a profound effect on their chemical behavior. Ions are fragmenting due to high-energy collisions with background gas particles, which gives rise to analytical methods as for example collision induced dissociation (CID), where the deliberate fragmentation is used to gain structural information. Also significantly lower collision energies than required for covalent bond breaking potentially affect the chemical kinetics and the reaction dynamics of ions. Particularly, reactive cluster systems are susceptible to effects of an increased reduced field: Proton bound water clusters for example can be readily electrically “declustered” down to cluster sizes  $n = 1 - 2$  at intermediate background pressures ( $\approx 10$  mbar) [179, 180] which significantly changes the chemical reactivity of the clusters [181].

If the reduced field intensity is moderate, such conditions can be modeled as an increase of the *effective temperature* ions locally experience [12]. Since such high field effects have potentially a profound impact on the performance of an ion optical instrument, the RS algorithm was extended with a model of the field dependent effective ion temperature. This is mandatory for the further application of RS on simulation problems considering low background pressure and therefore increasing reduced field intensity. This section presents the theoretical fundamentals of such an ion temperature model, the necessary modifications in RS and some exemplary simulation results of the modified RS model. Since the incorporation of an ion temperature model in RS marks a final (but yet unfinished) step in the presented work, this section has much of a proof-of-concept and outlook character. The main purpose of this section is to demonstrate that ion temperature simulation in RS provide an useful basis for the analysis of medium pressure ion dynamics problems as well as for the development of

more detailed and specialized numerical models.

### 7.3.1 Ion temperature model

The motion of ions in an electromagnetic field at conditions where collisions with neutral gas particles have to be considered can be described in terms of the kinetic theory of the transport of diluted charged particles through a neutral bulk gas [12, 182]. The basic transport equation of this theoretical approach is the Boltzmann equation [12, 183–186] which therefore has to be solved for the present conditions. The solution function of the Boltzmann equation is a function  $f(\vec{r}, \vec{v}, t)$  which yields the ion density distribution in dependence of the position  $\vec{r}$ , the velocity  $\vec{v}$ , and the time  $t$ . Every experimentally observable variable would be calculatable by integrating this function. However, since it is not possible to find a general solution of the Boltzmann equation, even deriving exact solutions for specific boundary conditions is generally extremely complicated and nontrivial. Therefore, in the context of ion motion, it is useful to determine solutions for velocity moments, which are essentially average values of arbitrary functions of the velocity  $\Psi v$ , instead of  $f(\vec{r}, \vec{v}, t)$  itself [182] [12, p.193]. However, further simplifications and assumptions are required to gain an useful solution: The ion density is assumed to be low in comparison to the bulk gas particle density, so that ion-ion interactions can be neglected. Further, chemically reactive collisions have to be infrequent in comparison to the non-reactive collision frequency and the ions are assumed not to have internal degrees of freedom in which they store internal energy. Finally, the velocity distribution of the ions is assumed to be Maxwellian, but with a distinct and generally elevated ion temperature resulting from the acceleration by an electrostatic field. This mathematical approach is referred to as *two temperature model* of the ion motion [12, 182]. The result of this model is an *effective ion temperature*  $T_{\text{eff}}$ . For the drift of ions through a neutral bulk gas with a diluted neutral reactive gas component which can chemically react with the ions, the effective temperature is given as [12, p. 417]:

$$T_{\text{eff}} = T + \frac{M_R v_d^2 \frac{m+M_B}{m+M_R}}{3k} \quad (7.4)$$

with the background temperature  $T$ , the ion drift velocity  $v_d$ , the bulk gas particle mass  $M_B$ , the reactive gas particle mass  $M_R$ , the ion mass  $m$  and the Boltzmann constant  $k$ . If all particle masses are assumed to be identical, equation 7.4 can be simplified to [182, 187]

$$T_{\text{eff}} = T + \frac{M v_d^2}{3k} \quad (7.5)$$

with the gas molecule mass  $M$ . The ion velocity  $v_d$  can also be expressed in terms of the ion mobility  $K$  and the present electric field  $E$ :

$$T_{\text{eff}} = T + \frac{M(K E)^2}{3k} \quad (7.6)$$

### 7.3 An outlook towards ion temperature simulation

With this simple equation it is in principle possible to calculate the effective reaction temperature of the ions from known parameters. This temperature then can be used in the chemical reaction model for the calculation of the local reaction probabilities. As mentioned, the deduction of equation 7.6 required some simplifications, in particular the assumption of absent internal degrees of freedom in the ions. It is possible to extend the underlying theory so that also internal degrees of freedom are considered [12, p. 471 ff.], but the resulting mathematical treatment is rather complex and beyond the scope of this section.

**High field ion mobility models** The calculation of the ion velocity from the ion mobility as  $v_d = KE$  becomes more complex with increasing reduced field. As mentioned in the introduction in section 2.2.1, due to field dependent physical interactions between the ions and background gas particles, the electric mobility becomes a function of the reduced field strength, even for chemically inert ions [188–190]. In the context of DMS or FAIMS, the field dependence of the ion mobility is described by the function

$$\alpha(E) = \frac{K(E)}{K(0)} - 1 \quad (7.7)$$

with the low field mobility  $K(0)$  and the mobility  $K(E)$  at field strength  $E$ . Depending on the interactions of the ions with the background gas, the  $\alpha$  function shows distinct progressions in dependence of parameters as for example the reduced field or concentration of reaction partners [190]. The development of a theoretical model for the high field ion mobility is difficult, due to the complex physical processes involved. Progress in this regard was possible for rather simple systems. In particular the motion of noble gas ions in neutral noble gases was used for theoretical investigations, since internal degrees of freedom in molecules and chemistry can be ignored in those systems [12, 182, 189, 191–193]. More recently also simple molecular systems, e.g., the drift of noble gas ions in diatomic gases [194], were theoretically investigated, also with numerical methods [195, 196], but today there is still no applicable uniform theory of the high field ion mobility of molecule ions in molecular gases.

In terms of high field mobility behavior, ions are commonly classified into three groups [197]: Type A, which expose a positive  $\alpha$  function, which increases with increasing field strength; ions of type C which show an increasingly negative  $\alpha$  and type B ions, which ultimately expose also a negative  $\alpha$  but have a positive peak at intermediate field strength. Small clustered ions, as the proton bound water clusters, are generally of type A since the clusters become smaller with increasing effective ion temperature at high field conditions while other small ions tend to fall in the categories B or C [190, 198]. Despite the lack of applicable theoretical models, the dependence of the ion mobility can be investigated empirically by systematic measurements. Ellis et al. and Viehland et al. have compiled a series of extensive compilations of experimentally field dependent ion parameters, including the high field ion mobility, ion diffusion coefficients, and momentum transfer collision integrals [199–202]. This comprehensive

## 7 Simulation of reacting ions at AP

data set potentially provides a basis for empirical ion mobility functions in numerical ion dynamics simulations like RS.

**Calculation of temperature dependent rate constants of the proton bound water cluster system** To simulate the effects of elevated effective ion temperatures, the temperature dependence of the kinetics of a given reaction system has to be known in terms of temperature dependent rate constants. For the presented system of proton bound water clusters, rate constants for different temperatures can be calculated from the temperature dependence of the cluster reaction equilibrium constants  $K_{n-1,n}$ . The Van't Hoff reaction isobar [8] allows to estimate the equilibrium constant  $K_2$  at temperature  $T_2$  from a known equilibrium constant  $K_1$  at a given temperature  $T_1$ :

$$\ln\left(\frac{K_2}{K_1}\right) = \frac{-\Delta_R H^0}{R} \left(\frac{1}{T_2} - \frac{1}{T_1}\right) \quad (7.8)$$

with the standard reaction enthalpy  $\Delta_R H^0$  and the universal gas constant  $R$ . This temperature corrected equilibrium constant is used in combination with the temperature dependent collision controlled rate constant of the cluster formation reaction to calculate the temperature dependent backward rate constants by combining equations 7.2 and 7.3. The forward rate constant is given by the collision frequency  $z$ . In principle  $z$  can be calculated with equation 2.3, but in the actual case it has to be considered that the gas consists of at least two different chemical species. This consideration [7] allows the calculation of the collision controlled forward rate constant:

$$k_f = \sigma \sqrt{\frac{16RT}{\pi\mu}} \quad (7.9)$$

with  $\sigma$  as the collision cross section, for the reacting particles with the masses  $m_a$  and  $m_b$ , and  $\mu$  is the *reduced mass*:

$$\mu = \frac{m_a m_b}{m_a + m_b} \quad (7.10)$$

Figure 7.10 depicts the result of the estimation of the temperature dependent cluster destruction (backward) reaction rate constants. The temperature dependence is mainly due to the shift of the equilibrium constants. The change of the calculated forward rate constant, only a factor of  $\approx 2$  in the temperature interval from 270 to 600 K, is negligible in comparison.

**Modifications in RS** The RS algorithm described in section 7.1 was used to simulate ion temperature effects in the proton bound water cluster system. To allow this kind of calculation, numerical functions to estimate the forward and backward rate constants as described above were integrated into the RS algorithm. Since the simulations presented in this section had primarily a proof-of-concept character, no formal syntax for the general definition of temperature dependent rate constants was defined for

### 7.3 An outlook towards ion temperature simulation

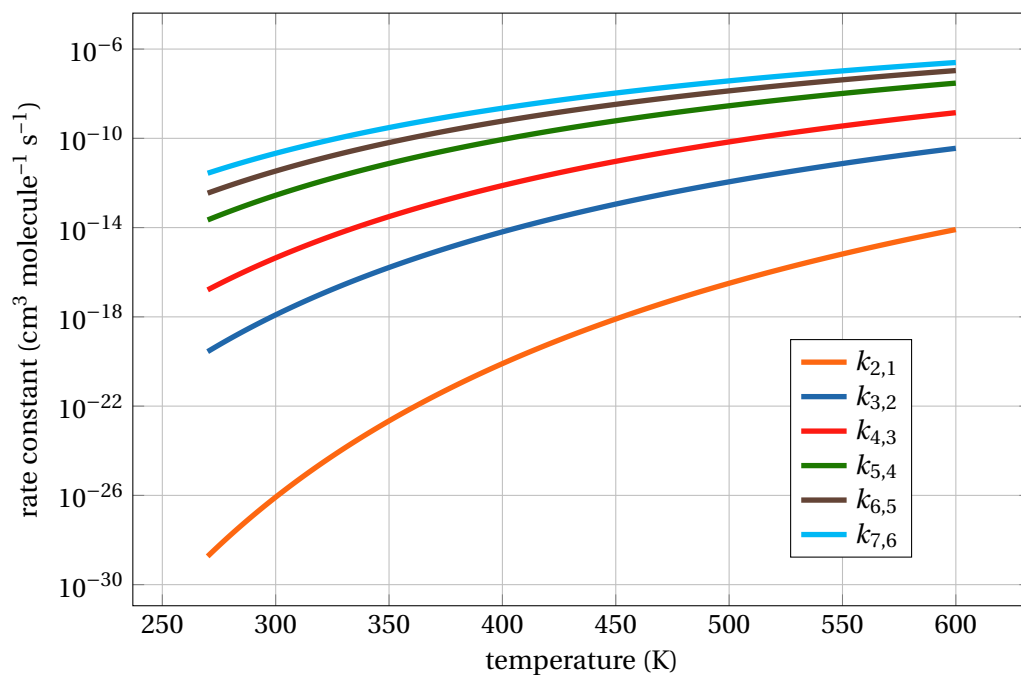


**Figure 7.10:** Calculated, temperature dependent rate constants of the cluster destruction (backward) rate constants of the proton bound water cluster system defined in section 7.2.2

the RS configuration files. Instead, the functions for the rate constants were explicitly defined in the RS source code and were selected by their name given as keyword in the reaction definition in the RS configuration. In addition, the standalone RS mode was modified: The ion temperature was calculated according to equation 7.6 from a given electrical field, which could be static (isothermal mode) or defined by an arbitrary time dependent function. In experimental simulations, a freely configurable field dependent ion mobility function for  $K$  (equation 7.6) was used.

### 7.3.2 Model examples

In this section, selected numerical calculations are presented, which demonstrate the applicability of ion dynamics simulations considering the field driven ion temperature.

#### 7.3.2.1 Temperature dependent RIP drift in AP-IMS

The analysis of the humidity dependency of the water cluster RIP in an AP-IMS allowed the validation of the system of estimated isothermal reaction rate constants calculated in section 7.2.2. Similarly, the validity of the estimated temperature dependent rate constants can be assessed by analyzing the shift of the water cluster RIP with varying temperature. If the RIP temperature dependence is reasonably modeled, the water cluster system, and therefore the system of reaction rate constants, is reasonably modeled as well.

Experimental data were gathered in cooperation with the Institute of Electrical Engineering and Measurement Technology (GEM)<sup>3</sup> of the university of Hannover. A high performance AP-IMS, which was designed and constructed by the group of Stefan Zimmermann [155] was used to measure the drift times of proton bound water clusters, acetone water clusters, and ethanole water clusters. In principle, the used instrument is similar to the ISAS-IMS presented in section 7.2.3, but provides much better separation resolutions in a much smaller drift tube with an increased electric gradient. The drift distance was 75.5 mm with a drift potential of 4850 V, which results in a potential gradient of  $642 \text{ V cm}^{-1}$  instead of  $317 \text{ V cm}^{-1}$  in the case of the ISAS instrument. In addition, the drift tube temperature could be varied with controlled external heating elements, which allowed temperature dependent ion mobility measurements. The temperature was varied between 23 and 85 °C. Humid synthetic air was used as drift gas. The water content in this gas was controlled by a mixture setup, which mixed gas saturated with water, which contained therefore a known humidity, with dry gas of a known residual water content. The background water mixing ratio in the temperature dependent experiments was 24 ppmV.

All experiments shown in this section were conducted by Yessica Brachthäuser and Christine Polaczek from the physical and theoretical chemistry group of the University of Wuppertal in the labs of GEM. Details of the experimental setup and the additional experimental data, which were determined but is not explicitly presented here, can be found in the theses of the experimenters [176, 203]. In the following, only the water cluster peak is considered. It should be noted that the analysis of the experimental data allowed the estimation of a similar set of temperature dependent reaction rate constants for the system of acetone water clusters ( $[\text{H} + \text{CH}_3\text{COCH}_3 + (\text{H}_2\text{O})_n]$ ) [152], which was also used for drift time calculations. Instead of explicitly simulating the cluster drift times with SIMION-RS, the drift time was calculated via the mean cluster size with the assumption of fully equilibrated conditions described in section 7.2.5.1. The results were validated against experimental data [176, 177]

---

<sup>3</sup><http://www.gem1.uni-hannover.de>

### 7.3 An outlook towards ion temperature simulation

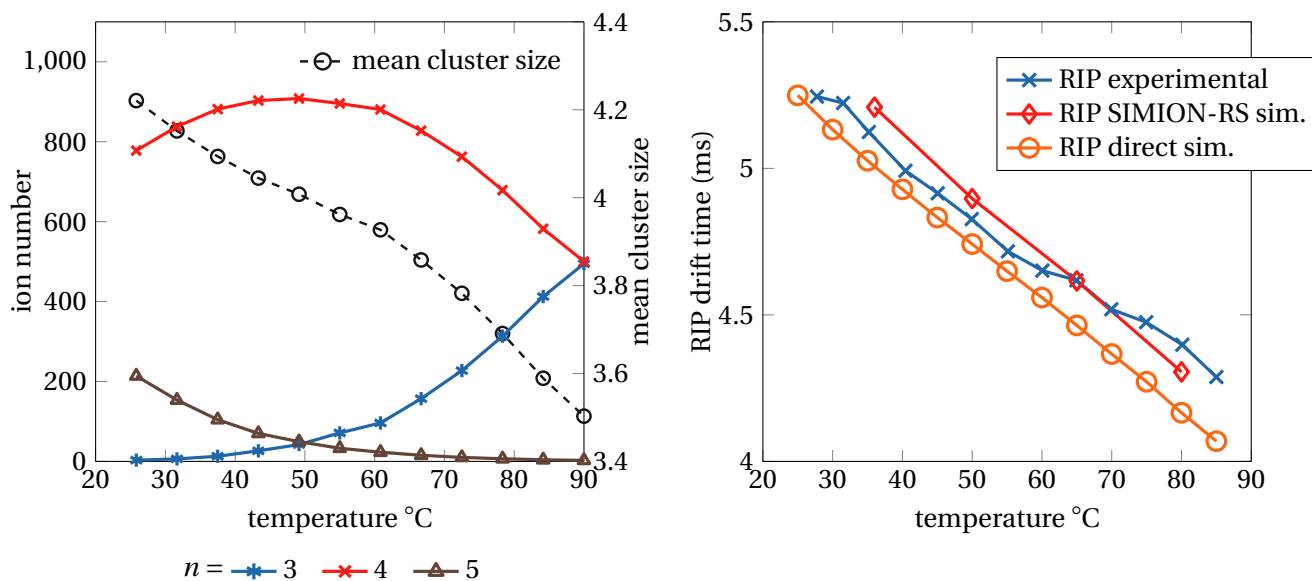


**Figure 7.11:** Results of the temperature dependent water cluster RIP simulation: The left panel depicts the temperature dependence of the calculated cluster distribution. Clusters of size  $n = 1, 2, 6$  was not abundant in the simulation. The right panel shows the calculated RIP drift time obtained with explicit SIMION-RS simulations and the direct calculation of the RIP drift time via the mean ion mobility assuming equilibrium in comparison to experimental data. The background water mixing ratio was 24 ppmV. Both, the direct simulations and the experimental drift time measurements were conducted by C. Polaczek [176]. Despite the notable divergence between the simulations and the experiment, it becomes apparent that the general trend of the RIP temperature dependence is well reproduced by the calculations.

and showed good qualitative agreement with the measurements. This demonstrates that the techniques discussed in this chapter are successfully applied to other cluster systems if the corresponding rate constants can be correctly estimated.

The water cluster RIP drift times in the GEM-IMS were simulated explicitly for multiple temperatures according to the descriptions in section 7.2. The reaction rate constants of the water cluster system were calculated for the individual temperatures as described in section 7.3.1. In addition, C. Polaczek calculated the drift times with the direct approach via the weighted cluster mobility, assuming ideally equilibrated conditions [176], referred to as “direct simulation” in the following.

Figure 7.11 depicts the results of those simulations: The left panel demonstrates the effect of a temperature variation on the system of water clusters and the resulting mean cluster size at a background water mixing ratio of 24 ppmV. With increasing

## 7 Simulation of reacting ions at AP

temperature, the clusters of size  $n = 5$  and 4 are increasingly depleted due to their lower stability. This leads to a shift of the mean cluster size from approximately 4.2 at 25 °C to 3.5 at 90 °C. The right panel of figure 7.11 shows that the decreasing average water cluster size leads to significantly and linearly decreasing drift times of the water cluster RIP. The absolute change in the experimental RIP drift time is approximately 1 ms, from 5.25 to 4.29 ms. The measurement results show a notable level of unsteadiness in the temperature dependent drift times. This is probably induced by a considerable level of experimental scattering, which could not be assessed in detail since the available experimental data is not sufficient in terms of measurement replications. Both simulation approaches basically reproduce the experimental results qualitatively. The decreasing drift time is reproduced by the simulations. There is however a constant offset between the calculation results: The direct calculation predicts drift times which are approximately 0.1 ms shorter than the results generated with the explicit simulation in SIMION-RS. This is surprising, since identical calculated reaction rate constants were used in both simulation methods. To date, there is no satisfying hypothesis to explain this significant offset between the two calculation approaches.

Despite the differences between both calculations and the RIP drift time measurements, the simulations reproduce the observed experimental behavior of the water cluster system comparably well. Considering the level of experimental uncertainty, which can be roughly estimated from the statistical error of the experimental data, the calculated RIP drift times are probably within the error margins of the experiment. This demonstrates that the derived system of temperature dependent rate constants, despite of the relatively rough estimations in its derivation, is basically valid, at least in the analyzed temperature interval. Therefore, this reaction system serves as a feasible basis for further ion dynamics simulations including field driven and thus high ion temperatures, which are presented in the subsequent sections. Additionally, the temperature dependent chemical processes often lead to deviations from the linearly temperature corrected reduced ion mobility. This potentially renders the reduced ion mobility approach insufficient for the valid comparison of ion mobility signals determined at different temperatures which probably could be compensated by appropriate parameterization considering the cluster chemistry [178].

### 7.3.2.2 Water Cluster destruction in a medium pressure collision cell

It is generally not possible to reach strong electrical accelerations and therefore high reduced field strengths at atmospheric pressure due to the high collision number of ions with background particles. Equation 7.6 shows that even for a voltage gradient of 50 kV cm<sup>-1</sup>, which is probably near or even above the electrical breakdown voltage of air and nitrogen [173], the resulting additional electrical “heating” of the water cluster of size  $n = 4$  ( $K_0 = 2.085 \times 10^{-4} \text{ m}^2 \text{ V}^{-1} \text{ s}^{-1}$ ) is only 12.6 K. Therefore, the reduction of the background pressure is the only way to significantly increase the ion temperature and to observe field driven effects in the chemical behavior of a reactive ion. Such

### 7.3 An outlook towards ion temperature simulation

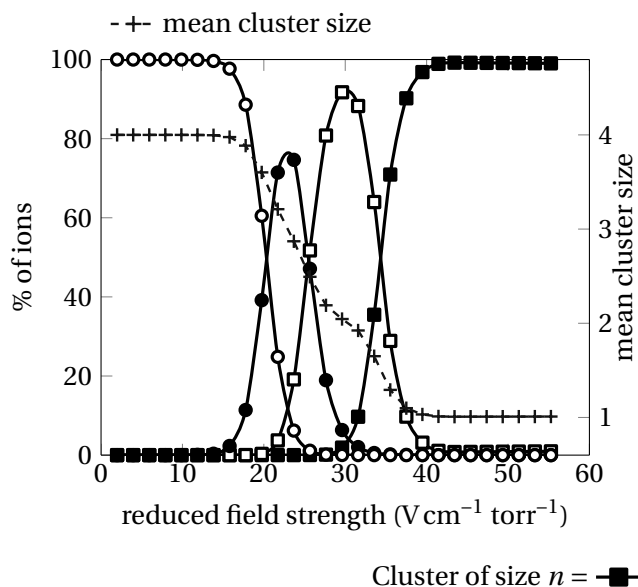
reduced pressure conditions, so that ions can gain comparably large collision energies from the electric field and simultaneously a gas density which allows in a considerable collision probability are typically present in the transfer stages of commercial AP-MS instruments [204]. Thus, the possibly massively increasing ion temperature in such ion transfer setups leads to potentially strong chemical effects on the transferred analyte ions. This is one motivation to assess the applicability of the derived ion temperature model and the modified RS method in combination with the estimated temperature dependent rate constants of the water clusters at such high reduced field strengths.

Young et al. have provided excellent experimental data [179], which serve as a basis for an assessment of the RS calculations. In those experiments, water cluster ions were deliberately destroyed (“declustered”) by controlled electrically driven collisions with neutral gas particles in a medium pressure collision cell and the resulting cluster distribution was analyzed by mass spectrometry. The pressure of the neutral gas in the collision region, in this case humidified oxygen with a water mixing ratio of 1.21 %, was in the range of 2.56 mbar (1.92 torr) which is similar to typical pressures in the first differential pumping stage of common commercial API-MS instruments. The right panel of figure 7.12 shows the original data analysis of the experiments (cf. [179]). Clearly, the initially present water clusters of size  $n = 4$  are collisionally dissociated to bare  $\text{H}_3\text{O}^+$  at a reduced field of  $50 \text{ V cm}^{-1} \text{ torr}^{-1}$ . At first glance it is surprising that at such humid conditions the largest present cluster in absence of a declustering field is only  $n = 4$ . In fact, the initial cluster distribution was not in thermal equilibrium due to electrical heating of the ions in a preceding drift cell [179]. The authors state that the initial present ion distribution consisted exclusively of clusters of size  $n = 4$  and all other observed ions result from collision induced water detachment.

This process was simulated with the modified RS algorithm in stand alone mode considering the field dependent ion temperature. RS was used to calculate the *equilibrium* concentrations of the water clusters under the variation of the reduced electrical field. Thus, the simulation assumes that the chemical system has sufficient time in the collision cell to reach equilibrium conditions. This assumption is most likely to be valid for the processes in the collision cell itself, since only collision induced dissociation and no cluster association reactions are relevant there. To reflect the non-equilibrium state of the cluster ions injected into the collision cell, the reaction system was limited to clusters of size  $n \leq 4$  in the simulation. Otherwise, at low reduced field, larger clusters would occur in the fully equilibrated state [177] in the calculations. Since nitrogen serves as collision partner (“M”) in the reaction system described in section 7.2.2 and the physical characteristics (e.g., collision cross sections) of nitrogen and oxygen do not strongly differ, the change of the collision gas probably does not noticeably affect the simulation results. Therefore, the estimated reaction rate constants of the water cluster system were used without modifications.

Since there are no experimental data available for the field dependent ion mobility of water cluster species in  $\text{O}_2$ , a series of simulations was performed to investigate the effect of different ion mobility functions. The ion mobilities of bare  $\text{H}_3\text{O}^+$  and the water clusters of size  $n = 2$  and 3 in *nitrogen* are comparably stable [200] up to a

## Best fit simulation



## Experimental data (as shown in [179])

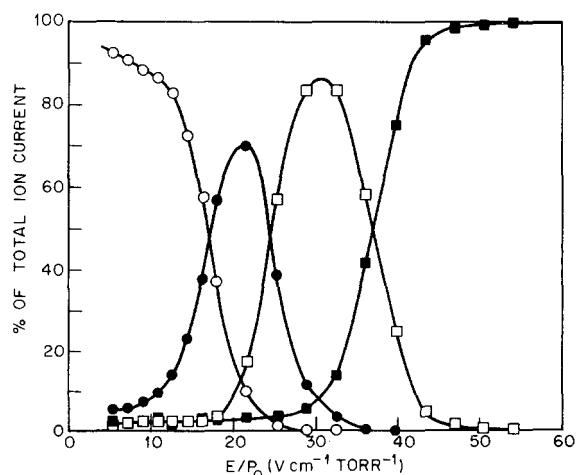


**Figure 7.12:** Results of the cluster destruction simulation in an intermediate pressure collision cell: The left panel shows the best fitting simulation results obtained with the modified version of RS including ion temperature modeling. The assumed static ion mobility in the ion temperature calculation was  $K_0 = 2.08 \times 10^{-4} \text{ m}^2 \text{ V}^{-1} \text{ s}^{-1}$  for all cluster species. The right panel was copied from [179] and shows experimental data. Despite the observable differences, the simulation shows a good qualitative agreement to the literature data.

reduced field strength of 100 Td. Therefore, in a first approximation the ion mobility was assumed to be constant.

The left panel of figure 7.12 depicts the results of the RS simulation, which fits best the experimental data. The assumed ion mobility was  $2.08 \times 10^{-4} \text{ m}^2 \text{ V}^{-1} \text{ s}^{-1}$  for *all* four cluster species. With this assumption, the calculation results are in good agreement to the experimental data shown on the right of figure 7.12: Both, the general shape of the individual water cluster peaks and the concentration ratios of the clusters are within the same range as the experimental data. However, a systematic divergence is also observed: In the calculated results, the field intensity interval in which the transition from cluster  $n = 4$  to bare  $\text{H}_3\text{O}^+$  takes place is considerably narrower. Despite the generally good agreement between the simulation and the experiment, the assumption of an identical ion mobility for all cluster species is rather

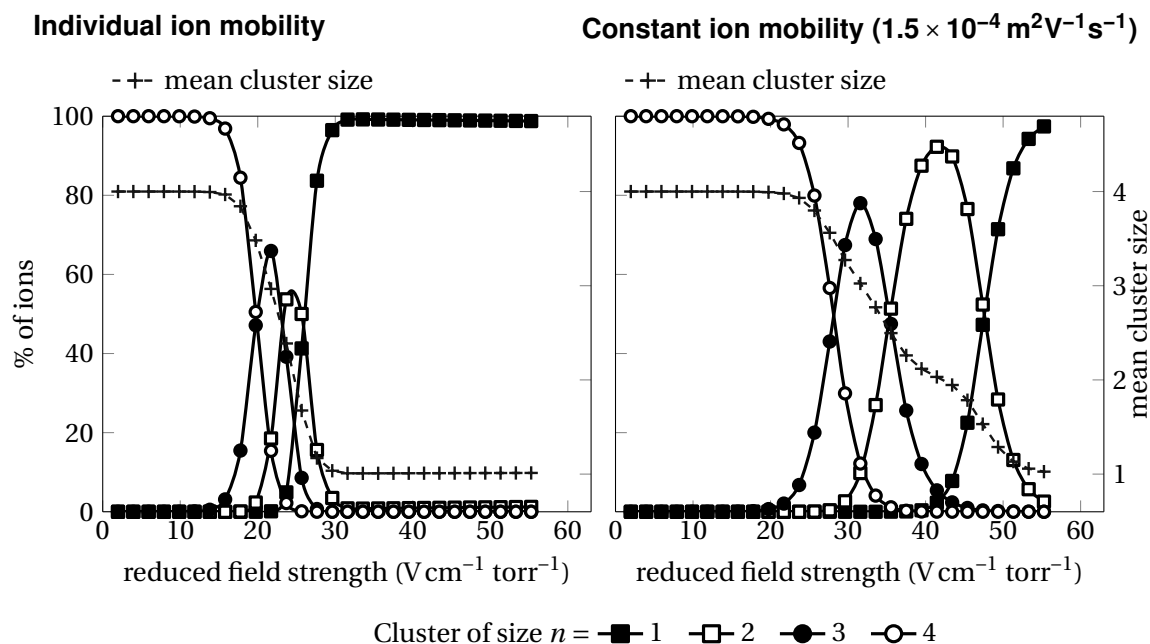


**Figure 7.13:** Effects of the assumed ion mobility of the cluster species on the simulation of the cluster destruction simulation in an intermediate pressure collision cell: The individual ion mobilities of the water clusters [200] for the simulation on the left panel were (given in  $10^{-4} \text{m}^2 \text{V}^{-1} \text{s}^{-1}$ )  $n = 1$ : 2.76,  $n = 2$ : 2.28,  $n = 3$ : 2.13 and  $n = 4$ : 2.09. On the right, a constant ion mobility of  $1.5 \times 10^{-4} \text{m}^2 \text{V}^{-1} \text{s}^{-1}$  was assumed.

questionable. Further simulations revealed that the calculation is susceptible to the ion mobility, which is not surprising due to the quadratic influence of  $K$  in equation 7.6. Figure 7.13 shows this effect with selected simulation results: The left panel shows a simulation with static ion mobilities of the water clusters of size  $n = 1$  to 3 which were individually determined in nitrogen [200]. The ion mobility of the cluster of size  $n = 4$  was taken from the estimation of SDS. In general, this simulation shows a similar response as observed experimentally: The water clusters are shifted towards bare  $\text{H}_3\text{O}^+$  with increasing field, but the deviation from the experiment is significantly higher: The relative intensities of the intermediate cluster species differ considerably from the experimental measurements and the field strength interval in which the cluster destruction occurs is much smaller than in the experiment. This is an expected result, since the ion mobilities are higher than in the best fit calculation presented in figure 7.12. In analogy, the decrease of the ion mobility dampens the effect of the electric field and higher field strengths are required to decluster the ions. This is shown in the right panel of figure 7.13.

The presented results show that the calculation approach reasonable models the

## 7 Simulation of reacting ions at AP

chemical behavior of water clusters under high field conditions. It is evident, that the field dependent ion mobility function is a critical parameter in this type of simulation. Therefore, a detailed investigation of the high field mobility of the modeled individual cluster species (or a valid model for  $\nu_d$  in equation 7.5) are required for actual high-quality simulations at increased reduced field strengths. Due to the lack of validated ion mobility functions, the simulation configuration presented in the left panel of figure 7.12, which lead to a good qualitative agreement with the experimental data, serves as a basis for the calculations presented in the following sections.

### 7.3.2.3 Trajectories of water cluster ions in an ion funnel

An important element in ion transfer stages at intermediate pressures is the *ion funnel* [3]. This device consists of a series of stacked electrodes with a converging circular inner orifice, which results in a funnel like shape viewed in the axial cross section. An electric RF field is applied between the adjacent electrodes and an additional DC voltage gradient is established along the electrode stack [205, 206]. In this geometry, ions are repelled from the ring electrodes and are in consequence focused due to the converging inner diameter of the funnel device. Simultaneously, the background gas pressure is reduced by pumping the bulk gas through the gaps between the electrodes.

The trajectories of reacting water cluster ions in an exemplary ion funnel were simulated with SIMION and RS at an intermediate background gas pressure of 133 Pa. At such pressures, the assumptions of SDS become invalid, therefore the discrete hard sphere collision model HS1 was used for the calculations. The simulated electrode geometry was taken from the ion funnel example, which is shipped with SIMION 8. The simulated funnel consists of 16 converging electrodes, 0.5 mm thick and with 0.5 mm gaps between the electrodes. The spatial resolution of the SIMION electrode geometry was 0.125 mm per grid unit, as presented in figure 7.14. The potential on the electrodes was controlled by the original user program of the SIMION ion funnel example. The RF voltage between the electrodes and the RF frequency was controlled via adjustable variables. All simulations were performed with an RF frequency of 500 kHz and amplitudes ranging from 50 to 100 V. A gentle linear DC gradient of 32 V was applied to induce a directed forward motion of the ions in the funnel. The collision gas in the funnel was nitrogen at 1.33 mbar. The gas was assumed to be static, no bulk gas flow was assumed in the exemplary simulations. Since the bulk gas pressure is still relatively high for an explicit hard sphere collision model like HS1, leading to a relatively high collision frequency and therefore a significant numerical effort, the number of simulated particles was limited to 200 ions. As in the best fit calculation presented in the preceding section (figure 7.12), the ion mobilities of all water cluster species were assumed to be constant with a value of  $2.08 \times 10^{-4} \text{ m}^2 \text{ V}^{-1} \text{ s}^{-1}$ . The calculations were initialized with water clusters of size  $n = 6$ .

Figure 7.14 depicts the results of two exemplary simulation runs. It is clearly observable that the water clusters are rapidly shifted down to bare  $\text{H}_3\text{O}^+$  in the funnel. The ion trajectories clearly indicate the region near to the electrodes where the RF

### 7.3 An outlook towards ion temperature simulation

field induces high reduced field strength and therefore high ion temperatures. It is apparent that even with a gentle configuration of the ion funnel (50 V RF amplitude in figure 7.14), the water cluster ions become hot enough to be shifted down to size 1, at least when penetrating deeper into the funnel. The increase of the RF amplitude has only a gentle effect on the temporal evolution of the relative concentrations of the cluster species. Instead, the mean cluster size is immediately reduced to 4 in the first simulation time steps when the RF amplitude is increased to 150 V (cf. right panel of figure 7.14). The further temporal development of the cluster system is similar to 50 V but starts with a lower mean cluster size in the calculation with 150 V. The effect of the RF amplitude is also notable in the spatial distribution of the cluster size as illustrated by the simulated ion trajectories: The area in which the clusters are shifted down to bare  $\text{H}_3\text{O}^+$  becomes larger with an increasing RF amplitude.

Even if the presented simulations are of a qualitative nature only and are not experimentally validated, they strongly support the notion that in most common RF ion guides with similar residual gas pressures it is readily possible to reach high effective ion temperatures. This also leads to a shift of systems as the proton bound water clusters which would strongly affect the chemical dynamics in such devices since the declustered species often exhibit very different and mostly increased reactivities than larger clustered species [181, 207]. The results presented in this section show that the numerical simulation of such processes at intermediate pressures is possible with SIMION-HS1 and RS, if the interesting reaction systems are known and critical simulation parameters, as the field dependent ion mobility function required the ion temperature calculation, can be estimated with sufficient precision.

7 Simulation of reacting ions at AP

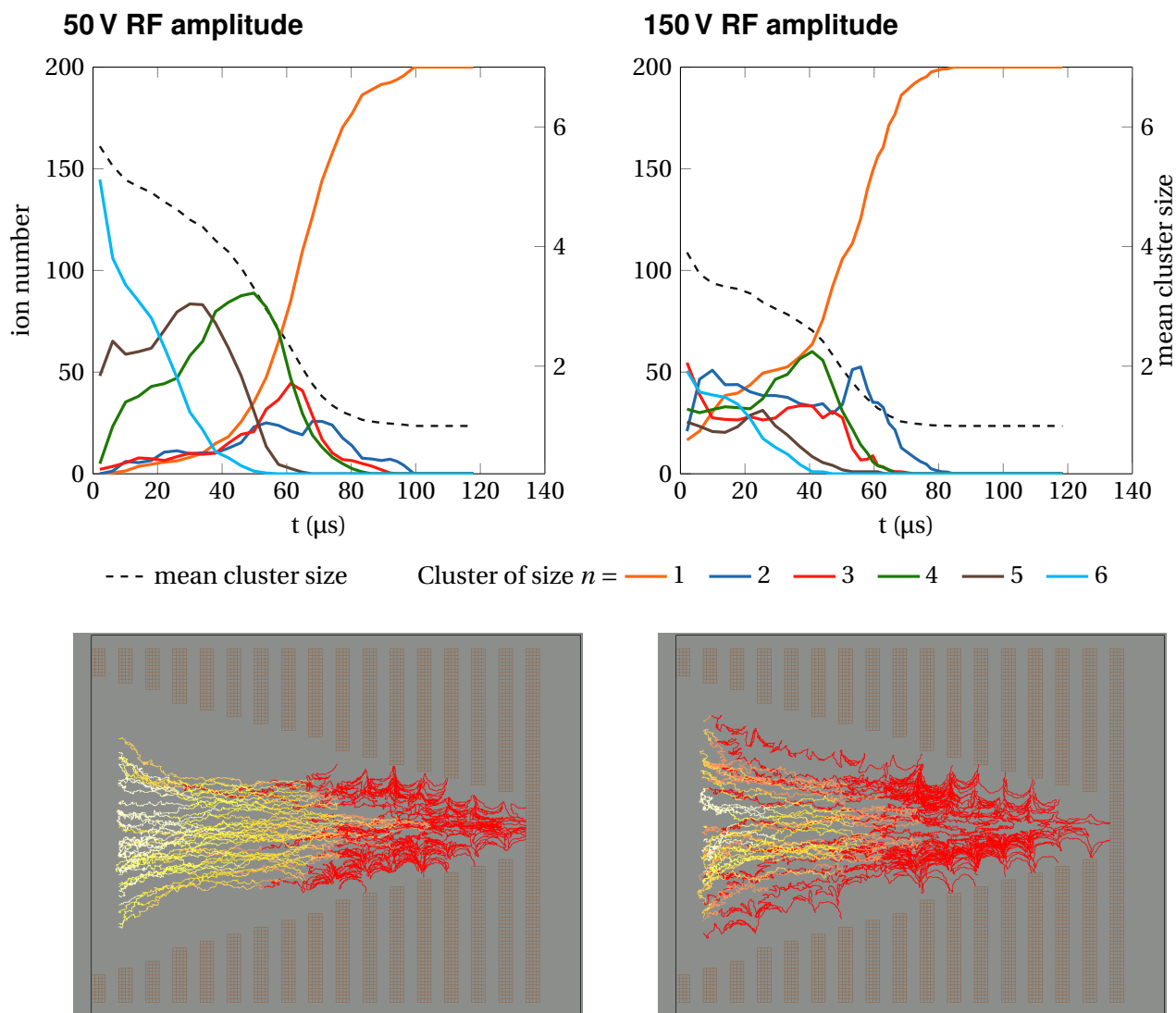


**Figure 7.14:** Simulation of the water cluster destruction in a medium pressure ion funnel with modified SIMION-RS: The ion trajectories of reacting water cluster ions in a medium pressure ion funnel (1.33 mbar background pressure) were simulated with SIMION-RS in combination with the HS1 hard sphere collision model. The ion trajectories in the lower panels were colored according to the cluster sizes, larger clusters ( $n = 5 - 6$ ) appear yellow, smaller clusters ( $n = 1 - 2$ ) appear red. The upper panels depict the temporal development of the cluster concentrations.

#### 7.3.2.4 Water cluster ions in a differential mobility separation device

As already mentioned in section 7.2.1, differential ion mobility spectrometry (DMS) which is also referred to as FAIMS, is a method which utilizes the characteristic difference between the high and low field electrical mobilities of ions to separate analytes [156, 159, 187]. Despite the physical effects, which also lead to a differential mobility, the kinetics of the clustering processes at elevated field strengths is one of the most relevant causes for the occurrence of differential mobilities of reactive ion molecule clusters. In fact, actual DMS experiments show a strong influence of parameters as the background concentration of water, which generally serves as clustering agent, on the differential mobility of distinct analyte molecules and the signal of the proton bound water clusters itself, which corresponds to the water cluster RIP in IMS [208]. Therefore, it should be possible to at least qualitatively reproduce the dynamics leading to a chemically induced differential mobility with a simulation in RS.

A classical DMS device is an arrangement of two plate electrodes with a small gap in between [187]: Analyte ions are transported through this gap by a gas flow, typically at atmospheric pressure. For the differential mobility analysis, an asymmetric high voltage RF waveform (called a dispersion field) is applied to the electrodes. This induces a drift motion according to the ion mobilities at the high and low field potentials, which is perpendicular to the flow of the transport gas. Therefore only ions for which this perpendicular drift motion is compensated pass through the DMS analyzer. By applying a variable DC compensation voltage, the passing differential mobilities are selected and by scanning this compensation voltage, a differential mobility spectrum is recorded.

The dynamics of the proton bound water cluster system under the influence of a DMS dispersion field were simulated with RS in stand alone mode. To allow such simulations, the Lua code which defines an asymmetric square waveform and an asymmetric superposition of two sine functions, are typically used in DMS devices, was taken from the user program of the FAIMS example of SIMION 8 and was integrated in the stand alone version of RS. The effective ion temperature calculation was performed with a constant mobility of  $2.08 \times 10^{-4} \text{m}^2 \text{V}^{-1} \text{s}^{-1}$  for all cluster species similar the simulations of the ion trajectories in the ion funnel presented in the preceding section. The temperature dependent reaction system of the proton bound water clusters was used as defined in section 7.3.1.

Figure 7.15 shows the temporal evolution of the water cluster concentrations in selected simulations with a RF frequency of 500 and 900 kHz and a dispersion field amplitude of  $19 \text{kV cm}^{-1}$ , which corresponds to values in DMS experiments [208]. The calculations clearly show that the chemical system is instantaneously responding to the rapid oscillation of the electric field and thus the ion temperature, even at comparably low water mixing ratios of 100 ppmV. This is due to the extremely high overall reaction rate of the water cluster system. With increased water cluster concentration, the chemical oscillations are also stronger, since the reaction rates of the cluster asso-

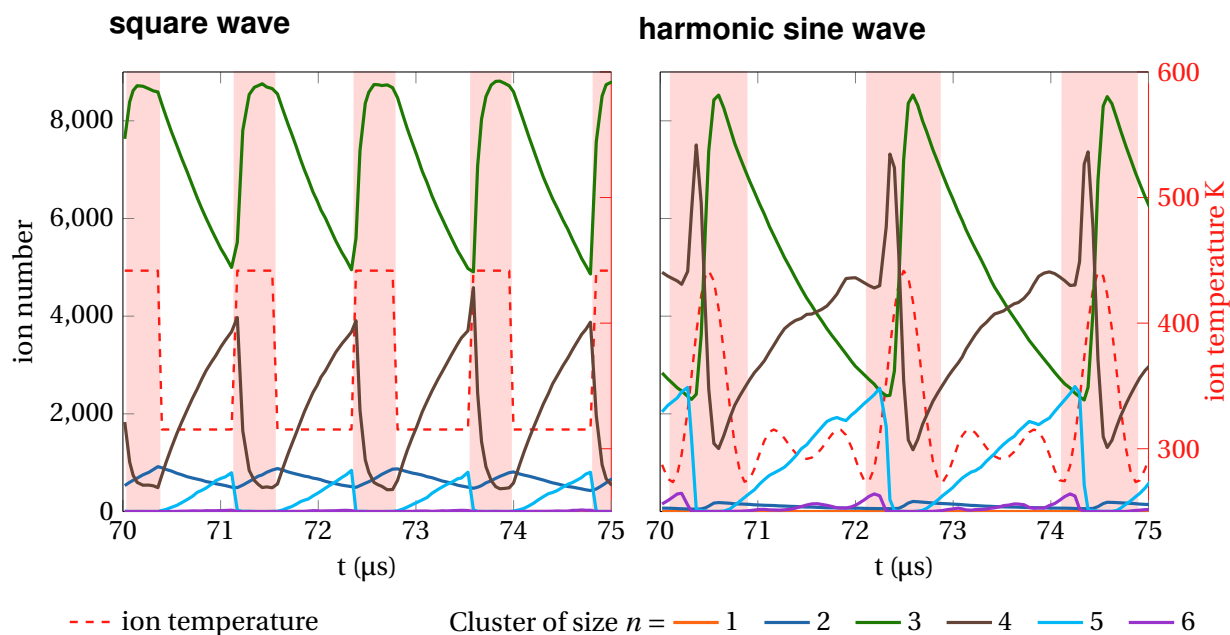


**Figure 7.15:** Section from the temporal development of the water cluster concentrations in a DMS/FAIMS field: The water cluster distribution was simulated with the modified RS algorithm in stand alone mode, assuming ideally stirred conditions. The simulated dispersion voltage was  $19 \text{ kV cm}^{-1}$  at atmospheric pressure (1 bar). The high field phases are marked by a red background. The ion temperature (drawn red dashed) constantly changes due to the varying field, which leads to an oscillation of the chemical system. As a result, the mean cluster concentrations in the high and low field phases differ which can be utilized for separation of chemical species. The amplitude of the chemical oscillation depends obviously on the RF amplitude and frequency but also on the chosen RF waveform as shown.

ciation reactions increase. Figure 7.15 shows that in common DMS devices, even at atmospheric pressure, the effective ion temperature changes readily exceed 100 K. The chemical cause for differential ion mobility also observable in figure 7.15: With both presented dispersion waveforms, which have a pronounced effect on the chemical oscillations, the mean cluster size in the high field phases (marked red) and the low field phases differ significantly. In every high field phase, cluster  $n = 4$  is destroyed and the concentration of cluster  $n = 3$  increases promptly. In the low field phase, the chemical system relaxes back to the initial state and the cluster size is shifted back to cluster  $n = 4$ .

### 7.3 An outlook towards ion temperature simulation

**Calculation of theoretical compensation voltage** It is possible to calculate the theoretical compensation voltage from the simulated mean cluster sizes in the high and low field phases. In a classical DMS experiment, an analyte ion passes through the device if the different distances traveled by the ion in the high and in the low field phase are compensated by the variable DC compensation voltage  $V_c$ . The distance  $d$  an ion travels is given by the product of ion mobility, field strength, and time:  $d = KEt$ . Therefore, the ion passes through the DMS device if

$$K_l t_l (V_l - V_c) = K_h t_h (V_h + V_c) \quad (7.11)$$

where the index  $l$  indicates low field and  $h$  indicates high field conditions. The field strength  $E$  can be expressed directly as voltage  $V$  on the electrode since the gap between the electrodes does not change between the low and high field phase. The compensation voltage is then

$$V_c = \frac{K_l V_l t_l - K_h V_h t_h}{K_l t_l + K_h t_h} \quad (7.12)$$

For the typical asymmetric waveform in DMS is  $V_h = 2V_l$  and therefore  $t_l = 2t_h$ .  $V_c$  is then

$$V_c = \frac{2(K_l - K_h) V_l}{K_h + 2K_l} \quad (7.13)$$

The mean electric mobility of the reacting cluster ions in both field phases can be calculated from the individual cluster mobilities weighted with the relative concentrations.

Expression 7.13 was used to calculate the theoretical compensation voltage. The results are depicted in figure 7.16. The simulation results show that the compensation voltage of the water cluster signal (referred to as “RIP” in [208]), which corresponds in principle to the  $\alpha$  function, is strongly dependent on the amplitude of the dispersion field and the water mixing ratio in the bulk gas. Similar findings are also reported in DMS experiments [208]. Fortunately, even the quantitative values of the compensation voltage predicted by the calculation agree well with the experimental data. As a consequence, it is in principle possible to simulate the ion trajectories in a DMS device with SIMION and RS, similarly to the presented calculations of ion trajectories in the ion funnel. This was demonstrated in proof of concept simulations. However, the temporal resolution in the calculation of such trajectories has to be relatively high, due to the fast oscillation of the dispersion field. This leads to a low numerical performance which renders such trajectory simulations difficult for high numbers of simulated particles. Nevertheless, with the future development and optimization of the user program interface of SIMION, such ion trajectory simulations will readily become possible for statistically significant numbers of simulated ions. Again, as already stated for the other presented simulations of the chemical kinetics of reactive ions, the most challenging part of such simulations is certainly the identification of the individual critical reactions of a potentially very complex reaction system and

## 7 Simulation of reacting ions at AP

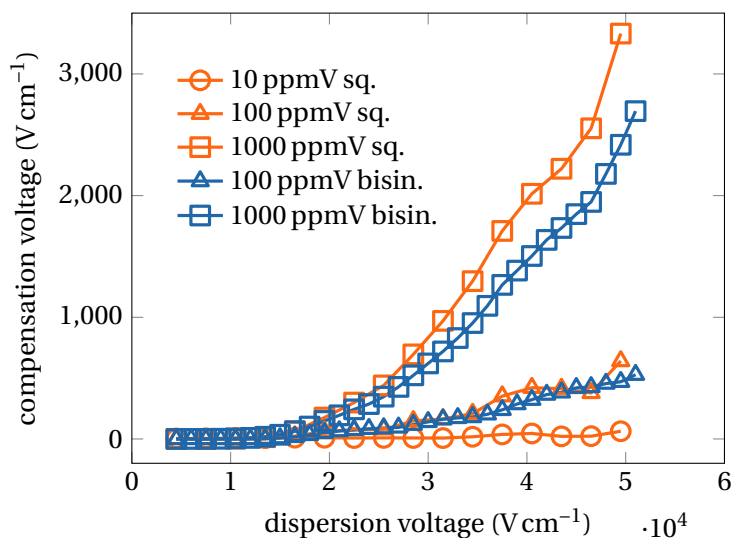


**Figure 7.16:** Simulated differential ion mobility: Dependence of the calculated DMS compensation voltage on the dispersion voltage for different background water concentrations and RF wave forms. (square wave - *sq.* or harmonic sine wave - *bisin.*). The results agree qualitatively well with experimental data known from the literature [208].

the estimation of the according temperature dependent reaction rate constants. In combination with a model of the purely physical field effects on the ion mobility, which is also an ongoing current research effort, RS would provide a general applicable basis for the modeling of ion dynamics in a DMS/FAIMS device.

### 7.3.3 Conclusions

The presented results demonstrate that a simulation of the chemical effects of a field induced increased ion temperature is possible on common computer hardware. The coupling of HS1 with RS allows the calculation of trajectories of reacting ions at medium or even low pressure conditions, while SDS in combination with RS allows this for atmospheric background pressure. However, several fundamental parameters of the simulated ions and their reaction system have to be known for a valid simulation. Particularly, the high field ion mobility function is such a critical parameter, since it potentially affects the effective ion temperature severely.

Often, such parameters cannot be readily estimated from fundamental characteristics of the simulated particles, which is particularly true for high field mobilities. In this case, purely empirical values, which are not yielded by a sophisticated theoretical framework, are still sufficient for valid productive simulations. For example, the presented calculated compensation voltages of the DMS model fit good with experiments, despite the fact that the high field mobilities of the clusters were roughly estimated

### 7.3 *An outlook towards ion temperature simulation*

from the results of the cluster dissociation in an intermediate pressure collision cell.

The results presented here strongly suggest that increased effective ion temperatures and the resulting chemical effects generally have to be considered in the modeling of the transfer of reactive ions into a mass analyzer. This holds true for a lot of organic analyte molecules. Typically, they are either part of a more or less reactive cluster system, which also includes the formation of analyte dimers, or can react with cluster species which potentially result from electric heating of cluster ions. Thus, the chemistry in ion transfer stages is very likely of general interest for the majority of actual problems in chemical analysis utilizing API-MS.

Subsequent work should focus on other chemical systems and the improvement of the effective ion temperature model. It was demonstrated elsewhere that the method presented here is basically applicable to further cluster systems [177]. An improved ion temperature model could be founded on a fundamental theory of the ion motion in gases but in the foreseeable future such a model will have to rely primarily on empirical and estimated parameters due to the current state of the basic theory. In summary, the efforts of setting up a simulation with the modified RS approach, is justified by the deep insight in the complex chemical dynamics of reactive ions which is crucial for a complete picture of modern mass spectrometric instruments.

## 8 Final conclusions and outlook

The initial goal of this work was to utilize available numerical methods, namely SIMION and SDS, to support the investigation of the dynamics of analyte ions in the MPIS, which is a commercial AP ion source. The available experimental data which reflect the conditions in the MPIS, albeit in a highly convoluted way, were the spatially resolved distributions of ion acceptance (DIA). For a numerical calculation of such distributions, an infrastructure was developed to transform the provided CFD simulation data of the MPIS and to automatize the simulation process, the result data analysis, and its visualization. The results of the DIA calculations show that the initial goal was achieved: Even under the very complex conditions of the non-stationary and probably oscillating bulk gas flow in the MPIS, the combination of CFD simulation, SIMION and SDS were able to qualitatively predict the experimentally determined DIA. The numerical model was also reproducing the experimentally observed dynamic changes in the ion acceptance distributions in dependence on ion source parameters as electric potentials and gas flows. This agreement of theoretical and experimental DIA lead to the notion that the individually simulated ion trajectories also essentially depict the physical reality in the AP ion source. This information is a valuable source for the further optimization of a high gas flow ion source as the MPIS. Further, it was shown that new ion source blueprints can be numerically assessed in detail without the requirement of physical fabrication. Nevertheless, it should be noted here that despite the valuable possibilities of the presented simulation methods the generation of an ion source model requires a significant amount of effort. Particularly, the fluid dynamic simulation of complex ion source geometries generally becomes demanding and generally requires an experienced modeler. Therefore, one has to evaluate individually if a fully validated numerical model as presented in this work is worth the required effort for a given problem.

Before the DIA simulations were conducted, the SIMION-SDS model and a continuous model in Comsol were validated with a simple benchmark problem. In analogy to the DIA simulations, a software tool chain was developed to allow the generation of appropriate input from the CFD simulation in Comsol, the automation of the SIMION/SDS simulations and the analysis of the simulation results. The comparison of both numerical models revealed that the SIMION/SDS model produced significantly better simulation results with less modeling efforts than the continuous Comsol model. In the meantime improved particle bases Comsol models were published which probably significantly increase the applicability of Comsol for ion trajectory simulations at AP. However, the purely continuous description of the ion migration (i.e.

electro-kinetic flow) turned out to be considerable less appropriate for the modeling of the ion motion under the conditions of the benchmark model.

In the third part of this work, with RS a newly developed Monte-Carlo model for the chemical kinetics of reactive ions was presented. This model, which integrates with SIMION, SDS and HS1, allowed an accurate simulation of the drift time of proton bound water clusters (water cluster RIP) in an AP-IMS. To achieve this, thermochemical data from the literature were used to estimate the actual rate constants of the water cluster formation and destruction reactions. The high agreement of the simulated and experimentally observed water cluster RIP drift times in dependence on the background water concentration essentially validated both, the simulation approach and the derived reaction system. The detailed assessment of the numerical performance and stability of RS showed that statistically significant ion trajectory simulations incorporating chemical kinetics are possible on advanced consumer class computer hardware, even with the fast water cluster reaction system.

The extension of RS with a model of the field dependent effective ion temperature and the estimation of temperature dependent rate constants of the water cluster formation and destruction reactions was presented in the last section of this work. The validity of the temperature dependent rate constants was shown by the reproduction of water cluster RIP drift times in dependence on the temperature by SIMION-SDS and RS. It was demonstrated that the combination of a hard sphere collision model (HS1) with RS, which extends the applicability of SIMION-RS to intermediate pressure conditions. In addition, the simulation of a DMS separation stage showed that even under high pressure conditions a field driven increased ion temperature severely affects the chemical kinetics of reactive ions. The good qualitative agreement between the simulated compensation voltage and the literature values underlines the general applicability of SIMION-RS on simulation problems as DMS or FAIMS.

In summary, this work demonstrates that it is possible to simulate the dynamics of reactive ions from atmospheric pressure conditions to intermediate pressures well below 1 mbar on affordable computer hardware, if the required input parameters, fluid dynamics of the bulk gas and relevant chemical reactions of the ions, are available. Possible future applications of the presented simulation methods are the development of an optimized high flow ion source and the detailed investigation of the cluster shift in RF ion guides which leads to an increased chemical reactivity of the resulting small clusters.

Despite the achieved good agreement between simulation and experiments, there are a number of opportunities to improve the presented simulation approach. Beside obvious optimizations like utilization of modern parallelized computing hardware (GPGPUs, multi core CPUs) which will probably become available with the next versions of SIMION, there are also some more fundamental deficiencies in the presented models. First, SDS originally only considered a static bulk gas flow field. It was readily possible to overcome this restriction in a basic proof of concept implementation of an extended, non-static version of SDS, which is able to consider a series of temporally resolved flow fields. This capability was not required for the calculations presented in

## 8 Final conclusions and outlook

this work since there was no temporally resolved CFD model of the MPIS available, but in future work non static flow fields will probably become relevant.

Another topic related to the effects of the bulk gas flow on the simulated ions is the consideration of turbulent diffusion in the ion trajectory simulation. It is likely that the additional diffusion induced by small scale turbulences in the bulk gas flow significantly affects the actual motion of the charged particles. In principle, it should be possible to derive an additional turbulent diffusion coefficient from the calculated parameters of a turbulence model of a CFD simulation, e.g. the turbulent kinetic energy and a turbulence scale parameter. The deduction of such a mapping however is complex and would be specific to a particular turbulence model. Nevertheless, further investigations in this topic are desirable, since even basic insights in this regard would potentially improve the simulation quality considerably.

The models presented in this work did not include regions of high space charge density. This is certainly not the case for many common AP ion sources which utilize a form of plasma as primary ionization source. Particularly a valid and complete model of an APCI source with a corona discharge as primary ion source inevitably has to include a capable space charge model. It is certainly possible to extend the capabilities of SIMION with an efficient simulation of the electrical force between the particles. Further, it is in principle even possible to implement a sophisticated particle-in-cell model to allow the simulation of the effects of the charged particles on the present electric field. However, it is also possible to choose a different basis which is better suited for such a model. A commercial product like Comsol, with its new particle tracing module, would provide such a basis but there are additional options. In particular, a mathematically highly capable open source framework like OpenFOAM<sup>1</sup> would provide a nearly ideal foundation for such a sophisticated extended ion trajectory model. The experience which was gained in the setup and analysis of the numerical simulations presented here would definitely provide a basis for the development of such new models. Certainly, one thing has become clear: This work only marks a starting point for the presented methods.

---

<sup>1</sup><http://openfoam.com>

## 9 Appendix

### 9.1 Deduction of viscous damping

In the following, the mean Stokes damping of an ion moving in a continuous fluid in a time step of a particle tracing simulation is deduced. This definition of the viscous damping is used in the SDS and viscous drag example models which are shipped with SIMION 8 [129, 172]. The original deduction was presented by D. Manura in the source code of the viscous drag model user program.

The acceleration due to viscous drag  $a_v$  acting on an ion moving with the relative velocity  $v_i$  in a continuous fluid is given by Stokes Law:

$$a_v = -k_0 v_i \quad (9.1)$$

The total acceleration  $a$  of the ion is the sum of the viscous acceleration and the acceleration due to electromagnetic forces  $a_e$ :

$$a = a_v + a_e \quad (9.2)$$

Due to the dependence of the viscous acceleration on the velocity, the change of  $a_v$  with the time  $t$  depends on the total acceleration:

$$\frac{da_v}{dt} = -k_0 \frac{dv}{dt} = -k_0 a \quad (9.3)$$

This ordinary differential equation is solved with the assumption of a very small change of  $a_e$ :

$$a(t) = e^{-k_0 t} (-k_0 v(0) + a_e) \quad (9.4)$$

with the initial velocity  $v(0)$  at  $t = 0$ . The average of the total acceleration in the time

## 9 Appendix

interval  $\delta t$  between two simulation time steps then becomes:

$$\bar{a} = \frac{1}{\delta t} \int_0^{\delta t} a(t) dt \quad (9.5)$$

$$= \frac{1}{\delta t} \int_0^{\delta t} e^{-k_0 t} (-k_0 v(0) + a_e) dt \quad (9.6)$$

$$= \frac{1 - e^{-k_0 \delta t}}{\delta t k_0} (a_e - k_0 v(0)) \quad (9.7)$$

$$= f(\delta t) * (a_e - k_0 v(0)) \quad (9.8)$$

This solution is the term given in section 3.3.1 in equation 3.17.

## 9.2 Linearization of reaction probabilities

As described in chapter 7 in section 7.1.1, the reaction simulation (RS) model uses a Monte-Carlo approach to calculate the chemical reaction kinetics of charged particles in the gas phase. In this approach, the local reaction probabilities  $p_r$  for all reactions are calculated for every ion in every time step.

In the following the detailed reaction probabilities for first, second, and third order elementary reactions are presented and it is shown that with sufficiently small time steps, the local reaction probability can be approximated by a linear function. This deduction was presented also in the JASMS contribution where the reaction simulation code was introduced [165].

### Unimolecular reactions

As presented in the introduction in section 2.3, the reaction kinetics of unimolecular decay (first order) reactions is equivalent to the kinetics of radioactive decay processes. The probability of a reaction event  $p(t)$  in dependence on the time  $t$  is given as [209]:

$$p(t) = 1 - e^{-kt} \quad (9.9)$$

with a reaction rate constant  $k$ . As figure 9.1 shows, this probability can be approximated by the linear function

$$p(t) \approx kt \quad (9.10)$$

for sufficiently small simulation time steps.

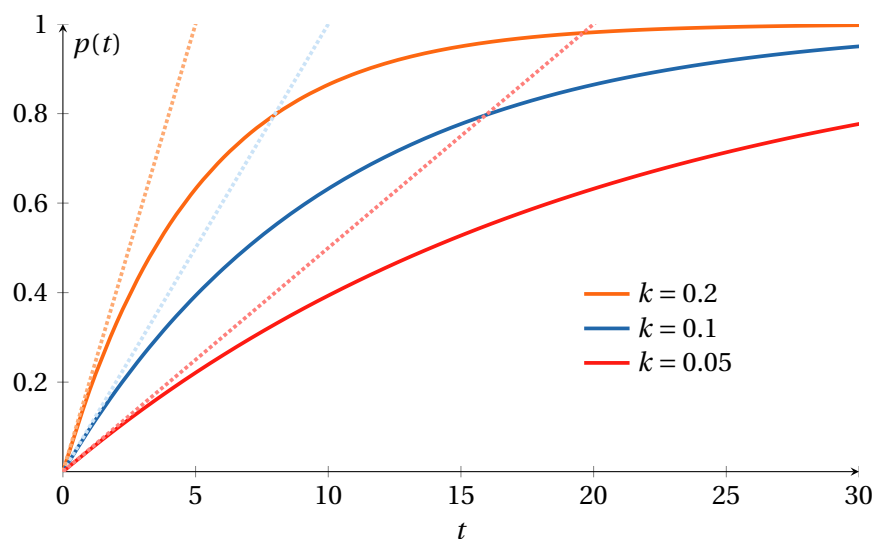


**Figure 9.1:** Plots of the unimolecular reaction probability  $p(t)$  and the linear approximation (dashed) for different individual static reaction probability constants  $k$ .

### Bimolecular reactions

In a bimolecular elementary reaction of the type  $A + B \rightarrow C$  with an ionic species A, there are non-reactive collisions, which are all collisions of particles of type A with any non reactive background component and potentially reactive collisions, which are all collisions of A with particles B. Further it is assumed, that the average probability for the reaction to take place in an eventually reactive collision event  $p$  is constant. Figure 9.2 shows a stochastic tree for multiple potentially reactive collisions. The basic pattern is obvious: A reaction event takes place after a series of collision events in which no reaction happened.

As figure 9.2 shows, the total probability of such a reaction is given by:

$$p_t = p + p(1-p) + p(1-p)^2 + p(1-p)^3 + \dots + p(1-p)^{n-1} \quad (9.11)$$

with the number of *potentially reactive* collisions  $n$ , which is proportional to the time  $t$ .

The tree graph in Figure 9.2 further reveals that the only path which does not contribute to  $p_t$  is the path in which *no* reaction takes place at all, with a probability of  $p_n = (1-p)^n$ . Therefore the total reaction probability is the complement of the probability of this path:

$$p_t = 1 - p_n = 1 - (1-p)^n \quad (9.12)$$

Figure 9.3 shows the total probability for different individual reaction probabilities in dependence on the reactive collisions. As seen in the figure, with sufficiently small

## 9 Appendix

time steps, which would lead to small numbers of potentially reactive collisions,  $p_t$  can be approximated by linear functions, which constitutes the actual approach of *RS*.

### **Termolecular reactions**

As presented in detail in section 2.3 termolecular reactions are generally comprised of at least two elementary steps of lower molecularity [29, 30], which can be modeled individually. Under high pressure conditions, termolecular reactions are often in the *high pressure limit*, and can be modeled as essentially bimolecular reactions [29].

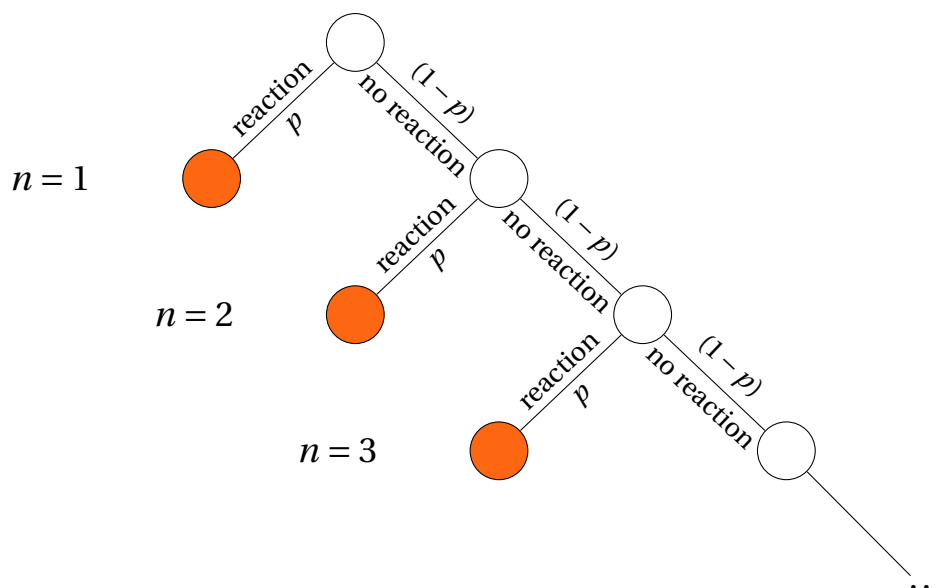


**Figure 9.2:** Probability tree for bimolecular reactions: In every potentially reactive collision (collision of a charged particle with a reaction partner) the reaction takes place with a probability  $p$  (successful reaction). If unsuccessful, the reaction can take place in the next potentially reactive collision with the same probability  $p$ .

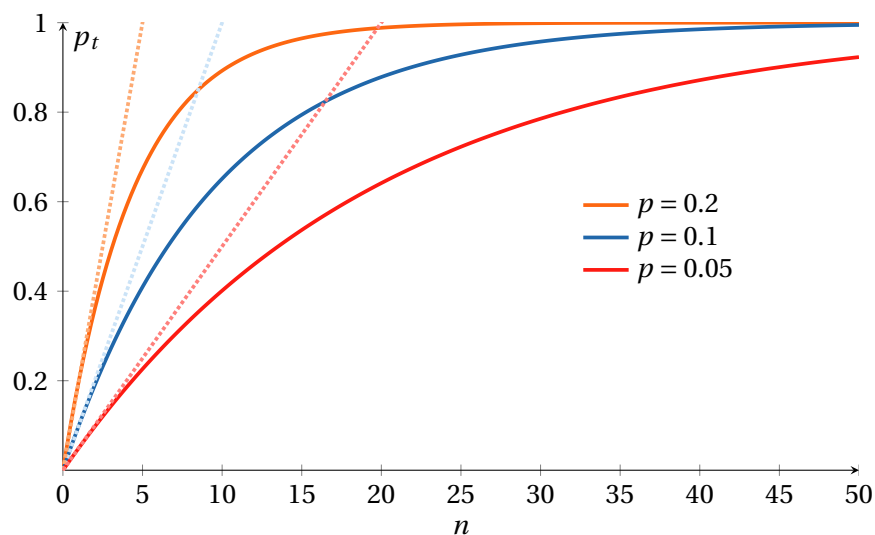


**Figure 9.3:** Plots of the bimolecular reaction probability  $p_t$  and the linear approximation (dashed) for different individual reaction probabilities  $p$ .

# Glossary

AP	.....	<u>A</u> tmospheric <u>P</u> ressure
APCI	.....	<u>A</u> tmospheric <u>P</u> ressure <u>C</u> hemical <u>I</u> onization
API	.....	<u>A</u> pplication <u>P</u> rogramming <u>I</u> nterface
API	.....	<u>A</u> tmospheric <u>P</u> ressure <u>I</u> onization
APLI	.....	<u>A</u> tmospheric <u>P</u> ressure <u>L</u> aser <u>I</u> onization
APPI	.....	<u>A</u> tmospheric <u>P</u> ressure <u>P</u> hoto <u>I</u> onization
CAD	.....	<u>C</u> omputer <u>A</u> ided <u>D</u> esign
CFD	.....	<u>C</u> omputational <u>F</u> luid <u>D</u> ynamics
CID	.....	<u>C</u> ollision <u>I</u> nduced <u>D</u> issociation
CK	.....	<u>C</u> hem <u>k</u> ed
DA-APPI	.....	<u>D</u> opant <u>A</u> ssisted <u>APPI</u>
DART	.....	<u>D</u> irect <u>A</u> nalysis in <u>R</u> eal <u>T</u> ime
DC	.....	<u>D</u> irect <u>C</u> urrent
DIA	.....	<u>D</u> istribution of <u>I</u> on <u>A</u> cceptance
DMS	.....	<u>D</u> ifferential <u>M</u> obility <u>S</u> pectrometry
DOF	.....	<u>D</u> egrees of <u>F</u> reedom
ESI	.....	<u>E</u> lectro <u>S</u> pray <u>I</u> onization
FAIMS	.....	<u>F</u> ield <u>A</u> symmetric <u>I</u> on <u>M</u> obility <u>S</u> pectrometry
FDM	.....	<u>F</u> inite <u>D</u> ifference <u>M</u> ethod
FEM	.....	<u>F</u> inite <u>E</u> lement <u>M</u> ethod
FVM	.....	<u>F</u> inite <u>V</u> olume <u>M</u> ethod
GC	.....	<u>G</u> as <u>C</u> hromatography
GUI	.....	<u>G</u> raphical <u>U</u> ser <u>I</u> nterface
HS	.....	<u>H</u> ard <u>S</u> phere
HV	.....	<u>H</u> igh <u>V</u> oltage
IE	.....	<u>I</u> onization <u>E</u> nergy
IMS	.....	<u>I</u> on <u>M</u> obility <u>S</u> pectrometry
LASER	.....	<u>L</u> ight <u>A</u> mplification by <u>S</u> timulated <u>E</u> mission of <u>R</u> adiation
LC	.....	<u>L</u> iquid <u>C</u> hromatography
MPI	.....	<u>M</u> ulti <u>P</u> hoton <u>I</u> onization
MPIS	.....	<u>M</u> ulti <u>P</u> urpose <u>I</u> on <u>S</u> ource
MS	.....	<u>M</u> ass <u>S</u> pectrometry
ODE	.....	<u>O</u> rdinary <u>D</u> ifferential <u>E</u> quation
PAH	.....	<u>P</u> olycyclic <u>A</u> romatic <u>H</u> ydrocarbon
PDE	.....	<u>P</u> artial <u>D</u> ifferential <u>E</u> quation

PI .....	<u>Photo Ionisation</u>
PIV .....	<u>Particle Image Velocitmetry</u>
REMPI .....	<u>Resonance Enhanced Multi-Photon Ionisation</u>
RF .....	<u>Radio Frequency</u>
RIP .....	<u>Reactant Ion Peak</u>
RS .....	<u>Reaction Simulation</u>
SDS .....	<u>Statistical Diffusion Simulation</u>
TIC .....	<u>Total Ion Current</u>
TOF .....	<u>Time of Flight</u>
UV .....	<u>Ultra Violet</u>
VTK .....	<u>Visualization Tool Kit</u>
VUV .....	<u>Vacuum Ultra Violet</u>
XML .....	<u>Extensible Markup Language</u>

## List of Symbols

$\delta t$	time interval / time step length
$\epsilon_0$	vacuum permittivity
$\lambda$	mean free path
$\mu$	dynamic viscosity
$\Phi$	electric potential
$\rho$	density
$\sigma$	collision cross section
$\vec{a}$	acceleration
$\vec{E}$	electric field vector
$\vec{F}$	force
$\vec{v}, \mathbf{u}$	velocity vector
$B$	magnetic field
$c$	concentration
$D$	diffusion coefficient
$K$	ion mobility
$k$	Boltzmann constant / reaction rate constant
$K_0$	reduced ion mobility
$M$	molar mass
$m$	mass
$p$	pressure
$q$	charge
$R$	universal gas constant
$T$	temperature
$t$	time
$T_{\text{eff}}$	effective ion temperature
$U$	voltage
$v_d$	drift velocity

## List of Tables

5.1	Parameters of the bulk gas flow simulation . . . . .	37
5.2	Parameters of the electrokinetic flow simulation . . . . .	39
5.3	Parameters of the particle tracing simulation . . . . .	40
6.1	Operational parameters of the AP ion source (MPIS) in the DIA measurements . . . . .	75
7.1	Thermodynamic parameters and rate constants of the formation and dissociation reactions for $[H + (H_2O)_n]^+$ clusters . . . . .	130
7.2	Reduced electrical ion mobilities for the individual proton bound water clusters . . . . .	139

# List of Figures

3.1	Example of a two dimensional discretized spatial domain . . . . .	19
3.2	Examples of parabolic one dimensional shape functions . . . . .	19
5.1	Schematic overview of the benchmark experiment. . . . .	35
5.2	Geometry of the measurement chamber used in the benchmark experiments . . . . .	36
5.3	Experimentally determined ion current in dependence of the deflection voltage for different mean bulk gas velocities . . . . .	42
5.4	Experimental determined ion current in dependence of the deflection voltage for different corona voltages and polarities . . . . .	43
5.5	Turbulent bulk gas flow simulation . . . . .	45
5.6	Laminar bulk gas flow simulation . . . . .	46
5.7	Three dimensional representation of turbulent bulk gas flow simulation . . . . .	47
5.8	Velocity profile of the bulk gas flow . . . . .	48
5.9	Simulation of static electric field in the measurement chamber . . . . .	49
5.10	SIMION simulation results: Simulated ion trajectories for $0.45 \text{ m s}^{-1}$ bulk gas flow . . . . .	50
5.11	SIMION simulation results: Simulated ion trajectories for $1.25 \text{ m s}^{-1}$ bulk gas flow . . . . .	51
5.12	SIMION simulation results: Simulated ion current for different bulk gas flow velocities . . . . .	53
5.13	SIMION simulation results: Simulated ion current for different ion mobilities and bulk gas flows . . . . .	54
5.14	SIMION simulation results: Effects of the turbulence model on the simulated ion current . . . . .	55
5.15	Comsol simulation results: Static steady state ion concentration distribution and flow lines of the total electrokinetic flow for different deflection voltages . . . . .	57
5.16	Comsol simulation results: Comparison of simulated ion current on receiver electrode with experimental data . . . . .	59
5.17	Comsol simulation results: Effects of variations of the ion mobility and the bulk gas velocity on the simulated ion current . . . . .	60
5.18	Comsol simulation results: Effects of the turbulence model on the simulated ion current . . . . .	61

5.19 Comsol simulation results: Effects of space charge modeling on the simulated ion current . . . . .	62
6.1 Schematics of photoionization modes . . . . .	67
6.2 Measurement of DIAs: Basic laser beam control . . . . .	68
6.3 Measurement of DIAs: Projection of volume elements . . . . .	69
6.4 Measurement of DIAs: Overlapping of volume elements . . . . .	70
6.5 Schematic overview of the transfer and pressure reduction stage of the microTOF . . . . .	71
6.6 Schematic overview of the experimental setup to measure DIAs . . . . .	73
6.7 Simulation domain of CFX model of the MPIS . . . . .	77
6.8 CFD data interpolation toolchain . . . . .	80
6.9 Electrode surfaces in SIMION MPIS model . . . . .	82
6.10 Scheme of the DIA simulation . . . . .	83
6.11 Screenshot of the Web DIA Explorer. . . . .	87
6.12 Simulated bulk gas velocity and flow lines in MPIS . . . . .	88
6.13 Simulated gas flow in the MPIS . . . . .	89
6.14 Flowline integration times for simulated gas flow in MPIS . . . . .	91
6.15 Simulated gas flow in the MPIS . . . . .	93
6.16 DIA: Capillary voltage variation, 2.0 L min <sup>-1</sup> dry-gas flow . . . . .	94
6.17 DIA: 1000 V capillary voltage, 2.0 L min <sup>-1</sup> dry-gas flow . . . . .	95
6.18 DIA: 1000 V capillary voltage, 3.8 L min <sup>-1</sup> dry-gas flow . . . . .	96
6.19 Experimental DIA: Dry-Gas dependent switching point . . . . .	98
6.20 Experimental and simulated DIA: Variation of the dry-gas flow . . . . .	99
6.21 Ion trajectory simulations and neutral analyte distribution . . . . .	101
6.22 Electric potential in MPIS . . . . .	102
6.23 Effect of the simulation geometry on the simulated DIA . . . . .	103
6.25 Effect of the ion mobility on the simulated DIA . . . . .	105
6.26 Effect of the ion destruction rate on the simulated DIA . . . . .	106
6.27 Effect of the bulk gas temperature on the simulated DIA . . . . .	107
6.28 Three dimensional DIA simulations . . . . .	109
6.29 Comparison of experimental and simulated temporally resolved cumulative ion signal . . . . .	111
6.30 Comparison of experimental and simulated minimal ion transfer times . . . . .	113
6.31 Effect of an artificial oscillation of the bulk gas flow . . . . .	114
6.32 Two dimensional projections of spatially resolved <i>mean</i> ion transfer time and DIA . . . . .	115
6.33 Two dimensional projections of spatially resolved <i>minimum</i> ion transfer time and DIA . . . . .	116
7.1 Schematic overview of the RS algorithm . . . . .	123
7.2 Scheme of the electrode geometry in the SIMION-RS simulations . . . . .	132

## List of Figures

7.3	Comparison of RS and Chemked: Temporal development of water cluster concentrations for 50 ppmV and 100 ppmV water mixing ratio . . . . .	135
7.4	Simulated relative water cluster equilibrium concentrations in dependence of the water mixing ratio . . . . .	136
7.5	Simulated and experimental drift times of water cluster RIP in dependence on the water mixing ratio . . . . .	138
7.6	Simulated drift time of water cluster RIP in dependence on the water mixing ratio under variation of the cluster dissociation rate constants . .	140
7.7	Comparison of the simulated and experimental temporally resolved ion signal of the water cluster RIP . . . . .	141
7.8	Effect of the particle number on the result of the RS simulation . . . . .	144
7.9	Effects of inappropriate time step length ( $\delta t$ ) on the RS simulation result	145
7.10	Calculated, temperature dependent rate constants of the cluster destruction (backward) rate constants of the water cluster system . . . . .	151
7.11	Results of the temperature dependent water cluster RIP simulation . . .	153
7.12	Results of the cluster destruction simulation in an intermediate pressure collision cell . . . . .	156
7.13	Effects of the ion mobility of the cluster species on the simulation of the cluster destruction in an intermediate pressure collision cell . . . . .	157
7.14	Simulation of the water cluster shift in a medium pressure ion funnel with modified SIMION-HS1-RS . . . . .	160
7.15	Temporal development of the water cluster concentrations in a DMS/-FAIMS field . . . . .	162
7.16	Simulated differential ion mobility . . . . .	164
9.1	Plots of the unimolecular reaction probability $p(t)$ and the linear approximation (dashed) for different individual static reaction probability constants $k$ . . . . .	171
9.2	Probability tree for bimolecular reactions . . . . .	173
9.3	Plots of the bimolecular reaction probability $p_t$ and the linear approximation (dashed) for different individual reaction probabilities $p$ . . . . .	173

## Bibliography

- [1] E. de Hoffmann and V. Stroobant. *Mass Spectrometry: Principles and Applications*. John Wiley & Sons, Chichester, 3rd edition, 2007.
- [2] W. M. Niessen. *Liquid Chromatography-Mass Spectrometry*. Chromatographic science series. CRC Press, Boca Raton, 3rd edition, 2006.
- [3] T. R. Covey, B. A. Thomson, and B. B. Schneider. Atmospheric pressure ion sources. *Mass spectrometry reviews*, 28(6):870–97, 2009.
- [4] C. G. Herbert and R. A. Johnstone. *Mass Spectrometry Basics*. CRC Press, Boca Raton, 2003.
- [5] R. A. Cairns. *Plasma Physics*. Springer Netherlands, Dordrecht, 1985.
- [6] A. Piel. *Plasma Physics*. Springer Berlin Heidelberg, Berlin, Heidelberg, 2010.
- [7] P. Atkins and J. De Paula. *Atkins' Physical Chemistry*. Oxford University Press, Oxford, 8th edition, 2006.
- [8] R. Mortimer. *Physical Chemistry*. Academic Press, Amsterdam, 3rd edition, 2008.
- [9] H. D. Young, R. A. Freedman, and L. Ford. *University Physics with Modern Physics*. Addison Wesley, 12th edition, 2007.
- [10] R. Fitzpatrick. Plasma Physics. Lecture Notes, 2011. <http://farside.ph.utexas.edu/teaching/plasma/plasma.html>.
- [11] G. Eiceman and Z. Karpas. *Ion Mobility Spectrometry*. CRC Press, Boca Raton, 2nd edition, 2004.
- [12] E. A. Mason and E. W. McDaniel. *Transport Properties of Ions in Gases*. Wiley-Interscience, New York, 1988.
- [13] F. Helfferich. *Ion Exchange*. Dover Publications, Mineola, 1995.
- [14] G. Eiceman and Z. Karpas. *Ion Mobility Spectrometry*. CRC Press, Boca Raton, 1st edition, 1993.
- [15] A. Engel von. *Ionized Gases*. American Institute of Physics, Woodbury, 1994.

## Bibliography

- [16] E. W. McDaniel and L. Viehland. The transport of slow ions in gases: Experiment, theory, and applications. *Physics Reports*, 110(5-6):333–367, 1984.
- [17] G. Wedler. *Physikalische Chemie*. Wiley-VCH Verlag GmbH, Weinheim, 3rd edition, 1989.
- [18] J. Crank. *The Mathematics of Diffusion*. Oxford University Press, Oxford, 1975.
- [19] H. Versteeg and W. Malalasekera. *An Introduction to Computational Fluid Dynamics: The Finite Volume Method Approach*. Prentice Hall, Essex, 1996.
- [20] Comsol AB. Comsol 4.2a - Chemical Reaction Engineering User's Guide. Software Manual, 2011.
- [21] C. Pozrikidis. *Fluid Dynamics: Theory, Computation, and Numerical Simulation*. Kluwer Academic Publishers, Dordrecht, 2001.
- [22] K. A. Hoffmann and S. T. Chiang. *Computational Fluid Dynamics (Vol. 1)*. Engineering Education System, Wichita, 2000.
- [23] T. Petrilă and D. Trif. *Basics of Fluid Mechanics and Introduction to Computational Fluid Dynamics (Numerical Methods and Algorithms)*. Springer, Boston, 2004.
- [24] R. P. King. *Introduction to Practical Fluid Flow*. Butterworth-Heinemann, Oxford, 2003.
- [25] J. Wilkinson and A. D. McNaught, editors. *Compendium of Chemical Terminology (Gold Book)*. Blackwell Scientific Publications, Oxford, 2nd edition, 1997.
- [26] J. I. Steinfeld, J. S. Francisco, and W. L. Hase. *Chemical Kinetics and Dynamics*. Prentice Hall, Upper Saddle River, 2nd edition, 1999.
- [27] C. Giles and O. University. *Chemical Kinetics and Mechanism*. Royal Society of Chemistry, Cambridge, 2002.
- [28] G. Raj. *Chemical Kinetics*. Krishna Prakashan, Meerut, 8th edition, 2010.
- [29] D. Jacob. *Introduction to Atmospheric Chemistry*. Princeton University Press, Princeton, 1999.
- [30] R. W. Carr, editor. *Modeling of Chemical Reactions*, volume 42 of *Comprehensive Chemical Kinetics*. Elsevier Science, Amsterdam, 2007.
- [31] J. H. Gross. *Mass Spectrometry: A Textbook*. Springer, Heidelberg, 2011.
- [32] L. N. Trefethen. The definition of numerical analysis. *Bulletin of the Institute for Mathematics and Applications*, 29:47–49, 1993.

- [33] H. R. Schwarz and N. Köckler. *Numerische Mathematik*. Vieweg+Teubner Verlag, Wiesbaden, 2011.
- [34] L. N. Trefethen. Numerical Analysis. In G. Timothy and J. Barrow-Green, editors, *Princeton Companion of Mathematics*, pp. 604–615. Princeton University Press, Princeton, 2006.
- [35] M. H. Kalos and P. A. Whitlock. *Monte Carlo Methods*. Wiley-VCH, Weinheim, 2008.
- [36] Comsol AB. Comsol 4.2a - Users Guide. Software Manual, 2011.
- [37] M. Jugroot, C. P. T. Groth, B. A. Thomson, V. Baranov, and B. A. Collings. Numerical investigation of interface region flows in mass spectrometers: ion transport. *Journal of Physics D: Applied Physics*, 37(4):550–559, 2004.
- [38] O. C. Zienkiewicz and R. L. Taylor. *Finite Element Method: Volume 1 The basis*. Butterworth-Heinemann, Oxford, 2000.
- [39] C. Ashcraft and R. G. Grimes. SPOOLES: An Object-Oriented Sparse Matrix Library. In *Proceedings of the ninth SIAM Conference on Parallel Processing for Scientific Computing*. San Antonio, Texas, 1999.
- [40] O. Schenk, K. Gärtner, and W. Fichtner. Efficient Sparse LU Factorization with Left-Right Looking Strategy on Shared Memory Multiprocessors. *BIT Numerical Mathematics*, 40(1):158–176, 2000.
- [41] C. T. Kelley. *Iterative Methods for Linear and Nonlinear Equations*. Society for Industrial and Applied Mathematics, Philadelphia, 1995.
- [42] M. Hanke-Bourgeois. *Grundlagen der Numerischen Mathematik und des Wissenschaftlichen Rechnens*. Vieweg+Teubner Verlag, Wiesbaden, 2008.
- [43] Comsol AB. Comsol 4.2a - Reference Guide. Software Manual, 2011.
- [44] A. I. Segal. Finite element methods for the incompressible Navier-Stokes equations. Lecture Script, Delft University of Technology, Delft, 2011. [http://ta.twi.tudelft.nl/users/vuik/burgers/fem\\_notes.pdf](http://ta.twi.tudelft.nl/users/vuik/burgers/fem_notes.pdf).
- [45] O. C. Zienkiewicz and R. L. Taylor. *Finite Element Method: Volume 3, Fifth Edition*. Butterworth-Heinemann, Oxford, 2000.
- [46] R. Eymard, T. Gallouet, and R. Herbin. Finite Volume Methods. In J. Lions and G. Ciarlet, editors, *Handbook of Numerical Analysis, Vol. 7, Solution of equations in  $R^n$  (pt. 3). Techniques of scientific computing (pt. 3)*, pp. 713–1020. North-Holland, 2000.

## Bibliography

- [47] Y. Saad. *Iterative Methods for Sparse Linear Systems, Second Edition*. Society for Industrial and Applied Mathematics, Philadelphia, 2nd edition, 2003.
- [48] J. H. Ferziger and M. Peric. *Computational Methods for Fluid Dynamics*. Springer Verlag, Berlin, 2001.
- [49] D. G. Robertson. *Relaxation Methods for Partial Differential Equations: Applications to Electrostatics*. Lecture Module, Otterbein University, Westerville, 2010.
- [50] D. J. Manura and D. A. Dahl. *SIMION Version 8.0 User Manual*. Scientific Instrument Services, Inc., Ringoes, NJ, 4. revised edition, 2008.
- [51] R. Plato. *Numerische Mathematik kompakt: Grundlagenwissen für Studium und Praxis*. Vieweg+Teubner Verlag, Wiesbaden, 3rd edition, 2006.
- [52] C. M. Lock and E. W. Dyer. Simulation of ion trajectories through a high pressure radio frequency only quadrupole collision cell by SIMION 6.0. *Rapid Communications in Mass Spectrometry*, 13(5):422–431, 1999.
- [53] L. Ding, M. Sudakov, and S. Kumashiro. A simulation study of the digital ion trap mass spectrometer. *International Journal of Mass Spectrometry*, 221(2):117–138, 2002.
- [54] A. Appelhans and D. A. Dahl. Measurement of external ion injection and trapping efficiency in the ion trap mass spectrometer and comparison with a predictive model. *International Journal of Mass Spectrometry*, 216(3):269–284, 2002.
- [55] A. Tolmachev, I. Chernushevich, A. Dodonov, and K. Standing. A collisional focusing ion guide for coupling an atmospheric pressure ion source to a mass spectrometer. *Nuclear Instruments and Methods in Physics Research Section B: Beam Interactions with Materials and Atoms*, 124(1):112–119, 1997.
- [56] J. Xu and W. B. Whitten. Monte Carlo simulation of ion transport in ion mobility spectrometry. *International Journal for Ion Mobility Spectrometry*, 11(1-4):13–17, 2008.
- [57] X. Xiong, W. Xu, X. Fang, Y. Deng, and Z. Ouyang. Accelerated Simulation Study of Space Charge Effects in Quadrupole Ion Traps Using GPU Techniques. *Journal of the American Society for Mass Spectrometry*, 23(10):1799–1807, 2012.
- [58] K. Saito, P. Corbitt, P. T. Reilly, E. Koizumi, and H. Koizumi. A Hybrid Approach to Calculating Coulombic Interactions: An Effective and Efficient Method for Simulations Ion Storage Device with SIMION. In *Proceedings of the 60th ASMS Conference on Mass Spectrometry and Allied Topics*. Vancouver, Canada, 2012.
- [59] A. D. Appelhans and D. A. Dahl. SIMION ion optics simulations at atmospheric pressure. *International Journal of Mass Spectrometry*, 244(1):1–14, 2005.

- [60] Scientific Instrument Services Inc. SIMION 8.0, 2008. <http://www.simion.com>.
- [61] J.-S. Chang, P. Lawless, and T. Yamamoto. Corona discharge processes. *IEEE Transactions on Plasma Science*, 19(6):1152–1166, 1991.
- [62] R. S. Sigmond. Simple approximate treatment of unipolar space-charge-dominated coronas: The Warburg law and the saturation current. *Journal of Applied Physics*, 53(2):891, 1982.
- [63] R. Hockney and J. Eastwood. *Computer Simulation Using Particles*. Taylor & Francis, New York, 1988.
- [64] V. Springel, S. D. M. White, A. Jenkins, C. S. Frenk, N. Yoshida, L. Gao, J. Navarro, R. Thacker, D. Croton, J. Helly, J. a. Peacock, S. Cole, P. Thomas, H. Couchman, A. Evrard, J. Colberg, and F. Pearce. Simulations of the formation, evolution and clustering of galaxies and quasars. *Nature*, 435(7042):629–36, 2005.
- [65] S. J. Aarseth. *Gravitational N-Body Simulations: Tools and Algorithms (Cambridge Monographs on Mathematical Physics)*. Cambridge University Press, Cambridge, 2003.
- [66] R. A. Serway and J. W. Jewett. *Physics for Scientists and Engineers*. Brooks Cole, Belmont, 2009.
- [67] D. E. Knuth. *Art of Computer Programming, Volume 1: Fundamental Algorithms*, volume 1. Addison Wesley, Reding, 1997.
- [68] A. V. Mariano, W. Su, and S. K. Guharay. Effect of space charge on resolving power and ion loss in ion mobility spectrometry. *Analytical Chemistry*, 81(9):3385–3391, 2009.
- [69] J. Barnes and P. Hut. A hierarchical  $O(N \log N)$  force-calculation algorithm. *Nature*, 324(6096):446–449, 1986.
- [70] J. Dawson. Particle simulation of plasmas. *Reviews of Modern Physics*, 55(2):403–447, 1983.
- [71] H. Matsumoto and T. Sato, editors. *Computer Simulation of Space Plasmas*. Advances in Earth and Planetary Sciences. Terra Scientific Publishing, Tokyo, 1985.
- [72] D. Seldner and T. Westermann. Algorithms for interpolation and localization in irregular 2D meshes. *Journal of Computational Physics*, 79(1):1–11, 1988.
- [73] G. Skölleremo. A Fourier method for the numerical solution of Poisson’s equation. *Mathematics of Computation*, 29(131):697–697, 1975.

## Bibliography

- [74] C. Birdsall and A. Langdon. *Plasma Physics via Computer Simulation*. Series in Plasma Physics. Institute of Physics Publishing, Bristol, 1991.
- [75] J. S. Bagla. TreePM: A code for cosmological N-body simulations. *Journal of Astrophysics and Astronomy*, 23(3-4):185–196, 2002.
- [76] Comsol AB. Comsol Multiphysics 4.2, Stockholm, 2011. <http://www.comsol.com>.
- [77] D. A. Dahl. SIMION for the personal computer in reflection. *International Journal of Mass Spectrometry*, 200(1-3):3–25, 2000.
- [78] R. Ierusalimschy. *Programming in Lua*. Lua.org, Rio de Janeiro, 2nd edition, 2006.
- [79] D. A. Dahl, T. R. McJunkin, and J. R. Scott. Comparison of ion trajectories in vacuum and viscous environments using SIMION: Insights for instrument design. *International Journal of Mass Spectrometry*, 266(1-3):156–165, 2007.
- [80] S. Prasad, K. Tang, D. Manura, D. Papanastasiou, and R. D. Smith. Simulation of ion motion in FAIMS through combined use of SIMION and modified SDS. *Analytical Chemistry*, 81(21):8749–8757, 2009.
- [81] Z. Baird, W.-P. Peng, and R. G. Cooks. Ion transport and focal properties of an ellipsoidal electrode operated at atmospheric pressure. *International Journal of Mass Spectrometry*, 330-332:277–284, 2012.
- [82] Y. Du, W. Wang, and H. Li. Bradbury–Nielsen–Gate–Grid Structure for Further Enhancing the Resolution of Ion Mobility Spectrometry. *Analytical Chemistry*, 84(13):5700–5707, 2012.
- [83] S. Barth and S. Zimmermann. Modeling Ion Motion in a Miniaturized Ion Mobility Spectrometer. In *Proceedings of the COMSOL Conference*. Hannover, Germany, 2008.
- [84] J. Langejuergen, P. Cochems, and S. Zimmermann. Results of a transient simulation of a drift tube ion mobility spectrometer considering charge repulsion, ion loss at metallic surfaces and ion generation. *International Journal for Ion Mobility Spectrometry*, 15(4):247–255, 2012.
- [85] Comsol AB. Comsol 4.2a - CFD Module User's Guide. Software Manual, 2011.
- [86] The Mathworks Inc. Matlab R2010a, 2010. <http://www.mathworks.com>.
- [87] J. W. Eaton and Gnu Octave Community. Gnu Octave, 2012. <https://gnu.org/software/octave/>.
- [88] Python Software Foundation. Python, 2010. <http://www.python.org/>.

- [89] R. Klein. *Algorithmische Geometrie: Grundlagen, Methoden, Anwendungen*. Springer, Berlin, Heidelberg, 2005.
- [90] M. de Berg, O. Cheong, M. van Kreveld, and M. Overmars. *Computational Geometry*. Springer, Berlin, Heidelberg, 2008.
- [91] SciPy Community. SciPy. <http://www.scipy.org/>.
- [92] A. P. Bruins. Mass spectrometry with ion sources operating at atmospheric pressure. *Mass Spectrometry Reviews*, 10(1):53–77, 1991.
- [93] M. Jugroot, C. P. T. Groth, B. a. Thomson, V. Baranov, and B. a. Collings. Numerical investigation of interface region flows in mass spectrometers: neutral gas transport. *Journal of Physics D: Applied Physics*, 37(8):1289–1300, 2004.
- [94] S. Klee, S. Albrecht, V. Derpmann, H. Kersten, and T. Benter. Generation of ion-bound solvent clusters as reactant ions in dopant-assisted APPI and APLI. *Analytical and Bioanalytical Chemistry*, 405(22):6933–6951, 2013.
- [95] C. N. McEwen and R. G. McKay. A combination atmospheric pressure LC/MS:GC/MS ion source: advantages of dual AP-LC/MS:GC/MS instrumentation. *Journal of the American Society for Mass Spectrometry*, 16(11):1730–1738, 2005.
- [96] T. Poehler, R. Kunte, H. Hoenen, P. Jeschke, W. Wissdorf, K. J. Brockmann, and T. Benter. Numerical simulation and experimental validation of the three-dimensional flow field and relative analyte concentration distribution in an atmospheric pressure ion source. *Journal of the American Society for Mass Spectrometry*, 22(11):2061–2069, 2011.
- [97] R. B. Cody, J. a. Laramée, and H. D. Durst. Versatile new ion source for the analysis of materials in open air under ambient conditions. *Analytical Chemistry*, 77(8):2297–2302, 2005.
- [98] M. Lorenz. *Räumlich und zeitlich aufgelöste Photoionisierung als Werkzeug zur Charakterisierung von Atmosphärendruckionenquellen in der Massenspektrometrie*. Dissertation, Bergische Universität Wuppertal, Germany, 2010. <http://elpub.bib.uni-wuppertal.de/servlets/DerivateServlet/Derivate-2469/dc1031.pdf>.
- [99] M. Lorenz, R. Schiewek, K. J. Brockmann, O. J. Schmitz, S. Gäb, and T. Benter. The distribution of ion acceptance in atmospheric pressure ion sources: spatially resolved APLI measurements. *Journal of the American Society for Mass Spectrometry*, 19(3):400–10, 2008.
- [100] O. J. Schmitz and T. Benter. Atmospheric pressure laser ionization (APLI). In A. Cappiello, editor, *Advances in LC-MS Instrumentation*, chapter 6. Elsevier B.V., Amsterdam, 2007.

## Bibliography

- [101] C. Y. Ng, editor. *Vacuum Ultraviolet Photoionization and Photodissociation of Molecules and Clusters*. World Scientific Publishing Co. Pte. Ltd., Singapore, 1991.
- [102] D. J. Butcher. Vacuum Ultraviolet Radiation for Single-Photoionization Mass Spectrometry: A Review. *Microchemical Journal*, 62(3):354–362, 1999.
- [103] D. B. Robb, T. R. Covey, and A. P. Bruins. Atmospheric Pressure Photoionization: An Ionization Method for Liquid Chromatography-Mass Spectrometry. *Analytical Chemistry*, 72(15):3653–3659, 2000.
- [104] M. Constapel, M. Schellenträger, O. J. Schmitz, S. Gäb, K. J. Brockmann, R. Giese, and T. Benter. Atmospheric-pressure laser ionization: a novel ionization method for liquid chromatography/mass spectrometry. *Rapid communications in mass spectrometry: RCM*, 19(3):326–36, 2005.
- [105] T. Benter. Atmospheric Pressure Laser Ionization MS. In M. Gross and R. M. Caprioli, editors, *The Encyclopedia of Mass Spectrometry Volume 6: Molecular Ionization Methods*. Elsevier Science, Oxford, 2007.
- [106] J. A. Syage, B. J. Nies, M. D. Evans, and K. A. Hanold. Field-portable, high-speed GC/TOFMS. *Journal of the American Society for Mass Spectrometry*, 12(6):648–55, 2001.
- [107] A. Raffaelli and A. Saba. Atmospheric pressure photoionization mass spectrometry. *Mass Spectrometry Reviews*, 22(5):318–331, 2003.
- [108] H. Kersten, V. Funcke, M. Lorenz, K. J. Brockmann, T. Benter, and R. O'Brien. Evidence of neutral radical induced analyte ion transformations in APPI and near-VUV APLI. *Journal of the American Society for Mass Spectrometry*, 20(10):1868–80, 2009.
- [109] D. B. Robb and M. W. Blades. Effects of solvent flow, dopant flow, and lamp current on dopant-assisted atmospheric pressure photoionization (DA-APPI) for LC-MS. Ionization via proton transfer. *Journal of the American Society for Mass Spectrometry*, 16(8):1275–1290, 2005.
- [110] C. Weikhardt, F. Moritz, and J. Grotemeyer. Account: Multiphoton ionization mass spectrometry: principles and fields of application. *European Journal of Mass Spectrometry*, 2(1):151–160, 1996.
- [111] J. R. Lakowicz, editor. *Principles of Fluorescence Spectroscopy*. Springer US, Boston, MA, 2006.
- [112] R. Schiewek, M. Schellenträger, R. Mönnikes, M. Lorenz, R. Giese, K. J. Brockmann, S. Gäb, T. Benter, and O. J. Schmitz. Ultrasensitive determination of polycyclic aromatic compounds with atmospheric-pressure laser ionization as an interface for GC/MS. *Analytical chemistry*, 79(11):4135–4140, 2007.

- [113] R. J. Cotter. *Time-of-flight mass spectrometry: instrumentation and applications in biological research*. ACS professional reference book. American Chemical Society, Washington DC, 1997.
- [114] R. Schiewek, M. Lorenz, R. Giese, K. Brockmann, T. Benter, S. Gäb, and O. J. Schmitz. Development of a multipurpose ion source for LC-MS and GC-API MS. *Analytical and Bioanalytical Chemistry*, 392(1-2):87–96, 2008.
- [115] F. R. Menter. Two-equation eddy-viscosity turbulence models for engineering applications. *Journal of the American Institute of Aeronautics and Astronautics*, 32(8):1598–1605, 1994.
- [116] H. Kersten. *Development of an Atmospheric Pressure Ionization source for in situ monitoring of degradation products of atmospherically relevant volatile organic compounds*. Dissertation, Bergische Universität Wuppertal, Germany, 2011. <http://elpub.bib.uni-wuppertal.de/servlets/DerivateServlet/Derivate-2085/dc1104.pdf>.
- [117] M. Wutz and H. Adam. *Theorie und Praxis der Vakuumtechnik*. Vieweg+Teubner Verlag, Braunschweig, 1988.
- [118] A. Michalke. Beitrag zur Rohrströmung kompressibler Fluide mit Reibung und Wärmeübergang. *Archive of Applied Mechanics*, 57(5):377–392, 1987.
- [119] J. Westerweel. Fundamentals of digital particle image velocimetry. *Measurement Science and Technology*, 8(12):1379–1392, 1997.
- [120] C. Tropea, A. L. Yarin, and J. F. Foss, editors. *Springer Handbook of Experimental Fluid Mechanics*. Springer Verlag, Berlin, Heidelberg, 2007.
- [121] M. Raffel, C. E. Willert, S. T. Wereley, and J. Kompenhans. *Particle Image Velocimetry*. Experimental Fluid Mechanics. Springer Verlag, Berlin, Heidelberg, 2007.
- [122] R. J. Adrian and J. Westerweel. *Particle Image Velocimetry*. Cambridge Aerospace Series. Cambridge University Press, New York, 2011.
- [123] C. B. Barber, D. P. Dobkin, and H. Huhdanpaa. The quickhull algorithm for convex hulls. *ACM Transactions on Mathematical Software*, 22(4):469–483, 1996.
- [124] Computational Engineering International Inc. EnSight version 10 User Manual. Software Manual, 2012. [http://www3.ensight.com/EnSight10\\_Docs/UserManual.pdf](http://www3.ensight.com/EnSight10_Docs/UserManual.pdf).
- [125] Kitware Inc. Paraview 3.8, 2010. <http://www.paraview.org/>.
- [126] VTK Developer Community. Visualization Toolkit (VTK). <http://www.vtk.org/>.

## Bibliography

- [127] W. Schroeder, K. Martin, and B. Lorensen. *Visualization Toolkit: An Object-Oriented Approach to 3D Graphics, 4th Edition*. Kitware Inc., 2006.
- [128] Kitware. *VTK User's Guide Version 11 (2010)*. Kitware Inc., 2010.
- [129] Scientific Instrument Services Inc. SIMION 8.1, 2011. <http://www.simion.com>.
- [130] R. A. Drebin, L. Carpenter, and P. Hanrahan. Volume rendering. *ACM SIGGRAPH Computer Graphics*, 22(4):65–74, 1988.
- [131] C. D. Hansen and C. R. Jhonson, editors. *The Visualization Handbook*. Elsevier, Burlington, 2005.
- [132] H. Ray, H. Pfister, D. Silver, and T. Cook. Ray casting architectures for volume visualization. *IEEE Transactions on Visualization and Computer Graphics*, 5(3):210–223, 1999.
- [133] J. D. Hunter. Matplotlib: A 2D graphics environment. *Computing In Science & Engineering*, 9(3):90–95, 2007.
- [134] D. Dale, M. Droettboom, E. Firing, and J. Hunter. Matplotlib Release 1.1.0, 2011. <http://matplotlib.org>.
- [135] NumPy Community. NumPy Reference, 2011. <http://docs.scipy.org/doc/numpy/reference/>.
- [136] D. Crockford. The application/json Media Type for JavaScript Object Notation (JSON). Request for Comments: 4627, Internet Engineering Task Force, 2006. <http://www.ietf.org/rfc/rfc4627.txt>.
- [137] jQuery Developer Community. jQuery, 2012. <http://jquery.com/>.
- [138] jQuery Developer Community. jQuery mobile, 2012. <http://jquerymobile.com/>.
- [139] W. Wißdorf, M. M. Lorenz, K. J. Brockmann, O. J. Schmitz, S. S. Gäb, and T. Benter. Determination of the Distribution of Ion Acceptance (DIA) of Atmospheric Pressure Ionization Sources. In *Proceedings of the 55th ASMS Conference on Mass Spectrometry and Allied Topics*. Indianapolis, IN, USA, 2007.
- [140] W. Wißdorf, M. Lorenz, H. Kersten, S. Klee, K. J. Brockmann, and T. Benter. Atmospheric Pressure Laser Ionization (APLI): Systematic DIA Measurements for APLI Method Development. In *Proceedings of the 57th ASMS Conference on Mass Spectrometry and Allied Topics*. Philadelphia, PA, USA, 2009.

- [141] T. Pöhler, R. Kunte, H. Hoenen, P. Jeschke, and T. Benter. Computational Fluid Dynamic Model of a Commercial Atmospheric Pressure Ion Source. In *Proceedings of the 59th ASMS Conference on Mass Spectrometry and Allied Topics*. Denver, CO, USA, 2011.
- [142] M. E. Swartz. UPLC™ : An Introduction and Review. *Journal of Liquid Chromatography & Related Technologies*, 28(7-8):1253–1263, 2005.
- [143] R. Plumb, J. Castro-Perez, J. Granger, I. Beattie, K. Joncour, and A. Wright. Ultra-performance liquid chromatography coupled to quadrupole-orthogonal time-of-flight mass spectrometry. *Rapid Communications in Mass Spectrometry*, 18(19):2331–2337, 2004.
- [144] M. Lorenz, K. J. Brockmann, W. Wißdorf, D. Klink, O. J. Schmitz, and T. Benter. Distribution of Ion Acceptance in a Fluid-dynamically Optimized Multi-purpose Ion Source. In *Proceedings of the 59th ASMS Conference on Mass Spectrometry and Allied Topics*. Denver, CO, USA, 2011.
- [145] M. Lorenz, W. Wißdorf, S. Klee, H. Kersten, K. J. Brockmann, and T. Benter. Spatially and temporally resolved atmospheric pressure laser ionization as a powerful tool for the characterization of ion sources: An overview. In *Proceedings of the 58th ASMS Conference on Mass Spectrometry and Allied Topics*. Salt Lake City, UT, USA, 2010.
- [146] W. Wißdorf. *Räumliche Ionenakzeptanzverteilungen (DIA) in der Atmospheric Pressure Laser Ionization Mass Spectrometry (APLI-MS)*. Master thesis, Bergische Universität Wuppertal, Germany, 2009. <http://www.walterwissdorf.de/science/master-thesis-DIA-in-der-APLI-MS>.
- [147] M. Lorenz, S. Klee, R. Mönnikes, A. L. Mangas Suarez, K. J. Brockmann, O. J. Schmitz, S. Gäb, and T. Benter. Atmospheric Pressure Laser Ionization (APLI): Investigations on Ion Transport in Atmospheric Pressure Ion Sources. In *Proceedings of the 56th ASMS Conference on Mass Spectrometry and Allied Topics*. Denver, CO, USA, 2008.
- [148] D. J. Manura and D. A. Dahl. *SIMION Version 8.1 Supplemental Documentation*. Scientific Instrument Services, Inc., Ringoes, NJ, 2012.
- [149] K. J. Brockmann, W. Wißdorf, M. Lorenz, D. Müller, T. Pöhler, R. Kunte, and T. Benter. Investigation of Ion Transfer Times in a commercial Atmospheric Pressure Ion Source. In *Proceedings of the 60th ASMS Conference on Mass Spectrometry and Allied Topics*. Vancouver, Canada, 2012.
- [150] M. Lorenz, R. Schiewek, K. J. Brockmann, A. L. Mangas Suarez, S. Gäb, O. J. Schmitz, and T. Benter. Investigations of Ionization Mechanisms present in Atmospheric Pressure Ion Sources using APLI. In *Proceedings of the 55th ASMS Conference on Mass Spectrometry and Allied Topics*. Indianapolis, IN, USA, 2007.

## Bibliography

- [151] D. C. Wilcox. *Turbulence Modeling for CFD*. DCW Industries, Inc., La Canada, 1994.
- [152] J. Sunner, G. Nicol, and P. Kebarle. Factors determining relative sensitivity of analytes in positive mode atmospheric pressure ionization mass spectrometry. *Analytical Chemistry*, 60(13):1300–1307, 1988.
- [153] V. Anicich. *An index of the literature for bimolecular gas phase cation-molecule reaction kinetics*. JPL Publication 03-19. Jet Propulsion Laboratory, National Aeronautics and Space Administration, 2003.
- [154] N. Bradbury and R. Nielsen. Absolute Values of the Electron Mobility in Hydrogen. *Physical Review*, 49(5):388–393, 1936.
- [155] A. T. Kirk, M. Allers, P. Cochems, J. Langejuergen, and S. Zimmermann. A compact high resolution ion mobility spectrometer for fast trace gas analysis. *The Analyst*, 138(18):5200–5207, 2013.
- [156] A. B. Kanu, P. Dwivedi, M. Tam, L. Matz, and H. H. Hill. Ion mobility-mass spectrometry. *Journal of Mass Spectrometry*, 43(1):1–22, 2008.
- [157] R. Mukhopadhyay. IMS/MS: its time has come. *Analytical Chemistry*, 80(21):7918–20, 2008.
- [158] A. A. Shvartsburg and R. D. Smith. Fundamentals of traveling wave ion mobility spectrometry. *Analytical Chemistry*, 80(24):9689–99, 2008.
- [159] B. M. Kolakowski and Z. Mester. Review of applications of high-field asymmetric waveform ion mobility spectrometry (FAIMS) and differential mobility spectrometry (DMS). *The Analyst*, 132(9):842–64, 2007.
- [160] R. Guevremont. High-field asymmetric waveform ion mobility spectrometry: A new tool for mass spectrometry. *Journal of Chromatography A*, 1058(1-2):3–19, 2004.
- [161] M. M. Shahin. Mass-Spectrometric Studies of Corona Discharges in Air at Atmospheric Pressures. *The Journal of Chemical Physics*, 45(7):2600–2605, 1966.
- [162] E. C. Horning, M. G. Horning, D. I. Carroll, I. Dzidic, and R. N. Stillwell. New picogram detection system based on a mass spectrometer with an external ionization source at atmospheric pressure. *Analytical Chemistry*, 45(6):936–943, 1973.
- [163] A. Good. Ion–Molecule Reactions in Pure Nitrogen and Nitrogen Containing Traces of Water at Total Pressures 0.5–4 torr. Kinetics of Clustering Reactions Forming  $H^+(H_2O)_n$ . *The Journal of Chemical Physics*, 52(1):212–221, 1970.

- [164] I. Dzidic, D. I. Carroll, R. N. Stillwell, and E. C. Horning. Comparison of positive ions formed in nickel-63 and corona discharge ion sources using nitrogen, argon, isobutane, ammonia and nitric oxide as reagents in atmospheric pressure ionization mass spectrometry. *Analytical Chemistry*, 48(12):1763–1768, 1976.
- [165] W. Wissdorf, L. Seifert, V. Derpmann, S. Klee, W. Vautz, and T. Benter. Monte Carlo Simulation of Ion Trajectories of Reacting Chemical Systems: Mobility of Small Water Clusters in Ion Mobility Spectrometry. *Journal of the American Society for Mass Spectrometry*, 24(4):632–641, 2013.
- [166] F. W. Karasek, S. H. Kim, and H. H. Hill. Mass identified mobility spectra of p-nitrophenol and reactant ions in plasma chromatography. *Analytical Chemistry*, 48(8):1133–1137, 1976.
- [167] P. Kebarle, S. K. Searles, A. Zolla, J. Scarborough, and M. Arshadi. Solvation of the hydrogen ion by water molecules in the gas phase. Heats and entropies of solvation of individual reactions:  $\text{H}^+(\text{H}_2\text{O})_{n-1} + \text{H}_2\text{O} \rightarrow \text{H}^+(\text{H}_2\text{O})_n$ . *Journal of the American Chemical Society*, 89(25):6393–6399, 1967.
- [168] Y. K. Lau, S. Ikuta, and P. Kebarle. Thermodynamics and kinetics of the gas-phase reactions  $\text{H}_3\text{O}^+(\text{H}_2\text{O})_{n-1} + \text{H}_2\text{O} = \text{H}_3\text{O}^+(\text{H}_2\text{O})_n$ . *Journal of the American Chemical Society*, 104(6):1462–1469, 1982.
- [169] T. Perl, E. Carstens, A. Hirn, M. Quintel, W. Vautz, J. Nolte, and M. Jünger. Determination of serum propofol concentrations by breath analysis using ion mobility spectrometry. *British Journal of Anaesthesia*, 103(6):822–827, 2009.
- [170] T. Perl, M. Jünger, W. Vautz, J. Nolte, M. Kuhns, M. Borg-von Zepelin, and M. Quintel. Detection of characteristic metabolites of *Aspergillus fumigatus* and *Candida* species using ion mobility spectrometry – metabolic profiling by volatile organic compounds. *Mycoses*, 54(6):e828–e837, 2011.
- [171] M. Jelezniak and I. Jelezniak. CHEMKED- A Program for Chemical Kinetics of Gas Phase Reactions. Software Documentation, 2007. <http://www.chemked.com>.
- [172] Scientific Instrument Services Inc. SIMION 8.0.4, 2008. <http://www.simion.com>.
- [173] D. R. Lide, editor. *CRC Handbook of Chemistry and Physics, 84th edition*. CRC Press, Boca Raton, 2003.
- [174] M. Jelezniak and I. Jelezniak. Reaction Kinetics Simulation. Software Documentation, 2008. [http://mark.jelezniak.de/chemical\\_reactions/samples.pdf](http://mark.jelezniak.de/chemical_reactions/samples.pdf).
- [175] M. Jelezniak and I. Jelezniak. Differential Equations of Gas-Phase Chemical Kinetics. Software Documentation, 2009. [http://chemked.com/aux\\_files/difeq.pdf](http://chemked.com/aux_files/difeq.pdf).

## Bibliography

- [176] C. Polaczek. *Untersuchung protonengebundener Clustersysteme mithilfe eines Atmosphärendruck- Ionenmobilitätsspektrometers*. Bachelor thesis, Bergische Universität Wuppertal, Germany, 2013.
- [177] W. Wißdorf, Y. Brachthäuser, C. Polaczek, P. Cochems, S. Zimmermann, and T. Benter. Field driven chemical effects in API: Numerical modeling of the ion temperature at atmospheric and intermediate pressure with SIMION-RS. In *Proceedings of the 61th ASMS Conference on Mass Spectrometry and Allied Topics*. Minneapolis, MN, USA, 2013.
- [178] P. Cochems, W. Wissdorf, Y. Brachthäuser, C. Polaczek, T. Benter, and S. Zimmermann. Reduced ion mobilities: A need for parameterization of chemical analyte properties? In *Proceedings of the 61th ASMS Conference on Mass Spectrometry and Allied Topics*. Minneapolis, MN, USA, 2013.
- [179] C. E. Young. Water Cluster Ions: Formation and Decomposition of Cluster Ions in the Oxygen-Water System. *The Journal of Chemical Physics*, 57(2):918–929, 1972.
- [180] H. Kambara and I. Kanomata. Collision-induced dissociation of water cluster ions at high pressure. *International Journal of Mass Spectrometry and Ion Physics*, 25(2):129–136, 1977.
- [181] A. J. Midey, S. T. Arnold, and a. a. Viggiano. Reactions of  $\text{H}_3\text{O}^+(\text{H}_2\text{O})_n$  with Formaldehyde and Acetaldehyde. *The Journal of Physical Chemistry A*, 104(12):2706–2709, 2000.
- [182] L. A. Viehland and W. F. Siems. Uniform moment theory for charged particle motion in gases. *Journal of the American Society for Mass Spectrometry*, 23(11):1841–54, 2012.
- [183] G. Wannier. Motion of Gaseous Ions in a Strong Electric Field. I. *Physical Review*, 87(5):795–798, 1952.
- [184] L. Boltzmann. Weitere Studien über das Wärmegleichgewicht unter Gas-molekülen. In F. Hasenörl, editor, *Wissenschaftliche Abhandlungen*, pp. 316–403. Cambridge University Press, Cambridge, 2012.
- [185] H. Haug. *Statistische Physik*. Springer-Lehrbuch. Springer-Verlag, Berlin/Heidelberg, 2006.
- [186] C. Cercignani. *The Boltzmann Equation and Its Applications*, volume 67 of *Applied Mathematical Sciences*. Springer Science+Business Media, New York, 1988.
- [187] A. A. Shvartsburg. *Differential Ion Mobility Spectrometry: Nonlinear Ion Transport and Fundamentals of FAIMS*. CRC Press, Boca Raton, 2008.

- [188] J. Hornbeck. The Drift Velocities of Molecular and Atomic Ions in Helium, Neon, and Argon. *Physical Review*, 84(4):615–620, 1951.
- [189] H. E. Revercomb and E. A. Mason. Theory of plasma chromatography/gaseous electrophoresis. Review. *Analytical Chemistry*, 47(7):970–983, 1975.
- [190] E. Krylov and E. Nazarov. Electric field dependence of the ion mobility. *International Journal of Mass Spectrometry*, 285(3):149–156, 2009.
- [191] L. A. Viehland and E. Mason. Gaseous Ion mobility in electric fields of arbitrary strength. *Annals of Physics*, 91(2):499–533, 1975.
- [192] L. A. Viehland and E. Mason. Gaseous ion mobility and diffusion in electric fields of arbitrary strength. *Annals of Physics*, 110(2):287–328, 1978.
- [193] L. A. Viehland and S. Lin. Application of the three-temperature theory of gaseous ion transport. *Chemical Physics*, 43(1):135–144, 1979.
- [194] L. A. Viehland and Y. Chang. Beyond the Monchick–Mason approximation: the mobility of  $\text{Li}^+$  Ions in  $\text{H}_2$ . *Molecular Physics*, 110(5):259–266, 2012.
- [195] S. Robertson and Z. Sternovsky. Monte Carlo model of ion mobility and diffusion for low and high electric fields. *Physical Review E*, 67(4):046405, 2003.
- [196] G. Balla and A. D. Koutselos. Molecular dynamics simulation of ion transport in moderately dense gases in an electrostatic field. *The Journal of Chemical Physics*, 119(21):11374–11379, 2003.
- [197] R. W. Purves, D. a. Barnett, and R. Guevremont. Separation of protein conformers using electrospray-high field asymmetric waveform ion mobility spectrometry-mass spectrometry. *International Journal of Mass Spectrometry*, 197(1-3):163–177, 2000.
- [198] E. Krylov, E. G. Nazarov, R. a. Miller, B. Tadjikov, and G. a. Eiceman. Field dependence of mobilities for gas-phase-protonated monomers and proton-bound dimers of ketones by planar field asymmetric waveform ion mobility spectrometer (PFAIMS). *The Journal of Physical Chemistry A*, 106(22):5437–5444, 2002.
- [199] H. Ellis, R. Pai, E. McDaniel, E. Mason, and L. Viehland. Transport properties of gaseous ions over a wide energy range. *Atomic Data and Nuclear Data Tables*, 17(3):177–210, 1976.
- [200] H. Ellis, E. McDaniel, D. Albritton, L. Viehland, S. Lin, and E. Mason. Transport properties of gaseous ions over a wide energy range. Part II. *Atomic Data and Nuclear Data Tables*, 22(3):179–217, 1978.

## Bibliography

- [201] H. Ellis, M. Thackston, E. McDaniel, and E. Mason. Transport properties of gaseous ions over a wide energy range. Part III. *Atomic Data and Nuclear Data Tables*, 31(1):113–151, 1984.
- [202] L. Viehland and E. Mason. Transport Properties of Gaseous Ions over a Wide Energy Range, IV. *Atomic Data and Nuclear Data Tables*, 60(1):37–95, 1995.
- [203] Y. Brachthäuser. *Aufbau, Inbetriebnahme und Charakterisierung eines AP-IMS*. Master thesis, Bergische Universität Wuppertal, Germany, 2013.
- [204] S. Klee, V. Derpmann, W. Wißdorf, S. Klopotoski, H. Kersten, K. J. Brockmann, T. Benter, S. Albrecht, A. P. Bruins, F. Dousty, T. J. Kauppila, R. Kostianen, R. O’Brien, D. B. Robb, and J. Syage. Are Clusters important in understanding the Mechanisms in Atmospheric Pressure Ionization? Part 1 + 2, 2013.
- [205] R. T. Kelly, A. V. Tolmachev, J. S. Page, K. Tang, and R. D. Smith. The ion funnel: Theory, implementations, and applications. *Mass Spectrometry Reviews*, 29(2):294–312, 2010.
- [206] R. R. Julian, S. R. Mabbett, and M. F. Jarrold. Ion funnels for the masses: experiments and simulations with a simplified ion funnel. *Journal of the American Society for Mass Spectrometry*, 16(10):1708–12, 2005.
- [207] R. S. Blake, P. S. Monks, and A. M. Ellis. Proton-transfer reaction mass spectrometry. *Chemical reviews*, 109(3):861–96, 2009.
- [208] S. K. Ross, G. McDonald, and S. Marchant. The use of dopants in high field asymmetric waveform spectrometry. *The Analyst*, 133(5):602–7, 2008.
- [209] D. Koks. *Explorations in Mathematical Physics: The Concepts Behind an Elegant Language*. Springer, New York, 2006.